HAL
open science

A V-shape superconducting artificial atom for circuit quantum electrodynamics

Etienne Dumur

To cite this version:

Etienne Dumur. A V-shape superconducting artificial atom for circuit quantum electrodynamics. Condensed Matter [cond-mat]. Université Grenoble Alpes, 2015. English. NNT : 2015GREAY003 . tel-01147222

HAL Id: tel-01147222

https://theses.hal.science/tel-01147222v1

Submitted on 30 Apr 2015

HAL is a multi-disciplinary open access archive for the deposit and dissemination of scientific research documents, whether they are published or not. The documents may come from teaching and research institutions in France or abroad, or from public or private research centers.

L'archive ouverte pluridisciplinaire **HAL**, est destinée au dépôt et à la diffusion de documents scientifiques de niveau recherche, publiés ou non, émanant des établissements d'enseignement et de recherche français ou étrangers, des laboratoires publics ou privés.

UNIVERSITÉ DE GRENOBLE

THÈSE

Pour obtenir le grade de

DOCTEUR DE L'UNIVERSITÉ DE GRENOBLE

Spécialité : **Physique**

Arrêté ministériel : 7 août 2006

Présentée par

Étienne Dumur

Thèse dirigée par **Olivier Buisson**

préparée au sein de **l'institut Néel, CNRS**
et de **l'école Doctorale de Physique**

A V-shape superconducting artificial atom for circuit quantum electrodynamics

Thèse soutenue publiquement le **4 février 2015**,
devant le jury composé de :

M. Frank Hekking
Prof, LPMMC, Président
M. Denis Vion
Dr, CEA-Saclay, Rapporteur
M. Evgeni Ilichev
Prof, IPHT, Rapporteur
M. Jean-Michel Raimond
Prof, LKB, Examinateur
M. Göran Johansson
Prof, Chalmers, Examinateur
M. Olivier Buisson
Dr, Insitut Néel, Directeur de thèse
M. Max Hofheinz
Dr, CEA-Grenoble, Co-encadrant de thèse

Remerciement

Je tiens tout d'abord à remercier Dr. Denis Vion et Prof. Evgeni Ilichev pour avoir accepté d'être les rapporteurs de mon rapport de thèse. Je les remercie particulièrement d'avoir respecté les délais imposés par l'école doctorale malgré leur travail. Je remercie également Prof. Jean-Michel Raimond et Prof. Gorän Johansson d'avoir accepté d'en être les examinateurs. Enfin, un grand merci au Prof. Frank Hekking pour avoir accepté d'être le président de mon jury, j'en retire une grande fierté personnelle.

Merci à Olivier Buisson pour avoir été mon encadrant de thèse. Si au début de ma thèse ta hantise des « boîtes noires » me faisait sourire, tu as réussi à me transmettre le goût du modèle discuté dans le coin d'un tableau. Merci pour ta pugnacité dans toutes choses, ta disponibilité, ton sens physique et ton appétit à l'égard de mes pâtisseries. J'espère avoir été à la hauteur des attentes du grand chef.

Je remercie également le reste de l'équipe : Alexey Feofanov, Bruno Küng, Thomas Weißl, Cécile Naud, Wiebke Guichard, Yuriy Krupko et le petit nouveau Nicolas Roch. C'était quand même bien sympathique de travailler avec vous tous, je vous souhaite le meilleur pour l'avenir. Un merci particulier pour Bruno Küng qui est devenu au fil des mois plus qu'un collègue. Ça a été très agréable de travailler avec toi, la Suisse peut être fière. Le mot de la fin : « Chrüterchraft ». J'en profite pour souhaiter un bon stage et une bonne thèse à mon remplaçant Rémy Dassonneville. Je te lègue absolument tout, fais en bon usage.

J'ai eu la chance d'être co-encadré par Max Hofheinz que je remercie également. Ta compréhension des systèmes d'électrodynamique quantique m'impressionnera toujours.

J'ai démarré ma thèse avec un cryostat à dilution câblé et fonctionnel. Pour cela, je remercie Iulian Mattei, Pierre Chanthib, Olivier Tissot et Cyril Bruyère.

Une thèse expérimentale est confrontée sans cesse à des « soucis techniques » qui seraient hautement problématiques sans l'aide des services techniques de l'institut Néel. Je remercie le service « Électronique » et « Cryogénie » et en particulier Christophe Hoarau, Olivier Exshaw et Guillaume Donnier-Valentin pour leur aide toujours appréciable. Merci aussi à l'équipe de NanoFab qui garde le sourire malgré tout ce qu'on leur demande. Enfin, merci au service administratif et particulièrement à Sabine Gadal et Florence Pois.

Un projet parallèle à l'étude du système « V-shape » a été l'étude de résonateur micro-onde gravé en rhénium. Je remercie Bruno Gilles, Benjamin Delsol et Kitty Ratter pour nous avoir

fourni les couches de rhénium épitaxiés.

Je remercie Alessandro Monfardini et Nicolas Boudou pour les discussions sur les résonateurs micro-ondes, les filtres et les peintures absorbantes. Grâce à vous, une meilleure compréhension des facteurs de qualité a été possible.

Je remercie Alexia Auffèves et Igor Diniz pour les nombreuses discussions enrichissantes sur la théorie « input-output » appliquée à notre circuit.

Une importante partie de mes trois années de thèse a été dévolue à l'enseignement à l'IUT « Mesures Physiques » (MPh) et « Génie Mécanique et Productique » (GMP). Durant ce travail, j'ai pu rencontrer des personnes d'une grande générosité que je remercie aujourd'hui. Un grand merci à Zette pour tout le travail qu'elle réalise à l'IUT MPh. Sans elle l'IUT tournerait sûrement moins bien (ou s'effondrerait, au choix). Merci au Prof. Frédéric Bossard pour m'avoir intégré à l'équipe pédagogique de l'IUT GMP. C'était un plaisir de discuter et de préparer les cours avec vous. Merci à Céline Dalla-Costa, François Montanet et Loïc Laplatine pour l'encadrement des TD et TP donnés à l'IUT MPh. Enfin, merci à Denis Buttard qui a compris mon désir d'autonomie et m'a laissé enseigner sans contraintes.

Un merci spécial à la communauté du logiciel libre, le travail que vous abattez est colossal.

Un grand merci à toute l'équipe des non-permanents, je suis très heureux d'avoir partagé les diverses joies et peines de la thèse avec vous. Sans se mentir, on a quand même été un bon cru ! Je suis heureux d'avoir assisté à la naissance du mythe « Benoit Bertrand », courage à celui qui voudra te surpasser. Je remercie Martial Defoort pour son amitié indéfectible depuis cinq ans maintenant. En avoir bavé à tes côtés durant toutes ces années a rendu le voyage plus doux.

L'homme que je suis devenu doit énormément à certaines personnes que j'ai croisées le long de mon chemin. Je profite alors de l'occasion qui m'est donné pour remercier chaleureusement David Heini, tu m'as tellement apporté que je ne peux imaginer ce qu'aurait été ma vie sans toi; Guillaume Ferreres, tu as été un exemple pour moi et sans toi je ne saurais sans doute pas allé si loin. Un grand merci à la « bande du 18 » et à la « bande de Morez », notre amitié vit depuis plus de dix ans désormais et c'est un honneur d'être à vos côtés.

Maman et Papy, la vie n'a pas toujours été rose mais vous avez toujours été là pour moi. Merci de m'avoir soutenu sans jamais comprendre un mot de ce que je faisais. Papy, tu as été mon modèle, j'espère être digne de ton héritage.

Le mot de la fin sera pour cette demoiselle si jolie qu'il m'a fallu des années pour oser l'aborder et qui partage désormais ma vie. Te voir sourire illumine toujours autant mon cœur.

"*I think I can safely say that nobody understands quantum mechanics*"

Richard Feynman, in The Character of Physical Law (1965)

Contents

Page

Introduction and summary **11**

1 Theory **45**
1.1 The 2D-SQUID . . . 45
1.1.1 Josephson junction dynamics . . . 45
1.1.2 Classical dynamics of a current and flux biased SQUID . . . 48
1.1.3 Quantum dynamics of the SQUID . . . 58
1.1.4 A V-shape artificial atom . . . 68
1.2 Microwave resonator . . . 69
1.2.1 Transmission line . . . 70
1.2.2 Quarter-wave resonator . . . 71
1.2.3 The current and voltage quantum operators . . . 72
1.3 The V-shape device coupled to a quarter-wave resonator . . . 74
1.3.1 Coupling between the SQUID and the electromagnetic field . . . 75
1.3.2 Logical and ancilla qubits coupled to the fundamental mode of the resonator . . . 76
1.4 Transmission of the V-shape device coupled to a $\lambda/4$ resonator . . . 77
1.4.1 Input-Output theory of a resonator evanescently coupled . . . 78
1.4.2 Logical-qubit readout . . . 80

2 Setup **91**
2.1 Dilution refrigerator . . . 92
2.2 Low temperature microwave setup . . . 92
2.2.1 Thermalisation . . . 93
2.2.2 Amplification chain . . . 98
2.3 Room temperature microwave setup . . . 103
2.3.1 Microwave pulse generation . . . 105
2.3.2 Device synchronisation . . . 106
2.3.3 Frequency down–conversion . . . 107

2.3.4 Data acquisition . . . 108
2.3.5 Transmission coefficient measurement . . . 110
2.3.6 Noise of the measured signal . . . 110
2.4 Software environment . . . 113
2.4.1 Python . . . 113
2.4.2 Qtlab . . . 113
2.5 Superconducting coil . . . 115
2.6 Sample holder . . . 116
2.6.1 Presentation . . . 116
2.6.2 Microwave properties . . . 119
2.7 Shielding . . . 121
2.7.1 Electromagnetic shielding . . . 121

3 Sample fabrication 123
3.1 Introduction . . . 123
3.2 Aluminium quantum circuits . . . 124
3.2.1 Design considerations . . . 124
3.2.2 Fabrication of the different patterns . . . 132
3.2.3 A fight against the screening effect . . . 140
3.2.4 Test junctions . . . 140
3.3 Rhenium microwave resonators . . . 143
3.3.1 Epitaxy of rhenium . . . 144
3.3.2 Design of coplanar waveguide resonator . . . 147
3.3.3 Microwave resonator fabrication . . . 149

4 Superconducting quarterwave microwave resonators 153
4.1 Introduction . . . 153
4.2 Model of the quarterwave resonator . . . 154
4.3 Lumped–element model . . . 154
4.4 Transmission of a feedline capacitevely coupled to a quarterwave resonator . 156
4.4.1 Why certain resonances are asymmetric ? . . . 157
4.5 Rhenium microwave resonator . . . 159
4.5.1 Extraction of resonator parameters . . . 159
4.5.2 Measurement of the resonance frequency as function of temperature . 162
4.5.3 Low internal quality factor . . . 167
4.6 Aluminium resonators . . . 168
4.6.1 Characterisation of the resonance . . . 168
4.6.2 A tunable resonance frequency . . . 171

5 The V-shape superconducting artificial atom 175
5.1 Introduction . . . 176
5.2 The V-shape coupled to a resonator . . . 176
5.2.1 Two-tone spectroscopy . . . 176
5.2.2 Spectroscopy as function of the magnetic field . . . 178

5.2.3 Extraction of the V-shape parameters 181
5.2.4 Estimation of the coupling strength 185
5.3 Logical qubit 185
5.3.1 Coherent oscillations 185
5.3.2 Coherent oscillations as function of detuning and power 188
5.3.3 Relaxation time 191
5.3.4 AC-Stark shift and measurement-induced dephasing 192
5.3.5 Dependence of the qubit coherence versus probe power 196
5.4 Logical qubit anharmonicity measurements 200
5.4.1 Two-photon process 200
5.4.2 Direct spectroscopy of the second level of the *in-phase* mode 201
5.4.3 A transition forbidden at $\phi_b = 0$ 203
5.5 Ancilla qubit 204
5.5.1 Coherent oscillations of the ancilla qubit 204
5.5.2 Relaxation time of the ancilla qubit 206
5.6 Cross-anharmonicity 208
5.6.1 Measurement via pulse sequence 208
5.6.2 Measurement via continuous drive 210
5.7 Experimental realisation of a V-shape energy diagram ? 212

Conclusion and perspectives **213**

Appendices **223**

A Software environment **223**

B Derivation of the quarter-wave resonator transmission **227**
B.1 Symmetric model 228
B.1.1 Calculation of the shift in frequency caused by the coupling capacitor 228
B.1.2 Calculation of the coupling capacitance Q_c 230
B.1.3 Calculation of the transmission coefficient S_{21} 230
B.2 Asymmetric model 231
B.3 Result 233
B.3.1 Coupling capacitor 233
B.3.2 Spurious inductance 233
B.3.3 Approximation verification 234

C Samples parameters **235**

D Corrected eigenstates **237**

Bibliography **241**

Introduction and summary

Français

Introduction

Calculateur quantique

Le concept d'utiliser des ordinateurs quantiques pour surpasser les limitations des ordinateurs classiques a été introduit par Richard Feynman en 1982[1]. Les ordinateurs quantiques sont différents des ordinateurs classiques basés sur les transistors. Alors que les ordinateurs numériques requièrent des données encodées en éléments binaires (bits), chacun d'entre eux étant toujours dans un des deux états prédéfinis (0 ou 1), les ordinateurs quantiques utilisent des qubits (quantum bits), qui peuvent être dans une superposition d'états. Avec un ordinateur classique, l'information est encodée par la présence ou l'absence d'un courant/tension électrique. Ainsi, l'état d'un transistor est allumé *ou* éteint. Formellement, un qubit est un système de mécanique quantique à deux niveaux qui peut être écrit par:

$$\left|\psi_{\mathrm{qb}}\right\rangle = \alpha\left|g\right\rangle + \beta\left|e\right\rangle \tag{1}$$

ou $|\alpha|^2 + |\beta|^2 = 1$. Un ensemble de n qubit (classique ou quantique) supporte 2^n états différents. Cependant un ordinateur classique peut être seulement dans un état à la fois. La puissance d'un ordinateur quantique tient dans sa capacité à être dans tous les états à la fois par superposition de ses n qubits. Une opération quantique est alors effectuée sur l'ensemble complet des états superposés. Des algorithmes quantique exploitant la particularité des ordinateurs quantiques existent déjà. Nous pouvons citer l'algorithme de Shor[2] qui permet la factorisation de grands nombres, l'algorithme de Grover[3] pour la recherche d'éléments dans une base de données non triée et l'échantillonnage de Métroplis[4] pour simuler des systèmes quantiques génériques.

Le développement d'un ordinateur quantique est un défi important dût au problème de décohérence. Une conséquence de la décohérence est le comportement probabiliste ou classique. En effet, un ordinateur quantique sans cohérence devient similaire à un ordinateur probabiliste classique. Garder la cohérence d'un système revient souvent à isoler ce système de son environnement. Cependant, sans mentionner la difficulté expérimentale d'une telle

tâche, un ordinateur quantique doit aussi être connecté au monde extérieur afin de recevoir et de transmettre de l'information. DiVincenzo[5,6] lista, dans un ensemble de cinq critères, les différent prérequis d'un ordinateur quantique:

- Le nombre de qubit est extensible,
- Les qubits peuvent être initialisés dans des états arbitraires,
- Les opérations sur les portes logiques s'effectuent plus rapidement que la décohérence,
- Il est possible d'implémenter un ensemble de portes logiques universelles,
- Les qubits peuvent être lus facilement.

Qubits supraconducteurs

En physique du solide, un candidat prometteur pour réaliser un qubit est le circuit quantique supraconducteur à base de jonctions Josephson. Les variables conjuguées décrivant la dynamique électronique d'une jonction Josephson sont le nombre de Paire-de-Cooper et la différence de phase au travers de la jonction. En choisissant la forme de la jonction, il est possible de fixer une variable et, par conséquent, d'avoir une grande indétermination sur sa conjuguée associée. Ainsi, lorsque la charge est bien déterminée, on parle alors de qubit de « charge » et lorsque la phase est bien déterminée, on parle de qubit de « phase ». Il est aussi possible de concevoir une jonction dans laquelle l'indétermination sur la charge et la phase est égale. Ce type de qubit est appelé « charge-phase » qubit.

Nous devons également mentionner le qubit de « flux » qui correspond à une boucle de métal supraconducteur interrompu habituellement par trois jonctions Josephson[7].

La première observation d'une quantification des niveaux d'énergie a été réalisée par Michel H. Devoret, John M. Martinis, Daniel Esteve, and John Clarke[8–10] en 1984–1985. En 1999, Nakamura *et al.*[11] démontrèrent la première manipulation cohérente d'un état quantique dans un qubit de charge. Pour ces expériences pionnières, le temps de cohérence des qubits était en deçà de 2 ns. Cependant, la cohérence des qubits de charge était limitée par les fluctuations de charge inhérent aux circuits électriques. Les qubits de phase atteignirent pour leur part des temps de cohérence de plusieurs centaines de nanoseconds[12–14]. Les qubit de phase souffraient de couplages parasites avec des systèmes à deux niveaux présents dans l'environnement ou directement dans la couche isolante de la jonction. En effet, la forme du qubit de phase oblige la fabrication de jonctions ayant une grande aire ce qui augmente la probabilité de coupler la jonction avec des systèmes à deux niveaux parasites. Le qubit de charge-phase, avec une petite aire de jonction et sans sensibilité aux fluctuations de charge à son point de fonctionnement optimal, a atteint des temps de cohérence de 500 ns[15].

En 2004, quatre ans après une proposition théorique[16,17], des expériences en électrodynamique de circuits supraconducteurs ont été démontrées en premier sur des qubits de charge. En 2007, J. Koch *et al.*[18] proposèrent un forme de qubit original, le transmon. La particularité du transmon est d'avoir un rapport entre l'énergie de charge et l'énergie Josephson auquel les premiers niveaux d'énergie sont insensibles aux bruits de charge. De

plus, ce rapport permet la fabrication de très petites jonctions limitant la probabilité de couplage avec des systèmes à deux niveaux parasites. Récemment, de tels transmons ont atteint un $T_1 = 9.7\,\mu s$ et un temps de cohérence de Ramsey de $T_2^* = 10.3\,\mu s$ en 2012[19], et un $T_1 = 53\,\mu s$ et un $T_2^* = 58\,\mu s$ en 2013[20]. Une augmentation du temps de cohérence du système a été obtenue en remplaçant le résonateur micro-onde bi-dimensionnel avec une cavité tri-dimensionnelle. De cette façon, le transmon 3D a atteint un $T_1 = 60\,\mu s$ et un $T_2^* = 10-20\,\mu s$ en 2011[21], et un $T_1 = 70\,\mu s$ et un $T_2^* = 92\,\mu s$ en 2012[22].

Finalement, nous soulignons le travail récent réalisé sur le fluxonium, une forme de qubit original menant à une insensibilité parfaite aux fluctuations de charge[23–25]. De tels qubits dans une cavité 3D ont exhibé[26] un temps de relaxation de $T_1 \approx 1000\,\mu s$ et un $T_2^* = 14\,\mu s$.

Mesure dispersive d'un qubit supraconducteur

Avec le circuit supraconducteur utilisant le transmon, la lecture de l'état du qubit dépend du couplage dispersif entre le qubit et le résonateur micro-onde. À travers ce couplage dispersif, il est possible de réaliser une mesure quantique non-destructive de l'état du qubit en sondant la fréquence de résonance du résonateur. En effet, le plus simple Hamiltonien d'un qubit couplé à un résonateur est donné par [18,27–31]:

$$\mathscr{H} = \underbrace{\hbar\omega_r\widehat{n}}_{\text{resonator}} + \underbrace{\frac{\hbar}{2}\omega_{qb}\widehat{\sigma}_z}_{\text{qubit}} + \underbrace{\frac{\hbar}{2}\chi\widehat{\sigma}_z\widehat{n}}_{\text{dispersive coupling}} \tag{2}$$

avec ω_r et ω_{qb} la fréquence angulaire de résonance du résonateur et du qubit, respectivement. L'opérateur $\widehat{n}$ donne le nombre de photons dans le mode de cavité et $\widehat{\sigma}_z$ est la matrice Pauli de l'état du qubit. La force du couplage dispersive $\chi = g^2/\Delta$ est le rapport entre la force de couplage g - entre le résonateur et le qubit - et le désaccord de fréquence Δ - entre la fréquence de résonance de la cavité et la fréquence de résonance du qubit. Il y a alors un compromis entre la force du couplage g et le désaccord de fréquence Δ: un important couplage dispersif conduit à un important rapport signal-sur-bruit en augmentant la différence de signal entre les deux états du qubit. Cependant, un important couplage dispersif implique un important couplage entre le résonateur et le qubit conduisant à une augmentation de la décohérence par effet Purcell[32].

La première lecture par couplage dispersif dans les circuits quantiques supraconducteurs donna une fidélité de lecture d'environ $\mathscr{F} = 30\,\%$ pour un temps d'intégration de $7\,\mu s$[33]. La faible fidélité de lecture par mesure dispersive était due à un faible rapport signal-sur-bruit. En effet, la puissance de signal utilisée pour réaliser la lecture de l'état du qubit doit être suffisamment faible pour ne pas induire des effets indésirables sur l'état du qubit[34]. Le signal transportant l'information sur l'état du qubit est alors de quelques photons par nano-secondes. De plus, lorsque le signal est amplifié, le bruit ajouté par un amplificateur paramétrique est extrêmement important comparé au signal sortant de l'amplificateur.

Une importante amélioration a été atteinte par le développement d'amplificateurs proches de la limite quantique basés sur l'amplificateur paramétrique Josephson[35]. Grâce à ces nouveaux amplificateurs, de plus hautes fidélités ont été atteintes. Par exemple, une fidélité de 98 % a été atteinte pour un temps d'intégration de 240 ns en 2013[36].

Ce type de lecture, basé sur des qubits couplés dispersivement à un résonateur micro-onde, semble avoir atteint sa limite. En effet, augmenter le rapport signal-sur-bruit implique d'augmenter la force de couplage dispersive χ ou le couplage du résonateur à la ligne de mesure micro-onde ce qui, dans les deux cas, augmentera l'effet Purcell.

Le diagramme d'énergie en V en optique quantique

Le diagramme d'énergie en V, défini en Fig. 1 (a), a été utilisé en optique quantique pour effectuer la lecture de l'état d'un qubit par fluorescence avec une fidélité exceptionnellement élevée[37] de l'ordre de 99.99 %. Originellement proposé par Dehmel*et al.* [38] et démontré plus tard par Wineland *et al.* [39], Nagourney *et al.* [40], Sauter *et al.* [41], et Bergquist *et al.* [42], la lecture consiste à exciter le système à la fréquence de résonance de l'ancillaire tout en mesurant la fluorescence de la transition de l'ancillaire. Dans la Fig. 1 (b), nous résumons le protocole de lecture d'un qubit logique via son qubit ancillaire dans une configuration en V. Le système est sondé avec un signal oscillant en résonance avec la transition de l'ancillaire à la fréquence $\omega_a/(2\pi)$. Lorsque le qubit est dans son état fondamental, il se produit de la fluorescence et le système est dit « brillant ». Lorsque le qubit est dans son état excité, il n'y a pas de transition disponible à la fréquence de l'excitation, il ne se produit aucune fluorescence, et le système est dit « sombre ». De cette manière, il est possible d'effectuer des mesures de l'état d'un qubit avec une très haute efficacité. Par exemple, nous montrons dans Fig. 2 l'observation de saut quantique d'un seul ion $^{138}Ba^+$ par Leibfried *et al.*[43] en 2003.

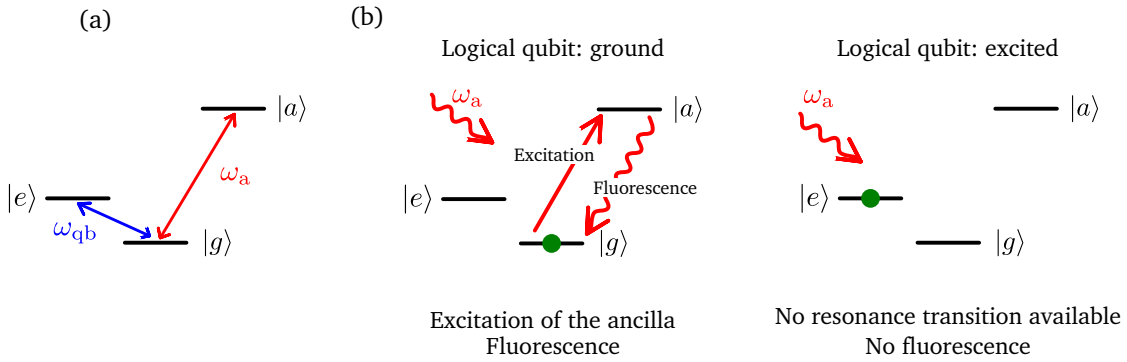

Figure (1): (a) Un diagramme d'énergie en V. Cela consiste en un qubit $|g\rangle$ et $|e\rangle$, montrant de bonnes propriétés de cohérence en parallèle avec un deuxième qubit, $|g\rangle$ et $|a\rangle$ réalisé par un deuxième degré de liberté. Le point clef d'un diagramme d'énergie en V est que toutes résonance depuis le niveau excité du qubit logique $|e\rangle$ à un niveau de plus haute énergie est hors résonance avec la transition de l'ancillaire $|g\rangle \rightarrow |a\rangle$. (b) Lecture de l'état du qubit logique par fluorescence. Un ton de lecture en résonance avec la transition de l'ancilla est envoyé. Lorsque le qubit logique est dans son état fondamental, de la fluorescence se produit. Le système est dit « brillant ». À l'inverse lorsque le qubit logique est dans son état excité, aucune transition en résonance avec le ton de lecture n'est disponible. Aucune fluorescence se produit, le système est alors dit « sombre ».

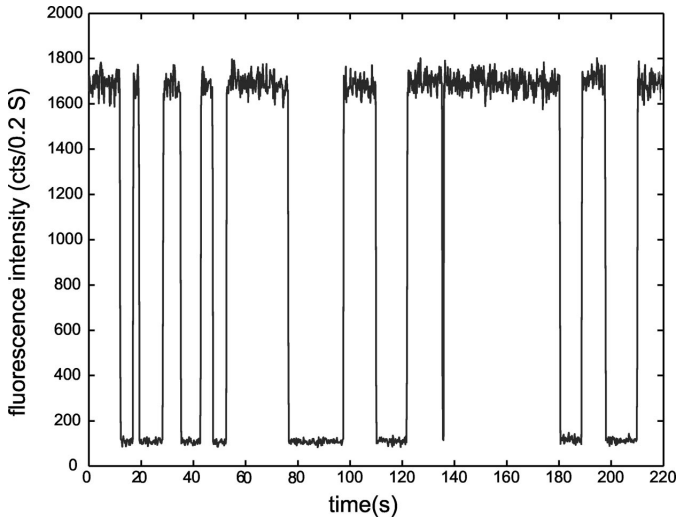

Figure (2): Saut quantique[41,43] *d'un ion* $^{138}Ba^{+}$*. Lorsque l'ion réalise la transition vers l'équivalent de l'état excité du qubit, la fluorescence chute. À l'inverse, lorsque l'ion relaxe vers l'équivalent de l'état fondamental du qubit, la fluorescence revient à son niveau initial.*

Résumé

La motivation de ma thèse était de concevoir et de réaliser un diagramme d'énergie en V en utilisant un atome artificiel supraconducteur et d'évaluer son potentiel pour effectuer la lecture de l'état d'un qubit.

Prédiction d'un diagramme d'énergie en V

Durant ma thèse, j'ai étudié la théorie d'un système quantique original composé de deux transmons couplés inductivement (voir Fig. 3 (a) et (b)). Lorsque l'inductance de couplage est de l'ordre de grandeur de l'inductance Josephson, ce circuit possède deux modes d'oscillation de la différence de phase à travers les jonctions : un premier mode, appelé mode « en-phase », correspondant à une oscillation en-phase de la différence de phase, et un second mode, appelé « hors-phase », correspondant à une oscillation hors-phase de la différence de phase (représentés par des flèches rouges et bleues sur la Fig. 3 (a), respectivement). En développant l'Hamiltonien du circuit par des séries de Taylor, je démontre l'anharmonicité de chaque mode ainsi que le couplage existant entre les deux modes. Le mode « en-phase » est équivalent au mode transmon, il montre une forte non-linéarité due à l'effet Josephson. Le mode « hors-phase » est principalement relié à l'inductance de couplage, son énergie est inversement proportionnelle à l'inductance. Il possède une faible anharmonicité. Un de ces couplages a été utilisé pour réaliser des conversions de fréquences cohérentes entre le premier état excité du mode « hors-phase » et le deuxième état excité du mode « en-phase »[13]. L'autre terme de couplage dénoté g_{zz}, est similaire au terme de couplage cross-Kerr : il modifie l'énergie d'un mode en fonction du nombre d'excitations présents dans l'autre mode. Dans la limite des faibles excitations, les modes « en-phase » et « hors-phase » peuvent être considérés comme deux qubits appelés ci-après logique et ancillaire, respectivement. Ils sont décris par des matrices de Pauli, σ_z^{qb} and σ_z^{a}. Le couplage cross-Kerr devient alors un couplage de type $\sigma_z^{qb}\sigma_z^{a}$ induisant un déplacement conditionnel de fréquence d'un qubit en fonction de l'état de l'autre qubit, voir Fig. 3 (d). Dans ce manuscrit, je ferai référence à cet effet soit comme une anharmonicité croisée soit comme un couplage cross-Kerr. Dans la limite d'une importante anharmonicité croisée, le diagramme d'énergie du circuit devient celui d'un diagramme d'énergie en V.

Nous avons considéré un atome artificiel incorporé dans une architecture d'électrodynamique de circuit quantique en utilisant un résonateur quart-d'onde. En suivant le travail d'Alexander Blais dans le cas d'un résonateur demi-onde[44], je calcule l'Hamiltonien d'un résonateur quart-d'onde. En considérant des excitations de basses énergies, seuls les couplages entre les qubits logique et ancillaire et le mode fondamental du résonateur doivent être pris en compte. Je montre alors, en utilisant la dépendance spatiale de l'amplitude de la tension et du courant le long du résonateur, ainsi que la nature différente des modes d'oscillation donnant lieu au deux qubits, qu'il est possible de coupler seulement un qubit au résonateur, l'autre restant alors complètement isolé du résonateur. Par exemple, en positionnant l'atome artificiel du coté du court-circuit d'un résonateur quart-d'onde, seulement le qubit ancillaire sera couplé au résonateur.

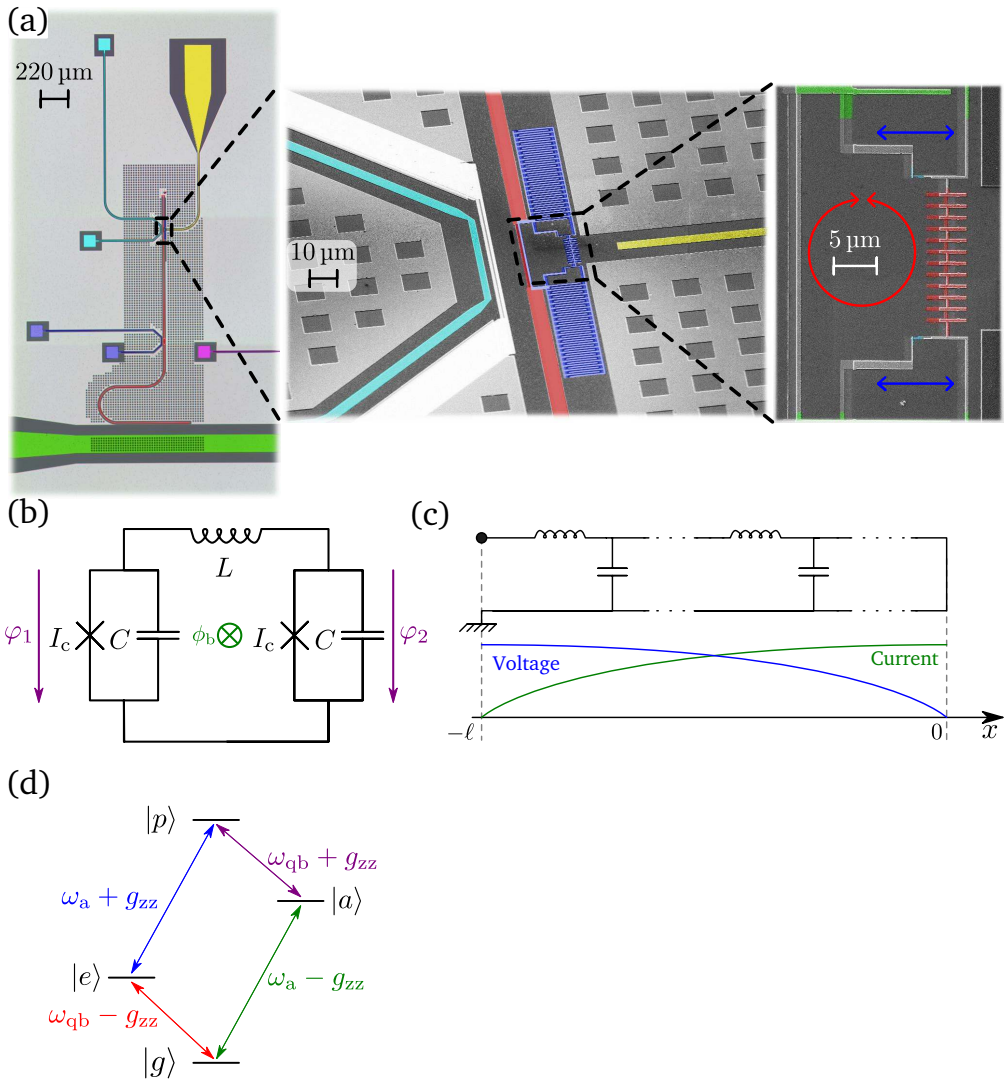

Figure (3): (a) Image MEB du circuit supraconducteur avec deux zooms successifs sur le circuit réalisant l'atome artificiel. (b) Schéma électrique équivalent de deux transmons couplés inductivement. (c) Schéma électrique équivalent d'un résonateur quart-d'onde avec une représentation de la dépendance spatiale de l'amplitude de la tension et du courant pour le mode fondamental. (d) Diagramme d'énergie de l'atome artificiel a $\phi_b = 0$. Lorsque le terme cross-Kerr g_{zz} est grand comparé à la largeur de résonance de la cavité, le diagramme d'énergie du système peut être considéré comme un diagramme d'énergie en V.

Étude théorique : Mesure quantique extrêmement rapide, de haute fidélité et non destructive

Dans ce manuscrit, je propose une méthode de lecture quantique extrêmement rapide, de haute fidélité et non destructive de l'état d'un qubit en utilisant un atome artificiel, ayant un diagramme d'énergie en V, couplé à un résonateur quart-d'onde dans une architecture d'électrodynamique de circuit quantique. Ce travail a été inspiré par un travail antérieur sur un résonateur demi-onde réalisé conjointement avec Igor Diniz[45]. Le circuit ainsi que la chaîne de mesure sont schématisés en Fig. 4. N'oublions pas que dû aux différentes natures des modes d'oscillations et de la position de l'atome artificiel dans le résonateur, seulement le qubit ancillaire est couplé au résonateur micro-onde. De cette façon, il est possible d'avoir un fort couplage g_{a} entre le qubit ancillaire et le résonateur tout en gardant le qubit logique isolé de son environnement. Les qubits ancillaire et logique sont couplés par le terme cross-Kerr g_{zz}.

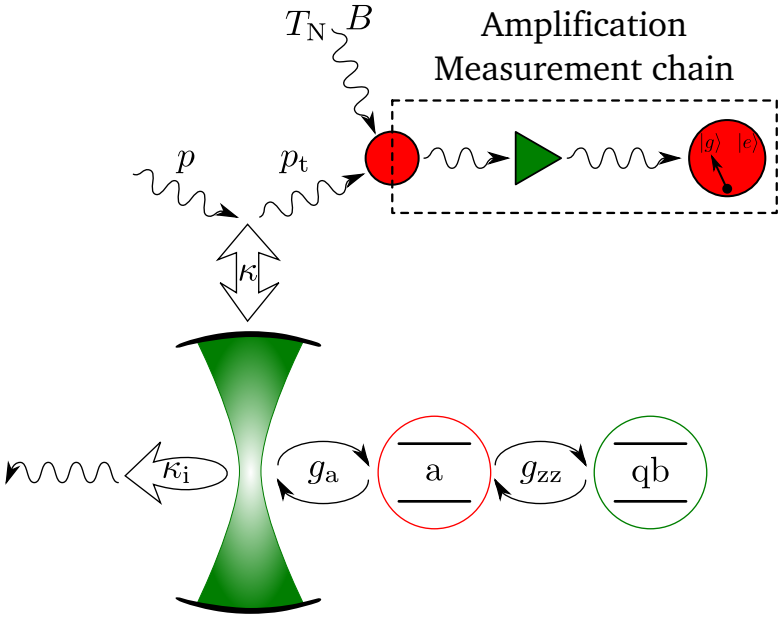

Figure (4): Schéma de la chaîne de mesure. Le qubit logique est couplé au qubit ancillaire par un couplage terme cross-Kerrg_{zz}. Le qubit ancillaire est couplé au résonateur avec une force de couplage dénotée g_a. À l'entrée du système, la puissance est notée p; à la sortie, la puissance transmise est notée p_t. Le résonateur est couplé à une feedline par κ. Les pertes internes du résonateur sont modelisées par une voie virtuelle ayant un couplage κ_i. La chaîne d'amplification est modélisée comme un simple amplificateur ayant une température de bruit T_N et une bande passante B. À la fin de la chaîne de mesure, le signal micro-onde est digitalisé et l'état du qubit est déduit à partir de l'amplitude du signal.

Afin de calculer la transmission du système, résonateur et atome artificiel, montré en Fig. 4, nous utilisons la théorie dite « input-output ». Dans la Fig. 5, nous montrons la transmission du système lorsque le qubit logique est dans son état fondamental, en bleu, et dans son

état excité, en vert. La transmission d'un tel circuit dépend fortement de l'état du qubit logique. On note que le déplacement de fréquence entre les deux plus proches pics atteint ici 110 MHz. Cette valeur est deux ordres de grandeur plus grande que les déplacements de fréquence usuellement obtenus en utilisant un couplage dispersif χ. Tirant parti de ce large déplacement de fréquence de la fréquence de résonance du résonateur en fonction de l'état du qubit, nous augmentons le couplage du résonateur avec la feedline, menant à une identification de l'état du qubit plus rapide. Encore une fois, l'augmentation du couplage entre le résonateur et la feedline n'engendre pas d'augmentation de l'effet Purcell puisque le qubit logique n'est pas couplé au résonateur.

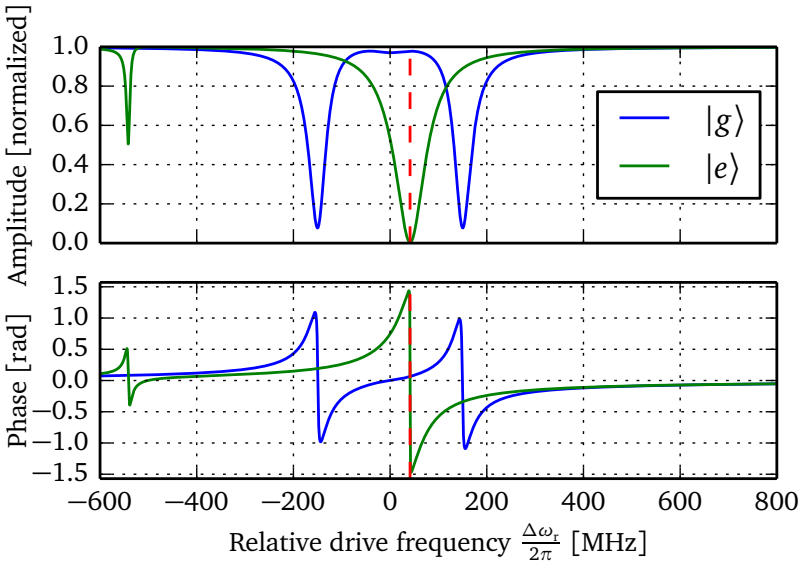

Figure (5): Transmission du système, résonateur et atome artificiel, en fonction de la fréquence d'excitation relative. La courbe bleue correspond à la transmission du système lorsque le qubit logique est dans son état fondamental tandis que la courbe verte correspond à la transmission du système lorsque le qubit logique est dans son état excité. En pointillés rouge, nous montrons la fréquence de contraste maximal entre le signal transmis lorsque le qubit logique est excité ou dans son état fondamental. Nous avons pris $g_{zz}/(2\pi) = 250$ MHz, $g_a/(2\pi) = 150$ MHz et la largeur de résonance $\kappa/(2\pi) = 40$ MHz.

Afin d'estimer la fidélité de lecture de l'état du qubit logique, nous avons pris en compte le bruit ajouté par la chaîne d'amplification, voir Fig. 4. En effet, la principale source de bruit est habituellement due au premier amplificateur de la chaîne d'amplification. Nous montrons en Fig. 6 des distributions de photons mesurés à la sortie de la chaîne de mesure. La fidélité est estimée à travers la superposition entre les deux distributions du nombre de photons obtenus pour les deux états du qubit. Nous notons que, dans le cas où un amplificateur proche de la limite quantique est utilisé ($T_N = 140$ mK et $B = 50$ MHz), une fidélité de 99.7 % peut être théoriquement atteinte avec une durée de mesure de seulement 50 ns. Pour atteindre cette

lecture optimale, le couplage entre le résonateur et la chaîne de mesure doit être important avec une largeur de résonance de $\kappa/(2\pi) = 40\,\text{MHz}$. Cela correspond à un facteur de qualité externe de $Q_c = 250$. Aussi, la puissance de lecture optimale a été estimée à quelques photons par nano-seconde. À large puissance, une saturation de l'ancillaire se produit menant à une perte de contraste.

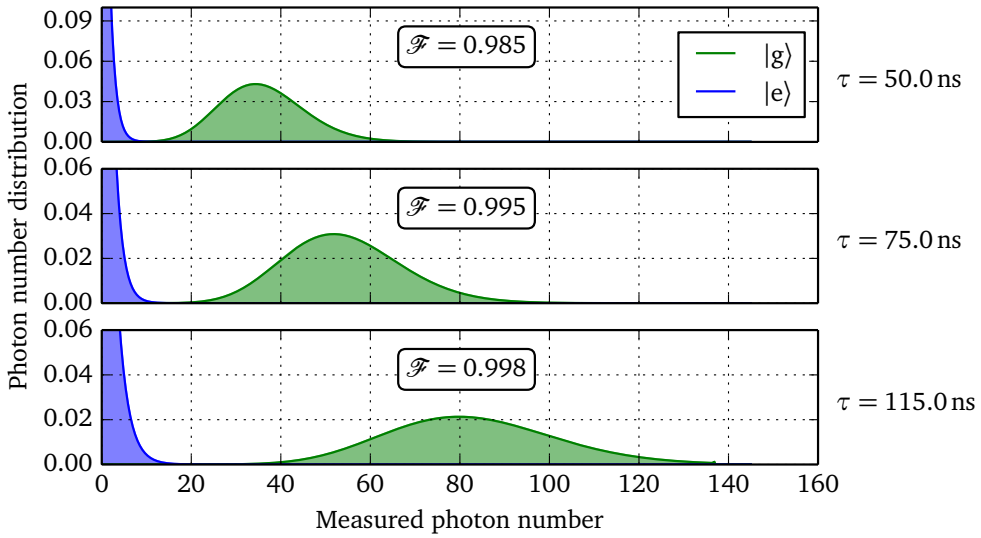

Figure (6): Évolution de la distribution de photons mesurés $\mathscr{F}$ suivant le temps de mesure τ. Les paramètres sont les mêmes que pour la Fig. 5. Nous avons pris une puissance d'entrée de $p = 1\,\text{photon.ns}^{-1}$, une bande passante de $B = 50\,\text{MHz}$, et une température de bruit $T_N = 140\,\text{mK}$. Le temps de mesure minimal utilisé pour le graphique correspond au temps de corrélation minimal permis par le circuit. Lorsque le temps de mesure augmente, la superposition des distributions de photons diminue ce qui mène à une plus haute fidélité.

Développements expérimentaux

Durant ma thèse et en collaboration avec Thomas Weißl, j'ai implémenté , une installation micro-onde complète capable de mesurer la transmission de nos circuits supraconducteurs. Nous avons calculé l'atténuation requise sur la ligne d'entrée pour atteindre la limite dite quantique où $\hbar\omega \gg k_B T$. À partir de ce calcul, nous avons installé des atténuateurs le long de la ligne coaxiale à différents étages du frigo à dilution avec une attention particulière sur la thermalisation. Nous avons estimé le bruit de photon résiduel à environ 1×10^{-3} photon à 7 GHz, la fréquence de résonance de nos résonateurs micro-ondes. La ligne coaxiale de sortie qui amplifie le signal transmis est composée de deux circulateurs et un amplificateur cryogénique connectés par un câble coaxial supraconducteur. Pour obtenir plus d'amplification deux amplificateurs complètent la chaîne à température ambiante. La ligne a été calibré expérimentalement, nous avons obtenu une température de bruit de $T_N = 4.5\,\mathrm{K}$ avec un gain d'environ 63 dB, en accord avec les données constructeur.

Nous avons implémenté, à température ambiante, une installation micro-onde capable de mesurer l'amplitude et la phase d'un signal transmis par méthode hétérodyne. De plus, j'ai codé un environnement Python a été codé afin d'effectuer les mesures avec des scripts Python. Ce travail inclus l'écriture de pilotes Python utilisant le protocole VISA « Virtual Instrument Software Architecture » pour plusieurs appareils comme des sources micro-ondes ou de courant, et l'écriture de divers objets Python. L'installation complète est capable d'effectuer des mesures de transmission micro-onde par méthode hétérodyne à très basse puissance, de l'ordre de 1 photon·ns^{-1} (≈ -110 dBm at 10 GHz).

La fabrication du circuit supraconducteur a été effectué par Alexey Feofanov et Bruno Küng à la « PTA » et à « Nanofab ». En parallèle de ce travail, j'ai développé un procédé de fabrication de résonateur micro-onde à partir de couche Rhénium épitaxié par Benjamin Delsol[46] durant sa thèse. La lithographie et le procédé de gravure a été réalisé à « Nanofab ».

Les résonateurs micro-ondes fabriqués à partir d'Aluminium ou de Rhénium ont été mesurés en utilisant notre installation expérimentale ou avec un analyseur de réseau vectoriel (VNA). La détermination des paramètres des cavités, comme les pertes internes et le couplage externe, est important pour caractériser le circuit quantique. Nous proposons un modèle analytique permettant l'extraction des paramètres des résonateurs. En particulier, ce modèle explique la forme asymétrique des figures de résonance mesurées au cours de ma thèse. Un exemple de forme de résonance est montré en Fig. 7. En pointillés rouges, nous montrons la forme de résonance théorique prédite par notre modèle. L'ajustement entre les données expérimentales et le modèle est très bon.

Démonstration expérimentale d'un diagramme énergétique en forme de V avec un atome artificiel

Le résultat principal de ma thèse est la réalisation et la démonstration expérimentales d'un atome artificiel avec un diagramme d'énergie en forme de V. Le circuit supraconducteur est montré en Fig. 3 (a) avec deux zooms successifs sur l'atome artificiel. Nous avons mesuré le spectre d'énergie de l'atome artificiel en fonction du champ magnétique par des spectroscopies deux-ton, voir Fig. 8. Ces mesures sont basées sur la lecture dispersive décrite plus tôt. Un

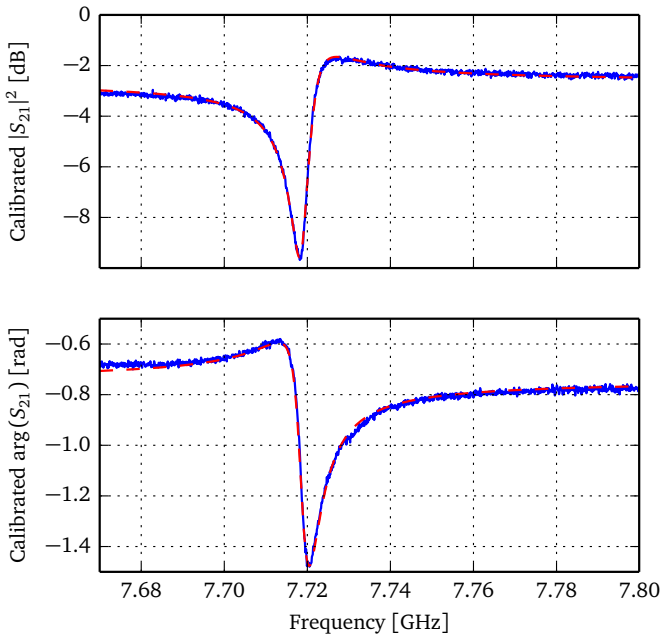

Figure (7): Résonance d'un résonateur micro-onde réalisé en Aluminium. Le panneau supérieur présente la transmission en décibel, et le panneau inférieur la différence de phase. Les pointillés rouges sont l'ajustement calculé à partir du modèle.

ton effectue la lecture de la transmission proche de la fréquence de résonance du résonateur tandis que le second ton effectue des balayages en fréquence pour sonder le spectre d'énergie de l'atome artificiel. En analysant la dépendance en flux magnétique des différents niveaux d'énergies, nous pouvons déduire quel niveau est dû au mode *en-phase* ou au mode *hors-phase*. Dans la Fig. 8, nous observons les deux premiers niveaux excités du mode « en-phase » qui semblent chuter à zéro à la moitié d'un quantum de flux, et le premier niveau excité du mode « hors-phase » qui atteint une limite à $\phi_b = \phi_0/2$. Ces mesures démontrent l'existence des deux modes de l'atome artificiel. De plus, nous avons numériquement résolu l'Hamiltonien du circuit quantique pour ajuster notre modèle théorique afin d'obtenir la dépendance en champ magnétique des résonances (pointillés rouges dans la Fig. 8). Les courbes théoriques sont en accord avec les résultats expérimentaux sauf aux abords de $\phi_0/2$.

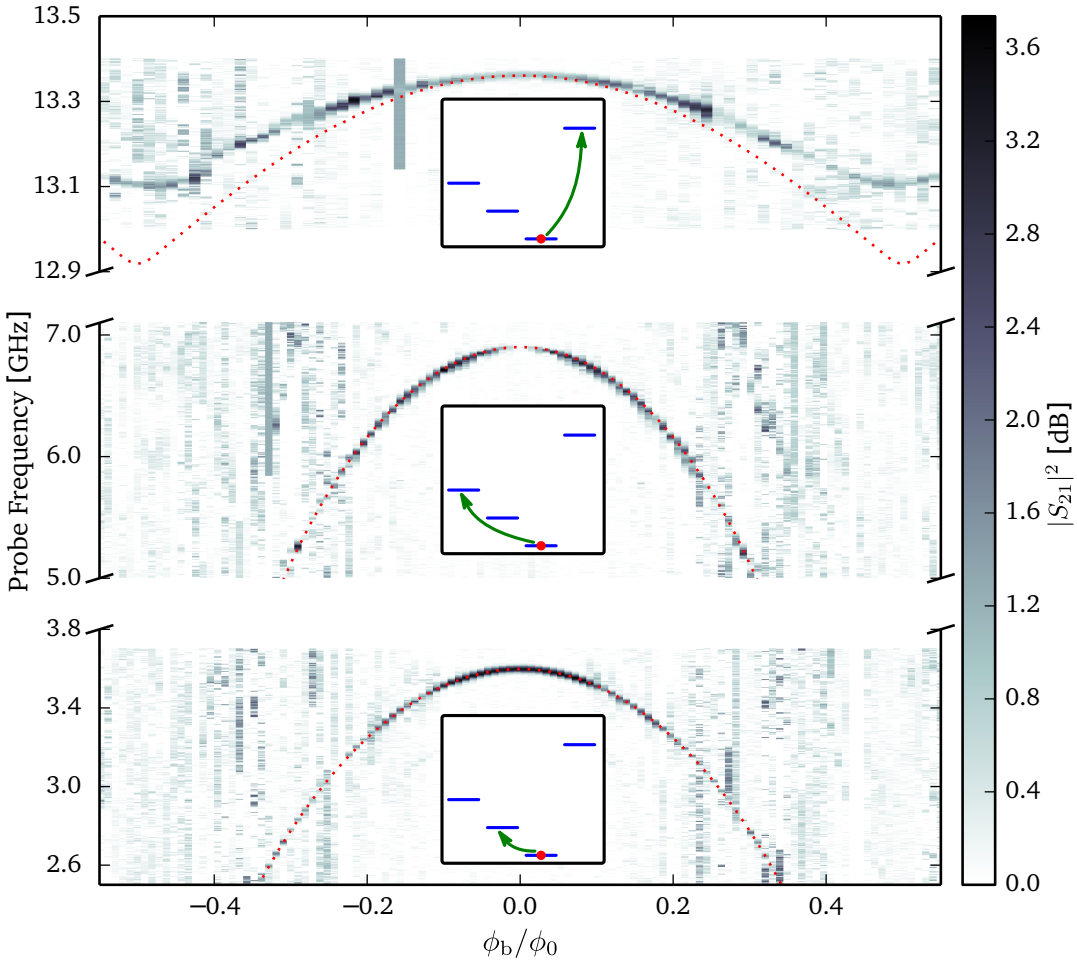

Figure (8): Spectroscopies deux-ton en fonction du champ magnétique pour l'échantillon « V-shape-2 ». Les deux premiers niveaux du qubit logique semblent chuter à zéro pour $|\phi_b| \approx 0.5$ *tandis que le qubit ancillaire atteint une limite. Pour chaque résonance mesuré, nous associons un encadré montrant, en diagramme d'énergie, la transition équivalente. En pointillés rouges, nous montrons la prédiction théorique.*

À $\phi_b = 0$, le système atteint un point « doux » où les niveaux d'énergie sont protégés au premier ordre contre le bruit de flux. Considérant seulement le premier niveau excité du mode *en-phase* et *hors-phase*, nous obtenons alors les qubits logique et ancillaire, Fig. 3 (d). Par des mesures résolues en temps, nous contrôlons l'état des deux qubits et nous extrayons leurs temps de relaxation et de cohérence. Dans la Fig. 9, nous montrons les oscillations cohérentes et les mesures de temps de relaxation pour les deux qubits.

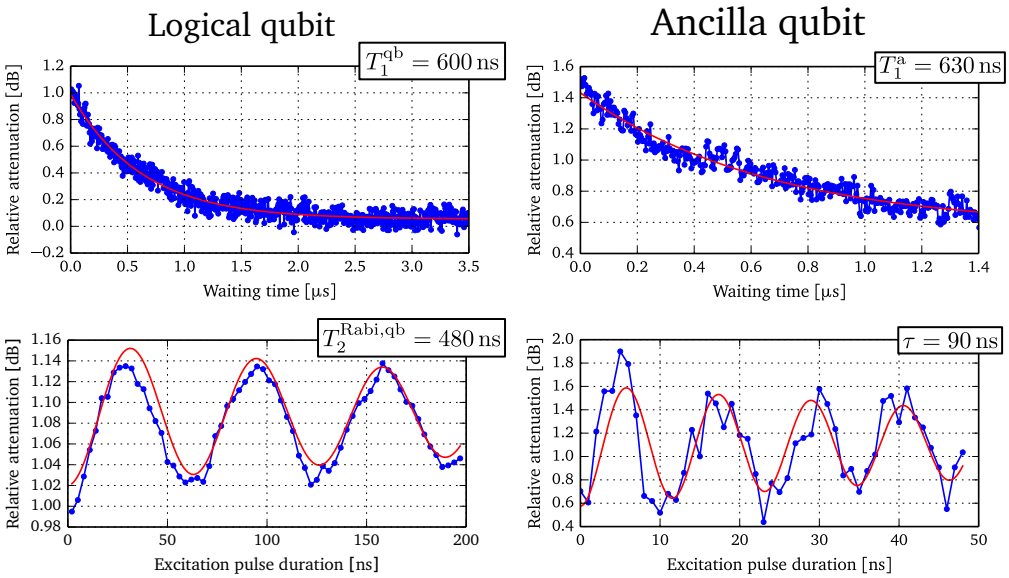

Figure (9): Relaxation et temps de décroissance pour les qubits logique et ancillaire.

Pour démontrer l'anharmonicité croisée, nous avons effectué des spectroscopies trois-ton. Par exemple, pour mesurer l'effet de l'anharmonicité croisée sur la fréquence de résonance du qubit logique nous avons réalisé l'expérience suivante. Nous effectuons la spectroscopie deux-ton précédemment discutée sur le qubit logique mais nous ajoutons un troisième ton en résonance avec la transition de l'ancillaire $\omega_a/(2\pi)$. La mesure est montrée en Fig. 10 (a) par en courbe bleu. Nous observons deux pics, un à la fréquence de résonance du qubit logique 3.634 GHz et un autre décalé de 110 MHz. Comme référence, nous mesurons la même courbe mais sans troisième ton pour exciter la transition de l'ancillaire (pointillés verts dans la Fig. 10 (a)). Nous observons le pic de résonance du qubit logique centré à 3.634 GHz.

Le pic de résonance du qubit correspond à la transition entre $|g\rangle \rightarrow |e\rangle$. Nous identifions le second pic comme la transition entre $|a\rangle \rightarrow |p\rangle$. Ce second pic est rendu possible grâce au troisième ton qui peuple le niveau d'énergie excité de l'ancilla. Le décalage en fréquence entre ces deux pics correspond alors à l'anharmonicité croisé $(2g_{zz})/(2\pi) = 110$ MHz.

Nous effectuons des mesures complémentaires pour tester la reproductibilité et la consistance de ces résultats. Nous interchangeons le rôle des qubits logique et ancillaire. Dans la Fig. 10 (b), nous traçons en pointillés verts et courbe bleu, une mesure montrant une spectroscopie autour de la fréquence de résonance de l'ancillaire tandis que le troisième ton sur le qubit logique est allumé et éteint, respectivement. Le résultat est parfaitement

consistant avec ce que nous montrons en Fig. 10 (a), avec une séparation de pic de 110 MHz.

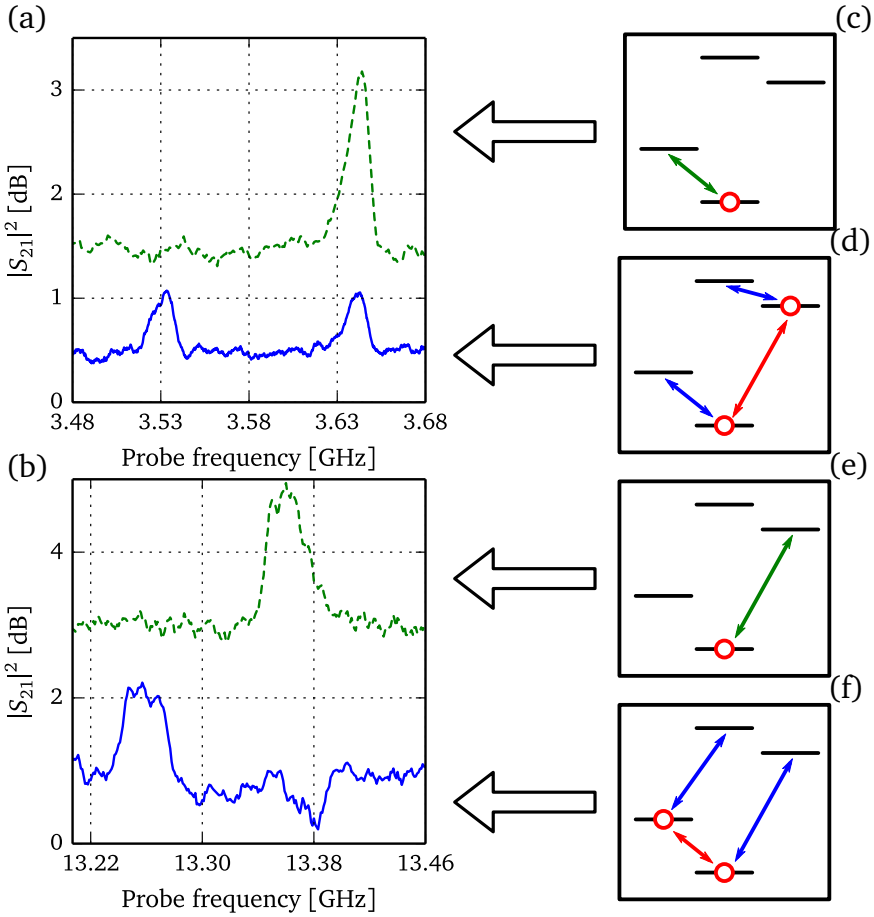

Figure (10): (a) Les pointillés verts supérieur correspondent à une spectroscopie deux-ton de la résonance du qubit, voir le diagramme d'énergie (c). Un ton d'excitation est appliqué constamment à la fréquence de transition de l'ancilla, tandis que le ton de sonde parcourt la transition du qubit logique, voir (d). Nous observons l'émergence d'un second pic séparé du pic de résonance du qubit logique par l'anharmonicité croisée $(2g_{zz})/(2\pi)$. *(b) Mesure de contrôle de l'anharmonicité croisée en échangeant le rôle des qubits logique et ancillaire, c'est à dire que le ton de sonde est balayé autour de la fréquence de résonance de l'ancillaire à* $\omega_a/(2\pi)$ *comme montré en (e) et (f). Les deux mesures sont consistantes entre-elles avec une anharmonicité croisée de* $(2g_{zz})/(2\pi) = 110\,\mathrm{MHz}$.

Organisation du manuscrit

Le manuscrit est divisé en cinq chapitres. Une description théorique de l'atome artificiel ainsi que du circuit quantique est donnée dans le premier chapitre. Dans le second chapitre, nous présentons l'installation expérimentale utilisée durant nos expériences et mise en place au début de ma thèse. La fabrication des échantillons est présentée en détail au chapitre trois. Un projet parallèle a été de fabriquer des résonateurs micro-ondes en Rhénium. Ce travail est également présenté au chapitre trois. Les chapitres quatre et cinq présentent les résultats expérimentaux obtenus sur les résonateurs micro-ondes et l'atome artificiel, respectivement.

English

Introduction

Quantum computing

The concept of using quantum computers to overcome the limitations of classical computers has been introduced by Richard Feynman in 1982[1]. Quantum computers are different from classical computers based on transistors. Whereas digital computers require data to be encoded into binary digits (bits), each of which is always in one of two definite states (0 or 1), quantum computation uses qubits (quantum bits), which can be in superpositions of states. With a classical transistor, information is encoded into the presence or absence of an electrical current/voltage. Thus the transistor states are on *or* off. Formally, a qubit is a two-state quantum-mechanical system which can be written as:

$$\left|\psi_{\mathrm{qb}}\right\rangle = \alpha\,|g\rangle + \beta\,|e\rangle \tag{3}$$

where $|\alpha|^2+|\beta|^2 = 1$. An ensemble of n bits (classical or quantum) supports 2^n different states. However a classical computer can only be in one state at a time. The power of a quantum computer lies in its capability to be in all states simultaneously by using superposition of its n qubits. Furthermore a quantum operation influences the complete superposition of states. Quantum algorithms exploiting the specificity of a quantum computer already exist. Some examples include Shor's algorithm[2] which allows factorisation of large numbers, Grover's algorithm[3] for searching an unsorted database and the Metropolis sampling[4] to simulate generic quantum mechanical systems.

The development of a quantum computer is a great challenge due to the problem of decoherence. One consequence of decoherence is its classical or probabilistically additive behaviour. Thus a quantum computer without coherence becomes similar to a probabilistic classical computer. To keep the coherence of a system often implies to isolate this system from the environment. However, without mentioning the experimental difficulty of such tasks, a quantum computer should also be connected to the external world to receive and to transmit information. DiVincenzo[5,6] listed, in a set of five criteria, the different requirements for a practical quantum computer:

- Physically scalable to increase the number of qubits,
- Qubits can be initialized to arbitrary values,
- Quantum gates faster than decoherence time,
- Universal gate set,
- Qubits can be read easily.

Superconducting qubit

In solid state physics, one promising candidate to realise a qubit is superconducting quantum circuits based on Josephson junctions. The conjugate observables describing the electronic

dynamics of a Josephson junction are the Cooper-pair number and the phase difference across the junction. By carefully designing the junction, it is possible to fix one variable and consequently to get a huge indeterminacy on the other. Thus when the charge is well determined, we talk about "charge" qubit and when the phase is well determined, we talk about "phase" qubit. It is also possible to design a junction in which the indeterminacy of the phase and the charge are equal. This type of qubit is called "charge-phase" qubit.

We also have to mention the "flux qubit" which consists of a micrometer sized loop of superconducting metal interrupted by usually three Josephson junctions[7].

The first observation of quantised energy levels has been realised by Michel H. Devoret, John M. Martinis, Daniel Esteve, and John Clarke[8–10] in 1984–1985. In 1999, Nakamura *et al.*[11] demonstrated the first coherent manipulation of quantum states in a charge qubit. For this pioneering experiment the coherence time of the qubit was below 2 ns. However the coherence of the charge qubits was limited by charge fluctuations inherent to electrical circuits. Phase qubits reached, for their part, coherence times up to hundreds of nanoseconds[12–14]. The phase qubits suffered from coupling to spurious two-level systems present in the environment or directly in the isolating layer of the junction. Indeed the phase qubit design involved to fabricate junctions with large area which increases the probability to couple the junction with parasitic two-level systems. The charge-phase qubit with small junction size and no charge sensitivity at its optimal working point has reached coherence times as long as 500 ns[15].

In 2004, four years after a theoretical proposal[16,17], circuit quantum electrodynamics experiments were demonstrated firstly on charge qubit devices. In 2007 J. Koch *et al.*[18] proposed an original qubit design, the transmon. The particularity of the transmon is to operate at a ratio between the charging energy and the Josephson energy at which the first energy levels are insensitive to charge noise. Moreover this ratio enables the fabrication of very small junctions limiting the probability of coupling to spurious two-level systems. Recently such transmons reached a $T_1 = 9.7\,\mu s$ and a Ramsey coherence time of $T_2^* = 10.3\,\mu s$ in 2012[19] and $T_1 = 53\,\mu s$ and $T_2^* = 58\,\mu s$ in 2013[20]. An increase of the coherence time of the system has been obtained by replacing the 2D microwave resonator by a 3D bulk cavity. That way, the so-called 3D transmon reached $T_1 = 60\,\mu s$ and $T_2^* = 10 - 20\,\mu s$ in 2011[21] and $T_1 = 70\,\mu s$ and $T_2^* = 92\,\mu s$ in 2012[22].

Finally, we highlight the recent work realised on the fluxonium, an original qubit design leading to a perfect insensitivity to charge offset[23–25]. Such qubits in 3D cavity exhibit[26] a relaxation time of $T_1 \approx 1000\,\mu s$ and $T_2^* = 14\,\mu s$.

Superconducting dispersive qubit readout

With the transmon design, the qubit readout depends on the dispersive coupling between the qubit and a microwave resonator. Through the dispersive coupling, it is possible to perform a quantum non destructive measurement of the qubit state by probing the resonance frequency of the resonator. Indeed, the simple Hamiltonian of a qubit dispersively coupled to a resonator

is given by[18,27–31]:

$$\mathscr{H} = \underbrace{\hbar\omega_r\widehat{n}}_{\text{resonator}} + \underbrace{\frac{\hbar}{2}\omega_{qb}\widehat{\sigma}_z}_{\text{qubit}} + \underbrace{\frac{\hbar}{2}\chi\widehat{\sigma}_z\widehat{n}}_{\text{dispersive coupling}} \tag{4}$$

with ω_r, ω_{qb} the resonance frequency of the resonator and qubit, respectively. The operator $\widehat{n}$ gives the photon number in the cavity mode and $\widehat{\sigma}_z$ is the Pauli matrix of the qubit state. The dispersive coupling strength $\chi = g^2/\Delta$ is a ratio between the coupling strength g — between the resonator and the qubit — and the detuning Δ — between the cavity resonance frequency and the qubit resonance frequency. There is then a trade-off between the coupling strength g and the detuning Δ: a large dispersive coupling strength leads to a large signal-to-noise ratio by increasing the signal difference between the two states of the qubit. However, a large dispersive coupling implies a large coupling between the resonator and the qubit leading to an increase of the qubit decoherence by the Purcell effect[32].

The first dispersive readout in circuit quantum electrodynamics experiment gives a fidelity of the qubit readout of about $\mathscr{F} = 30\,\%$ for an integration time of $7\,\mu$s[33]. The low qubit readout fidelity was due to a low signal-to-noise ratio. Indeed the signal power used to perform the qubit readout has to be low enough to not induce undesirable effects on the qubit state[34]. The signal carrying out the information about the qubit state is then about a few photons per nanosecond. Moreover, when this signal is amplified, the noise added by a cryogenic amplifier is very large compared to the signal coming out of the resonator.

An important improvement has been achieved by the development of near quantum limited amplifiers based on the Josephson parametric amplifier[35]. Through these new amplifiers higher fidelity has been reached. For instance a fidelity of 98 % was achieved for an integration time of 240 ns in 2013[36].

This type of readout, based on qubit dispersively coupled to a microwave resonator, seems to reach its limits. Indeed increasing the signal-to-noise ratio implies increasing the dispersive coupling strength χ or the coupling of the resonator to the measurement microwave line which will, in both cases, enhance the Purcell effect.

The V-shape energy diagram in quantum optics

The V-shape energy diagram, defined in Fig. 11 (a), has been used in quantum optics to perform qubit state readout by fluorescence with an exceptionally high fidelity[37] of about 99.99 %. Originally proposed by Dehmelt *et al.* [38] and later demonstrated by Wineland *et al.* [39], Nagourney *et al.* [40], Sauter *et al.* [41], and Bergquist *et al.* [42], the readout consists of driving the system at the ancilla resonance frequency while measuring the fluorescence of the ancilla transition. In Fig. 11 (b) we summarise the readout protocol of a logical qubit via its ancilla qubit in a V-shape configuration. The system is probed with an oscillating signal in resonance with the ancilla transition at frequency $\omega_a/(2\pi)$. When the qubit is in its ground state, fluorescence occurs and the system is called “bright”. When the qubit is in its excited state, there is no available resonance transition with the drive, fluorescence does not occur, and the system is called “dark”. This way, it is possible to perform the readout of the qubit state with very high efficiency. For instance, we show in Fig. 12 the observation of quantum

jump on a single $^{138}Ba^{+}$ ions by Leibfried *et al.*[43] in 2003.

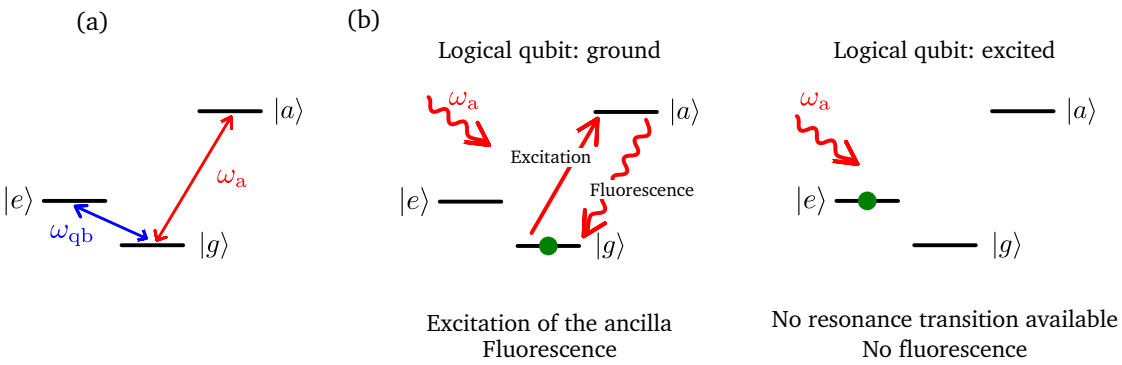

Figure (11): (a) V-shape energy diagram. It consists of a qubit, $|g\rangle$ and $|e\rangle$, exhibiting good quantum coherence properties in parallel with a second qubit, $|g\rangle$ and $|a\rangle$ realised by a second degree of freedom. The key point of a V-shape energy diagram is that any transitions from the logical qubit excited state $|e\rangle$ to a higher energy level are far out of resonance of the ancilla transition $|g\rangle \rightarrow |a\rangle$. (b) Readout of the logical qubit state via fluorescence. A readout tone is sent at resonance with the ancilla transition. When the logical qubit is in its ground state, fluorescence occurs. The system is called "Bright". In contrast when the logical qubit is in its excited state, no resonance transitions are available at the readout frequency. The fluorescence does not happen, the system is called "Dark".

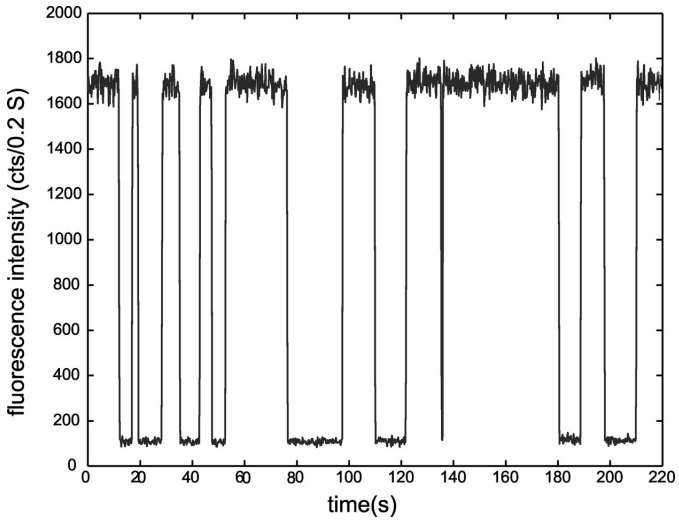

Figure (12): Quantum jumps of a single $^{138}Ba^{+}$ *ion*[41,43]*. When the ion makes the transition to its equivalent qubit excited state, the fluorescence drops. Inversely, when the ion return to its equivalent qubit ground state, the fluorescence returns to a higher level.*

Summary

The motivation of my thesis was to conceive and realise a V-shape energy diagram using a superconducting artificial atom and evaluate its potential to perform qubit state readout.

Prediction of a V-shape energy diagram

During my thesis I theoretically studied an original quantum device composed of two inductively coupled transmons (see Fig. 13 (a) and (b)). When the coupling inductance is of the order of the Josephson inductances, this circuit has two oscillating modes of phase difference across the junctions: a first mode, called *in-phase* mode, corresponding to the in-phase oscillations of the phase difference and a second mode, called *out-of-phase*, corresponding to the out-of-phase oscillations of the phase difference (depicted in red and blue arrows in Fig. 13 (a), respectively). By expanding the Hamiltonian of the circuit by Taylor expansion, I demonstrate the anharmoncity of each mode as well as the two couplings existing between the two modes. The *in-phase* mode is equivalent to the transmon mode, it exhibits a strong non-linearity due to the Josephson effect. The *out-of-phase* mode is mainly related to the coupling inductance, its energy is inversely proportional to the inductance. It has a weak anharmoncity. One of these couplings has been used to realise coherent frequency conversion between the first excited state of the *out-of-phase* mode and the second excited state of the *in-phase* mode[13]. The other coupling term, of strength denoted g_{zz}, is similar to the cross-Kerr coupling term: it modifies the energy of one mode depending on the number of excitations present in the other mode. In the limit of low energy excitations, the *in-phase* and *out-of-phase* modes can be considered as two qubits called hereafter logical and ancilla qubit, respectively. They are described by Pauli matrices, σ_z^{qb} and σ_z^{a}. The cross-Kerr coupling becomes then a $\sigma_z^{qb}\sigma_z^{a}$ coupling inducing a conditional frequency shift of one qubit transition depending of the state of the other qubit. This effect can be interpreted as a cross-anharmonicity between the two qubits, see Fig. 13 (d). In this manuscript I will refer to this effect either as a cross-anharmoncity or as a cross-Kerr. In the limit of large cross-anharmoncity, the energy diagram of the circuit becomes a V-shape energy diagram.

We have considered an artificial atom embedded in a circuit quantum electrodynamics architecture using a quarterwave resonator. Following the work of Alexandre Blais in a case of a halfwave microwave resonator[44], I derive the Hamiltonian of quarterwave resonators. Considering low-energy excitations, only couplings between the logical and ancilla qubits and the fundamental mode of the resonator have to be taken into account. I show that, by using the spatial dependence of the voltage and current amplitude along the resonator length and the different natures of the oscillating modes giving rise to the two qubits, it is possible to couple only one qubit to the resonator, the other staying completely isolated from the resonator. For instance, by positioning the V-shape device at the short-circuit side of a quarterwave resonator, only the ancilla qubit will be coupled.

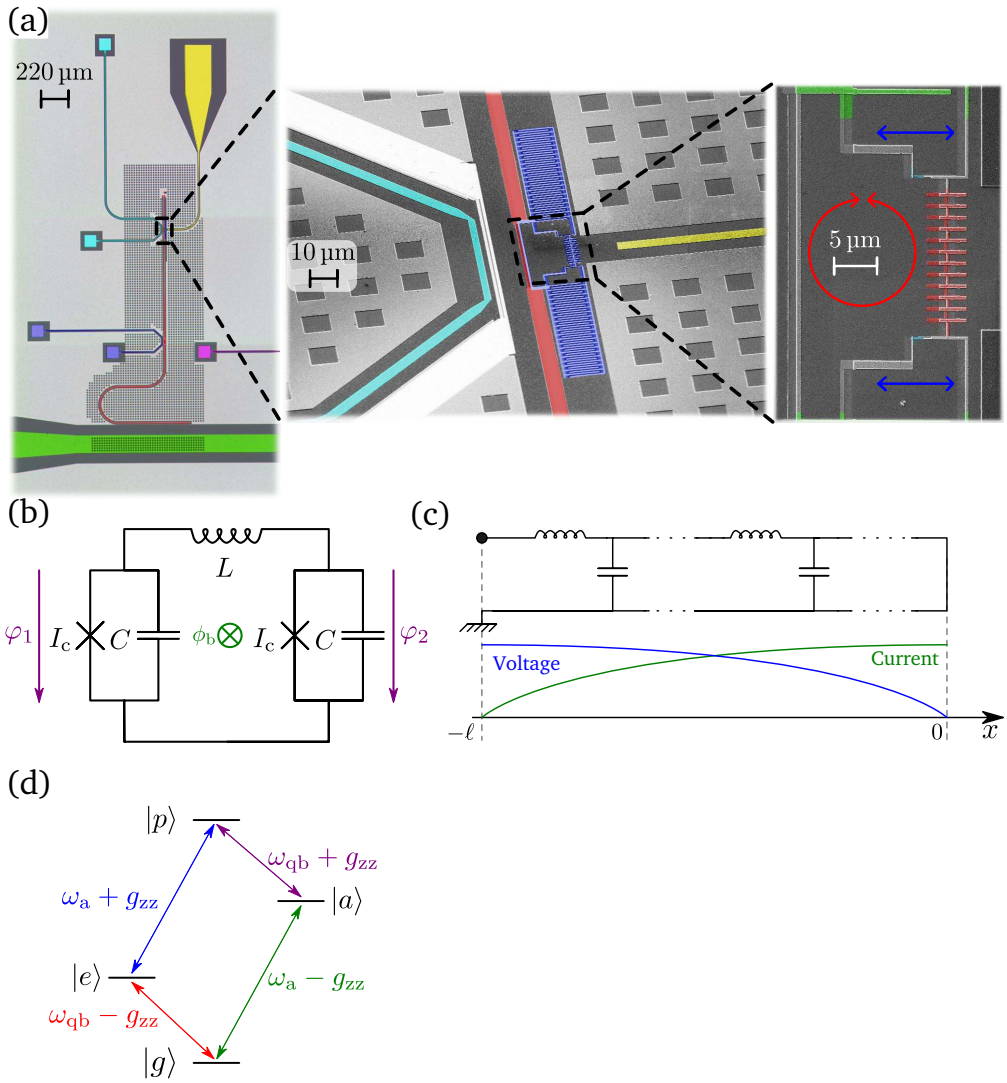

Figure (13): (a) SEM images of superconducting circuit with two successive zooms on the V-shape device. (b) Equivalent electrical scheme of two inductively coupled transmons. (c) Equivalent electrical scheme of a quarterwave resonator with a representation of the voltage and current amplitude spatial dependence for the fundamental mode. (d) Energy diagram of the artificial atom at $\phi_b = 0$. When the cross-Kerr term g_{zz} is large compared to the cavity linewidth, the energy diagram can be considered as a V-shape energy diagram.

Theoretical study: Ultra fast and high fidelity quantum non destructive measurement

In this manuscript, I propose an ultra fast and high fidelity quantum non destructive readout of a qubit state by using the V-shape device in a circuit quantum electrodynamics architecture with a quarterwave resonator. This work was inspired from our previous study on a halfwave resonator realised in collaboration with Igor Diniz[45]. The circuit as well as the measurement chain is schematised in Fig. 14. Let us not forget that due to the different nature of the oscillating modes and of the position of the V-shape device in the resonator, only the ancilla is coupled to the microwave resonator. In this way, it is possible to have a strong coupling g_a between the ancilla and the resonator while keeping the logical qubit isolated from the environment. The ancilla and the logical qubit are coupled via the cross-Kerr coupling g_{zz}.

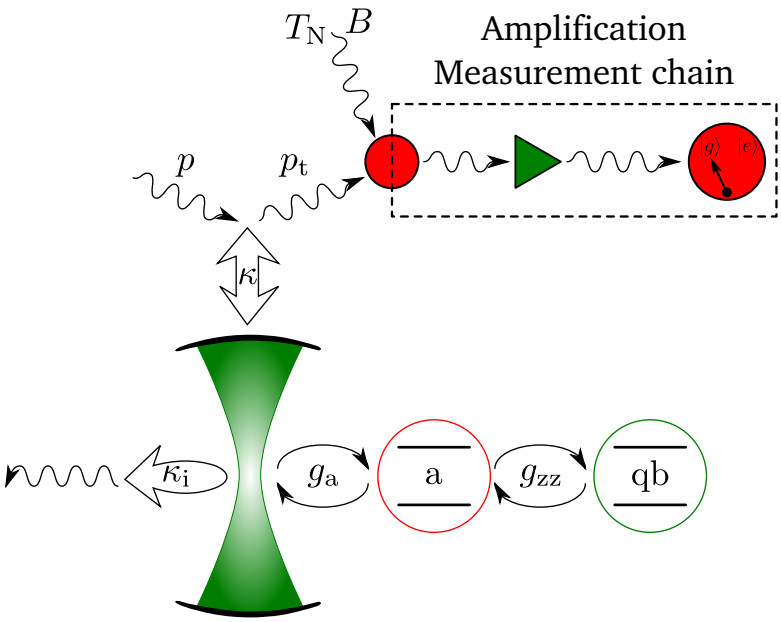

Figure (14): Scheme of the complete measurement chain. The logical qubit is coupled to the ancilla via the cross-Kerr coupling g_{zz}. The ancilla is coupled to the resonator with a coupling strength g_a. The input readout power is denoted p, at the output of the resonator the transmitted power is denoted p_t. The resonator is coupled to the feedline via κ_1 and κ_2. Internal losses of the resonator are modelled as a virtual channel with coupling κ_i. The amplification chain is modelled as a single amplifier with noise temperature T_N and a bandwidth B. At the end of the measurement chain, the microwave signal is digitised and the qubit state is inferred from the amplitude of the signal.

In order to calculate the transmission of the full circuit, resonator and V-shape device, shown in Fig. 14, we use the input-output theory. In Fig. 15, we show the transmission of the system when the logical qubit is in its ground state, in blue, and when it is in its excited state in green. The transmission of such a quantum circuit depends strongly on the logical qubit state. We note a frequency shift between the two closest peaks as high as 110 MHz. This value is two orders of magnitudes higher than usual frequency shifts using a dispersive

coupling strength χ. Taking advantage of the large frequency shift of the cavity resonance frequency depending on the logical qubit state, we increase the coupling of the resonator with the feedline, leading to a faster identification of the logical qubit state. Again, the increase of the resonator linewidth does not lead to an enhancement of the Purcell effect since the logical qubit is not coupled to the cavity.

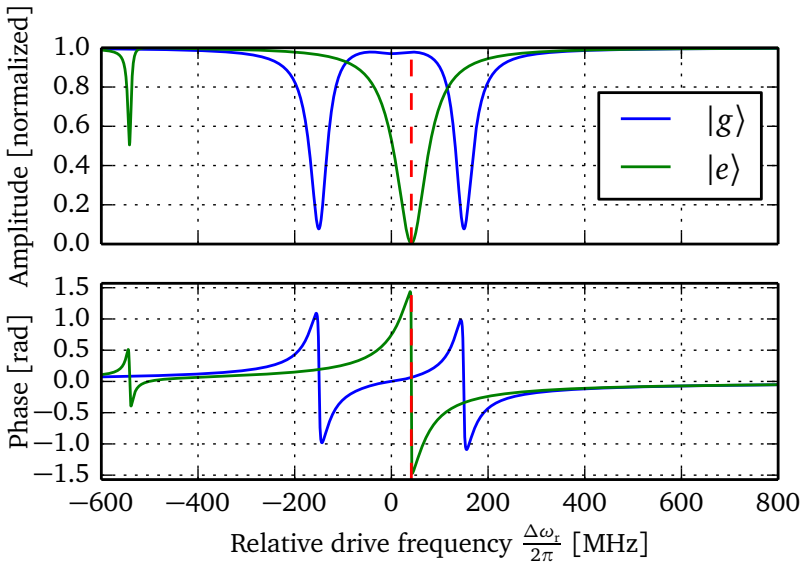

Figure (15): Transmission of the V-shape embedded in a quarterwave resonator as a function of the relative drive frequency. The blue line corresponds to the transmission of the system when the qubit is in its ground state while the green line is when it is in its excited state. In dashed red line, we show the frequency of maximum contrast between the transmitted signal when the logical qubit is in its excited or ground state. We took $g_{zz}/(2\pi) = 250\,\mathrm{MHz}$, $g_a/(2\pi) = 150\,\mathrm{MHz}$ *and the cavity linewidth* $\kappa/(2\pi) = 40\,\mathrm{MHz}$.

In order to estimate the fidelity of the qubit state readout, we take into account the noise added by the amplification chain, see Fig. 14. Indeed the main source of noise is usually due to the first amplifier of the amplification chain. We show in Fig. 16 a typical photon number distribution measurement at the output of the amplification chain expected with our V-shape device. The fidelity is estimated through the overlap between the two photon number distributions obtained for the two logical qubit states. We note that, in the case where a near quantum limited amplifier is used ($T_\mathrm{N} = 140\,\mathrm{mK}$ and $B = 50\,\mathrm{MHz}$), a fidelity of 99.7 % can be theoretically achieved with a measurement duration of only 50 ns. To reach this optimal readout the coupling of the resonator to the measurement line must be large with a linewidth of $\kappa/(2\pi) = 40\,\mathrm{MHz}$. It corresponds to an external quality factor of $Q_\mathrm{c} = 250$. Also, the optimal readout power has been estimated to few photons per nanosecond. At larger power, a saturation of the ancilla occurs leading to a loss of contrast.

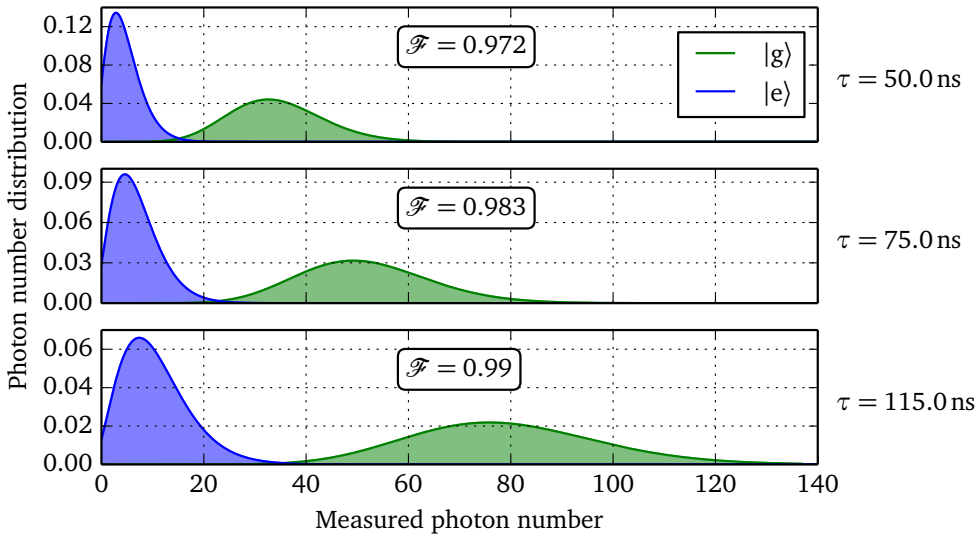

Figure (16): Evolution of the measured photon number distribution $\mathscr{F}$ following the measurement time τ. Parameters are the same as for Fig. 15. We took an input power $p = 1\,photon.ns^{-1}$, an amplifier bandwidth of $B = 50\,\mathrm{MHz}$, and a noise temperature $T_N = 140\,\mathrm{mK}$. The minimum measurement time used for the plots corresponds to the minimum correlation time allowed by the circuit. When the measurement time increases, the overlap of the photon number distributions for ground state (green) and excited state (blue) decreases, which leads to a higher fidelity.

Experimental developments

During my thesis, I have installed, in collaboration with Thomas Weißl, a complete microwave setup able to perform transmission measurements of our superconducting quantum circuits. We calculated the required attenuation of the input line to reach the so-called quantum limit $\hbar\omega \gg k_B T$. From this calculation, we installed attenuators along the input coaxial line at different stages of the dilution fridge with a particular care on thermalisation. We estimated the residual photon noise to be about 1×10^{-3} photons at 7 GHz, the resonance frequency of our microwave resonators. The output coaxial line which amplifies the transmitted signal is composed of two circulators and a cryogenic amplifier linked by a superconducting coax cable. To obtain further amplification, two room temperature amplifiers complete the chain. This line has been experimentally calibrated, we obtained a noise temperature of $T_N = 4.5\,\mathrm{K}$ with a gain of about 63 dB, in good agreement with the manufacturer datasheet.

We installed, at room temperature, a microwave setup able to measure the amplitude and the phase difference of a transmitted signal by a heterodyne method. Moreover a Python environment has been set up in order to perform measurements via modular Python scripts. This work included the writing of Python drivers using "Virtual Instrument Software Architecture" (VISA) for several devices as microwave sources and current sources and the quite consequent writing of Python objects. The complete microwave setup is able to perform microwave transmission measurements via a heterodyne method at very low power, of about $1\,\mathrm{photon{\cdot}ns^{-1}}$ ($\approx -110\,\mathrm{dBm}$ at 10 GHz).

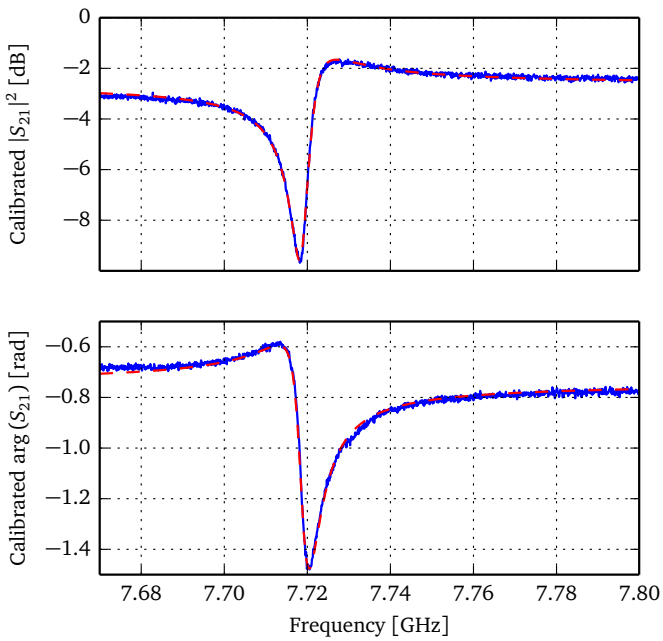

Figure (17): Resonance of a microwave resonator made from aluminium. The top panel presents the transmission in decibel and the bottom panel, the phase jump due to the resonance. The dashed red line is the fit calculated from the model.

The fabrication of the "V-shape" samples has been carried out by Alexey Feofanov and Bruno Küng at the "PTA" and "Nanofab" facilities. In parallel to this work, I developed a process to fabricate microwave resonators from epitaxial layers of rhenium grown by Benjamin Delsol[46] during his Ph.D. The lithography and etching process has been realised at the "Nanofab" facility.

Microwave resonators made from aluminium or rhenium were measured using our home-made heterodyne method or a commercial vector network analyser (VNA). The determination of cavity parameters as internal losses and external coupling rate, is important to characterise a quantum circuit. We propose an analytical model allowing the extraction of resonator parameters. In particular, this model explains the asymmetric shape of the cavity resonance line shapes measured during my thesis. An example of a cavity resonance line shape is shown in Fig. 17. In dashed red we show the theoretical line shape predicted by our model which fits quite well with the experimental data.

Experimental demonstration of a V-shape energy diagram with an artificial atom

The main result of my thesis is the experimental realisation and demonstration of an artificial atom with a V-shape energy diagram. The superconducting circuit is shown in Fig. 13 (a) with two successive zooms in the artificial atom. We measured the energy spectrum of the V-shape device as function of the magnetic field by two-tone spectroscopies, see Fig. 18. These measurements are based on the dispersive readout described previously. One tone performs the transmission readout close to the cavity resonance while the second tone is swept in frequency to probe the energy spectrum of the artificial atom. By analysing the flux dependence of the different energy levels, we can infer which state is due to the *in-phase* or *out-of-phase* oscillating mode. In Fig. 18 we observe the two first excited levels of the *in-phase* oscillating mode, which seem to drop to zero at half a flux quantum, and the first level of the *out-of-phase* oscillating mode, which reaches a limit at $\phi_\mathrm{b} = \phi_0/2$. These measurements demonstrate the existence of the two modes in the artificial atom. Moreover, we have numerically solved the Hamiltonian of the quantum circuit to fit the magnetic field dependence of the resonances (see the red dashed lines in Fig. 18). The theoretical curves are in very good agreement with experimental results except close to $\phi_0/2$.

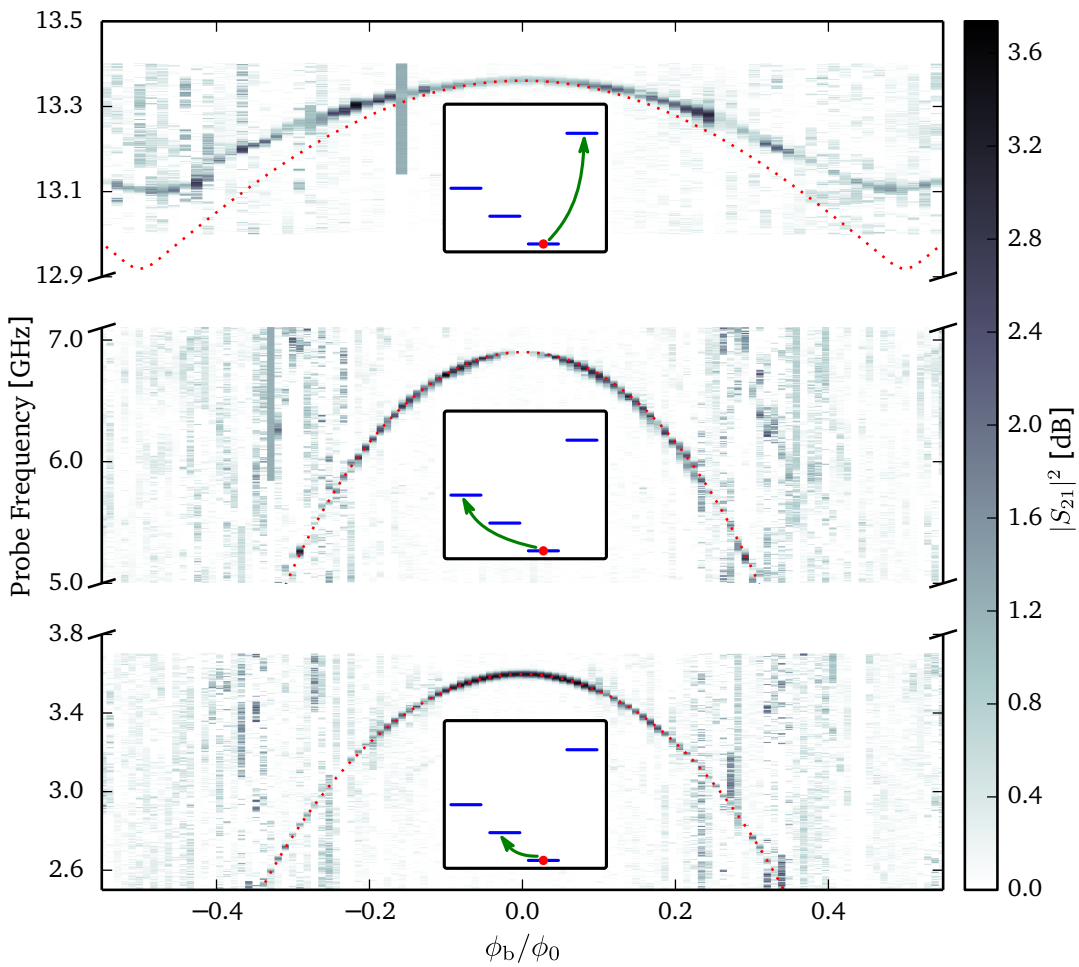

Figure (18): Two-tone spectroscopy as function of the magnetic field for sample "V-shape-2". The first two levels of the logical qubit seem to drop to zero for $|\phi_b| \approx 0.5$ whereas the ancilla level reaches a limit. For each measured resonance, we associate an inset showing, in an energy diagram, the equivalent transition. In dashed red, we show the theoretical prediction.

At $\phi_b = 0$, the system reaches a "sweet" point where the energy levels are protected at the first order against flux noise. Considering only the first level of the *in-phase* and of the *out-of-phase* mode, we obtain then the logical and ancilla qubit, see Fig. 13 (d). By time-resolved experiments, we control the states of the two qubits and we extract their relaxation and their coherence time. In Fig. 19, we show coherent oscillations and relaxation time measurement for the two qubits.

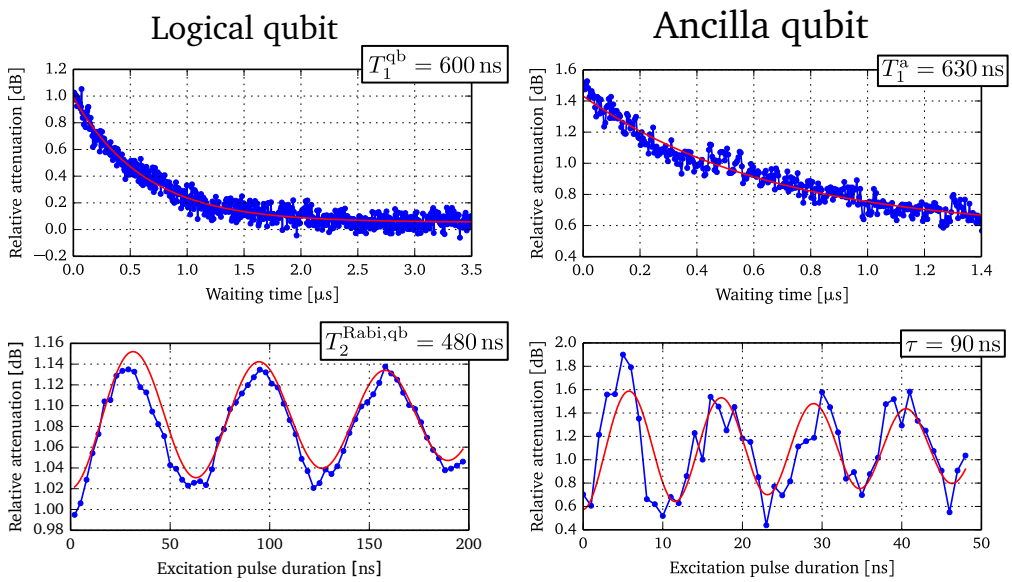

Figure (19): Relaxation and decay time of logical and ancilla qubit.

To demonstrate the cross-anharmonicity, we perform a three-tone spectroscopy. For instance to measure the effect of the cross-anharmonicity on the logical qubit resonance we realise the following experiment. We perform the previously discussed two-tone spectroscopy on the logical qubit but in addition a third tone is applied at a frequency in resonance with the ancilla transition $\omega_a/(2\pi)$. The measurement is shown in Fig. 20 (a) as a solid blue curve. We observe two peaks, one at the qubit resonance frequency 3.634 GHz and another, shifted by 110 MHz. As reference, we measure the same curve but with no excitation tone to drive the ancilla transition (green dashed curve in Fig. 20 (a)). We observe the qubit resonance peak centered at 3.634 GHz.

The qubit resonance peak corresponds to the transition between $|g\rangle \rightarrow |e\rangle$. We identify the second peak as the transition $|a\rangle \rightarrow |p\rangle$. This second peak is made possible because of the third tone excitation which populates the higher energy level of the ancilla. The frequency shift between the two peaks corresponds then to the cross-anharmonicity $(2g_{zz})/(2\pi) = 110$ MHz.

We performed further measurement to test the reproducibility and consistency of this result. We interchanged the role of the qubit and the ancilla. In Fig. 20 (b) we plot in dashed green and solid blue, a measurement showing a spectroscopy around the ancilla frequency while the excitation tone on the qubit is turned off and turned on, respectively. The result is exactly consistent with that in Fig. 20 (a), with a peak separation of about 110 MHz.

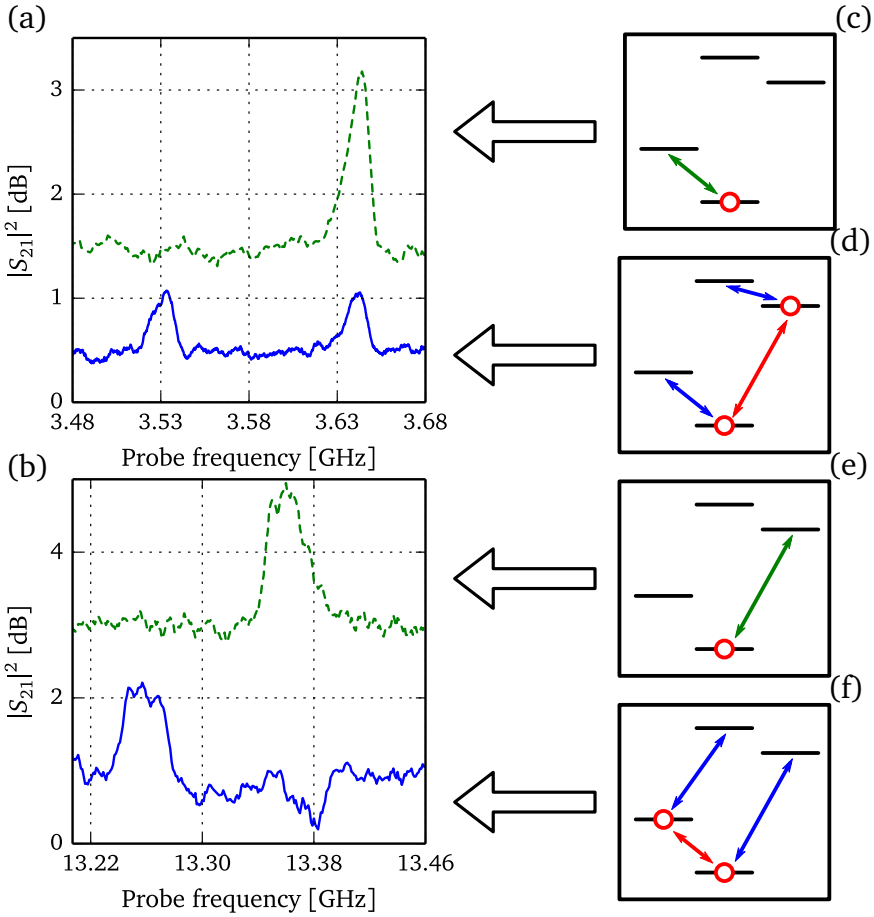

Figure (20): (a) Top green dashed curve, two–tone measurement of the qubit resonance, see energy diagram (c). Bottom blue solid curve, three–tone measurement. An excitation drives continuously the ancilla transition, while the probe tone scans the qubit transition, see (d). We observe the emergence of a second peak separated from the qubit resonance peak by the cross anharmonicity $(2g_{zz})/(2\pi)$*. (b) Control measurement of the cross-anharmonicity with inverted roles of logical and ancilla qubit, i.e., the probe tone is swept around the ancilla resonance frequency, whereas the excitation drive is resonant with the ancilla at* $\omega_a/(2\pi)$ *as shown in (e) and (f). The two measurements are consistent together with a cross-anharmonicity of* $(2g_{zz})/(2\pi) = 110\,\mathrm{MHz}$.

Manuscript organisation

The manuscript is divided in five chapters. A theoretical description of the V-shape device as well as the circuit quantum electrodynamics architecture achieved by coupling the V-shape device to a quarterwave resonator is given in the first chapter. In the second chapter, we present the setup used during the experiment and installed at the beginning of my thesis work. The fabrication of the “V-shape” sample is presented in details in chapter three. A side project during my thesis has been to fabricate microwave resonators from rhenium. This work is also presented in chapter three. The chapters four and five show the experimental results about the microwave resonator and V-shape device, respectively

Chapter 1

Theory

Contents

1.1 The 2D-SQUID **45**
1.1.1 Josephson junction dynamics 45
1.1.2 Classical dynamics of a current and flux biased SQUID 48
1.1.3 Quantum dynamics of the SQUID 58
1.1.4 A V-shape artificial atom 68
1.2 Microwave resonator **69**
1.2.1 Transmission line 70
1.2.2 Quarter-wave resonator 71
1.2.3 The current and voltage quantum operators 72
1.3 The V-shape device coupled to a quarter-wave resonator **74**
1.3.1 Coupling between the SQUID and the electromagnetic field 75
1.3.2 Logical and ancilla qubits coupled to the fundamental mode of the resonator 76
1.4 Transmission of the V-shape device coupled to a $\lambda/4$ resonator **77**
1.4.1 Input-Output theory of a resonator evanescently coupled 78
1.4.2 Logical-qubit readout 80

1.1 The 2D-SQUID

1.1.1 Josephson junction dynamics

In 1962, Brian David Josephson wrote a paper[47] in which he described: “the calculation of tunnelling currents between two metals that is sufficiently general to deal with the case when both metals are superconductors”. Josephson also wrote a second article about the

subject[48] in order to make some “clarification which has taken place in our ideas on the nature and behaviour of tunnelling supercurrents”. The idea of Josephson was to consider a system consisting of two superconductors separated by a barrier in which Cooper-pairs cannot exist. When the thickness of the barrier is large enough, the two superconductors will be completely isolated from each other whereas when the thickness is reduced to zero the system will be properly described as a single superconductor. Between these two extremes, when the wave functions of each superconductor overlap each other, the supercurrent passes through the junction by the tunnelling effect while keeping its phase coherence. This effect, nowadays known as the "Josephson effect" has earned B. D. Josephson a Nobel Prize in 1973. It can be summarised thanks to two simple equations called "Josephson equations"[49]:

$$i(t) = I_c \sin[\varphi(t)], \tag{1.1}$$

$$v(t) = \left(\frac{\phi_0}{2\pi}\right)\dot{\varphi}(t), \tag{1.2}$$

where $i(t)$ and $v(t)$ are the supercurrent through the junction and the voltage drop across the junction, respectively. The phase difference across the junction is denoted $\varphi(t) = \theta_l(t) - \theta_r(t)$, with $\theta_l(t)$ and $\theta_r(t)$ the superconducting phase on each side of the junction and ϕ_0 the magnetic flux quantum.

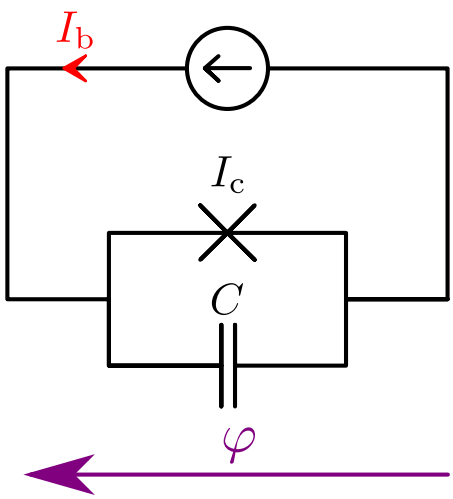

Figure (1.1): Equivalent electrical circuit of a Josephson junction in the CSJ model approximation The two elements describing a Josephson junction are a capacitor having a capacitance C in parallel with a pure Josephson element having a critical current I_c. The phase difference across the Josephson junction is denoted φ. The Josephson junction is biased with a DC current I_b by an ideal current source.

A simple picture of the Josephson junction can be obtained by describing the junction like an assembly of electrical components. Here we will use the so-called capacitively-shunted-junction model where a pure Josephson element is placed in parallel with a capacitance, see Fig. 1.1. The losses induced by the quasi-particle current through the Junction is assumed to be small enough to be neglected.

The pure Josephson element describes the passing of the supercurrent through the junction. It is characterised by a critical current I_c which indicates the maximum value of the supercurrent that the junction can handle before transiting to its normal state. The Josephson effect is related to the tunnel effect and shows an exponential dependence on the barrier thickness.

The capacitor C describes the charge coupling between the two metallic electrodes. A Josephson junction has an intrinsic capacitance which can be modelled as a parallel-plate capacitor. This capacitance grows as the ratio A/d[50] where A is the area of the capacitor plate and d the distance between the two plates. In our sample, Josephson junctions are shunted by inter-digital capacitors[50].

Lagrangian and Hamiltonian of a current biased Josephson junction

By deriving the different energies of the Josephson junction elements, we will establish the Hamiltonian of a Josephson junction. First we will calculate the Lagrangian.

The definition of the Lagrangian is given by Eq. (1.3) where T is the kinetic and V the potential energy of the system, respectively:

$$\mathscr{L} = T - V. \tag{1.3}$$

We calculate the kinetic energy term T by calculating the electrostatic energy stored in the capacitor:

$$T = \frac{1}{2} C v^2(t) = \frac{C}{2}\left(\frac{\phi_0}{2\pi}\right)^2 \dot{\varphi}^2. \tag{1.4}$$

The potential V is the sum of the Josephson energy E_{JJ} and the driven energy, E_{b}. The Josephson energy corresponds to the energy stored in the pure Josephson element[51]:

$$E_{\mathrm{JJ}} = \int i(t)\, v(t)\, \mathrm{d}t = -I_c\left(\frac{\phi_0}{2\pi}\right)\cos(\varphi). \tag{1.5}$$

The driven energy is calculated by following the same calculation, the bias current I_{b} replacing the critical current I_{c}[51]:

$$E_{\mathrm{b}} = -\int I_{\mathrm{b}} v(t)\, \mathrm{d}t = -I_{\mathrm{b}}\left(\frac{\phi_0}{2\pi}\right)\varphi. \tag{1.6}$$

Thus we obtain the Lagrangian from Eq. (1.3) to Eq. (1.6) as:

$$\mathscr{L}(\varphi, \dot{\varphi}) = T(\dot{\varphi}) - V(\varphi) = T - E_{\mathrm{JJ}} - E_{\mathrm{b}} \tag{1.7}$$

$$= \frac{C}{2}\left(\frac{\phi_0}{2\pi}\right)^2 \dot{\varphi}^2 + \frac{\phi_0}{2\pi} I_{\mathrm{c}}\left[\frac{I_{\mathrm{b}}}{I_{\mathrm{c}}}\varphi + \cos(\varphi)\right]. \tag{1.8}$$

The Lagrangian allows us to calculate the conjugate momentum:

$$p = \frac{\partial \mathscr{L}}{\partial \dot{\varphi}} = C\left(\frac{\phi_0}{2\pi}\right)^2 \dot{\varphi}. \tag{1.9}$$

We introduce the charge $q = C\left(\frac{\phi_0}{2\pi}\right)\dot{\varphi}$ and rewrite the momentum as:

$$p = \left(\frac{\phi_0}{2\pi}\right)q. \tag{1.10}$$

By using the Legendre transformation we derive the Hamiltonian:

$$\mathscr{H}(\varphi, p) = \dot{\varphi}p - \mathscr{L}(\varphi, \dot{\varphi}) \tag{1.11}$$

$$= \frac{1}{2C}q^2 - \frac{\phi_0}{2\pi}I_c\left[\frac{I_b}{I_c}\varphi + \cos(\varphi)\right]. \tag{1.12}$$

We introduce two characteristic energies for a Josephson junction. The Cooper-pair Coulomb energy E_C which represents the energy stored in the capacitor charged by one Cooper-pair. The Josephson energy E_J which corresponds to the maximum of energy that can be stored in the pure Josephson element. These quantities are defined in Table 1.1

Denomination	Formula
Cooper-pair Coulomb energy	$E_C = \frac{(2e)^2}{2C}$
Josephson energy	$E_J = \frac{\phi_0}{2\pi}I_c$

Table (1.1): Definition of the characteristic energies of the system. We draw attention about the definition of the Cooper-pair Coulomb energy which can be different of what the reader may be used to. We chose a definition which emphasise the Cooper-pair nature of the charge carriers.

Finally we introduce the dimensionless quantity $m = \frac{q}{2e}$ which corresponds to the number of Cooper-Pairs charged in the Josephson junction capacitance. The Hamiltonian can then be written as:

$$\mathscr{H}(\varphi, m) = E_C m^2 - E_J\left[\frac{I_b}{I_c}\varphi + \cos(\varphi)\right]. \tag{1.13}$$

1.1.2 Classical dynamics of a current and flux biased SQUID

The Superconducting QUantum Interference Device (SQUID) has been developed by Robert Jaklevic, John J. Lambe, James Mercereau, and Arnold Silver in 1964[52]. It consists of two Josephson junctions embedded in a superconducting loop.

Lagrangian and Hamiltonian of a SQUID

The description of the 2D-SQUID has already be done in the past, for example by Florent Lecocq[53]. Here we will concentrate our derivation on the most general case where the

critical currents, the capacitances, and the branch inductances are different from one junction to the other. Moreover, the SQUID is flux and current biased. The equivalent electrical circuit of a SQUID is drawn in Fig. 1.2.

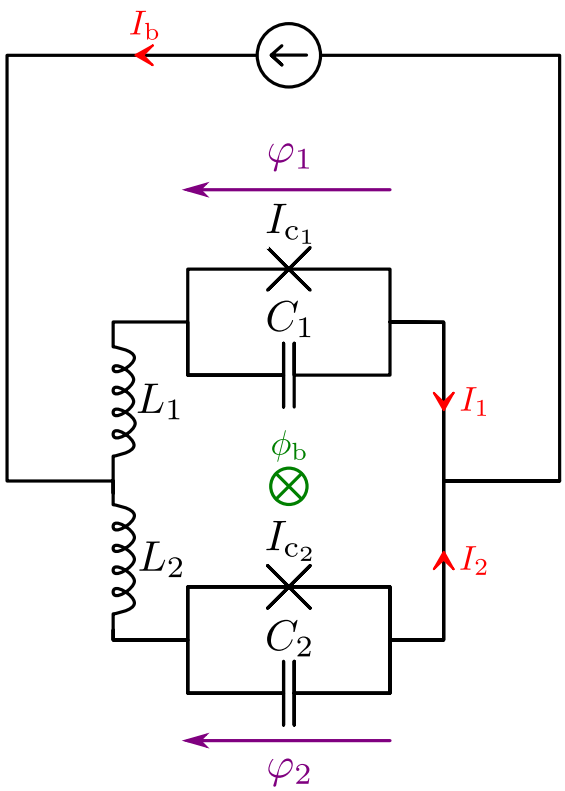

Figure (1.2): Equivalent electrical circuit of a SQUID in the CSJ model approximation. Each Josephson junction is pictured as in Fig. 1.1. The loop inductance of the SQUID is represented by the two inductors L_1 and L_2. The bias flux and current are denoted ϕ_b and I_b respectively. We also introduce branch currents I_1 and I_2.

The kinetic energy of each Josephson junction is equivalent to the one derived in Eq. (1.4):

$$T_1 = \frac{C_1}{2}\left(\frac{\phi_0}{2\pi}\right)^2 \dot{\varphi}_1^2 \quad , \quad T_2 = \frac{C_2}{2}\left(\frac{\phi_0}{2\pi}\right)^2 \dot{\varphi}_2^2. \tag{1.14}$$

The Josephson energies are equivalent to the energy in Eq. (1.5):

$$E_{\mathrm{jj}_1} = -I_{\mathrm{c}_1}\left(\frac{\phi_0}{2\pi}\right)\cos(\varphi_1) \quad , \quad E_{\mathrm{jj}_2} = -I_{\mathrm{c}_2}\left(\frac{\phi_0}{2\pi}\right)\cos(\varphi_2). \tag{1.15}$$

The driven energies are:

$$E_{\mathrm{b}_1} = -I_{\mathrm{b}}\left(\frac{\phi_0}{2\pi}\right)\varphi_1 \qquad , \qquad E_{\mathrm{b}_2} = -I_{\mathrm{b}}\left(\frac{\phi_0}{2\pi}\right)\varphi_2. \tag{1.16}$$

The flux quantization trapped in the superconducting loop requires the following condition on the Josephson junction phases[49]:

$$\varphi_1 - \varphi_2 = 2\pi\frac{\phi_{\mathrm{int}}}{\phi_0}. \tag{1.17}$$

The internal flux ϕ_{int} is the sum of the external biased flux ϕ_{b} and the flux created by the screening current $I_{\mathrm{screen}}(L_1 + L_2)$:

$$\phi_{\mathrm{int}} = \phi_{\mathrm{b}} + I_{\mathrm{screen}}(L_1 + L_2). \tag{1.18}$$

The screening current is obtained by inserting Eq. (1.18) into Eq. (1.17):

$$I_{\mathrm{screen}} = \frac{1}{L_1 + L_2}\left[\frac{\phi_0}{2\pi}(\varphi_1 - \varphi_2) - \phi_{\mathrm{b}}\right]. \tag{1.19}$$

The currents in the two branches can then be decomposed into two parts, one due to the bias current and the other due to the screening current,

$$I_1 = \frac{I_{\mathrm{b}}}{2} + I_{\mathrm{screen}} \qquad , \qquad I_2 = \frac{I_{\mathrm{b}}}{2} - I_{\mathrm{screen}}. \tag{1.20}$$

The energy stored in the inductors are:

$$E_{\mathrm{L}_1} = \frac{1}{2}L_1 I_1^2 \qquad , \qquad E_{\mathrm{L}_2} = \frac{1}{2}L_2 I_2^2. \tag{1.21}$$

According to the definition in Eq. (1.3), the Lagrangian is given by:

$$\mathscr{L} = \sum_{i=1}^{2} T_i - E_{\mathrm{jj}_i} - E_{\mathrm{b}_i} - E_{\mathrm{L}_i}. \tag{1.22}$$

Equation (1.22) gives constant terms which are neglected since an energy is always defined up to a constant. As we will see later, the dynamics of the system consists of two internal degrees of freedom coupled through the Josephson effect. One of then correspond to an *in-phase* oscillating current through Josephson junctions. This mode of oscillation is also referred as symmetric oscillations. The second one is an *out-of-phase* current oscillations across the junctions, also called anti-symmetric oscillations. This mode corresponds to a rotating current oscillation in the SQUID loop. We call the symmetric mode the *in-phase* current oscillations and the anti-symmetric mode the *out-of-phase* current oscillations. To

enhance these two modes, we define new phase coordinates x and y for the *in-phase* and *out-of-phase* mode as:

$$x = \frac{\varphi_1 + \varphi_2}{2} \quad , \quad y = \frac{\varphi_1 - \varphi_2}{2}. \tag{1.23}$$

We obtain the SQUID Lagrangian:

$$\begin{aligned} \mathscr{L}(x, y, \dot{x}, \dot{y}) \;=\; & \left(\tfrac{\phi_0}{2\pi}\right)^2 C_{\mathrm{m}} \quad \left(\dot{x}^2 + \dot{y}^2 - 2\gamma \dot{x}\dot{y}\right) \\ & -2\left(\tfrac{\phi_0}{2\pi}\right) I_{\mathrm{c_m}} \quad \Big[-\cos(x)\cos(y) - \alpha \sin(x)\sin(y) \\ & \qquad + b\left(y - \pi \tfrac{\phi_{\mathrm{b}}}{\phi_0}\right)^2 - s(x + \eta y)\Big]. \end{aligned} \tag{1.24}$$

We have introduced the mean values and the relative asymmetry of circuit parameters, see Table 1.2.

Quantity	Mean value	Relative asymmetry
Capacitance	$C_{\mathrm{m}} = \frac{C_1 + C_2}{2}$	$\gamma = \frac{C_2 - C_1}{2C_{\mathrm{m}}}$
Critical current	$I_{\mathrm{c_m}} = \frac{I_{\mathrm{c_1}} + I_{\mathrm{c_2}}}{2}$	$\alpha = \frac{I_{\mathrm{c_2}} - I_{\mathrm{c_1}}}{2I_{\mathrm{c_m}}}$
Inductance	$L_{\mathrm{m}} = \frac{L_1 + L_2}{2}$	$\eta = \frac{L_2 - L_1}{2L_{\mathrm{m}}}$

Table (1.2): New representation of the electrical components of the SQUID. The mean values are denoted with a subscript "m" while the asymmetries are denoted with Greek letters.

Finally other quantities have been defined, the inductance ratio $b = \frac{\phi_0}{2\pi I_{\mathrm{c_m}}} \frac{1}{L_{\mathrm{m}}}$ and the current ratio $s = \frac{I_{\mathrm{b}}}{2I_{\mathrm{c_m}}}$, respectively.

The conjugate momenta are derived from the Lagrangian:

$$\begin{aligned} p_x &= \frac{\partial \mathscr{L}}{\partial \dot{x}} = 2C_{\mathrm{m}} \left(\frac{\phi_0}{2\pi}\right)^2 (\dot{x} - \gamma \dot{y}), \\ p_y &= \frac{\partial \mathscr{L}}{\partial \dot{y}} = 2C_{\mathrm{m}} \left(\frac{\phi_0}{2\pi}\right)^2 (\dot{y} - \gamma \dot{x}). \end{aligned} \tag{1.25}$$

We define the charges q_x, q_y:

$$\begin{aligned} q_x &= \frac{q_1 + q_2}{2} = 2C_{\mathrm{m}} \frac{\phi_0}{2\pi} (\dot{x} - \gamma \dot{y}), \\ q_y &= \frac{q_1 - q_2}{2} = 2C_{\mathrm{m}} \frac{\phi_0}{2\pi} (\dot{y} - \gamma \dot{x}). \end{aligned} \tag{1.26}$$

With Eq. (1.26) we replace $\dot{x}$ and $\dot{y}$ by q_x and q_y in Eq. (1.25). We obtain:

$$\begin{aligned} p_x &= \frac{\phi_0}{\pi} q_x, \\ p_y &= \frac{\phi_0}{\pi} q_y. \end{aligned} \tag{1.27}$$

Finally the Legendre transformation gives us the Hamiltonian of the circuit:

$$\begin{aligned} \mathscr{H}\left(x, y, q_x, q_y\right) &= \tfrac{1}{C_\mathrm{m}} \tfrac{1}{1-\gamma^2} \left(q_x^2 + q_y^2 + 2\gamma q_x q_y \right) \\ &+ 2 \tfrac{\phi_0}{2\pi} I_{\mathrm{c_m}} \Big[-\cos(x)\cos(y) - \alpha \sin(x)\sin(y) \\ &\quad + b\left(y - \pi \tfrac{\phi_\mathrm{b}}{\phi_0}\right)^2 - s(x + \eta y) \Big]. \end{aligned} \tag{1.28}$$

We rewrite the Hamiltonian by introducing $E_{\mathrm{C_{SQUID}}}$ and $E_{\mathrm{J_{SQUID}}}$, the Josephson energy and Cooper-pair Coulomb energy for a SQUID, these quantities are defined in Table 1.3. From charge q_x and q_y, we introduce the dimensionless quantity $m_x = q_x/(2e)$ and $m_y = q_y/(2e)$. We obtain:

$$\begin{aligned} \mathscr{H}\left(x, y, m_x, m_y\right) &= E_{\mathrm{C_{SQUID}}} \left(m_x^2 + m_y^2 + 2\gamma m_x m_y \right) \\ &+ E_{\mathrm{J_{SQUID}}} \Big[-\cos(x)\cos(y) - \alpha \sin(x)\sin(x) \\ &\quad + b\left(y - \pi \tfrac{\phi_\mathrm{b}}{\phi_0}\right)^2 - s(x + \eta y) \Big]. \end{aligned} \tag{1.29}$$

Denomination	Formula
SQUID Cooper-pair Coulomb energy	$E_{\mathrm{C_{SQUID}}} = \frac{(2e)^2}{2}\left(\frac{1}{C_1} + \frac{1}{C_2}\right)$
SQUID Josephson energy	$E_{\mathrm{J_{SQUID}}} = \frac{\phi_0}{2\pi}\left(I_{\mathrm{c_1}} + I_{\mathrm{c_2}}\right)$

Table (1.3): Definition of the mean characteristic energies of the system.

The dynamics of the system in Eq. (1.29) have been widely described by Florent Lecocq in his thesis[53]. He has shown the existence of two particular regimes depending on the inductance ratio b.

In the limit where the loop inductance is null ($b \to \infty$) and where $I_\mathrm{c} = I_{\mathrm{c_1}} = I_{\mathrm{c_2}}$ and $C = C_1 = C_2$, the SQUID behaves like a single Josephson junction with a capacitance $2C$ and a critical current $2I_\mathrm{c}\cos(\pi\phi_\mathrm{b}/\phi_0)$. This regime is, for example, used for the possibility to tune *in-situ* the characteristic energy ratio $E_\mathrm{J}/E_\mathrm{C}$ of the system by applying a magnetic field[54].

In the other limit where the loop inductance is infinite ($b \to 0$), the Josephson junctions are decoupled from each other. The dynamics has to be described by two degrees of freedom[55].

The theory and the samples presented in this thesis are in an intermediate limit where b is about some unities.

The SQUID dynamics for $C_1 = C_2 = C$, $I_{c_1} = I_{c_2} = I_c$ and no current bias

Here after we will consider a 2D-SQUID with the same critical current and capacitance for both Josephson junction, $C_1 = C_2 = C$, $I_{c_1} = I_{c_2} = I_c$. Furthermore we will assume no current line connected to the SQUID. Without current line, it is meaningless to consider two different branch inductances. Thus in the following the inductance of the SQUID loop will be denoted L_{loop}. The system is shown in Fig. 1.3.

The Hamiltonian of Eq. (1.29) simplifies to:

$$\mathscr{H}\left(x, y, m_x, m_y\right) = 2E_C\left(m_x^2 + m_y^2\right) + 2E_J\left[-\cos(x)\cos(y) + b\left(y - \pi\frac{\phi_b}{\phi_0}\right)^2\right]. \tag{1.30}$$

The two energies of the Hamiltonian are the kinetic energy:

$$T\left(m_x, m_y\right) = 2E_C\left(m_x^2 + m_y^2\right), \tag{1.31}$$

and the potential energy:

$$V(x, y) = 2E_J\left[-\cos(x)\cos(y) + b\left(y - \pi\frac{\phi_b}{\phi_0}\right)^2\right]. \tag{1.32}$$

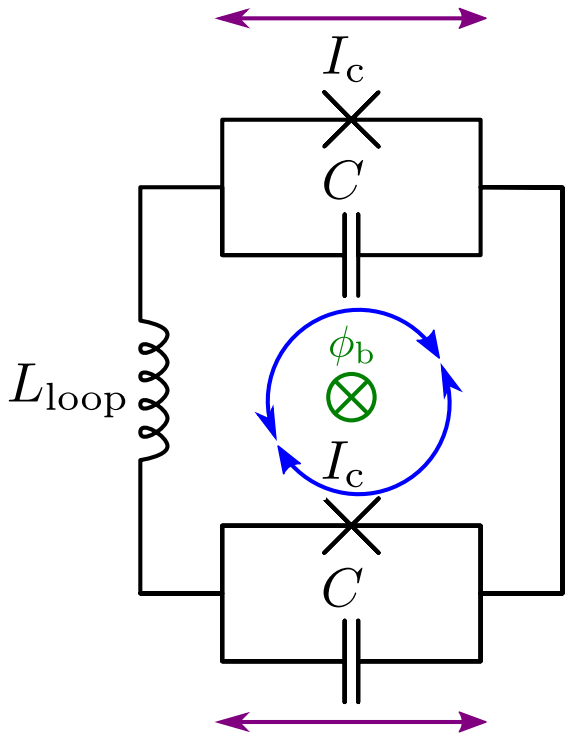

Figure (1.3): SQUID circuit for $C_1 = C_2 = C$, $I_{c_1} = I_{c_2} = I_c$ and no current bias. The in-phase and out-of-phase oscillations are depicted in purple and blue arrows, respectively.

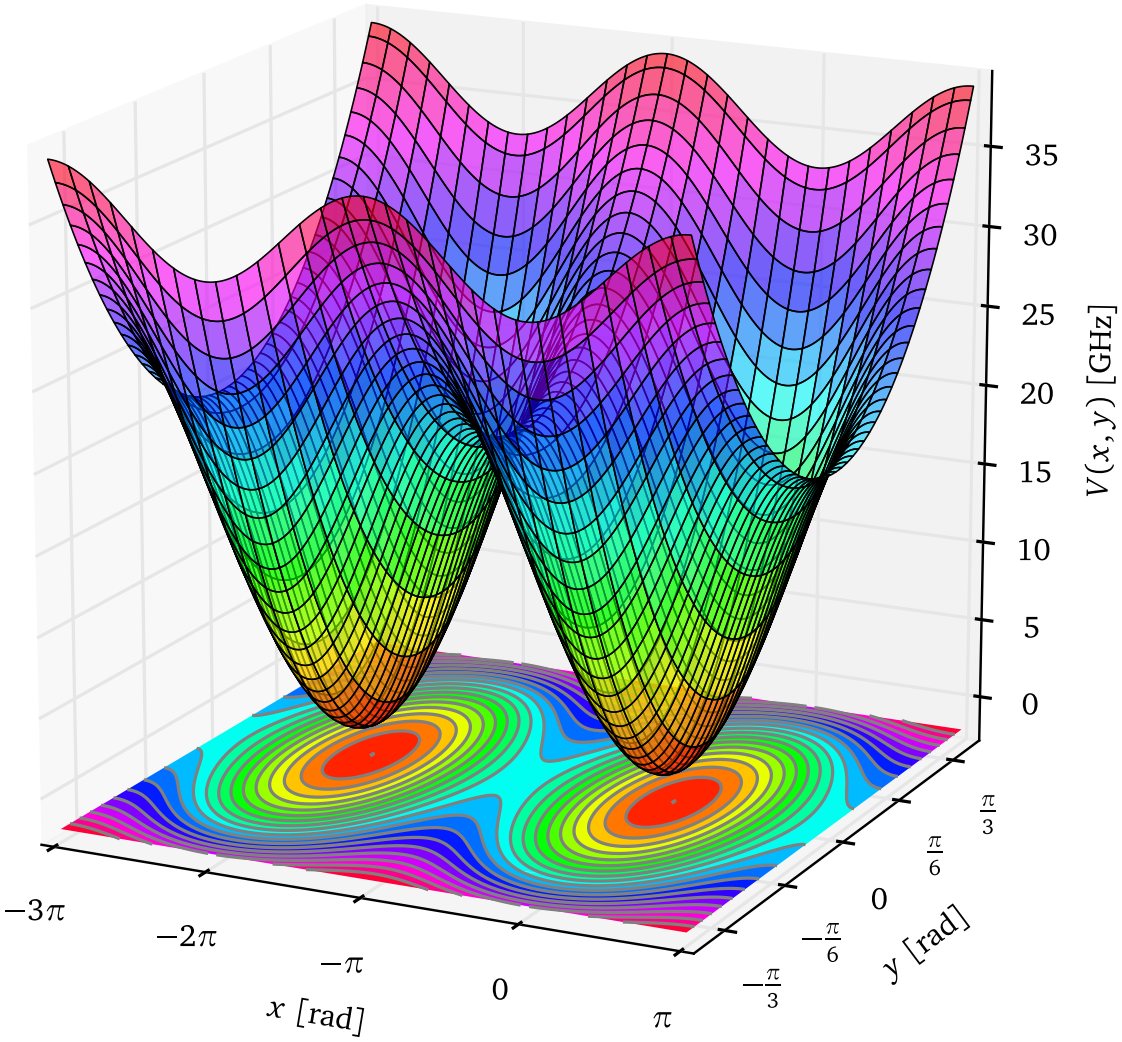

Figure (1.4): Potential of the Hamiltonian in Eq. (1.30) plotted for $\phi_b = 0$. We emphasise the fact that the scales in x and y are different, the y-dependence of the potential being much stronger than its x-dependence.

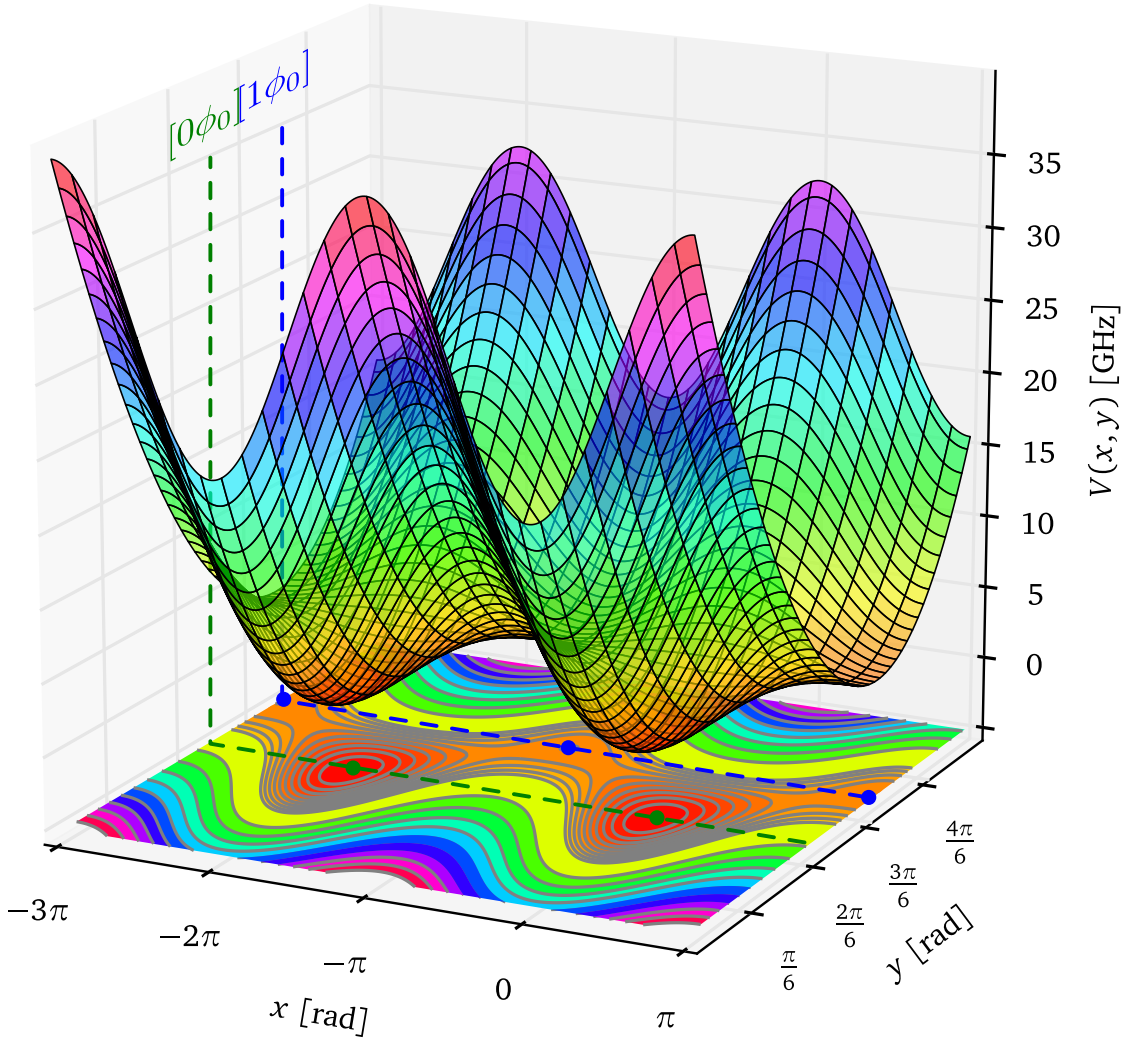

Figure (1.5): Normalised potential of the Hamiltonian in Eq. (1.32) plot for $\phi_b = 0.45\,\phi_0$. We emphasise the fact that the scales in x and y are different, the y-dependence on the potential being much stronger than in x.

One example of the potential energy is plotted in Fig. 1.4 for $\phi_b = 0$.

Along the x direction the potential is 2π-periodic. This periodicity is due to the Josephson effect.The Josephson effect also limits the well depth along the x direction with a maximum depth of $4E_J$.

Next, along the y direction the potential has two contributions. The first contribution is due to the Josephson effect which creates a 2π periodicity. The second one is the energy of the loop inductor which creates a parabolic dependence. In Fig. 1.4 the periodicity along the y direction is completely masked and only the energy of the inductor dominates the shape of the potential. Thus in this direction the potential well has an infinite depth.

For the same set of parameters the potential is plotted in Fig. 1.5 for $\phi_b = 0.45\,\phi_0$. The effect of an external flux is to create a screening current in the 2D-SQUID loop, see Eq. (1.19). The potential is still periodic along x. However the wells become shallower. We also notice the appearance of another well at the positions $x = \pi \pmod{2\pi}$. That is made possible by the large value of the loop inductance compared to the Josephson junction inductance, the b parameter. Potential wells can be classified in families, wells having the same position in y are in the same family. Each family corresponds to a number of flux quanta in the SQUID loop. These families are called "*flux states*" and are denoted by the number of flux quanta in the SQUID loop, $[n\phi_0]$. Figure 1.5 shows potential wells belonging to the *flux states* $[0\phi_0]$ and $[1\phi_0]$. The interested reader can find a wider description about *flux states* in Julien Claudon's thesis[56]. Hereafter we restrict ourself to the *flux state* $[0\phi_0]$.

Well positions

We will now derive the position of the minima of the wells noted (x_0, y_0). The application of an external bias flux shifts the bottom of the wells as indicated by the minima $(x_0, y_0) = (0, 0)$ and $(x_0, y_0) \approx \left(0, \frac{2.5\pi}{6}\right)$ in Figs. 1.4 and 1.5, respectively.

An extremum on the potential surface is characterised by the conditions:

$$\begin{cases} \partial_x V(x,y) = 0 & \text{(1.33a)} \\ \partial_y V(x,y) = 0. & \text{(1.33b)} \end{cases}$$

Equation (1.33) does not allow to distinguish between a local minimum, maximum or a saddle point. We can use the second derivative test[57] to differentiate a local minimum with the following conditions:

$$\begin{cases} \partial_{xx} V(x_0,y_0)\,\partial_{yy} V(x_0,y_0) - \partial_{xy} V(x_0,y_0)\,\partial_{yx} V(x_0,y_0) & > 0 & \text{(1.34a)} \\ \partial_{xx} V(x_0,y_0) & > 0\,. & \text{(1.34b)} \end{cases}$$

We obtain therefore:

$$\begin{cases} x_0 & = 0 & \text{(1.35a)} \\ \sin(y_0) + 2b\left(y_0 - \pi\dfrac{\phi_b}{\phi_0}\right) & = 0 & \text{(1.35b)} \\ \cos(y_0) & > 0\,. & \text{(1.35c)} \end{cases}$$

The position in x is given by Eq. (1.35a). We remark that the minimum of energy is always localised in $x_0 = 0$ independently of the biased flux. Eq. (1.35b) gives us the position in y. The equation is transcendental and can only be solved numerically. The nonlinear term of the equation comes from the Josephson effect while the linear one is due to the SQUID loop inductor. Finally, Eq. (1.35c) informs us about the range of validity of the position in y. Due to the periodicity of the Josephson effect, the validity domain given by Eq. (1.35c) are defined modulo 2π. Potential well families correspond to the domains defined by the equation Eq. (1.35c). Thus the *flux state* $[n\phi_0]$ is defined for $y_0 \in \left]\frac{\pi}{2}(4n-1); \frac{\pi}{2}(4n+1)\right[$. For the *flux state* $[0\phi_0]$, $y_0 \in \left]-\frac{\pi}{2}; \frac{\pi}{2}\right[$.

Taylor expansion

The analytical derivation of the eigenenergies of the Hamiltonian derived in Eq. (1.30) is made difficult by the nonlinear terms present in the potential. A simple approach is to make a Taylor expansion of the potential close to the bottom of the well to catch the main physical properties of the low-energy dynamics.

The Taylor expansion up to the fourth order gives us:

$$\begin{aligned} V(x,y) = \quad & E_J \cos(y_0)\, x^2 - \frac{E_J}{12}\cos(y_0)\, x^4 \\ & + E_J[\cos(y_0) + 2b]\, y^2 - \frac{E_J}{3}\sin(y_0)\, y^3 - \frac{E_J}{12}\cos(y_0)\, y^4 \\ & - E_J \sin(y_0)\, x^2 y - \frac{E_J}{2}\cos(y_0)\, x^2 y^2. \end{aligned} \tag{1.36}$$

The first line of Eq. (1.36) contains the expansion along the x direction, the second line along the y direction and, the last line contains nonlinear coupling terms. We note that along the x direction the expansion only has even terms which will be useful later on.

In the y direction we see a mixture of even and odd terms. In this direction the potential shape is determined by the Josephson effect and the inductance of the 2D-SQUID. We notice that at $\phi_b = \phi_0$ the odd terms disappear.

Finally the last line shows us two nonlinear coupling terms. The first term appears at the third order, it is even in x and odd in y. It is a consequence of the inductor energy and of the Josephson effect. The second term appears at the fourth order and is even in both directions. That coupling comes from the intrinsic nonlinearity of the Josephson effect. These coupling terms are discussed in more detail in Section 1.1.3.

1.1.3 Quantum dynamics of the SQUID

We introduce the quantum description of the Hamiltonian obtained in Eq. (1.30). The first step is to simplify the Hamiltonian by introducing a new set of canonical variables:

$$\tilde{x} = \sqrt{\frac{2E_J \cos(y_0)}{\hbar\omega_x}} x, \qquad \tilde{y} = \sqrt{\frac{2E_J [\cos(y_0) + 2b]}{\hbar\omega_y}} y,$$
$$\tilde{n}_x = \sqrt{\frac{4E_C}{\hbar\omega_x}} m_x, \qquad \tilde{n}_y = \sqrt{\frac{4E_C}{\hbar\omega_y}} m_y. \tag{1.37}$$

The angular frequency ω_x and ω_y correspond to the plasma frequencies at the bottom of the well along the x and y direction, respectively. Due to the different curvatures along the two directions, we have $\omega_x < \omega_y$. They are defined as:

$$\frac{\hbar^2}{E_C}\omega_x^2 = \partial_x^2 V(x,y)\Big|_{\substack{x=x_0\\y=y_0}}, \qquad \frac{\hbar^2}{E_C}\omega_y^2 = \partial_y^2 V(x,y)\Big|_{\substack{x=x_0\\y=y_0}}. \tag{1.38}$$

Applying the standard canonical quantization rules, we replace the classical variables ($\tilde{x}$, $\tilde{y}$, $\tilde{n}_x$, and $\tilde{n}_y$) by their corresponding quantum operators ($\widehat{x}$, $\widehat{y}$, $\widehat{n}_x$, and $\widehat{n}_y$). The conjugate pairs satisfy the following commutation relations:

$$[\widehat{x}, \widehat{n}_x] = \mathrm{i}, \qquad \left[\widehat{y}, \widehat{n}_y\right] = \mathrm{i}. \tag{1.39}$$

Finally we obtain the quantized Hamiltonian:

$$\begin{aligned}\widehat{\mathscr{H}} = \quad & \frac{1}{2}\hbar\omega_x\left(\widehat{n}_x^2 + \widehat{x}^2\right) - \hbar\omega_x\delta_x\widehat{x}^4 \\ & + \frac{1}{2}\hbar\omega_y\left(\widehat{n}_y^2 + \widehat{y}^2\right) - \hbar\omega_y\sigma_y\widehat{y}^3 - \hbar\omega_y\delta_y\widehat{y}^4 \\ & + \hbar\omega_{21}\widehat{x}^2\widehat{y} + \hbar\omega_{22}\widehat{x}^2\widehat{y}^2.\end{aligned} \tag{1.40}$$

The expressions of the different terms are summarised in Table 1.4.

The first line corresponds to the Hamiltonian of an anharmonic oscillator along the x direction. The anharmonicity is written as a dimensionless factor and is denoted δ_x. The correction term comes from the nonlinearity of the Josephson effect. At zero flux, the Josephson effect is maximum which involves a maximum value for ω_x and δ_x.

The second line corresponds to the Hamiltonian of an anharmonic oscillator along the y direction. The anharmonicity is described by σ_y and δ_y for the third and fourth order, respectively. The corrections are due to the nonlinearity of the Josephson effect. We remark that at zero flux $\sigma_y = 0$. The parameters ω_y and δ_y are then maximum.

The last line shows nonlinear couplings between the two oscillators. The coupling strengths are denoted ω_{ij} where i, j correspond to the Taylor expansion order in x, y direction. These coupling terms are discussed in more detail in Section 1.1.3.

Denomination	Formula
Plasma frequency	
Along the x direction	$\omega_x = \frac{1}{\hbar}\sqrt{2E_J E_C \cos(y_0)}$
Along the y direction	$\omega_y = \frac{1}{\hbar}\sqrt{2E_J E_C (\cos(y_0) + 2b)}$
nonlinear coupling terms	
Cross-Kerr	$\omega_{22} = -\frac{E_C}{4\hbar}\sqrt{\frac{\cos(y_0)}{\cos(y_0)+2b}}$
Coherent frequency conversion[13]	$\omega_{21} = -\sin(y_0)\sqrt[4]{\frac{E_J E_C^3}{8\hbar^4}\frac{1}{\cos^2(y_0)(\cos(y_0)+2b)}}$
Anharmonic correction	
Third order along the y direction	$\sigma_y = \frac{1}{6}\sqrt[4]{\frac{E_C}{2E_J}\frac{\sin^4(y_0)}{(\cos(y_0)+2b)^5}}$
Fourth order along the x direction	$\delta_x = \frac{1}{24}\sqrt{\frac{E_C}{2E_J}\frac{1}{\cos(y_0)}}$
Fourth order along the y direction	$\delta_y = \frac{1}{24}\sqrt{\frac{E_C}{2E_J}\frac{\cos^2(y_0)}{(\cos(y_0)+2b)^3}}$

Table (1.4): Definition of terms used in the quantized Hamiltonian in Eq. (1.40). The energies E_J and E_C are defined in Table 1.1.

Eigenenergies

The quantized Hamiltonian obtained in Eq. (1.40) is the sum of two nonlinearly coupled anharmonic oscillators. To solve it and derive the eigenenergies of the system we propose to follow the "ladder operator" method. We define ladder operators for the two oscillators:

$$\begin{aligned} \hat{a}_x &= \frac{\hat{x} + i\hat{n}_x}{\sqrt{2}}, \\ \hat{a}_x^\dagger &= \frac{\hat{x} - i\hat{n}_x}{\sqrt{2}}, \end{aligned} \quad , \quad \begin{aligned} \hat{a}_y &= \frac{\hat{y} + i\hat{n}_y}{\sqrt{2}}, \\ \hat{a}_y^\dagger &= \frac{\hat{y} - i\hat{n}_y}{\sqrt{2}}. \end{aligned} \tag{1.41}$$

The Hamiltonian of Eq. (1.40) becomes:

$$\begin{aligned}\widehat{\mathscr{H}} = \quad & \hbar\omega_x\left(\widehat{a}_x^\dagger\widehat{a}_x+\frac{1}{2}\right)-\frac{1}{4}\hbar\omega_x\delta_x\left(\widehat{a}_x+\widehat{a}_x^\dagger\right)^4 \\ & +\hbar\omega_y\left(\widehat{a}_y^\dagger\widehat{a}_y+\frac{1}{2}\right)-\frac{1}{\sqrt{2^3}}\hbar\omega_y\sigma_y\left(\widehat{a}_y+\widehat{a}_y^\dagger\right)^3-\frac{1}{4}\hbar\omega_y\delta_y\left(\widehat{a}_y+\widehat{a}_y^\dagger\right)^4 \\ & +\frac{1}{\sqrt{2^3}}\hbar\omega_{21}\left(\widehat{a}_x+\widehat{a}_x^\dagger\right)^2\left(\widehat{a}_y+\widehat{a}_y^\dagger\right)+\frac{1}{4}\hbar\omega_{22}\left(\widehat{a}_x+\widehat{a}_x^\dagger\right)^2\left(\widehat{a}_y+\widehat{a}_y^\dagger\right)^2. \end{aligned} \tag{1.42}$$

The eigenenergies of the system can be derived by diagonalizing the Hamiltonian. However the diagonalization of the Hamiltonian in Eq. (1.42) is difficult. In our problem the corrections in the form of anharmonic and coupling terms are small compared to the plasma frequencies, see Table 1.5. We propose then to approximate the solution by using quantum perturbation theory.

We write the Hamiltonian as:

$$\widehat{\mathscr{H}} = \widehat{\mathscr{H}_{0_x}} + \widehat{\mathscr{H}_{0_y}} + \widehat{\mathscr{W}_x} + \widehat{\mathscr{W}_y} + \widehat{\mathscr{W}_c}. \tag{1.43}$$

The parts $\widehat{\mathscr{H}_{0_x}}$ and $\widehat{\mathscr{H}_{0_y}}$ contain the harmonic oscillators along the x and y directions. The parts $\widehat{\mathscr{W}_x}$ and $\widehat{\mathscr{W}_y}$ contain the anharmonic corrections along the x and y directions, respectively. Finally, $\widehat{\mathscr{W}_c}$ contains corrections due to the nonlinear coupling terms.

We note $|\varphi_{n_x}\rangle$, $|\varphi_{n_y}\rangle$ the eigenstates of $\widehat{\mathscr{H}_{0_x}}$, $\widehat{\mathscr{H}_{0_y}}$ and E_{n_x}, E_{n_y} the associated eigenenergies. From that we build a global base $|\varphi_{n_x},\varphi_{n_y}\rangle = |\varphi_{n_x}\rangle\otimes|\varphi_{n_y}\rangle$.

At the first order, the corrected eigenenergies and eigenstates are given by[58]:

$$E_{n_x,n_y} = E_{n_x} + E_{n_y} + \left\langle\varphi_{n_x,n_y}\middle|\widehat{\mathscr{W}_x}+\widehat{\mathscr{W}_y}+\widehat{\mathscr{W}_c}\middle|\varphi_{n_x,n_y}\right\rangle, \tag{1.44}$$

$$\left|\psi_{n_x,n_y}\right\rangle = \left|\varphi_{n_x,n_y}\right\rangle + \sum_{\substack{p_x\neq n_x\\ p_y\neq n_y}} \frac{\left\langle\varphi_{p_x,p_y}\middle|\widehat{\mathscr{W}_x}+\widehat{\mathscr{W}_y}+\widehat{\mathscr{W}_c}\middle|\varphi_{n_x,n_y}\right\rangle}{E^0_{n_x,n_y}-E^0_{p_x,p_y}}\left|\varphi_{p_x,p_y}\right\rangle. \tag{1.45}$$

After some algebra, we obtain:

$$\begin{aligned} E_{n_x,n_y} = & \hbar\omega_x\left(n_x+\frac{1}{2}\right)-\frac{3}{2}\hbar\omega_x\delta_x\left[\left(n_x+\frac{1}{2}\right)^2+\frac{1}{4}\right] \\ & +\hbar\omega_y\left(n_y+\frac{1}{2}\right)-\frac{3}{2}\hbar\omega_y\delta_y\left[\left(n_y+\frac{1}{2}\right)^2+\frac{1}{4}\right] \\ & +\frac{1}{4}\hbar\omega_{22}\left(2n_x+1\right)\left(2n_y+1\right) \end{aligned} \tag{1.46}$$

where $n_x, n_y \in \mathbb{N}$ are the quantum numbers describing the quantization of the energy for the symmetric and anti-symmetric oscillators.

The formula for the eigenestate corrected by the perturbations is written in Appendix D.

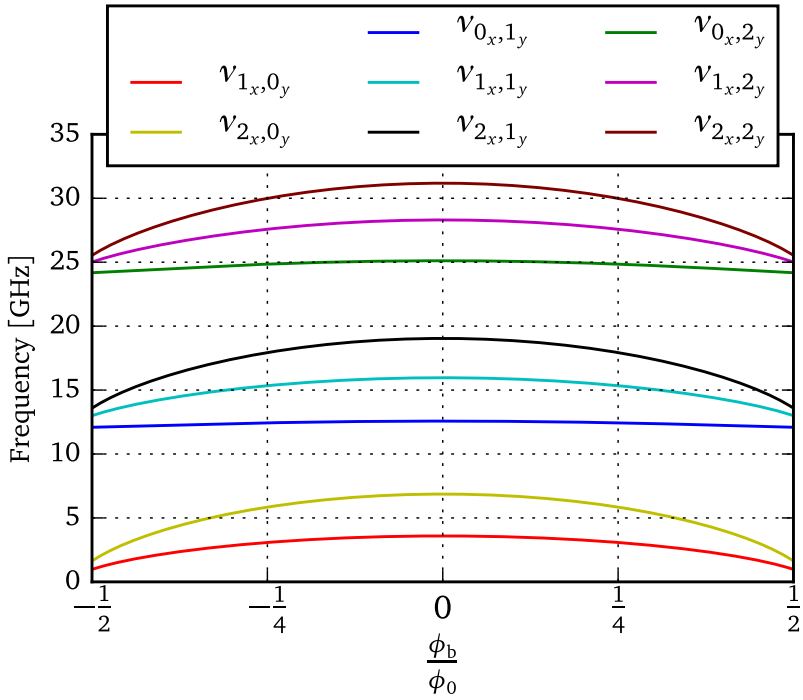

Figure (1.6): Energy levels as a function of magnetic flux. We remark the difference of flux dependence between levels of the symmetric and anti-symmetric oscillators. Circuit parameters used for the plot are summarised in Table 1.5.

The lowest energy levels are shown in Fig. 1.6. We observe that energy levels of the symmetric oscillator exhibit a strong dependence on the flux ϕ_b and seem dropping to zero when ϕ_b is about half flux quantum.

Energy levels of the anti-symmetric oscillator have a much weaker flux dependence and reach a limit at half a flux quantum. These levels are mainly due to the 2D-SQUID loop inductor. They have a weak flux dependence and do not disappear at half a flux quantum.

Energy levels constituted of excitations in the symmetric and anti-symmetric oscillators exhibit an intermediate behaviour since they show a flux dependence but do not drop to zero at half flux quantum.

Anharmonicity

The absolute anharmonicities are defined as:

$$\Delta_x = \left(E_{2_x,0_y} - E_{1_x,0_y}\right) - \left(E_{1_x,0_y} - E_{0_x,0_y}\right) = -3\hbar\delta_x\omega_x = -\frac{1}{8}E_C, \tag{1.47}$$

$$\Delta_y = \left(E_{0_x,2_y} - E_{0_x,1_y}\right) - \left(E_{0_x,1_y} - E_{0_x,0_y}\right) = -3\hbar\delta_y\omega_y = -\frac{1}{8}E_C\frac{\cos(y_0)}{\cos(y_0)+2b}. \tag{1.48}$$

Equation (1.47) shows that the anharmonicity of the symmetric oscillator depends only on

the charging energy of a Josephson junction. Moreover Δ_x does not depend on the magnetic flux. In contrast, Eq. (1.48) shows that the anharmonicty of the anti-symmetric oscillator has a dependence on the magnetic flux through the term $\cos(y_0)/[\cos(y_0)+2b]$ with a maximum at $\phi_b = 0$. This ratio is always smaller than one, leading to a lower anharmonicity for the anti-symmetric oscillator than for the symmetric one. Table 1.5 presents typical values for the anharmonicity of the two oscillators.

The nonlinear coupling terms

The Hamiltonian obtained in Eq. (1.40) contains two nonlinear coupling terms. Their coupling strength are plotted versus magnetic flux in Fig. 1.7.

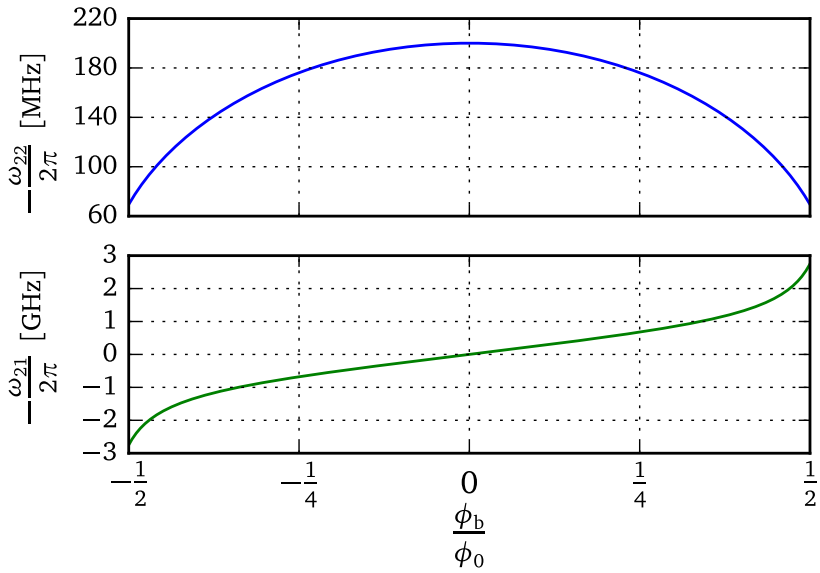

Figure (1.7): Dependence of the nonlinear coupling terms on a magnetic flux. We mention the fact that the vertical scale is different for the two curves. Indeed typical values for $\omega_{22}/(2\pi)$ are some hundreds of megahertz whereas $\omega_{21}/(2\pi)$ are around few gigahertz. Circuit parameters used for the plot are summarised in Table 1.5.

The nonlinear term, $\hbar\omega_{21}\hat{x}^2\hat{y}$, has been studied by Florent Lecocq[53] in his thesis. It has been used to realise coherent oscillations between two excitations in the symmetric oscillator and one in the anti-symmetric one[13]. The coupling strength ω_{21} can vary from −3 GHz to 3 GHz along one flux quanta. The coupling strength ω_{21} is an odd function of flux and hence vanishes at zero flux.

The coupling strength ω_{22} shows an even parity. It can vary from some ten of megahertz, in the experiments performed by Florent Lecocq[13], to some hundred of megahertz, in experiments presented in this thesis.

We note that, in the first-order perturbation theory, there is no effect of the coupling term ω_{21} on the eigenenergies. In contrast the coupling term ω_{22}, mainly due to the Josephson

effect, has a strong effect on the eigenenergies of the system. The effect of the coupling on the eigenenergy can be seen in Eq. (1.46). The coupling lowers all energy levels by an amount $\hbar\omega_{22}/2$. Moreover it induces a conditional energy shift for both modes governed by $\hbar\omega_{22}\, n_x n_y$. From now on, we will refer the ω_{22} term as the cross-Kerr coupling. The Kerr effect as been discovered in 1875 by John Kerr[59] in optics. It is defined as a change in the refractive index of a material in response to an applied electric field. In our system the Kerr effect modifies the energy levels of an oscillator depending on the energy of the other oscillator. Typical values for the coupling strengths ω_{21} and ω_{22} are written Table 1.5. We observe that in our device we may produce a giant Kerr effect since the cross-Kerr coupling is between 5 % to 10 % of the oscillator energies. In Section 1.1.4 we will see how we can use this property to build a readout of a qubit state with very high performance.

Discussion of circuit parameter values

In Table 1.5 we summarise typical values at $\phi_b = 0$ of circuit parameters defined previously. We notice that only three parameters, the loop inductance L_{loop}, the junction capacitance, and the critical current, are necessary to describe all the physics of the system. Here we consider equal capacitances and critical currents between the two Josephson junction.

	Symbol	S_{2D}	V-shape-2
Circuit parameters			
Critical current	I_c	713 nA	8 nA
Junction capacitance	C	510 fF	40 fF
Loop inductance	L_{loop}	0.6298 nH	7.5 nH
Characteristic energies			
Josephson energy	E_J	354.14 GHz	3.97 GHz
Cooper-pair charging energy	E_C	0.15 GHz	1.94 GHz
Dimensionless quantities			
Inductance ratio	b	0.733	5.49
Characteristic energy ratio*	E_J/E_C	2331*	2*
Characteristic frequencies			
Plasma frequency in the x direction	$\omega_x/(2\pi)$	10.37 GHz	3.93 GHz
Plasma frequency in the y direction	$\omega_y/(2\pi)$	16.29 GHz	13.58 GHz
Cross-Kerr coupling	$\omega_{22}/(2\pi)$	−37.98 MHz	−140 MHz
Anharmonicity of the x oscillator	Δ_x	−18.99 MHz	−320 MHz
Anharmonicity of the y oscillator	Δ_y	−7.70 MHz	−20 MHz

Table (1.5): The table presents quantities defined in the chapter and illustrates them by comparing two sets of parameters coming from a sample measured by Florent Lecocq[53] *during his thesis, the S_{2D} sample and the sample "V-shape-2" presented in Chapter 5. For flux dependent parameters we have taken $\phi_b = 0$. The definitions of E_C and E_J are written in Table 1.1.*

** Compared to the usual Transmon definition our ratio E_J/E_C should be multiplied by 16. To avoid confusion we will use, in the rest of this manuscript, the notation $(E_J/E_C)^* = 16E_J/E_C$ to compare our characteristic energy ratio with the transmon ratios. We then obtain a ratio of $(E_J/E_C)^* = 37\,296$ and $(E_J/E_C)^* = 33$ for the S_{2D} and the "V-shape-2" sample, respectively.*

Validity of the analytical model

The analytical model that we have developed above contains two approximations. The first one is the Taylor expansion of the potential written in Eq. (1.36). The initial potential of Eq. (1.32) and its Taylor expansion at different order are compared in Fig. 1.8 for $\phi_b = 0$. In our theoretical analysis, we have expanded the potential up to the fourth order, Eq. (1.36).

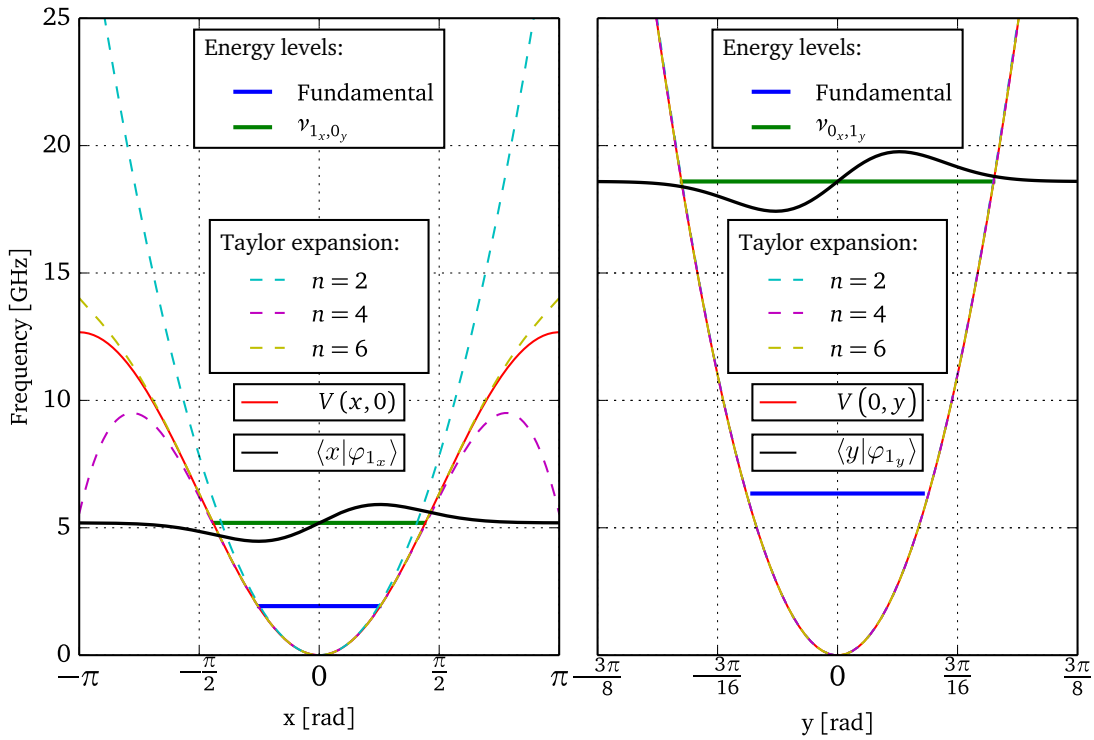

Figure (1.8): Cut of the potential in the x and y direction at $\phi_b = 0$. The potential is plotted in solid red line while expansions of different order are depicted s dashed lines. The zero-point energy is shown as thick blue solid line. The first levels frequency are shown as thick solid green line with respect to the zero-point energy. The wave function of the harmonic oscillators are plotted as thick solid black curves. Circuit parameters used for the plot are summarised in Table 1.5.

Along the y direction the potential is well approximated by the Taylor expansion. In this direction the potential energy is dominated by the loop inductance energy which is quadratic in y. The anharmonic quartic term δ_y is very weak at zero flux, $\delta_y \approx 0.008\,\%$.

Along the x direction, the approximation deviates noticeably from the potential even up to the sixth order. In this direction the Josephson effect has the main contribution of the potential energy with a highly nonlinear anharmonicity, $\delta_x \approx 3\,\%$.

In order to quantify the error produced by the description of the potential up to the fourth order, the relative error of the Taylor expansion with respect to the potential is shown in

Fig. 1.9 for different order expansion.

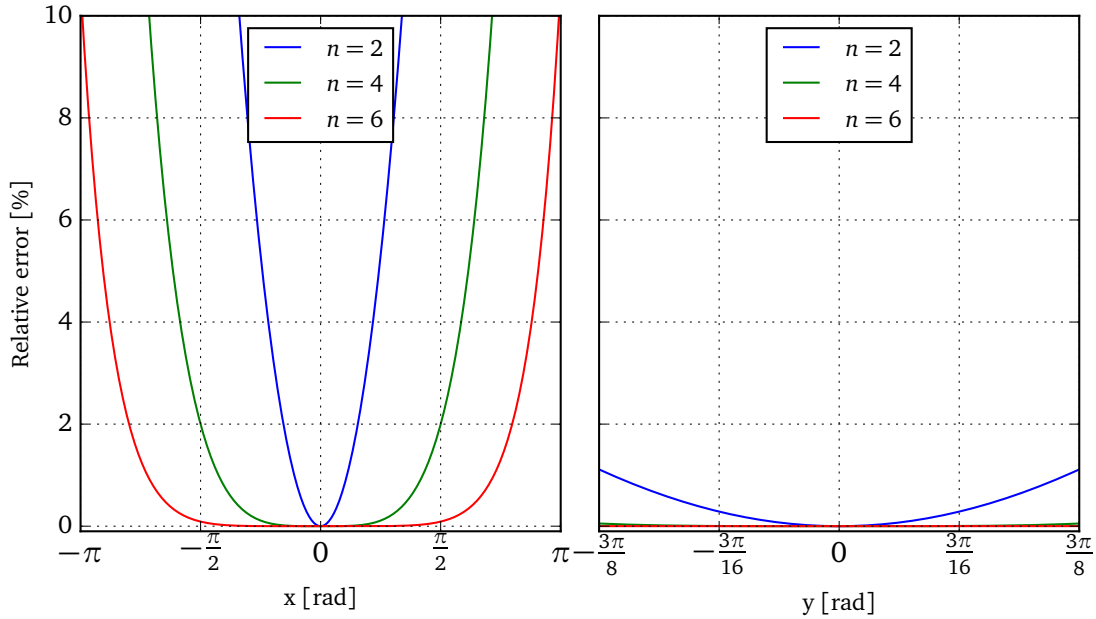

Figure (1.9): Relative error between the initial potential defined in Eq. (1.30) and the Taylor expansion defined in Eq. (1.36) in percent. Circuit parameters used for the plot are summarised in Table 1.5.

The error along the y direction is small, with only 0.12 % for the fourth order at $y = \pm\frac{\pi}{2}$.

In contrast, the error along the x direction grows rapidly and reaches 2 % for the fourth order at $x = \pm\frac{\pi}{2}$.

In Fig. 1.8 zero-point energy and eigenenergy of the first level for both oscillators are shown. The wave functions of the first levels are plotted relatively to the eigenenergy of that levels. They have been calculated in the limit of a harmonic oscillator by using the eigenstate at the zeroth order approximation, see Appendix D. The wave functions illustrate the confinement of the excitations inside the potential well. Thus the excitation is, approximately, confined between $x \in \left[-\frac{\pi}{2}; \frac{\pi}{2}\right]$ and $y \in \left[-\frac{3\pi}{11}; \frac{3\pi}{11}\right]$. Figure 1.9 shows that the relative error in these domains are below 2 % for the symmetric oscillator and 0.01 % for the anti-symmetric one.

The second approximation made during the analytical derivation is the use of the quantum perturbation theory. We compare the analytical result obtained in Eq. (1.46) to a numerical simulation of eigenenergies of the Hamiltonian written in Eq. (1.30). We have used the QuTiP python library[60] to simulate our system. The result is shown in Fig. 1.10. The eigenenergy calculated through the numerical simulation and the eigenenergy given by the analytical formula have nearly the same values. At zero flux we have a relative error of 0.98 % for the $\nu_{1_x,0_y}$ level, 0.0094 % for the $\nu_{0_x,1_y}$ transition and 0.28 % for the $\nu_{1_x,1_y}$ level. Moreover they exhibit the same behaviour as a function of the magnetic field. The error on the ω_{22} coupling

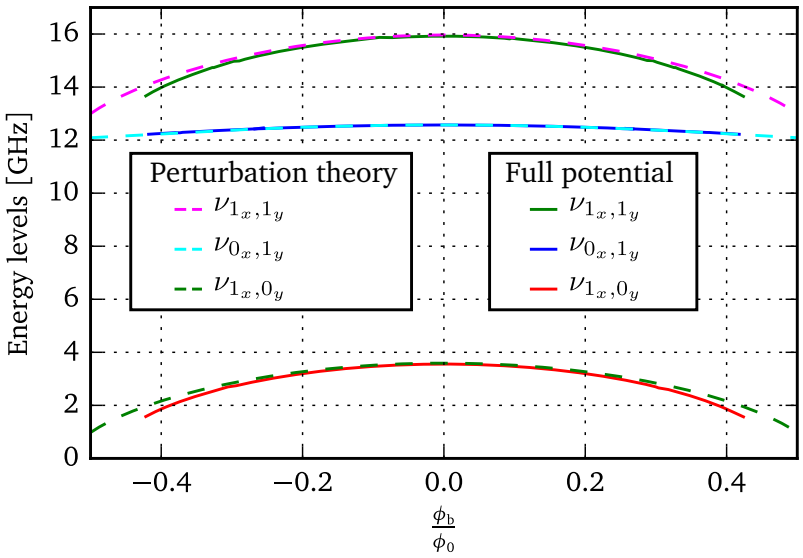

Figure (1.10): Three energy levels as a function of magnetic flux. The result of the quantum perturbation theory is plotted in dashed line while the result of the numerical simulation of the potential in Eq. (1.30) *is in solid line. Circuit parameters used for the plot are summarised in Table 1.5.*

term is of about 3.9 %. When the bias flux is going close to $\phi_b = \pm\phi_0/2$, the approximation is less and less correct. We attribute that discrepancy to higher nonlinear coupling which are not taken into account in our analytical derivation.

1.1.4 A V-shape artificial atom

At $\phi_b = 0$ the symmetric and anti-symmetric oscillators reach a symmetry point where they are protected, at the first order, against flux noise. Indeed Fig. 1.6 and Fig. 1.7 show that at this point the levels and the cross-Kerr coupling reach a sweet point while the coupling term ω_{21} is zero. Thus for the rest of the section we will set $\phi_b = 0$ as our working point. We note that the eigenenergy formula, Eq. (1.46), is still valid.

In quantum computing, a qubit or quantum bit is a two-state quantum-mechanical system. Hereafter we will name the qubit formed by the two first levels of the symmetric oscillator as the "logical qubit" while the second qubit, constituted by the two first levels of the anti-symmetric oscillator, will be called the "ancilla qubit".

Following the simplification introduced in the previous paragraph, we define ω_{qb} and ω_a the eigenfrequencies of the qubit and the ancilla. The cross-Kerr coupling strength becomes

g_{zz}. Theses quantities are defined as:

$$\omega_{\text{qb}} = \omega_x (1-3\delta_x) + \omega_{22} \tag{1.49}$$

$$\omega_{\text{a}} = \omega_y \left(1-3\delta_y\right) + \omega_{22} \tag{1.50}$$

$$g_{zz} = -\frac{\omega_{22}}{2} \tag{1.51}$$

Figure 1.11 illustrates the transformation from one notation to the other.. The ground state is denoted $|g\rangle = \left|0_x, 0_y\right\rangle$. The level $\left|1_x, 0_y\right\rangle$ becomes the qubit level $|e\rangle$. The level $\left|0_x, 1_y\right\rangle$ becomes the ancilla level $|a\rangle$. The level $\left|1_x, 1_y\right\rangle$ is denoted $|p\rangle$.

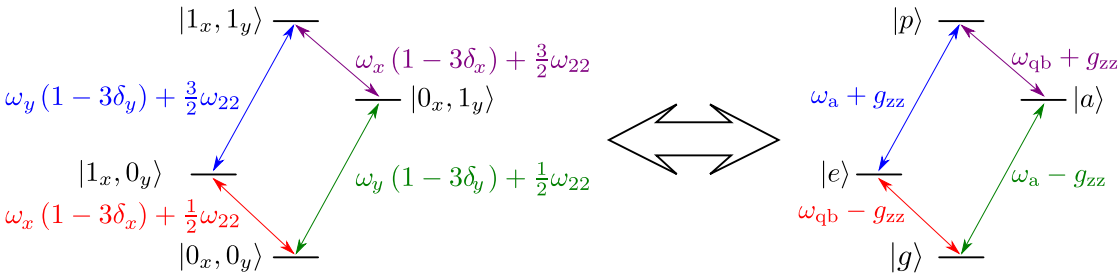

Figure (1.11): Equivalence of the two notations. The left side shows the system in the two oscillators notation. The right side presents the system in the two-level system notation.

The Hamiltonian given in Eq. (1.40) becomes:

$$\widehat{\mathscr{H}} = \frac{\hbar}{2}\omega_{\text{qb}}\widehat{\sigma}_z^{\text{qb}} + \frac{\hbar}{2}\omega_{\text{a}}\widehat{\sigma}_z^{\text{a}} + \frac{\hbar}{2}g_{zz}\widehat{\sigma}_z^{\text{qb}}\widehat{\sigma}_z^{\text{a}} \tag{1.52}$$

where the $\widehat{\sigma}_z$ operator is a Pauli matrice.

The qubit and the ancilla are modelled as simple two-level systems. The cross-Kerr term g_{zz} couples the two qubits through $\widehat{\sigma}_z$ operators.

A readout of the logical qubit can be realised by measuring the resonance frequency of the ancilla. The Hamiltonian Eq. (1.52) can indeed be rewritten as:

$$\widehat{\mathscr{H}} = \frac{\hbar}{2}\omega_{\text{qb}}\widehat{\sigma}_z^{\text{qb}} + \frac{\hbar}{2}\left(\omega_{\text{a}} + g_{zz}\widehat{\sigma}_z^{\text{qb}}\right)\widehat{\sigma}_z^{\text{a}} \tag{1.53}$$

Through the σ_z^{qb} operator, the resonance frequency of the ancilla depends of the qubit state. Depending on the qubit state the plasma frequency of the ancilla is modified by $2g_{zz}$. In the "V-shape-2" sample, this value has been measured to be $2g_{zz}/(2\pi) = 110\,\text{MHz}$. For such large g_{zz} values, the system behave like a V-shape artificial atom, justifying the name of our samples: the "V-shape" devices.

1.2 Microwave resonator

In this section we will start by a model of a transmission-line. Then we will introduce a $\lambda/4$ microwave resonator. Finally we consider the resonator coupled to the two coupled qubits introduced in the previous section.

1.2.1 Transmission line

In this part, we will summarise some important results of the electrical transmission line model. A transmission line is described as an infinite series of two-port elementary components, each component representing an infinitesimally short segment of the transmission line, see Fig. 1.12. R_ℓ, G_ℓ, L_ℓ and C_ℓ denotes the distributed resistance, conductance, inductance and capacitance along the line. By using Kirchhoff's voltage law on the circuit in Fig. 1.12 we get the so-called "Telegrapher's equations":

$$\begin{cases} \frac{\partial V}{\partial z}(z,t) &= R_\ell I(z,t) &+ L_\ell \frac{\partial I}{\partial t}(z,t) \\ \frac{\partial I}{\partial z}(z,t) &= G_\ell V(z,t) &+ C_\ell \frac{\partial V}{\partial t}(z,t) \end{cases} \tag{1.54}$$

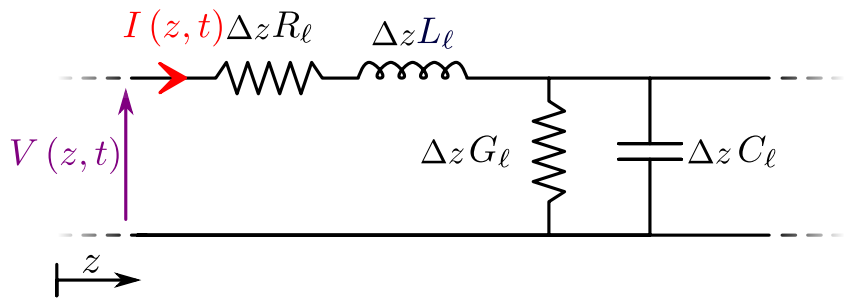

Figure (1.12): Infinitesimally short segment of a transmission line composed of elementary components, a resistance, an inductance, an conductance, and a capacitance. The current and voltage at the position z are represented through arrows.

We solve the set of equations by assuming a sinusoidal steady-state solution and the separation of variables. The solutions of these equations give the voltage and current distribution along the transmission line:

$$\begin{cases} V(z) &= V_0^+ e^{-\gamma z} + V_0^- e^{\gamma z} \\ I(z) &= I_0^+ e^{-\gamma z} + I_0^- e^{\gamma z}. \end{cases} \tag{1.55}$$

The term $e^{-\gamma z}$ and $e^{\gamma z}$ represent waves propagation in $+z$ and $-z$ direction respectively. The voltage and current amplitudes of the propagating waves in the $+z$ direction are denoted V_0^+ and I_0^+ while they are denote V_0^- and I_0^- is the $-z$ direction. The complex wave vector γ is given by:

$$\gamma = \sqrt{(R_\ell + \mathrm{i}\omega L_\ell)(G_\ell + \mathrm{i}\omega C_\ell)}. \tag{1.56}$$

We can also write the complex number as $\gamma = \alpha + \mathrm{i}\beta$, α representing the attenuation of the TL and β the wave number. These quantities are given by:

$$\alpha^2 = \frac{1}{2}\left(\sqrt{\left(R_\ell^2 + L_\ell^2\omega^2\right)\left(G_\ell^2 + C_\ell^2\omega^2\right)} + R_\ell G_\ell - L_\ell C_\ell \omega^2\right) \tag{1.57}$$

$$\beta^2 = \frac{1}{2}\left(\sqrt{\left(R_\ell^2 + L_\ell^2\omega^2\right)\left(G_\ell^2 + C_\ell^2\omega^2\right)} - R_\ell G_\ell + L_\ell C_\ell \omega^2\right). \tag{1.58}$$

Finally we introduce the characteristic impedance Z_0 of a TL which correspond to the ratio of voltage and current amplitudes of a propagating wave along the line:

$$Z_0 = \frac{V_0^+}{I_0^+} = -\frac{V_0^-}{I_0^-} = \sqrt{\frac{R_\ell + \mathrm{i}\omega L_\ell}{G_\ell + \mathrm{i}\omega C_\ell}}. \tag{1.59}$$

1.2.2 Quarter-wave resonator

In this section we introduce the formal description of a distributed $\lambda/4$ resonator. We mainly follow the calculation of David. M. Pozar[61].

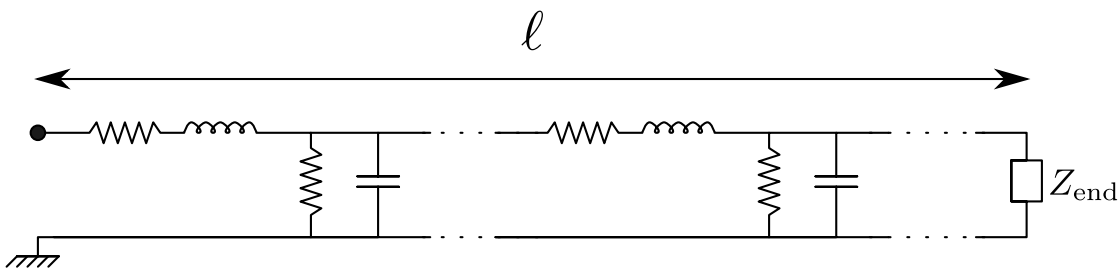

Figure (1.13): Transmission line of length ℓ with an open circuit at the left and a shunt impedance Z_{end} at the right.

The impedance of a transmission line of length ℓ, of characteristic impedance Z_0, ended by an impedance Z_{end} is[61]:

$$Z_{\mathrm{in}} = \frac{Z_{\mathrm{end}} \cosh(\gamma\ell) + Z_0 \sinh(\gamma\ell)}{Z_{\mathrm{end}} \sinh(\gamma\ell) + Z_0 \cosh(\gamma\ell)} Z_0. \tag{1.60}$$

In a case of a transmission line shorted to ground, $Z_{\mathrm{end}} \to 0$, we get:

$$Z_{\mathrm{in}} = Z_0 \tanh(\gamma\ell). \tag{1.61}$$

By expanding the real and imaginary part, we obtain:

$$Z_{\mathrm{in}} = \frac{Z_0}{1 + \tanh^2(\alpha\ell)\tan^2(\beta\ell)} \Big(\tanh(\alpha\ell)\sec^2(\beta\ell) + i\tan(\beta\ell)\operatorname{sech}^2(\alpha\ell) \Big). \tag{1.62}$$

At the resonance, the imaginary part of the impedance goes to infinity[61]. That gives the following condition from Eq. (1.62):

$$\tan(\beta\ell) = \infty. \tag{1.63}$$

The solution of Eq. (1.63) is equivalent to $\beta\ell = (2n+1)\pi/2$ with $n \in \mathbb{N}$. We can replace the wave vector β by $2\pi/\lambda$ which gives that at the resonance, $\ell = (2n+1)\lambda/4$. Thus the circuit resonates when $\ell = (2n+1)\lambda/4$. The lowest resonance occurs when $\ell = \lambda/4$ which justifies the name of these kind of resonators.

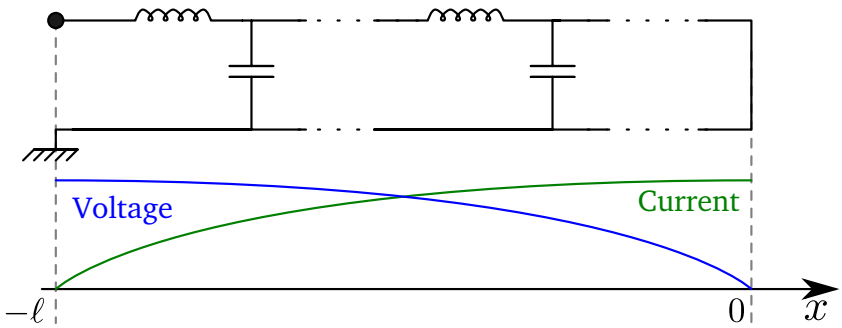

Figure (1.14): Parametrisation of a quarter-wave resonator used to derive current and voltage operators.

1.2.3 The current and voltage quantum operators

In this section we derive the current and voltage quantum operator of a $\lambda/4$ resonator. Such operators have already be derived by Alexender Blais in a case of a $\lambda/2$ resonator[44]. Following the derivation of A. Blais, we will, in a first time, calculate the Lagrangian and Hamiltonian of a quarter-wave resonator. Next the current and voltage quantum operators will be derived.

We introduce the branch flux variable[51,62]:

$$\psi(x,t) = \int_{-\infty}^{t} V(x,\tau)\, \mathrm{d}\tau. \tag{1.64}$$

The Lagrangian is the difference of the electric and magnetic energy stored in the distributed capacitance and inductance:

$$\mathscr{L} = \int_{-l}^{0} \left(\frac{1}{2} C_\ell \left[\partial_t \psi(x,t)\right]^2 - \frac{1}{2}\frac{1}{L_\ell}\left[\partial_x \psi(x,t)\right]^2 \right) \mathrm{d}x. \tag{1.65}$$

The Euler-Lagrange equantion gives us:

$$\frac{\mathrm{d}}{\mathrm{d}t}\left(\frac{\partial \mathscr{L}}{\partial\left[\partial_t \psi(x,t)\right]} \right) + \frac{\mathrm{d}}{\mathrm{d}x}\left(\frac{\partial \mathscr{L}}{\partial\left[\partial_x \psi(x,t)\right]} \right) - \frac{\partial \mathscr{L}}{\partial \psi(x,t)} = 0. \tag{1.66}$$

The result is:

$$\int_{-l}^{0} \left(C_\ell \partial_{tt}\psi(x,t) - \frac{1}{L_\ell}\partial_{xx}\psi(x,t) \right) \mathrm{d}x = 0. \tag{1.67}$$

To solve the differential equation, we use the separation of variables method. We assume that the solution can be written as:

$$\psi(x,t) = \sum_{n\in\mathbb{N}} \phi_n(t)\,\theta_n(x). \tag{1.68}$$

The boundary conditions used to obtain the solution corresponding to a $\lambda/4$ resonator are:

$$\begin{aligned} \partial_x \theta(x)\Big|_{x=-\ell} &= 0 \quad \text{(Zero current at } x=-\ell) \\ \partial_{xx} \theta(x)\Big|_{x=0} &= 0 \quad \text{(Short circuit at } x=0), \end{aligned} \tag{1.69}$$

Fig. 1.14 illustrates these conditions. We insert Eq. (1.68) in Eq. (1.66) and by using the boundary conditions, we obtain:

$$\psi(x,t) = \sum_{k_o \in \{2n+1 : n \in \mathbb{N}\}} \phi_{k_o}(t) \sin\left(\frac{k_o \pi}{2\ell} x\right). \tag{1.70}$$

The parameter k_o represents the different modes which exist in the resonator. Since only odd modes satisfy boundary conditions of a $\lambda/4$ resonator, k_o is a positive odd number. Hereafter the summation will only be denoted by k_o for reasons of simplicity.

By introducing the spatial dependence Eq. (1.70) in the Lagrangian Eq. (1.65), we obtain, after spatial integration, the Lagrangian in the form of a set of harmonic oscillators:

$$\mathscr{L}\left(\phi_1, \phi_3, \ldots, \dot{\phi}_1, \dot{\phi}_3, \ldots\right) = \sum_{k_o} \left[\frac{C_\ell \ell}{4} \dot{\phi}_{k_o}^2(t) - \frac{k_o^2 \pi^2}{16 L_\ell \ell} \phi_{k_o}^2(t) \right]. \tag{1.71}$$

The conjugate momentum is derived from the Lagragian:

$$\pi_{k_o}(t) = \frac{\partial \mathscr{L}}{\partial \dot{\phi}_{k_o}^2(t)} = \frac{C_\ell \ell}{2} \dot{\phi}_{k_o}(t). \tag{1.72}$$

The Hamiltonian is derived by using the Legendre transformation:

$$\mathscr{H}(\phi_1, \phi_3, \ldots, \pi_1, \pi_3, \ldots) = \sum_{k_o} \left[\frac{1}{C_\ell \ell} \pi_{k_o}^2(t) + \frac{k_o^2 \pi^2}{16 L_\ell \ell} \phi_{k_o}^2(t) \right]. \tag{1.73}$$

We introduce dimensionless variables:

$$\tilde{\pi}_{k_o}(t) = \sqrt{\frac{2}{\hbar \omega_{k_o} C_\ell \ell}} \pi_{k_o}(t), \qquad , \qquad \tilde{\phi}_{k_o}(t) = \sqrt{\frac{k_o^2 \pi^2}{8 \hbar \omega_{k_o} L_\ell \ell}} \phi_{k_o}(t). \tag{1.74}$$

where ω_{k_o} corresponds to the resonance frequency of the resonator and is defined as:

$$\omega_{k_o} = \frac{k_o \pi}{2\ell} \sqrt{\frac{1}{L_\ell C_\ell}}. \tag{1.75}$$

The reduced Hamiltonian is then:

$$\mathscr{H}\left(\tilde{\phi}_1, \tilde{\phi}_3, \ldots, \tilde{\pi}_1, \tilde{\pi}_3, \ldots\right) = \sum_{k_o} \frac{\hbar \omega_{k_o}}{2} \left[\tilde{\pi}_{k_o}^2(t) + \tilde{\phi}_{k_o}^2(t) \right]. \tag{1.76}$$

Applying the standard canonical quantization rules, we replace the classical variables by their corresponding quantum operators. The conjugate pairs satisfy the following commutation operations:

$$\left[\widehat{\phi}_{k_o}, \widehat{\pi}_{k'_o}\right] = \mathrm{i}\delta_{k_o k'_o}. \tag{1.77}$$

We introduce ladder operators:

$$\widehat{a}_{k_o}(t) = \frac{\widehat{\phi}_{k_o}(t) + i\widehat{\pi}_{k_o}(t)}{\sqrt{2}}, \qquad , \qquad \widehat{a}^{\dagger}_{k_o}(t) = \frac{\widehat{\phi}_{k_o}(t) - i\widehat{\pi}_{k_o}(t)}{\sqrt{2}}. \tag{1.78}$$

The Hamiltonian operator for a quarter-wave resonator is:

$$\widehat{\mathscr{H}} = \sum_{k_o} \hbar\omega_{k_o}\left(\widehat{a}^{\dagger}_{k_o}\widehat{a}_{k_o} + \frac{1}{2}\right). \tag{1.79}$$

The Hamiltonian shows that the energy of a $\lambda/4$ resonator is decomposed in modes k_o. In each mode, the energy scales as in a harmonic oscillator.

The current and voltage can be obtained from:

$$I(x,t) = \partial_x \psi(x,t)\frac{1}{L_\ell}, \tag{1.80}$$

$$V(x,t) = \partial_t \psi(x,t). \tag{1.81}$$

After some algebra we obtain the current and voltage quantum operators for a quarter-wave resonator:

$$\widehat{I}(x,t) = \sum_{k_o}\sqrt{\frac{2\hbar}{k_o\pi}\sqrt{\frac{L_\ell}{C_\ell}}\frac{k_o\pi}{2L_\ell\ell}}\cos\left(\frac{k_o\pi}{2\ell}x\right)\left[\widehat{a}^{\dagger}_{k_o}(t) + \widehat{a}_{k_o}(t)\right], \tag{1.82}$$

$$\widehat{V}(x,t) = i\sum_{k_o}\sqrt{\frac{\hbar k_o\pi}{2\ell^2 C_\ell}\sqrt{\frac{1}{L_\ell C_\ell}}}\sin\left(\frac{k_o\pi}{2\ell}x\right)\left[\widehat{a}^{\dagger}_{k_o}(t) - \widehat{a}_{k_o}(t)\right]. \tag{1.83}$$

1.3 The V-shape device coupled to a quarter-wave resonator

In this section we introduce the coupling between the 2D-SQUID described in the Section 1.1.2 and the microwave resonator. In a first time, we will show that the two oscillating modes exhibit different ways of coupling. At the end of the section, we explain how to place the 2D-SQUID in a microwave resonator in order to couple only one mode of the 2D-SQUID to the resonator.

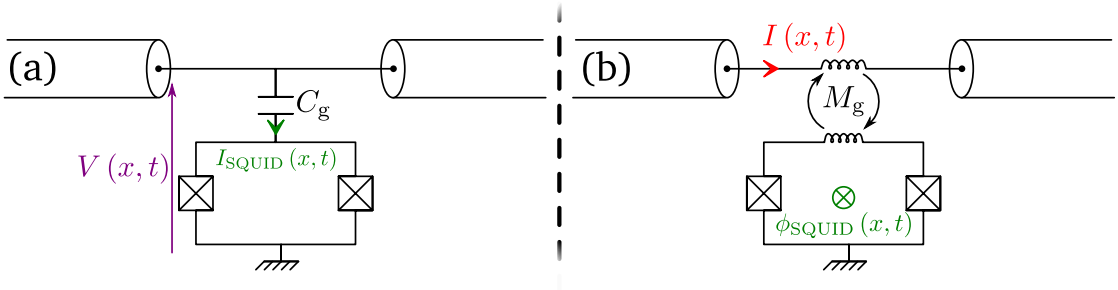

Figure (1.15): Model of the coupling between the qubit/ancilla and the resonator. (a): For the qubit mode, the coupling is due to the electric field inside the resonator. The coupling is then modelled by a capacitance C_g. (b): For the ancilla mode, the coupling is due to the magnetic field inside the resonator. The coupling is then modelled by a mutual indutance M_g.

1.3.1 Coupling between the SQUID and the electromagnetic field

Equation (1.29) gives the classical Hamiltonian for a current and flux biased SQUID with different junction parameters. From this Hamiltonian we derive the coupling of the SQUID to the electromagnetic field.

To the current and flux bias I_b and ϕ_b, we add time dependence excitations $\delta I(t)$ and $\delta\phi(t)$. Then we develop the Hamiltonian at the first-order in $\delta I(t)$ and $\delta\phi(t)$. Following the quantization method explained in Section 1.1.3, we obtain quantum coupling operators between the external electromagnetic field and the SQUID. In case of a SQUID with Josephson junction having the same critical current and the same capacitance, the coupling terms are:

$$\widehat{\mathscr{W}}_x^{\delta I(t)} = -\frac{\phi_0}{2\pi}\sqrt{\frac{E_C}{2\hbar\omega_x}}\widehat{\delta I}\left(\widehat{a}_x^\dagger + \widehat{a}_x\right), \tag{1.84}$$

$$\widehat{\mathscr{W}}_y^{\delta\phi(t)} = -\frac{\phi_0}{2\pi}\sqrt{\frac{E_C}{2\hbar\omega_y}\frac{1}{L_{loop}}}\widehat{\delta\phi}\left(\widehat{a}_y^\dagger + \widehat{a}_y\right). \tag{1.85}$$

The symmetric mode is only coupled to current excitation whereas the anti-symmetric mode is only coupled to flux excitation. A current excitation creates a symmetric oscillation of the phase difference in each Josephson junction. A flux fluctuation creates a anti-symmetric oscillation in each junction through a circulating current in the loop[1].

Current and flux in the SQUID

We now consider the SQUID coupled to a $\lambda/4$ resonator. In a first approximation we can model the coupling as a linear electric component making the link between the SQUID and the resonator. In the case of the symmetric oscillator, the coupling comes from the electric field and it is modelled with a capacitor of capacitance C_g. For the anti-symmetric oscillating mode

[1]In a case a SQUID with different Josephson junction parameters, other coupling terms arise. The interested reader can found the derivation of all coupling terms in the thesis of Julien Claudon[56].

the coupling is due to the magnetic field and a mutual inductance M_g between the SQUID and the resonator modelled the coupling. The model is illustrated in Fig. 1.15. The operators describing the flux and current in the SQUID due to the current and voltage evolving inside the resonator are derived as:

$$\widehat{\phi}_{\text{SQUID}}(x,t) = M_g \widehat{I}(x,t), \tag{1.86}$$

$$\widehat{I}_{\text{SQUID}}(x,t) = C_g \partial_t \widehat{V}(x,t). \tag{1.87}$$

Coupling between the SQUID and the resonator

The coupling terms between the symmetric and anti-symmetric oscillators and the $\lambda/4$ resonator are obtained by inserting Eq. (1.87) in Eq. (1.85):

$$\widehat{\mathscr{W}}_x^{\delta I(t)} = \sum_{k_o} \hbar g_{x,k_o} \left[\widehat{a}^\dagger(t) + \widehat{a}(t)\right]\left[\widehat{a}_x^\dagger + \widehat{a}_x\right], \tag{1.88}$$

$$\widehat{\mathscr{W}}_y^{\delta \phi(t)} = \sum_{k_o} \hbar g_{y,k_o} \left[\widehat{a}^\dagger(t) + \widehat{a}(t)\right]\left[\widehat{a}_y^\dagger + \widehat{a}_y\right]. \tag{1.89}$$

with:

$$g_{x,k_o} = \frac{1}{2e}\frac{C_g}{C_\ell L_\ell}\left(\frac{k_o\pi}{2\ell}\right)^2 \sqrt{\frac{E_C}{k_0\pi}\frac{1}{\omega_x}\sqrt{\frac{L_\ell}{C_\ell}}}\sin\left(\frac{k_o\pi}{2\ell}x\right), \tag{1.90}$$

$$g_{y,k_o} = -\frac{1}{2e}\frac{M_g}{L_{\text{loop}}L_\ell}\frac{k_o\pi}{2\ell}\sqrt{\frac{E_C}{k_0\pi}\frac{1}{\omega_y}\sqrt{\frac{L_\ell}{C_\ell}}}\cos\left(\frac{k_o\pi}{2\ell}x\right). \tag{1.91}$$

1.3.2 Logical and ancilla qubits coupled to the fundamental mode of the resonator

Hereafter we will restrain the derivation to the fundamental mode of the resonator. Next we consider low-energy excitation and so, we replace the symmetric and anti-symmetric oscillator by the logical and ancilla qubit, see Section 1.1.4. Thus we replace the $\left(\widehat{a}_{x|y}, \widehat{a}_{x|y}^\dagger\right)$ operators by $\left(\widehat{\sigma}_+^{\text{qb}|\text{a}}, \widehat{\sigma}_-^{\text{qb}|\text{a}}\right)$. Finally we will adopt the rotating-wave approximation thanks to which we neglect terms that oscillate rapidly. This approximation is valid only when $\omega_r - \omega_{x,y} \ll \omega_r + \omega_{x,y}$ (where ω_r is the fundamental resonance frequency of the resonator). We obtain:

$$\widehat{\mathscr{W}}_{\text{qb}} = \hbar g_{\text{qb}}\left(\widehat{a}\widehat{\sigma}_+^{\text{qb}} + \widehat{a}^\dagger\widehat{\sigma}_-^{\text{qb}}\right), \tag{1.92}$$

$$\widehat{\mathscr{W}}_{\text{a}} = \hbar g_{\text{a}}\left(\widehat{a}\widehat{\sigma}_+^{\text{a}} + \widehat{a}^\dagger\widehat{\sigma}_-^{\text{a}}\right), \tag{1.93}$$

where g_{qb} and g_{a} correspond to factors g_x and g_y given in Eq. (1.91) with $k_o = 1$, respectively.

Figure 1.16 shows the position dependence of the coupling between the fundamental mode of the resonator and the qubit/ancilla mode. We remark that g_{qb} goes from its maximum

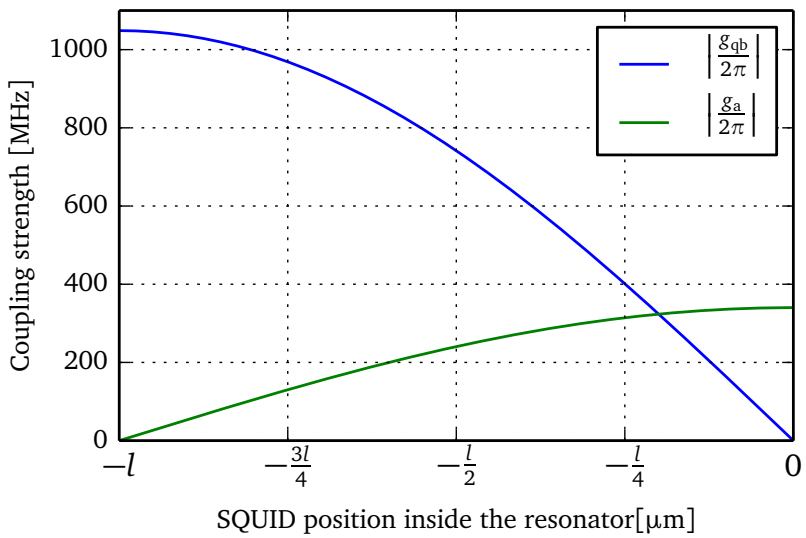

Figure (1.16): Absolute value of the coupling between the ancilla/qubit mode and the fundamental mode of the resonator. For this plot the coupling constants are $C_g = 10\,\mathrm{fF}$ and $M_g = 180\,\mathrm{pH}$ which roughly corresponds to our experimental circuit.

value to zero depending on the position of the SQUID within the resonator whereas g_a shows opposite behaviour. This behaviour is due to the nature of the field coupling which is electric in the case of g_{qb} and magnetic for g_a. The boundary conditions of the microwave resonator, see Eq. (1.69), impose zero voltage at $x = -\ell$ and zero current at $x = 0$. These conditions lead to a cosine electro-magnetic field distribution along the resonator length, see Eq. (1.83). The dependence of the g factors along the resonator length follows then the field distribution inside the cavity.

Figure 1.16 shows that $g_{qb}^{max}/g_a^{max} \approx 2$. The parameter used to plot are $C_g = 10\,\mathrm{fF}$ and $M_g = 180\,\mathrm{pH}$ which roughly correspond to our experimental circuit parameters.

In varying the position of the SQUID within the resonator, it is possible to control the coupling ratio g_{qb}/g_a. At $x = -\ell$ the electric field is maximum while the magnetic field is null. In this case the coupling strength between the logical qubit and the resonator reaches its maximum value. Additionally, the ancilla qubit will not be coupled to the resonator due to the absence of z magnetic field. At the other limit of the resonator, $x = 0$, the situation is inverted with a logical qubit decoupled from the resonator and the coupling of the ancilla qubit which reaches its maximum.

1.4 Transmission of the V-shape device coupled to a $\lambda/4$ resonator

We obtain the Hamiltonian of the full system by adding the Hamiltonian of the SQUID Eq. (1.53), of the microwave resonator Eq. (1.79), and of the coupling between the microwave resonator and the SQUID Eq. (1.93):

$$\widehat{\mathscr{H}} = \frac{\hbar}{2}\omega_{\mathrm{qb}}\widehat{\sigma}_{\mathrm{z}}^{\mathrm{qb}} + \frac{\hbar}{2}\left(\omega_{\mathrm{a}} + g_{\mathrm{zz}}\widehat{\sigma}_{\mathrm{z}}^{\mathrm{qb}}\right)\widehat{\sigma}_{\mathrm{z}}^{\mathrm{a}} + \hbar\omega_{\mathrm{R}}\widehat{a}^{\dagger}\widehat{a}$$
$$+ \hbar g_{\mathrm{qb}}\left(\widehat{a}\widehat{\sigma}_{+}^{\mathrm{qb}} + \widehat{a}^{\dagger}\widehat{\sigma}_{-}^{\mathrm{qb}}\right) + \hbar g_{\mathrm{a}}\ \left(\widehat{a}\widehat{\sigma}_{+}^{\mathrm{a}}\ + \widehat{a}^{\dagger}\widehat{\sigma}_{-}^{\mathrm{a}}\ \right). \tag{1.94}$$

In Section 1.3.1 we have seen that the position of the SQUID whithin the resonator modifies the coupling strength between the ancilla/qubit mode and the resonator. In the following we choose an optimal position where $g_{\mathrm{qb}} = 0$ and the g_{a} is maximum, $x = 0$. Equation (1.94) becomes:

$$\widehat{\mathscr{H}} = \frac{\hbar}{2}\omega_{\mathrm{qb}}\widehat{\sigma}_{\mathrm{z}}^{\mathrm{qb}} + \frac{\hbar}{2}\left(\omega_{\mathrm{a}} + g_{\mathrm{zz}}\widehat{\sigma}_{\mathrm{z}}^{\mathrm{qb}}\right)\widehat{\sigma}_{\mathrm{z}}^{\mathrm{a}} + \hbar\omega_{\mathrm{R}}\widehat{a}^{\dagger}\widehat{a} + \hbar g_{\mathrm{a}}\left(\widehat{\sigma}_{-}^{\mathrm{a}}\widehat{a}^{\dagger} + \widehat{\sigma}_{+}^{\mathrm{a}}\widehat{a}\right). \tag{1.95}$$

1.4.1 Input-Output theory of a resonator evanescently coupled

We briefly present here the input-output theory developed by C. W. Gardiner and M. J. Collett[63] and adapted for evanescently coupled by system B.Peropadre *et. al*[64]. The theory offers a simple way to analyse the dynamics of a quantum system described through a Hamiltonian $\mathscr{H}$ coupled to an environment via one port whose energy decay rate is denoted κ. This port links the Hamiltonian to N connections.

The input field is defined as an incoming wave to the resonator while the output field is defined as an outgoing wave from the resonator:

$$\begin{cases} \widehat{b}_{\mathrm{i}}(t) &= \frac{1}{\sqrt{2\pi}}\int e^{-i\omega[t-t_0]}\widehat{d}_{i_0}(\omega)\ \mathrm{d}\omega, \\ \widehat{b}'_{\mathrm{i}}(t) &= \frac{1}{\sqrt{2\pi}}\int e^{-i\omega[t-t_1]}\widehat{d}'_{i_0}(\omega)\ \mathrm{d}\omega. \end{cases} \tag{1.96}$$

$\widehat{d}_{i_0}$ is the initial condition imposed to the incoming wave for time $t_0 < t$ and $\widehat{d}'_{i_0}$ is the final condition imposed for the outgoing wave for time $t_1 > t$.

For each connection we have a relation between the input, the output field, and one of the several possible operators of the quantum system:

$$\widehat{b}'_i(t) - \widehat{b}_i(t) = \sqrt{\frac{\kappa_i}{N}}\widehat{c}(t). \tag{1.97}$$

The general dynamic equation of these operators is given by:

$$\partial_t\widehat{c}(t) = \frac{\left[\widehat{c}(t), \widehat{\mathscr{H}}\right]}{i\hbar} - \left(\sum_i \frac{\kappa_i}{2}\right)\widehat{c}(t) + \sum_i \sqrt{\frac{\kappa_i}{N}}\widehat{b}_i(t). \tag{1.98}$$

The first term of Eq. (1.98) describes the internal dynamics of the quantum system. The second term is the damping due to output ports while the last term shows an energy provision through input ports.

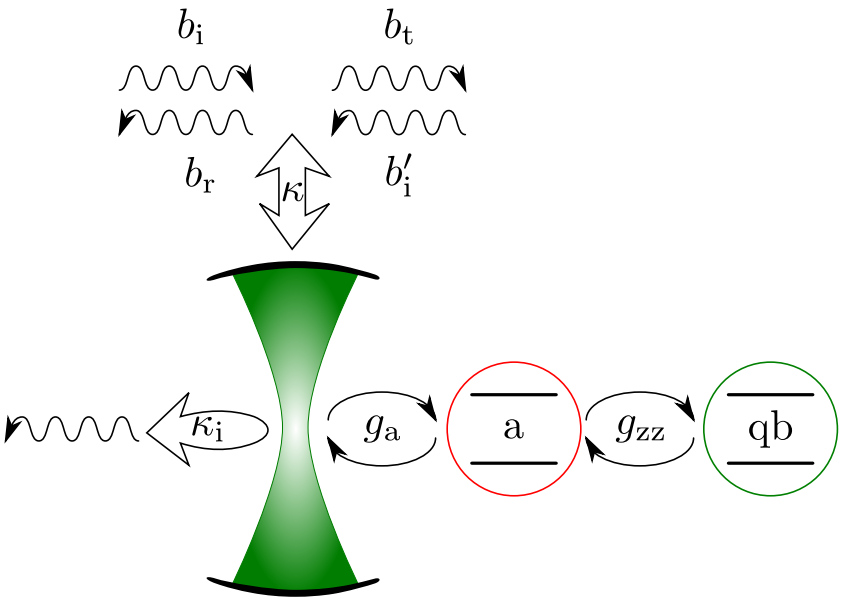

Figure (1.17): Sketch of the model used to derive the transmission of the system. The logical and ancilla qubits are depicted as two-level systems. They are coupled together through the cross-Kerr coupling g_{zz}. Only the ancilla is coupled to the microwave resonator through a coupling g_a. The microwave resonator is evanescently coupled to the environment with one port through which energy exchange is possible at rate κ. The losses of the resonator are modelled as a virtual port with energy decay rate κ_i.

Application of the Input-Ouput theory

The Langevin equation, Eq. (1.98), is the starting point to derive the dynamics of a the SQUID coupled to a resonator. A sketch of the system is shown in Fig. 1.17.

The qubit and the ancilla are coupled through the cross-Kerr coupling g_{zz}. Only the ancilla is coupled to the microwave resonator via the coupling g_a. As we already mentioned this is made possible by the position of the SQUID in the microwave resonator.

The microwave resonator is evanescently coupled to the environment with one port. The decay rate of the port is denoted κ.

The losses of the resonator are modelled by adding an additional virtual port i. The port i does not bring excitation but allows internal relaxation inside the resonator. The decay rate κ_i models all the losses of the resonator.

Finally at the left we have the input and reflected field denoted b_i and b_r. At the right we have the transmitted field denoted b_t and a second input field b'_i.

The dynamic of the intra-resonator operator is then given by:

$$\partial_t \widehat{a}(t) = -i\omega_\mathrm{R}\widehat{a} - ig_\mathrm{a}\widehat{\sigma}^\mathrm{a}_- - \frac{\kappa+\kappa_\mathrm{i}}{2}\widehat{a} + \sqrt{\frac{\kappa}{2}}\widehat{b}_\mathrm{i} + \sqrt{\frac{\kappa}{2}}\widehat{b}'_\mathrm{i}. \tag{1.99}$$

We remark that the dynamics of the intra-resonator operator depends on the ancilla through the operator $\widehat{\sigma}^\mathrm{a}_-$. By using Heisenberg's picture we derive the time dependence of the different

system operators. The full dynamics of the system correspond to the following set of coupled differential equations:

$$\begin{cases} \partial_t \widehat{a}(t) & = -i\omega_{\mathrm{R}}\widehat{a} - ig_{\mathrm{a}}\widehat{\sigma}_-^{\mathrm{a}} - \frac{\kappa+\kappa_{\mathrm{i}}}{2}\widehat{a} + \sqrt{\frac{\kappa}{2}}\widehat{b}_{\mathrm{i}} + \sqrt{\frac{\kappa}{2}}\widehat{b}_{\mathrm{i}}' \\ \partial_t \widehat{\sigma}_-^{a}(t) & = -i\left(\omega_{\mathrm{R}} + \delta_{\mathrm{qb}} - \delta_{\mathrm{a}}\right)\widehat{\sigma}_- a - ig_{\mathrm{a}} a \widehat{\sigma}_{\mathrm{z}}^{\mathrm{a}} \\ \partial_t \widehat{\sigma}_{\mathrm{z}}(t) & = -2ig_{\mathrm{a}}\left(\widehat{a}^\dagger \widehat{\sigma}_-^{a} - \widehat{\sigma}_+^{a}\widehat{a}\right) \end{cases}. \tag{1.100}$$

The input and the output field are related to the intra-resonator operator through:

$$\begin{cases} \widehat{b}_{\mathrm{i}}(t) - \widehat{b}_{\mathrm{t}}(t) & = \sqrt{\frac{\kappa}{2}}\widehat{a}(t) \\ \widehat{b}_{\mathrm{i}}'(t) - \widehat{b}_{\mathrm{r}}(t) & = \sqrt{\frac{\kappa}{2}}\widehat{a}(t) \end{cases}. \tag{1.101}$$

We define the transmission in a steady-state regime as:

$$T = \frac{\langle \widehat{b}_{\mathrm{t}}(t)\rangle}{\langle \widehat{b}_{\mathrm{i}}(t)\rangle}. \tag{1.102}$$

Moreover, we suppose no second input field and so have:

$$\langle \widehat{b}_{\mathrm{i}}\prime(t)\rangle = 0 \tag{1.103}$$

We then derive the transmission of the overall system in a steady-state regime as:

$$T(\omega) = t_{\lambda/4}(\omega)\left(1 + \frac{\kappa}{\kappa_{\mathrm{i}} + \mathrm{i}2\Delta\omega}\frac{1}{1 - \frac{\delta\omega}{2g_{\mathrm{a}}^2}(2\Delta\omega - \mathrm{i}[\kappa + \kappa_{\mathrm{i}}])}\frac{1}{1 + \frac{p}{p_{\mathrm{s}}}}\right). \tag{1.104}$$

The expressions of the different terms used in Eq. (1.104) are given in Table 1.6. The transmission amplitude and phase are plotted in Fig. 1.18 for the two possible qubit states.

The blue and green solid curve shows the transmission of the system when the logical qubit is in its ground state and excited state, respectively. When the logical qubit is in its ground state, the ancilla level is in resonance with the bare resonance frequency of the microwave resonator. Due to the coupling between the ancilla and the resonator, an avoided crossing occurs. This phenomena is visible in the transmission in the two blue peaks equally spaced from the the bare resonance frequency of the resonator by g_{a}.

The green curve corresponds to the transmission of the system when the qubit is in its excited state. Due to the g_{zz} coupling the ancilla level is not anymore in resonance with the microwave resonator. We have the central peak corresponding to the resonator which is slightly shifted to higher frequency compared to the bare resonator. The shift of the resonator is equal to $\delta_{\mathrm{L}} = g_{\mathrm{zz}}\left(\sqrt{1 + (g_{\mathrm{a}}/g_{\mathrm{zz}})^2} - 1\right)$. This regime is the so-called "dispersive limit". The central peak corresponds to the cavity and the small peak at the left correspond to the ancilla qubit. Also the peak due to the ancilla resonance is slightly shifted to lower frequency.

1.4.2 Logical-qubit readout

The read-out of the qubit state is realised by probing the system at the frequency $\omega_{\mathrm{readout}} = \omega_{\mathrm{R}} + \delta_{\mathrm{L}}$. This special frequency is represented in Fig. 1.18 by a red dashed line. At this specific frequency the transmission difference of the overall system between grounded and excited state is maximal.

Denomination	Formula
The qubit-state-dependent shift	$\delta_{\mathrm{qb}} = g_{\mathrm{zz}}\left(1+\sigma_{\mathrm{z}}^{\mathrm{qb}}\right)$
The resonator–pump detuning	$\Delta\omega_{\mathrm{R}} = \omega_{\mathrm{R}} - \omega$
The ancilla–resonator detuning	$\delta_{\mathrm{a}} = \omega_{\mathrm{R}} - \omega_{\mathrm{a}}$
The relative frequency	$\delta\omega = \Delta\omega_{\mathrm{R}} + \delta_{\mathrm{qb}} - \delta_{\mathrm{a}}$
The saturation photon flux	$p_{\mathrm{s}}(\omega) = \frac{g_{\mathrm{a}}^2}{2\kappa}\frac{1+\left\{1+\frac{\delta\omega}{g_{\mathrm{a}}^2}\frac{\kappa+\kappa_{\mathrm{i}}}{2}\left[1+\left(\frac{2\Delta\omega}{\kappa+\kappa_{\mathrm{i}}}\right)^2\right]\right\}^2}{1+\left(\frac{2\Delta\omega}{\kappa+\kappa_{\mathrm{i}}}\right)^2}$
The input photon flux	$p = \lvert b_{\mathrm{i}}\rvert^2$
The transmission of a $\lambda/4$ resonator	$T_{\lambda/4}(\omega) = \frac{\kappa_{\mathrm{i}}+\mathrm{i}2\Delta\omega_{\mathrm{R}}}{\kappa+\kappa_{\mathrm{i}}+\mathrm{i}2\Delta\omega_{\mathrm{R}}}$

Table (1.6): Definition of terms used in the transmission of the system, see Eq. (1.104).

The frequency shift

The frequency difference between the two closest peaks is here about 150 MHz (Fig. 1.18). This value is two orders of magnitude higher than the usual dispersive shift obtained with a transmon coupled to a microwave resonator which is usually about a few megahertz[65,66].

This is made possible thanks to the large value of the cross-Kerr coupling g_{zz}, here about 250 MHz. Thus depending on the qubit state, the shift of the ancilla resonance frequency will be quite large. This allows the system to reach two different regimes, a resonant regime, when the qubit is in its ground state or a dispersive regime, when the qubit is in its excited state.

Resonator correlation time

The linewidth of the resonance dip is mainly given by the external coupling as soon as the internal quality of the microwave resonator is high enough. Hereafter we will discuss a limit where the linewidth of the resonator is totally determined by the external coupling. Furthermore the qubit and ancilla lifetime, T_1^{qb} and T_1^{a} respectively, are assumed much longer than the measurement duration.

The rate of information coming out of the microwave resonator is determined by the external coupling of the resonator. We define the resonator correlation time, $\tau_{\mathrm{c}} = \frac{2}{\kappa}$, the mean time takes by the resonator to release uncorrelated information. A small linewidth κ gives a better contrast but leads to a long correlation time, and conversely, a large linewidth gives a small constrast but leads to a short correlation time. The trade-off is then to have

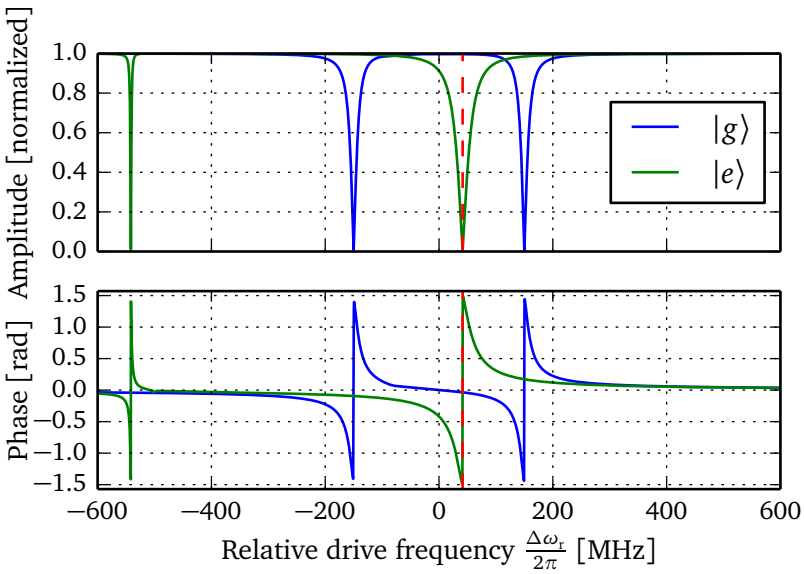

Figure (1.18): Transmission of the SQUID embedded in a microwave resonator as a function of the relative drive frequency. The blue line corresponds to the transmission of the system when the qubit is in its ground state while the green line is when it is in its excited state. In dashed red line, we show the frequency of maximum contrast between the transmitted signal when the logical qubit is in its excited or ground state. We chose $g_{zz}/(2\pi) = 250\,\mathrm{MHz}$, $g_a/(2\pi) = 150\,\mathrm{MHz}$ *and* $\kappa = 40\,\mathrm{MHz}$.

the largest information rate while keeping a good enough separation of the dips. As we discuss previously the large value of g_{zz} leads to a large frequency difference between the two closest dips of about 150 MHz. We can have a large external coupling without loss in contrast. In Fig. 1.18, $\kappa = 40\,\mathrm{MHz}$, corresponding to an external quality factor of $Q_c \approx 250$, and a correlation time of $\tau_c = 50\,\mathrm{ns}$, does not affect the contrast, yet.

Quantum non-demolition measurement

A quantum non demolition measurement is often described as an ideal quantum measurement[67]. Hereafter we summarise the formal description of a quantum non-demolition system given by Serge Haroche and Jean-Michel Raimond[68]. The first condition is that the state in which the system is projected after the measurement is exactly the eigenstate of the measured observable. Another condition is that this state has to be stable under free evolution of the system. Thus a QND measurement can be repeated and the result of the measurements will be the same than the first one.

The Hamiltonian of a quantum system is decomposed as follows:

$$\mathscr{H} = \mathscr{H}_S + \mathscr{H}_M + \mathscr{H}_{SM}. \tag{1.105}$$

The Hamiltonian $\mathscr{H}_{\mathrm{S}}$ describes the quantum system, $\mathscr{H}_{\mathrm{M}}$ describes the meter and $\mathscr{H}_{\mathrm{SM}}$ their mutual coupling.

The conditions that the Hamiltonian $\mathscr{H}$ must fulfil to allow QND measurement are:

$$[\mathscr{H}_{\mathrm{SM}}, \mathscr{O}_{\mathrm{M}}] \neq 0, \tag{1.106a}$$
$$[\mathscr{H}_{\mathrm{SM}}, \mathscr{O}_{\mathrm{S}}] = 0, \tag{1.106b}$$
$$[\mathscr{H}_{\mathrm{S}} \ \ , \mathscr{O}_{\mathrm{S}}] = 0, \tag{1.106c}$$

where $\mathscr{O}_{\mathrm{M}}$ and $\mathscr{O}_{\mathrm{S}}$ are the observables of the meter and of the investigated quantum system, respectively. The observable $\mathscr{O}_{\mathrm{M}}$ is a pointer towards the observable $\mathscr{O}_{\mathrm{S}}$.

Equation (1.106a) ensures that the system induces an evolution of the meter, which means that we are able to extract some information about the observable $\mathscr{O}_{\mathrm{S}}$ via the observable $\mathscr{O}_{\mathrm{M}}$. Equation (1.106b) tells us that the measurement should not affect the eigenstates of $\mathscr{O}_{\mathrm{S}}$. Finally Eq. (1.106c) shows that the eigenstates of $\mathscr{O}_{\mathrm{S}}$ should not evolve under the action of the Hamiltonian $\mathscr{H}_{\mathrm{S}}$. This condition allows to perform repeated measurements.

Our circuit is described in the Hamiltonian Eq. (1.95). We can identify the quantum system, the meter and their mutual coupling as follow:

$$\widehat{\mathscr{H}} = \underbrace{\frac{\hbar}{2}\omega_{\mathrm{qb}}\widehat{\sigma}_{\mathrm{z}}^{\mathrm{qb}} + \frac{\hbar}{2}\left(\omega_{\mathrm{a}} + g_{\mathrm{zz}}\widehat{\sigma}_{\mathrm{z}}^{\mathrm{qb}}\right)\widehat{\sigma}_{\mathrm{z}}^{\mathrm{a}}}_{\text{system}} + \underbrace{\hbar\omega_{\mathrm{R}}\widehat{a}^{\dagger}\widehat{a}}_{\text{meter}} + \underbrace{\hbar g_{\mathrm{a}}\left(\widehat{\sigma}_{-}^{\mathrm{a}}\widehat{a}^{\dagger} + \widehat{\sigma}_{+}^{\mathrm{a}}\widehat{a}\right)}_{\text{mutual coupling}}. \tag{1.107}$$

The qubit and the ancilla, coupled through the cross-Kerr term, correspond to the quantum system that we want to investigate. The microwave resonator is used as a meter. Finally as we have seen before (Section 1.3.1) the ancilla is magnetically coupled to the microwave resonator.

Furhtermore the meter's observable is $\mathscr{O}_{\mathrm{M}} = \widehat{a}^{\dagger}\widehat{a}$, the number of photons inside the microwave resonator. The observable that we want to measure is the qubit state $\mathscr{O}_{\mathrm{S}} = \widehat{\sigma}_{\mathrm{z}}^{\mathrm{qb}}$.

We get:

$$[\mathscr{H}_{\mathrm{SM}}, \mathscr{O}_{\mathrm{M}}] = \hbar g_{\mathrm{a}}\left(\widehat{\sigma}_{+}^{\mathrm{a}}\widehat{a} - \widehat{\sigma}_{-}^{\mathrm{a}}\widehat{a}^{\dagger}\right), \tag{1.108}$$
$$[\mathscr{H}_{\mathrm{SM}}, \mathscr{O}_{\mathrm{S}}] = 0, \tag{1.109}$$
$$[\mathscr{H}_{\mathrm{S}} \ \ , \mathscr{O}_{\mathrm{S}}] = 0. \tag{1.110}$$

Equation (1.110) shows that all conditions of QND measurements are fulfilled in our circuit. The master key is the cross-Kerr coupling g_{zz} between the qubit and the ancilla. Thanks to this special coupling we can probe the ancilla's eigenenergies without interaction with the logical qubit. The ancilla plays the role of buffer between the qubit and the microwave cavity.

Moreover the two degrees of freedom offered by the SQUID allow to only have the ancilla coupled to the microwave resonator while the qubit stays uncoupled.

Input-power dependences

Figure 1.19 presents the transmitted power of the system for the two qubit states $|g\rangle$ or $|e\rangle$. For low input power the transmission dips correspond to what we described in Section 1.4.1. At high input power, dips collapse and give rise to a single dip at the bare resonator frequency. Indeed at high power the second term in Eq. (1.104) becomes negligible, we obtain:

$$\lim_{p\to\infty} T(\omega) = \frac{\kappa_{\mathrm{i}} + \mathrm{i}2\Delta\omega_{\mathrm{R}}}{\kappa + \kappa_{\mathrm{i}} + \mathrm{i}2\Delta\omega_{\mathrm{R}}} = T_{\lambda/4}(\omega) \tag{1.111}$$

Thus at high power the overall system behaves like a bare $\lambda/4$ microwave resonator independent of the qubit state.

A simple explanation of the disappearance of dips can be found by considering the flow of photons compared to the different coupling strengths. When $p \ll p_{\mathrm{s}}$, all photons extract information from the system. We obtain the top panel of Fig. 1.19. In contrast, when $p \gg p_{\mathrm{s}}$ the number of photons having been coupled to the ancilla are in minority. The bottom panel of Fig. 1.19 shows that the resonance dips tend to the resonance dip of a $\lambda/4$ resonator. When the $p \approx p_{\mathrm{s}}$, only a part of the photons will be coupled to the ancilla. We get the intermediate pictures shown in the middle panels where the dips due to ancilla-resonator anti-level crossing are still visible and the bare resonator dip emerges. These pictures correspond to a trade-off between a large input power leading to a large signal-to-noise ratio and a low input power leading to an important contrast in the transmission between the two logical qubit states.

Read-out fidelity

An important quantity used to define the quality of a qubit state readout is the fidelity $\mathscr{F}$. The fidelity refers to the degree to which the result of the measurement is close to the real quantum state. In order to have a correct estimation of the measurement fidelity we have to take into account the whole measurement chain (Fig. 1.20).

A microwave signal of power p is sent to the sample. The transmitted power can be derived by using the transmission of the system (Eq. (1.104)) $p_{\mathrm{t}} = |t(\omega)|^2 p$. The input power p has to be low enough to avoid ancilla saturation. Thus the transmitted power p_{t} will also be quite low (some photon.ns^{-1}). In our setup, photons are amplified before being sent to the digitiser. We model the amplifier through two parameters, its noise temperature T_{N} and its bandwidth B. The noise temperature describes the white thermal of the amplifier and the bandwidth the finite frequency domain of the amplifier. At the end of the measurement chain the microwave signal is digitised and the qubit state is deduced from the signal amplitude.

We note that it is important to take into account the amplification chain because it adds two constraints on the qubit state readout. First, it modifies the signal-to-noise ratio by adding some noise to the microwave signal. The total noise power N added by the amplifier can be calculated from the Johnson-Nyquist noise formula[69]:

$$N = \frac{k_{\mathrm{B}} T_{\mathrm{N}}}{\hbar\omega} B. \tag{1.112}$$

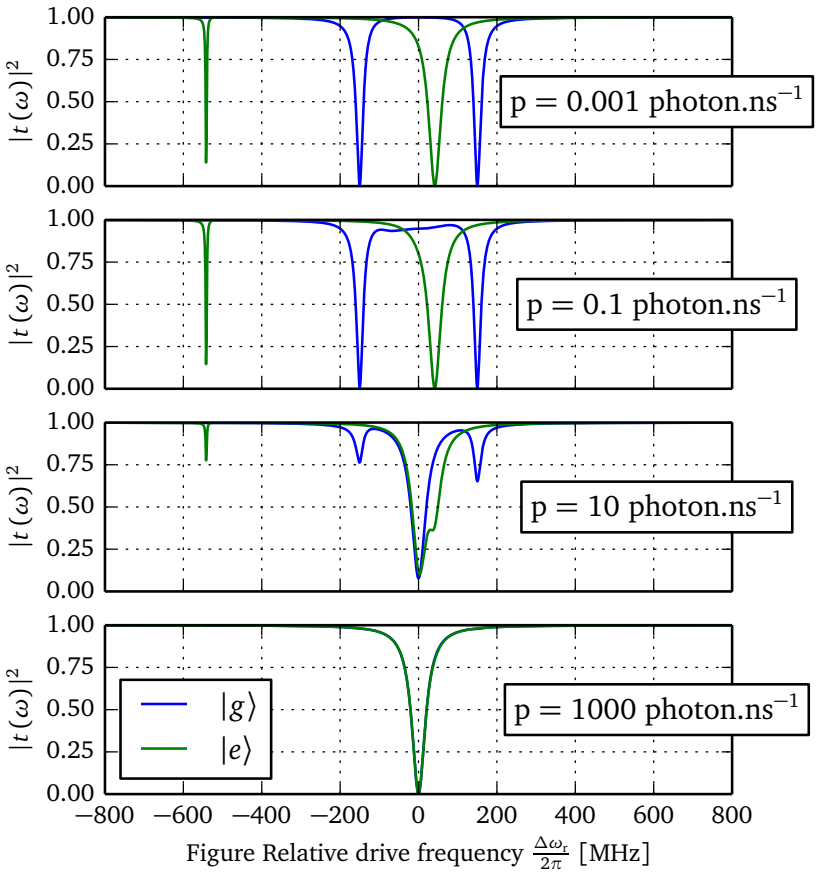

Figure (1.19): Transmitted power as a function of the relative frequency. We show four figures for four different input powers, each of them presents the transmission of the system for the two qubit states $|g\rangle$ or $|e\rangle$. Parameters used are the same as in Fig. 1.18.

Second, it involves an additional correlation time $\tau_c' = B^{-1}$ due to the internal finite bandwidth of the amplifier. We note that the optimal bandwidth is a trade-off between a low noise power (Eq. (1.112)) and a short correlation time.

The estimation of the readout fidelity is based on the conditional photon number distributions $\mathscr{P}(n|j)$, where n is the number of photons measured and j is the qubit state. The derivation of the distribution has been done by Igor Diniz[45]. We used the Glauber-Sudarshan P representation[70]. In our case, this simply corresponds to the P representation of a thermal field of temperature T_N displaced by a coherent field of amplitude $\sqrt{p_t(j)}$. Thus we can readily calculate the generating function[71] for the photon statistics, from which we extract the coefficients:

$$\mathscr{P}(n|j) = \frac{N^n \tau^n}{(1+N\tau)^{n+1}} \exp\left(\frac{-p_t(j)\,\tau}{1+N\tau}\right) L_n\left(\frac{-p_t(j)}{N(1+N\tau)}\right), \tag{1.113}$$

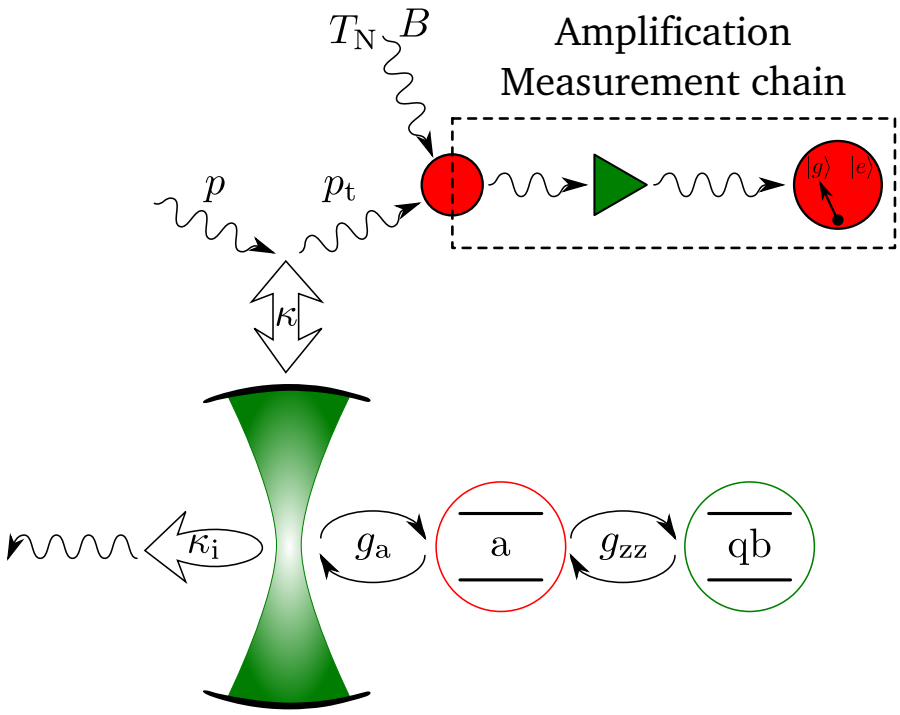

Figure (1.20): Scheme of the complete measurement chain. At the output of the resonator the transmitted power is denoted p_t. The amplification chain is modelled as a single amplifier with noise temperature T_N and a bandwidth B. At the end of the measurement chain, the microwave signal is digitised and the qubit state is inferred from the amplitude of the signal.

where τ is the measurement duration and L_n is the nth-order Laguerre polynomial.

To explain some features of the probability distribution $\mathscr{P}(n|j)$, we remind here some properties of thermal and coherent field. The thermal field is characterised by a decreasing exponential photon number function whose decay constant is related to the noise power. When the noise power increases, this can be due to a larger noise temperature or a larger bandwidth (Eq. (1.112)), the distribution becomes wider and smaller. A coherent field is mathematically equivalent to a Poisson distribution. Thus a coherent field of power P has a probability distribution centred at P and a variance P. When the power of the coherent field increases, the centre of the distribution is shifted to the higher mean power value and it becomes wider.

The total distribution $\mathscr{P}(n|j)$ corresponds to a convolution between a Poisson distribution due to the input microwave coherent field and a thermal distribution due to the noise coming from the amplifier. Various distributions are plotted in Fig. 1.21. They clearly show how the amplification has a large effect on the statistics of the counts associated with each qubit states $|g\rangle$ (large number of measured photons) or $|e\rangle$ (small number of measured photons).

The distribution given in Eq. (1.113) is a convolution of these two distributions. Thus when the noise temperature increases, the distribution becomes wider, flatter and tends to a smaller number of measured photons. These effects can be easily understood as an

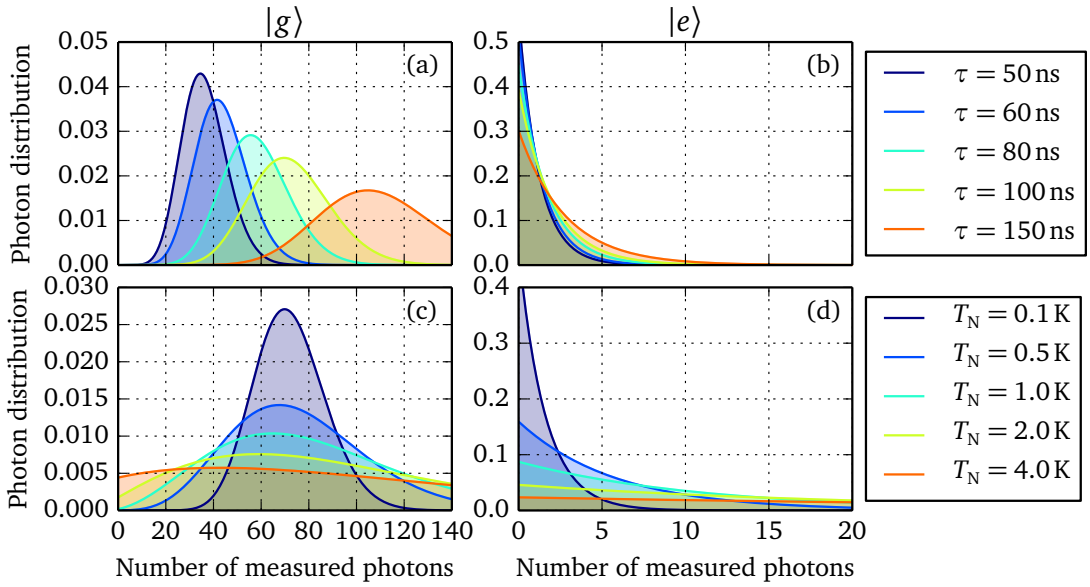

Figure (1.21): Photon number distribution $\mathscr{P}(n|j)$. Parameters used for the circuit are the same as in Fig. 1.18. For the rest we took: input power $p = 1$ photon.ns^{-1} and $B = 50$ MHz. The panels (a) and (c) show photon distributions for the qubit in its ground state and the panels (b) and (d) for the qubit in its excited state. Moreover the panels (a) and (b) present different distributions depending of the measurement time τ. Finally, the panels (c) and (d) present the evolution of the distributions as a function of the noise temperature T_N. The minimum measurement time used for the plots correspond to the minimum correlation time allowed by the circuit which is $\tau = max\left(\tau_c|\tau'_c\right) = 50$ ns.

increase of the weight of the thermal field with respect to the coherent field. In other words, the signal-to-noise ratio decreases. This fact is shown in panels (c) and (d) in Fig. 1.21. The panels (a) and (b) present the evolution of the distribution as the measurement time increases. The position of the distribution is shifted to a larger number of measured photons and the distribution gets wider. This is a manifestation of the coherent field which becomes predominant as the signal-to-noise ratio increases.

The fidelity is calculated through the overlap of the two photon number distributions obtained for the two qubit states[72]:

$$\mathscr{F} = 1 - \frac{1}{2}\sum_n \left\{\mathscr{P}(n,e)\Theta[\mathscr{P}(n,g) - \mathscr{P}(n,e)] + \mathscr{P}(n,g)\Theta[\mathscr{P}(n,e) - \mathscr{P}(n,g)]\right\}, \tag{1.114}$$

where Θ denotes the Heaviside step function, and $\mathscr{P}(n,e)\Theta[\mathscr{P}(n,g) - \mathscr{P}(n,e)]$, $\mathscr{P}(n,g)\Theta[\mathscr{P}(n,e) - \mathscr{P}(n,g)]$ denotes the error made in the readout when the qubit state is excited and grounded, respectively.

The two photon distributions are shown for the two qubit states and for different mea-

surement times in Fig. 1.22.

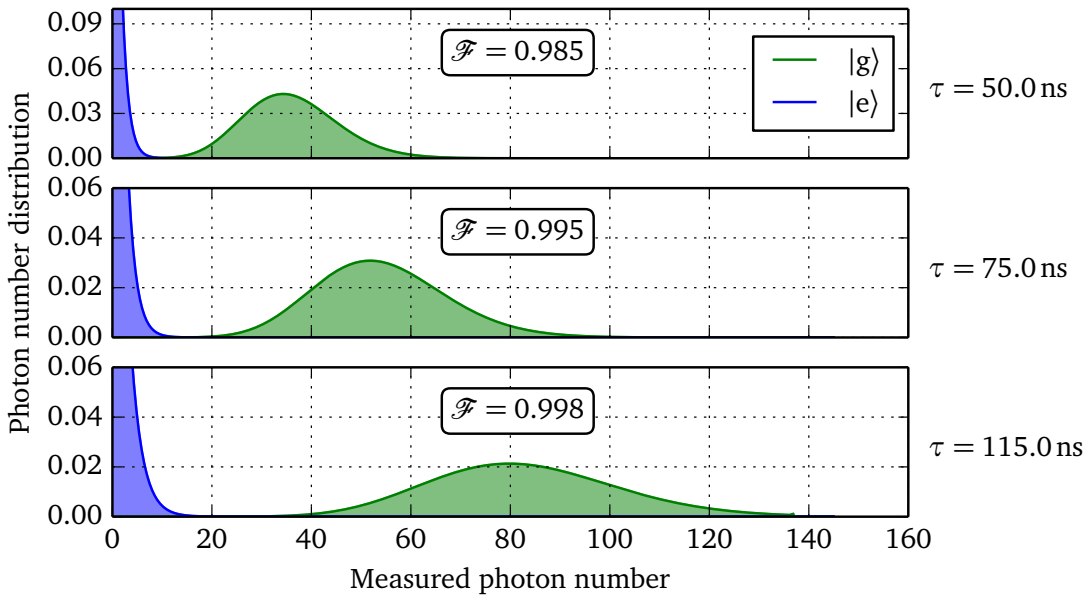

Figure (1.22): Evolution of the measured photon number distribution $\mathscr{F}$ following the measurement time τ. Parameters used the circuit are the same as for Fig. 1.21. We took an input power $p = 1\,photon.ns^{-1}$, an amplifier bandwidth of $B = 50\,\mathrm{MHz}$, and a noise temperature $T_N = 140\,\mathrm{mK}$. The minimum measurement time used for the plots correspond to the minimum correlation time allowed by the circuit which is $\tau = max\left(\tau_c|\tau'_c\right) = 50\,\mathrm{ns}$. When the measurement time increases, the overlap of the photon number distributions for ground state (green) and excited state (blue) decreases, which leads to a higher fidelity.

The increase of measurement time leads to a shift of the distribution to higher measured photon number as well as an increase of the width of the distribution. However, the increase of measured photon number is faster than the increase of the distribution width leading to an increase of the signal-to-noise ratio. Nevertheless the distributions obtained for the two qubit states exhibit different behavior. For the qubit in its ground state, the system should be practically transparent whereas, when the qubit is in its excited state, almost no photon should be measured. When the measurement time increases, the distribution obtained when the qubit is in its excited state is slightly shifted to higher measured photon number. In contrast, the distribution obtained when the qubit is in its ground state is much more shifted which leads to a reduction of the overlap between the two distribution and so, a higher fidelity.

For state of the art quantum limited amplifier[73], the noise temperature can be as low as $T_\mathrm{N} = 140\,\mathrm{mK}$. A measurement duration of $\tau = 50\,\mathrm{ns}$, the minimum measurement time allowed by the setup, is enough to reach a fidelity $\mathscr{F} \approx 98.5\,\%$. For a commercial cryogenic amplifier, the noise temperature is about 4 K which leads to a fidelity of 90 % for a measurement time of 50 ns.

We compare these predictions to two examples found in literature, the first one based on the transmon qubit and the second one on the "Xmon" qubit. The first example consists[36] of a transmon qubit coupled to a compact resonator in series with a quantum-limited amplifier (Josephson parametric converter). This sample reached a fidelity of 98 % for an integration time of 240 ns. The second example achieved[74] the fidelity of 99.8 % for an integration time of 140 ns. The circuit is composed of an "Xmon" qubit coupled to a half-wave resonator and an on-chip bandpass filter in series with a quantum-limited amplifier (Josephson parametric amplifier). The bandpass filter allows an increase of the resonator–environment coupling rate κ without causing an increase of the Purcell effect. We remark that in both cases, the fidelity obtained by these circuits are lower than the fidelity achievable by our proposal for the same integration time.

Chapter 2

Setup

Contents

2.1 Dilution refrigerator **92**

2.2 Low temperature microwave setup **92**

2.2.1 Thermalisation 93

2.2.2 Amplification chain 98

2.3 Room temperature microwave setup **103**

2.3.1 Microwave pulse generation 105

2.3.2 Device synchronisation 106

2.3.3 Frequency down–conversion 107

2.3.4 Data acquisition 108

2.3.5 Transmission coefficient measurement 110

2.3.6 Noise of the measured signal 110

2.4 Software environment **113**

2.4.1 Python 113

2.4.2 Qtlab 113

2.5 Superconducting coil **115**

2.6 Sample holder **116**

2.6.1 Presentation 116

2.6.2 Microwave properties 119

2.7 Shielding **121**

2.7.1 Electromagnetic shielding 121

Figure (2.1): Photography of the experimental room with the blue cryostat. The outside magnetic shield in MμMeta is visible at the bottom of the cryostat. At the left of the picture, a rack containing microwave and pulse generators.

2.1 Dilution refrigerator

Figure 2.1 presents the dilution fridge used for our experiments. It has been designed by the SERAS "Service Etudes et Réalisation d'Appareillages Scientifiques" at the Neel institute in 2008 and mounted by the "Pôle cryogénique" in 2009. During 2009 and 2010, Iulian Matei installed the cryogenic setup and started cool-down. The base temperature at the mixing chamber is 30 mK with and 70 mK without roots vacuum pump. The measured cooling power is about 65 μW at a temperature of 100 mK without heating on the still.

2.2 Low temperature microwave setup

One of the mission of my Ph.D has been to install, in collaboration with Thomas Weißl, a complete microwave setup able to perform quantum measurements. The aim of the microwave setup is to measure the amplitude and the phase difference of a transmitted signal through a sample by a heterodyne method at very low power, $\approx 1\,\text{photon}\cdot\text{ns}^{-1}$ ($\approx -110\,\text{dBm}$ at 10 GHz). This work included the installation of cables and various microwave elements (mixers, filters, amplifiers, ...) in the dilution fridge, the realisation of a microwave circuit allowing generation and measurement of microwave pulses, and the writing of python drivers and measurement scripts.

2.2.1 Thermalisation

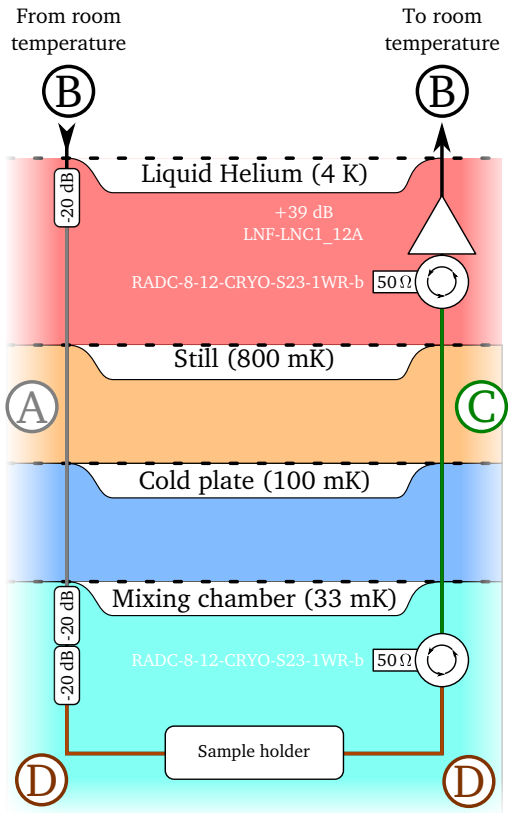

Coax-cables				
Reference	UT-085SS-SS	UT-85B-SS	NbTi085/50	SC-219/50-SC
Item	A	B	C	D
Inner conductor	Stainless steel	Copper-Beryllium	Niobium-Titanium	Oxygen-free copper
Dielectric	PTFE	PTFE	PTFE	PTFE
Outer conductor	Stainless steel	Stainless steel	Niobium-Titanium	Silver platted copper
Attenuation at 10 GHz [dB/m]	13	5	0.3 (T = 4 K)	5

Figure (2.2): Sketch of the microwave setup inside the inner vacuum chamber. The different temperature stages are depicted by different colour. Except the superconducting coax cable, all elements are thermalised at the temperature stage where they are depicted. At the bottom of the figure, a table summarises information about the difference coax cables.

The setup at low temperature is shown in Fig. 2.2. The figure displays the interior of the inner vacuum chamber by enhancing the different temperature stages.

Thermalisation of phonons

The thermalisation of phonons is important to minimise the heat load on the cryostat. To estimate the heat load due to cables, we can calculate the power brought by a homogeneous metal cylinder. The differential form of Fourier's Law of thermal conduction shows that the local heat flux density, $\vec{q}$, is equal to the product of thermal conductivity, k, and the negative local temperature gradient, $-\vec{\nabla} T$. The heat flux density is the amount of energy that flows through a unit area per unit time.

$$\vec{q} = -k\vec{\nabla} T \tag{2.1}$$

where $\vec{q}$ is the local heat flux density in $\mathrm{W{\cdot}m^{-2}}$, k is the material's conductivity in $\mathrm{W{\cdot}m^{-1}{\cdot}K^{-1}}$, and $\vec{\nabla} T$ is the temperature gradient in $\mathrm{K{\cdot}m^{-1}}$. In the limit of a one-dimensional infinitely long cable we get $q_x = -k\partial_x T$. At very low temperature, we can assume a linear temperature dependence of the thermal conductivity, we obtain the heat load as:

$$P = \frac{k^{1\,\mathrm{K}} S}{L}\left(T_2^2 - T_1^2\right) \tag{2.2}$$

where S is the cross section of the cable, L its length, and $k^{1\,\mathrm{K}}$ the thermal conductivity at 1 K.

From room temperature to 4 K, the coax cables are immersed in liquid helium. We chose coax cable with the inner conductor made in copper-berylium and the outer conductor in stainless steel. The cables are also bent to reach a length of 1.5 m in order to reduce the heat load. The thermalisation is realised by the liquid helium in which the cables are immersed.

Inside the inner vacuum chamber, we used coax with stainless steel as inner and outer conductor because of its very low thermal conduction. The length of cable is about 40 cm. At 1 K the thermal conductivity for the stainless steel is about[75] $k_{\mathrm{SS}} = 1.5 \times 10^{-5}\,\mathrm{W{\cdot}m^{-1}{\cdot}K^{-1}}$. By using Eq. (2.2), we get a heat load of $p_{\mathrm{SS}} = 2\,\mathrm{nW}$ per cable. To reduce the heat load at the mixing chamber level, the cables are thermalised at the still. Assuming a perfect thermalisation at the still level, the heat load at the mixing chamber becomes $P'_{\mathrm{SS}} = 86\,\mathrm{pW}$.

The coax cables with stainless steel as inner and outer conductor are efficient to avoid thermal conduction but have the drawback to also have high microwave losses, approximately $13\,\mathrm{dB{\cdot}m^{-1}}$ at 10 GHz. For this reason we only use this type of cables in the input line. At the amplification line, where losses become important, we use low loss superconducting coax cables. The superconducting cable is composed of niobium-titanium as inner and outer conductor. The cable is 30 cm long with an attenuation of $0.3\,\mathrm{dB{\cdot}m^{-1}}$ at 10 GHz. The transition temperature is about 8 K. At 1 K, its thermal conductivity is about $3 \times 10^{-6}\,\mathrm{W{\cdot}m^{-1}{\cdot}K^{-1}}$.

Inside the inner vacuum chamber, the thermalisation is realised by using clamps in copper in order to fasten components. The clamp is coated with grease[1] to increase the surface area of contact. Next a copper wire is screwed to the cryostat and to the clamp to realise the thermalisation.

[1] Apiezon N Grease: http://www.apiezon.com/products/vacuum-greases/n-grease

Thermalisation of photons

The thermalisation of the microwave signal is crucial for our experiment. Indeed to be able to observe quantum phenomena the thermal excitation has to be small compared to the characteristic energy of the system, $(k_B T)/(\hbar\omega) \ll 1$. We firts derive an equivalent temperature of the thermal photons at the sample place. In this calculation we model classically the thermal noise power spectral density through the Johnson–Nyquist formula. This restriction is correct as long as the frequency of photons are below $k_B \times T_{30\,\mathrm{mK}}/h \approx$ 600 MHz. Despite the fact that typical frequencies of our experiments are of a few gigahertz, this calculation gives an idea of the photons temperature at the sample stage. In a second calculation, we take into account the high frequency involved in our experiment by modelling the thermal photon power spectral density with a Bose–Einstein distribution. We then derive the thermal population of photons in the microwave resonator and estimate its effect on the qubit coherence time.

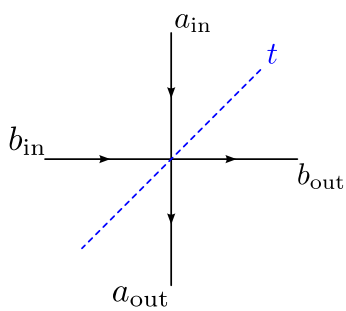

Figure (2.3): Schematic view of a beam splitter of intensity transparency t. $a_{in,out}$ and $b_{in,out}$ represent the amplitude of the incoming, outgoing electrical field at the two ports of the beam splitter.

The thermalisation of photons is performed by microwave attenuators thermalised at different stages of the cryostat. An attenuator can be modelled as a beam splitter with two different incoming signals. One incoming signal is the microwave signal that we want to thermalise and the second one is the noise added by the attenuator itself. In our derivation, we write a_{in} the signal amplitude coming from our microwave sources. The noise signal due to the attenuator is denoted b_{in}. The outgoing signal is a_{out} and the signal absorbed by the attenuator is b_{out}.

From the "Quantum optics" book from D. F. Walls and G. J. Milburn[76] we have the input-output relation[2]:

$$\begin{pmatrix} a_{\mathrm{out}} \\ b_{\mathrm{out}} \end{pmatrix} = \begin{pmatrix} \sqrt{t} & \mathrm{i}\sqrt{1-t} \\ \mathrm{i}\sqrt{1-t} & \sqrt{t} \end{pmatrix} \begin{pmatrix} a_{\mathrm{in}} \\ b_{\mathrm{in}} \end{pmatrix} \tag{2.3}$$

with t, the intensity transparency. From this equation, we derive the variance of the output

[2]We suppose a phase shift of $\pi/2$ upon reflection

fields[3]:

$$\begin{cases} \left\langle |a_{\text{out}}|^2 \right\rangle = & t\left\langle |a_{\text{in}}|^2 \right\rangle + (1-t)\left\langle |b_{\text{in}}|^2 \right\rangle \\ \left\langle |b_{\text{out}}|^2 \right\rangle = & t\left\langle |b_{\text{in}}|^2 \right\rangle + (1-t)\left\langle |a_{\text{in}}|^2 \right\rangle \end{cases}. \tag{2.4}$$

The first step of the thermalisation is handled by an attenuator of −20 dB thermalised at 4 K. At this temperature, the power spectral density is very well approximated by the Johnson–Nyquist power spectral density[77]:

$$S(\omega) = k_{\text{B}} T. \tag{2.5}$$

By considering an incoming noise signal at 300 K we obtain:

$$\left\langle |a_{\text{out}}|^2 \right\rangle_{4\,\text{K}} = t k_{\text{B}} T_{300\,\text{K}} + (1-t) k_{\text{B}} T_{4\,\text{K}}. \tag{2.6}$$

Numerical calculation leads to $\left\langle |a_{\text{out}}|^2 \right\rangle_{4\,\text{K}} / k_{\text{B}} = 7\,\text{K}$. Thus the noise emitted by the attenuator at 4 K is equivalent to the Johnson–Nyquist noise emitted by a virtual 50 Ω resistor thermalised at 7 K.

The thermalisation is completed by second step consisting of two −20 dB attenuators thermalised at 30 mK. At this stage the incoming signals is composed of the attenuated room temperature noise signal coming from the attenuator at 4 K. As we have seen in the previous paragraph, this noise can be modelled as a noise coming from a virtual 50 Ω resistor thermalised at 7 K. The noise coming from the two −20 dB attenuators thermalised at 30 mK is modelled as the noise of a virtual −40 dB attenuator thermalised at 30 mK. The equivalent noise temperature is then:

$$\left\langle |a_{\text{out}}|^2 \right\rangle_{30\,\text{mK}} = t k_{\text{B}} T_{7\,\text{K}} + (1-t) k_{\text{B}} T_{30\,\text{mK}}. \tag{2.7}$$

We obtain $\left\langle |a_{\text{out}}|^2 \right\rangle_{30\,\text{mK}} / k_{\text{B}} = 30.7\,\text{mK}$. Thus the noise temperature is very close to the base temperature of the cryostat, ensuring a good thermalisation of photons along the lines.

In order to estimate the influence of the photon noise on the artificial atom, we can calculate the number of photons inside the cavity due to the noise coming from room temperature through the coax line. The input-output theory gives the relation between the electromagnetic field inside a cavity and an incoming field, see Eq. (1.98). Let's then consider a high quality microwave resonator[4], as in Section 1.4.1, coupled to a feedline, we have:

$$\dot{a} = \left(-\text{i}\omega_{\text{r}} - \frac{\kappa_\Sigma}{2}\right) a + \sqrt{\kappa_1} a_{\text{in}} \tag{2.8}$$

with $\kappa_\Sigma = \kappa_1 + \kappa_2$ and $\kappa_{1,2}$ the decay rate of the cavity to the input and output line, respectively. Taking the Fourier transform of the above equation, and taking its absolute value squared, we obtain:

$$|a(\omega)|^2 = |S(\omega)|^2 \, |a_{\text{in}}(\omega)|^2 \tag{2.9}$$

[3]Correct for uncorrelated fields which implies, $\langle ab \rangle = \langle a \rangle \langle b \rangle$ and $\langle a \rangle = \langle b \rangle = 0$.

[4]This consideration allows to neglect the internal losses of the resonator: $\kappa_{\text{i}} \to 0$.

with:

$$|S(\omega)|^2 = \frac{4\frac{\kappa_1}{\kappa_\Sigma^2}}{1+\left(2\frac{\Delta\omega_r}{\kappa_\Sigma}\right)^2} \tag{2.10}$$

and:

$$|a_{\text{in}}(\omega)|^2 = \hbar\omega\left[\frac{t}{\exp\left(\frac{\hbar\omega}{k_B T_{7\,\text{K}}}\right)-1} + \frac{1-t}{\exp\left(\frac{\hbar\omega}{k_B T_{30\,\text{mK}}}\right)-1}\right]. \tag{2.11}$$

$|a_{\text{in}}|^2$ represents the noise spectral density in [W.Hz^{-1}]. We note that, in order to correctly take into account the noise at very low temperature $\hbar\omega \approx k_B T$, the noise spectral density is corrected by the Bose–Einstein distribution[78]. The noise spectral density has two main contributions. The first term represents the room temperature noise attenuated by −20 dB attenuator thermalised at 4 K. As we saw, this noise can be modelled by a virtual 50 Ω resistor thermalised at 7 K. The second term corresponds to the noise of the two −20 dB attenuators thermalised at 30 mK. This noise is modelled as a virtual 50 Ω resistor thermalised at 30 mK. $|S(\omega)|^2$ is the transfer function in [Hz^{-1}] between the the flow of photons in the environment and the energy inside the cavity. It has a Cauchy-Lorentz shape with a height and a FWHM given by $4\kappa_1/\kappa_\Sigma^2$ and κ_Σ, respectively. Typical energy spectral density obtained from Eq. (2.9) is shown in Fig. 2.4.

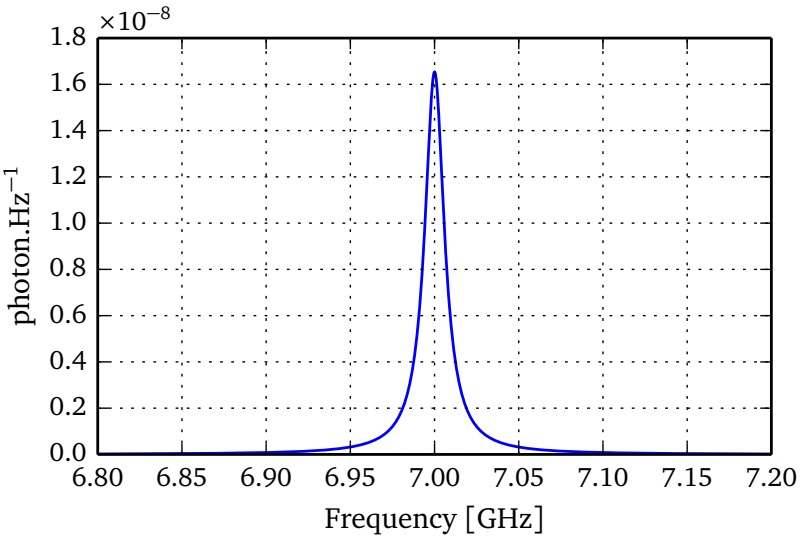

Figure (2.4): Photon spectral density in the microwave resonator due to thermal noise from room temperature. The peak and the width of the spectral density corresponds to the resonance frequency and the linewidth of the cavity.

To obtain the residual energy inside the cavity, we integrate over all frequencies:

$$E = \int_0^\infty |S(\omega)|^2 |a_{\text{in}}(\omega)|^2 \frac{d\omega}{2\pi}. \tag{2.12}$$

Equation (2.12) can be simplified by assuming that, only the noise power density close to the cavity resonance frequency has to be take into account. At this point, we assume that the power spectral density $|a_{\text{in}}|^2$ is constant inside the integral limits. We then remove the power spectral density from the integral, we obtain[5]:

$$E = |a_{\text{in}}(\omega)|^2 \int_{\omega_{\text{start}}}^{\omega_{\text{end}}} |S(\omega)|^2 \frac{\mathrm{d}\omega}{2\pi} = \frac{|a_{\text{in}}(\omega)|^2}{2}. \tag{2.13}$$

The final formula given the noise in unit of mean number of photon at given frequency is then:

$$n = \frac{|a_{\text{in}}(\omega)|^2}{2\hbar\omega} = \frac{1}{2}\left[\frac{t}{\exp\left(\frac{\hbar\omega}{k_{\text{B}}T_{7\text{K}}}\right)-1} + \frac{1-t}{\exp\left(\frac{\hbar\omega}{k_{\text{B}}T_{30\,\text{mK}}}\right)-1}\right]. \tag{2.14}$$

Thus in the case of the sample "V-shape-1" discussed in Chapter 5, Eq. (2.14) gives an amplitude of thermal photon of 0.001 photon. This photon noise will induce a dephasing of the qubit leading to a homogeneous broadening of the resonance peak[79]. We can estimate the coherence time due to this broadening as $T_2 = 1/(\pi\delta_{\text{fwhm}}) = 46\,\mu\text{s}$. The measured coherence time of our qubit (see Table C.1) being much smaller, we conclude that the thermal noise due to the input line will not affect our experiment. We note that Eq. (2.14) does not depend of the linewidth of the cavity. Indeed at the equilibrium, the energy stored in the cavity due to the noise power in the environment should be independent of the cavity lifetime.

2.2.2 Amplification chain

The microwave signal transmitted by the sample is about 1 photon·ns^{-1} (−110 dBm at 10 GHz). To amplify the signal we use several amplifiers in series. The Friis formula[80] gives the total gain and noise temperature of such a chain:

$$G_{\text{tot}} = G_1 \times G_2 \times \cdots \times G_{\text{N}}, \tag{2.15}$$

$$T_{\text{tot}} = T_1 + \frac{T_2}{G_1} + \cdots + \frac{T_{\text{N}}}{\Pi_{i=1}^{N-1} G_i}. \tag{2.16}$$

If the gain of the first amplifier is large enough, the total noise of the chain is then only due to the noise of the first amplifier. The optimal amplification chain has then to start with a high quality amplifier having a large amplification and a low noise temperature. In our setup the first amplifier is a cryogenic high electron mobility transistor (HEMT) amplifier[81] exhibiting a gain of 39 dB and a noise temperature of 5.5 K[6] over a bandwidth from 1 GHz to 12 GHz, according to the datasheet.

Hereafter we present an experimental measurement of the total gain and total noise temperature in our setup. The experiment models the whole amplification as a single amplifier

[5] A discrepancy of only 2 % is found between the simplified analytical formula given in Eq. (2.13) and a numerical integration using the Eq. (2.12), which valid our assumptions.

[6] LNF-LNC1_12A

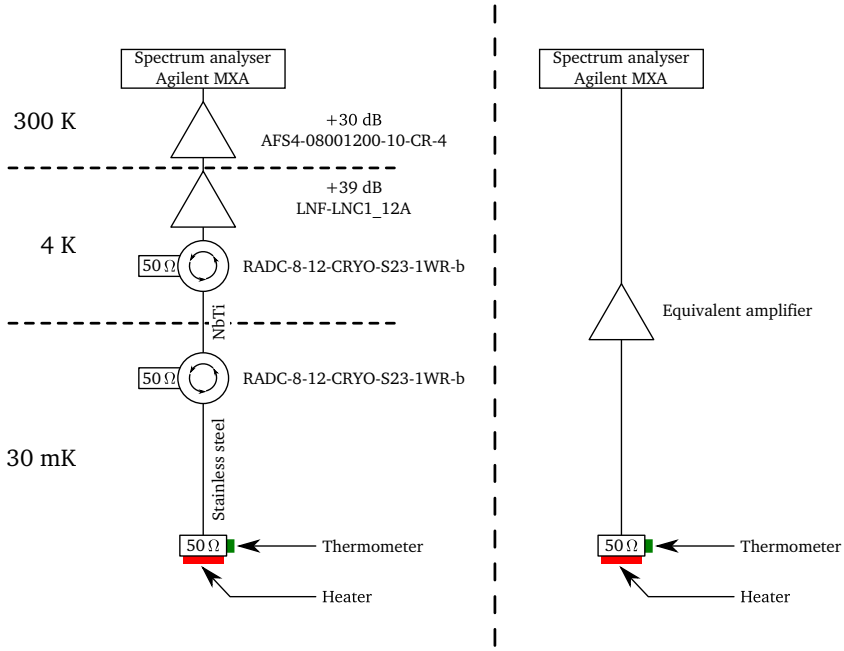

Figure (2.5): Left and right panels show the setup used for the calibration of the amplification chain and the model of the equivalent amplifier, respectively. The source of Johnson–Nyquist noise is a $50\,\Omega$ *resistor whose temperature is well controlled by a heater and a thermometer. The resistor is thermally decoupled from the amplification chain by a stainless steel, inner and outer conductor, coax.*

with a certain gain and a certain noise temperature, see Fig. 2.5. We use a $50\,\Omega$ resistor as Johnson–Nyquist source. The resistor is connected to the amplification chain by a stainless steel, inner and outer conductor, coax cable of 10 cm. By this way, the resistor is thermally decoupled to the rest of the chain. Nevertheless the photons emitted by the resistor are free to flow to the chain.

The power spectral density emitted by the resistor is, at temperature $T > \hbar\omega/k_B$:

$$S_R = k_B T. \tag{2.17}$$

At the output of the chain, the power spectral density becomes:

$$S_{out} = (A_R S_R + S_N)\, G_{tot} \tag{2.18}$$

where S_N is the power spectral density of the amplification chain defined at the input of the equivalent amplifier. We also take into account the spurious attenuation A_R which occurs between the resistor and the first amplifier. In our setup the noise temperature is high enough to have $(k_B T_N)/(\hbar\omega) > 1$. Equation (2.18) becomes:

$$S_{out} = k_B\,(A_R T + T_N)\, G_{tot} = k_B \left(T + \frac{T_N}{A_R} \right) A_R G_{tot}. \tag{2.19}$$

The experiment consists in measuring the power spectral density as a function of the temperature and frequency, see Fig. 2.6. This measurement was performed for a resistor temperature varying between 0.3 K and 4.8 K, the power spectral density was measured between 21 Hz and 16 GHz with a video bandwidth of 10 kHz. The two bottom panels present the power spectral density as function of temperature for two different frequencies, 7 GHz and 11 GHz. The power spectral density is proportional to the temperature without a saturation at low temperature as expected from Eq. (2.19). The slope of the temperature dependence is proportional to the gain of the amplification chain. The residual power spectral density at $T \to 0$ is related to the noise temperature.

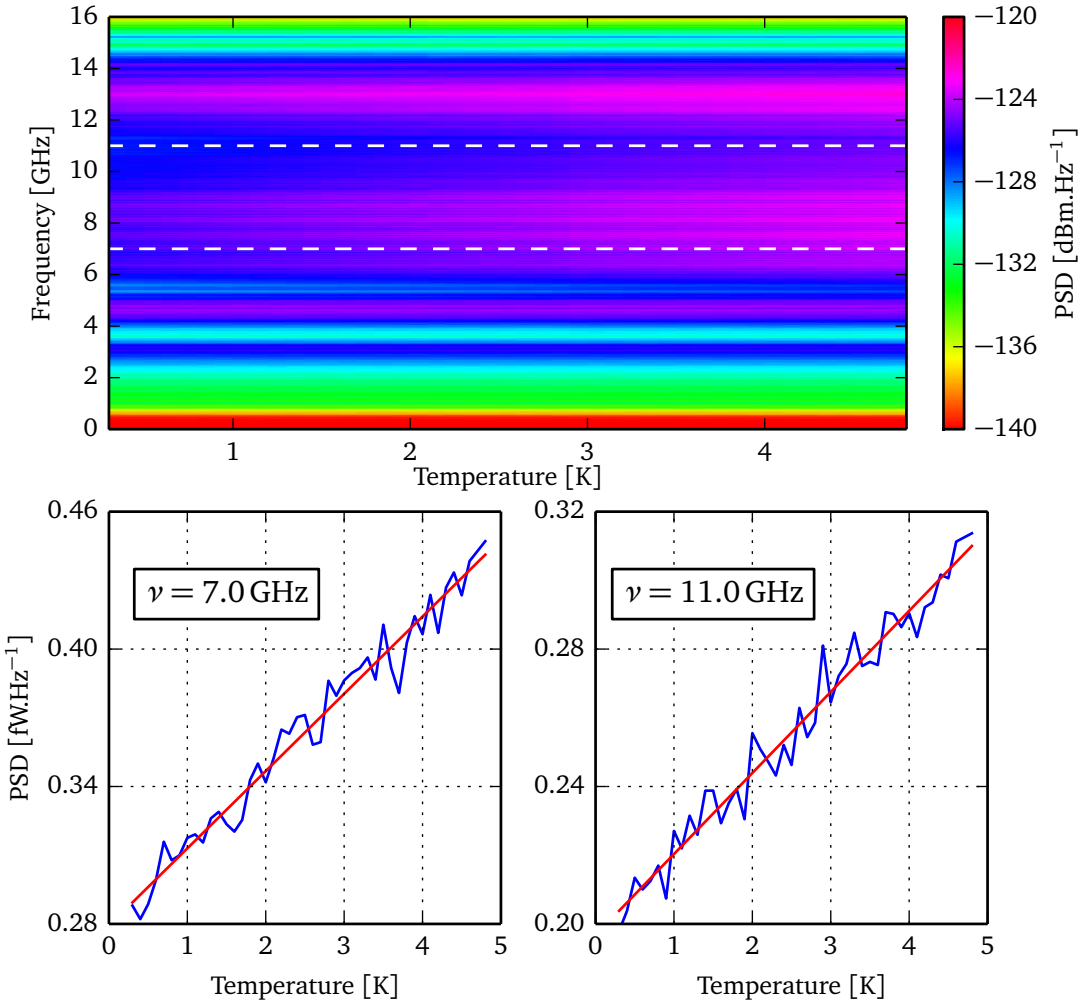

Figure (2.6): The colormap presents the power spectral density (PSD) as function of the temperature of the resistor and of the frequency. The two bottom panels show cuts of the colormap at two different frequencies, 7 GHz *and* 11 GHz*. The measurement is displayed in blue and the fit used to extract the gain and the noise temperature (Eq.* (2.19)*) is shown in red.*

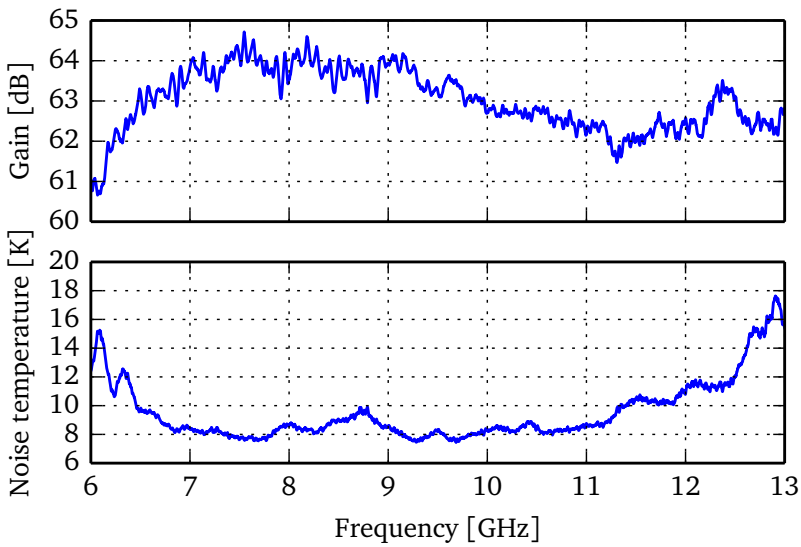

Figure (2.7): The top and bottom panels show the gain and the noise temperature of the amplification chain as a function of the frequency, respectively. In the bandwidth going from 7 GHz *to* 11 GHz *the gain and the noise temperature are about* 63 dB *and* 8 K*, respectively. A Savitzky–Golay filter*[82,83] *has been used during the data treatment.*

We use Eq. (2.19) to fit, for all frequencies, the temperature dependence of the power spectral density. We extract then, for each frequency, the gain and the noise temperature. Figure 2.7 presents in the top panel, the gain as a function of the frequency, and in the bottom panel, the noise temperature as a function of frequency. We note that the validity of Eq. (2.19) becomes questionable about 6 GHz and 300 mK. To ensure the validity of our results, we performed the same analysis by replacing the Johnson–Nyquist noise spectral density by the Bose–Einstein distribution. In both cases, we obtain the same values for the noise temperature and the gain. The gain fluctuates around a mean value of $G_{\text{exp}} \approx 63\,\text{dB}$. The measured noise temperature has a plateau at $T_{\text{N}}^{\text{exp}} \approx 8\,\text{K}$ which is higher than in the datasheet. An optimal bandwidth from 6.5 GHz to 11.5 GHz is extracted from Fig. 2.7. It corresponds to the frequency range in which the measured noise temperature is small and the gain large.

The expected noise temperature is of $T_{\text{N}}^{\text{datasheet}} = 5.5\,\text{K}$, 30 % smaller than the measured one. From the Friis formula (Eq. (2.16)) the noise due to the second amplifier is estimated to be about $\frac{T_{\text{miteq}}}{G_{\text{LNF}}} \approx \frac{66.8}{10^4} \approx 1 \times 10^{-2}\,\text{K}$. As expected, the second amplifier does not contribute to the total noise temperature of the amplification chain. The large value of the measured noise temperature is actually due to spurious attenuation which occurs before the amplification. Thus the signal-to-noise ratio at the input of the amplifier is lower than at the output of the resistor. It turns out, in our model (see Eq. (2.19)), an increase of the measured noise temperature. Between the resistor and the amplifier, several sources of losses can be identified. The stainless steel decoupling the heater from the rest of the chain is 10 cm long which induces

an attenuation of 1.3 dB. The insertion loss of the two circulators[7] is about 1.2 dB for both. Finally, a total loss of $A_R = -2.5$ dB can be expected between the resistor and the amplifier. Our model being linear, we obtain at the end a corrected noise temperature about 4.5 K.

The expected amplification is about 69 dB which corresponds to the amplification sum of the LNF[8], 39 dB, and of the Miteq[9] amplifier, 30 dB. As we wrote before, an attenuation of −2.5 dB is expected inside the inner vacuum chamber. A coax cable of 1.5 m length, in copper-beryllium for the inner conductor and in stainless steel for the outer one, makes the link between 4 K and room temperature. It causes 7.5 dB of losses. By adding the expected amplifications and attenuations, we get the expected theoretical total amplification $G_{\text{theo}} = 59$ dB, 60 % smaller than the measured gain.

The measured bandwidth is in accordance with the bandwidth of the circulators (8 GHz to 12 GHz according to datasheet) which have the narrowest band of the amplification chain.

2.3 Room temperature microwave setup

The setup to generate and measure microwave pulses is shown in Fig. 2.8. On the left side, one can see the part which creates microwave pulses. Our experiments require three microwave tones, one to make the readout of the microwave resonator and the two others to excite the logical and the ancilla qubit. Three microwave sources[10] are used to generate microwave signals. The experiments are performed by using microwave pulses. In that purpose, we used a pulse generator source[11] and microwave mixers[12] to generate microwave pulses with a desired power and duration. The three microwave pulses are sent to the cryostat by the same input line. Power combiners[13] add these pulses to the input line.

The signal coming out from the cryostat is amplified by using three amplifiers[14]. Next the cavity readout tone is down–converted to 60 MHz by using a fourth microwave source[15] and a mixer[16]. At the end, the signal is digitised by an acquisition board[17].

In parallel of the microwave signal which is used to perform the readout of the resonator, we acquire a *reference* signal. The reference signal is used to extract the phase difference taken by the signal which is transmitted by the resonator. By mixing the reference signal and the signal transmitted by the resonator we are able to extract the amplitude and the phase difference of the transmitted signal.

[7] Raditek RADC-8-12-Cryo-0.02-77K-S23-1WR-b
[8] LNF-LNC1_12A
[9] afs4-08001200-10-CR-4
[10] R&S SMA 100A, Agilent E8257D and HP 83630A
[11] Higland T560
[12] M8-0220-Sa, M8-0326-NS and M8-0420-LS
[13] ATM P214H and Minicircuit ZX10-2-183-S+
[14] Miqteq S/N 1211532 and two Minicircuit ZX60-14012L-S+
[15] R&S SMA 100A
[16] M8-0220-SA
[17] Spectrum M3I.4142

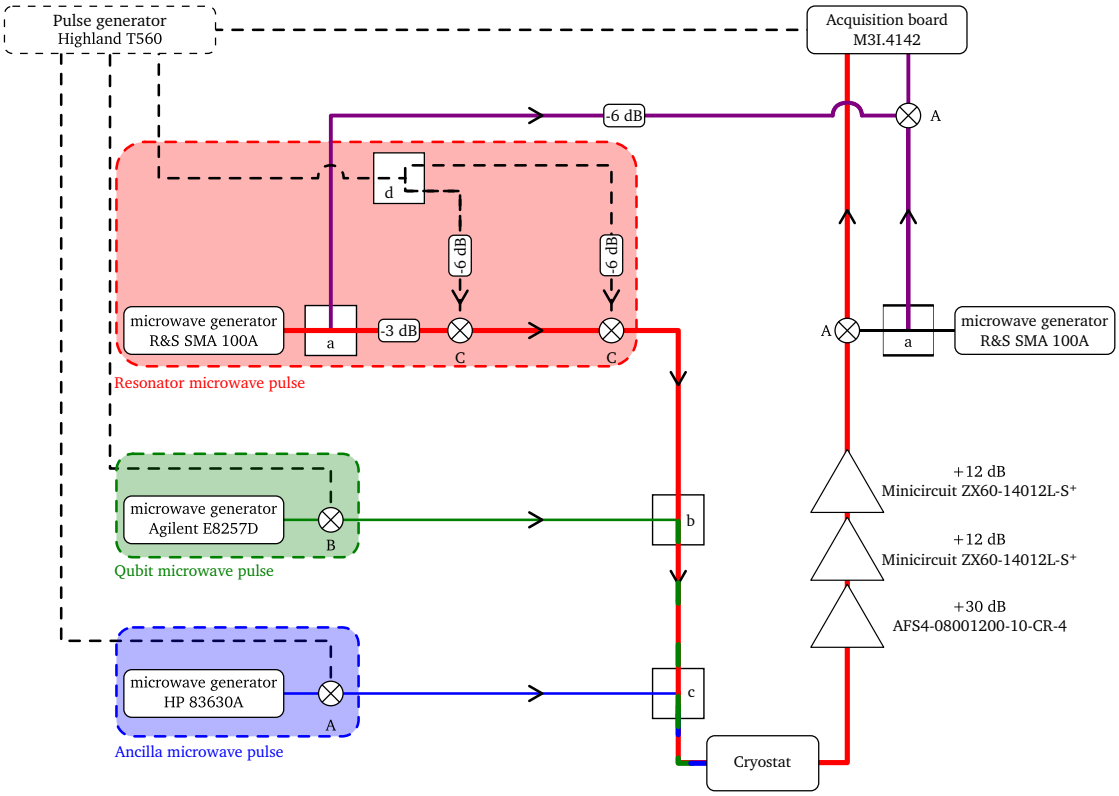

Power divider

Item	Name	Attenuation
a	Minicircuit ZFRSC-183-S+	-6.5 dB
b	ATM P214H	-3.0 dB
c	Minicircuit ZX10-2-183-S+	-3.5 dB
d	Picosecond Pulse Labs 933	-6.5 dB

Mixers

Item	Name	Attenuation
A	M8-0220-SA	-6.5 dB
B	M8-0326-NS	-5.5 dB
C	M8-0420-LS	-5.5 dB

Figure (2.8): Sketch of the microwave circuit realised for the experiment. Devices used to create microwave pulses are surrounded by color rectangles. The different microwave pulses are sent to the sample by the same main input line in red. The purple line depicts the reference signal lines. For the sake of simplicity synchronisation between devices is not shown.

In the following subsections, we will discuss in more detail the microwave pulse generation (Section 2.3.1), the synchronisation of the devices (Section 2.3.2), the frequency down–conversion (Section 2.3.3), and the data acquisition (Section 2.3.4). A comparison between our microwave setup with a commercial VNA will be shown (Section 2.3.5). Finally, we will compare the noise of the measured signal Section 2.3.6 with the calibrated noise temperature of the amplification chain.

2.3.1 Microwave pulse generation

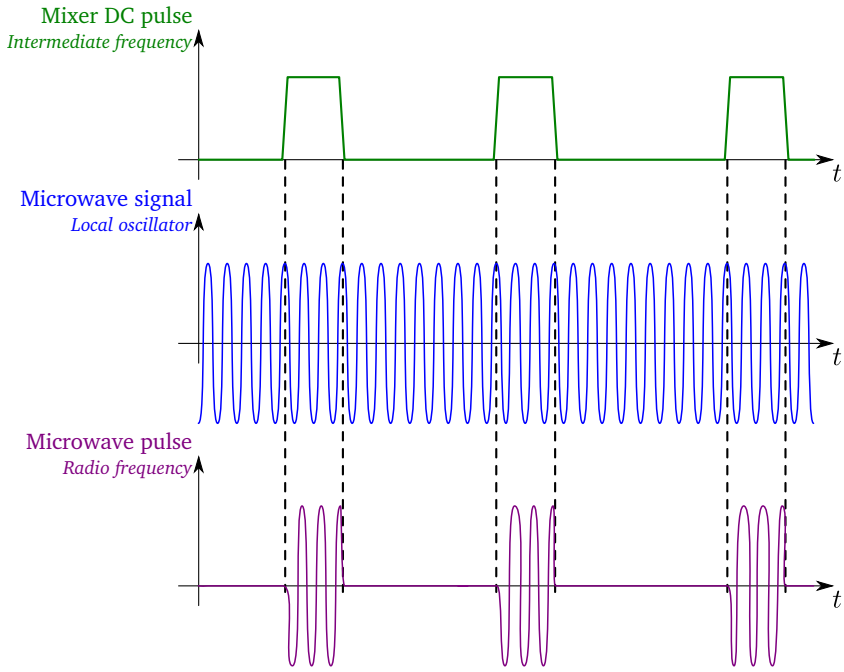

Figure (2.9): Illustration of the fabrication of microwave pulses. The first timeline shows the square pulses send to the intermediate frequency port. The second timeline presents the continuous microwave signal arriving to the andlocal oscillator port. The last timeline depicts the result of the mixing of the two previous signals, microwave pulses coming out the radio frequency port.

To generate microwave pulses we use two instruments, a microwave source and a pulse generator. The microwave source is tuned in order to generate a microwave signal with a desired frequency and power. The generated signal is sent to the *local oscillator* port of the mixer. At the *intermediate frequency* port, we send a square pulse. The square pulse defines the duration of the microwave pulse. At the *radio frequency* port, the microwave pulse is formed. The method is presented in Fig. 2.9.

All the microwave pulses in the experiment are generated in the same way. This method allows the generation of microwave pulses from 2 GHz to 24 GHz, depending on the mixer. The maximal power of the pulses are limited by the mixers and reaches typically 5 dBm. The

temporal resolution of the pulse is given by the quality of the pulse generator[18]. Specifications give a rise/fall time of 750 ps and a jitter about 35 ps. The resolution of the pulse length is 10 ps.

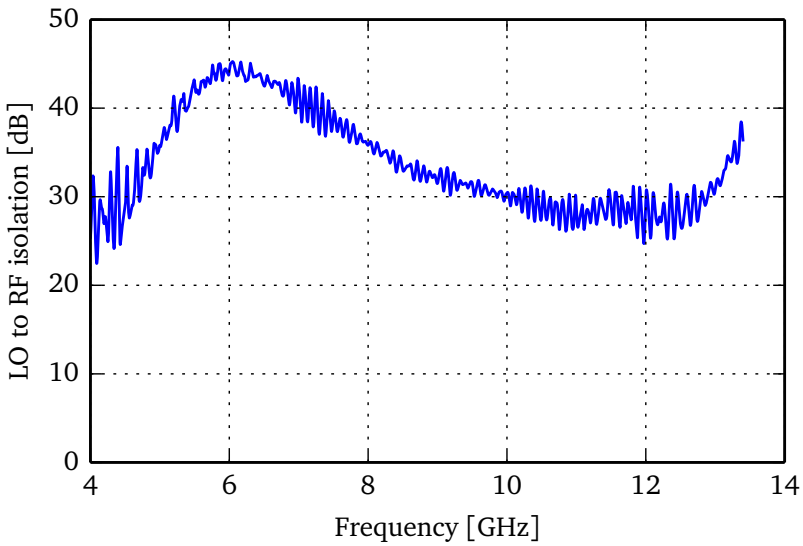

Figure (2.10): LO to RF isolation of the M8-0420-LS mixer. Measurements have been performed with a commercial VNA, the R&S ZVL13.

One of the main limitations of the method to generate microwave signal is the leakage of the mixers. The LO-RF isolation gives the ratio between the power at the *Local oscillator* port over the power which leaks through the *Radio frequency* port. We performed measurement of the LO to RF isolation of all mixers in our setup. A typical measurement is shown in Fig. 2.10. The other mixers present similar characteristics.

2.3.2 Device synchronisation

All devices are synchronised to avoid dephasing. One of our microwave source has a high performance 10 MHz reference oscillator with a RMS jitter of 105 fs[19]. The clock signal of this source is used as a reference to synchronise all devices of the setup. A homemade clock distributor[20], which consists of an amplifier and a signal divider, splits the 10 MHz of the clock reference into eight equivalent 10 MHz signals. Theses signals are used by the other devices as external clock.

Figure 2.11 shows the phase drift as function of time of a 10 MHz signal obtained by frequency down–conversion from two R&S sources at 10 GHz and 10.01 GHz in respect to the 10 MHz clock signal. For our experiments, the phase between microwave sources has to

[18]Highland T560
[19]One of the R&S microwave source has been purchase with the option "SMB-B1H" for this purpose.
[20]Pôle service electronique, institut Néel

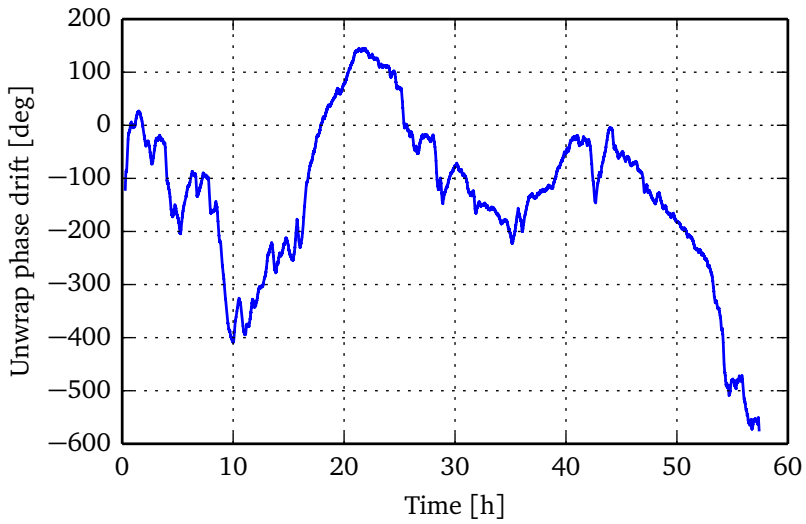

Figure (2.11): Unwrapped phase drift of a 10 MHz *signal obtained by frequency down–conversion from two R&S sources at* 10 GHz *and* 10.01 GHz *in respect to the* 10 MHz *clock signal.*

be constant during the acquisition of one data point. Since measurements are repeated, the phase has to stay the same during all the averaging process. A good criterion is then that the phase has to be constant during a time $N T_{\text{period}} < T_{\text{lost phase}}$ where N is the number of average, T_{period} is the measurement period, and $T_{\text{lost phase}}$ the phase coherence time. In our experiments this criterion is well respected since the longest measurement period is about 10 µs and the largest repetition about 10^6 which leads to a needed phase coherence time of 10 s. From Fig. 2.11 we observe that the phase make a 2π rotation in approximately 10 h which is very long compare to our needed phase coherence time.

Figure 2.12 presents the single side band phase noise for the microwave source having the best internal clock. Due to the clock distributor, the two R&S sources should exhibit the same phase noise. In our experiment the R&S are used to perform the readout of the microwave cavity (about 7 GHz) which corresponds to the purple line. Thus at 10 Hz of the generated frequency the spurious microwave signal is already attenuated by 70 dB. We measured the spurious signal for the other microwave sources used, we obtained, at 10 Hz of the generated frequency, −45 dBc for the HP 83630A and −45 dBc for the Agilent E8257D.

2.3.3 Frequency down–conversion

After amplification the signal is down–converted with a mixer and digitised by an acquisition board[21]. The down conversion is realised by using the heterodyne signal processing technique.

In order to explain the heterodyne method, let's consider that we have a microwave signal which is transmitted by the sample with a frequency ω_1. This signal is sent to the

[21] Spectrum M3I.4142

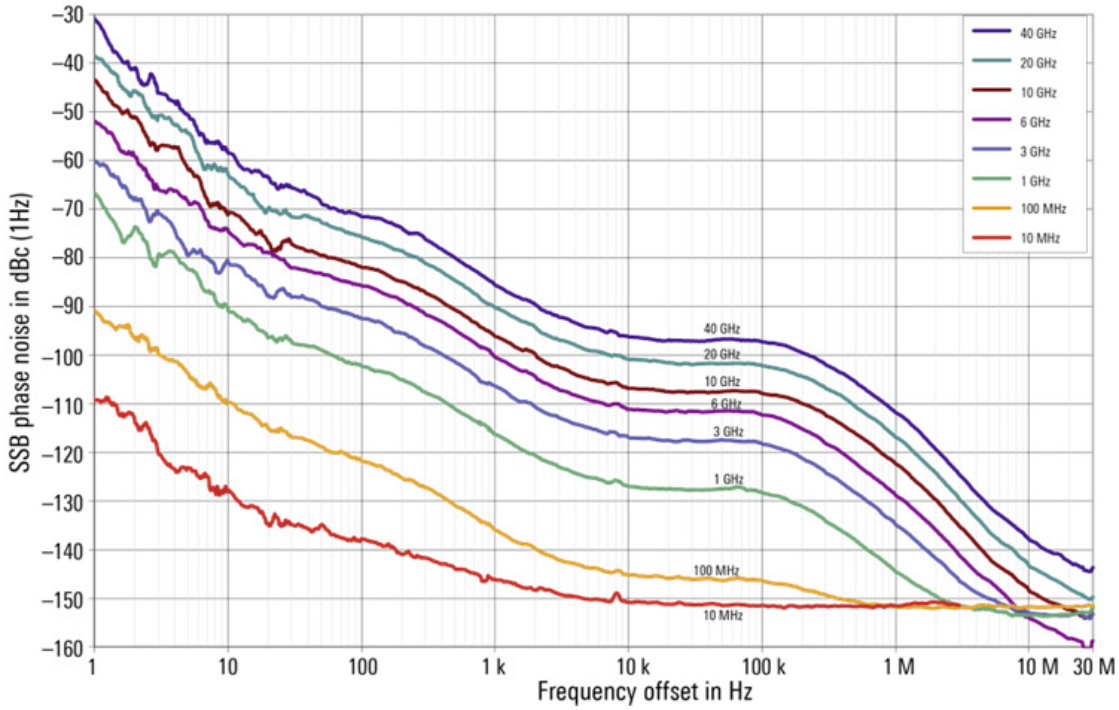

Figure (2.12): Single Side Band phase noise of the microwave source having the best internal clock. Measurements which used theses microwave sources, R&S SMB 100A, are performed for frequencies from 6 GHz *to* 10 GHz.

Radio frequency port of a mixer. At the *Local oscillator* port we send another microwave signal at a frequency ω_2. The mixer will produce two signals at the *Intermediate frequency* port at frequencies $\omega_\Sigma = \omega_1 + \omega_2$ and $\omega_\Delta = \omega_1 - \omega_2$. The signal at frequency ω_Δ is the down–converted signal which will be digitised by the board. The high frequency signal is, experimentally, not produced by the mixer. Indeed the *intermediate frequency* port of the mixer acts as a low-pass filter whose cutoff frequency is at 3 GHz. In our experiments, the high-frequency signal would be about 14 GHz and so, will be strongly attenuated.

2.3.4 Data acquisition

To acquire data we use an acquisition board[22] which is connected to our computer via a PCI-express interface. The board has an acquisition rate of 250 MS·s^{-1}. The Nyquist–Shannon sampling theorem states that if a function $x(t)$ contains no frequencies higher than $\nu = \nu_{\text{cut}}$, it is completely determined by giving its ordinates at a series of points spaced $1/(2\nu_{\text{cut}})$. In accordance with this theorem, we have chosen an intermediate frequency of 60 MHz which can be well measured with a sampling rate of 250 MS·s^{-1}.

The board has an internal high-pass filter with a cut-off frequency $\nu_{\text{cut}}^{\text{spectrum}} = 20$ kHz. The

[22] Spectrum M3I.4142

resolution of the board is 14 bit with 200 mV of acquisition range, so a resolution of about 15 µV.

The board has two analog inputs. The first one is used to digitise the microwave signal transmitted by the sample and the second one to digitised the reference signal. Both are down–converted to 60 MHz by using mixers as explained before.

The signals acquired by the board let us extract two parameters, namely the amplitude and the phase. Hereafter we present a numerical method to extract these information from the digitised signal. Let's consider that the intermediate frequency can be described by an oscillating signal with an amplitude A and a phase φ:

$$S(t) = A\cos(\omega_0 t + \varphi) \tag{2.20}$$

where $\omega_0/(2\pi) = 60\,\text{MHz}$. Numerically we multiplied $S(t)$ by a cosine and a sine of amplitude 1 and angular frequency ω_0:

$$\begin{aligned} S_\text{c}(t) &= A\cos(\omega_0 t + \varphi)\cos(\omega_0 t) &&, \quad S_\text{s}(t) = A\cos(\omega_0 t + \varphi)\sin(\omega_0 t) \\ S_\text{c}(t) &= \frac{A}{2}\Big[\cos(2\omega_0 t + \varphi) + \cos(\varphi)\Big] &&, \quad S_\text{s}(t) = \frac{A}{2}\Big[\sin(2\omega_0 t + \varphi) - \sin(\varphi)\Big] \end{aligned} \tag{2.21}$$

We integrate over an interger number of periods:

$$\begin{aligned} \overline{S}_\text{c} &= \frac{1}{nT}\int_t^{t+nT} S_\text{c}(t) &&, \quad \overline{S}_\text{s} = \frac{1}{nT}\int_t^{t+nT} S_\text{s}(t) \\ \overline{S}_\text{c} &= \frac{A}{2}\cos(\varphi) &&, \quad \overline{S}_\text{s} = \frac{A}{2}\sin(\varphi) \end{aligned} \tag{2.22}$$

where $n \in \mathbb{N}$ is the number of measured periods and T is the duration of one period. From $\overline{S}_\text{c}$ and $\overline{S}_\text{s}$ we can calculate the amplitude and the phase of the original signal $S(t)$:

$$A = 2\sqrt{\overline{S}_\text{c}^2 + \overline{S}_\text{s}^2} \qquad \varphi = \arg\left(\overline{S}_\text{c} + \text{i}\overline{S}_\text{s}\right) \tag{2.23}$$

From the reference signal we obtain A_ref and φ_{ref} and from the signal transmitted by the sample, A_t and φ_t. There is no global reference for the phase. For this reason we measured a reference signal from which we calculate the phase difference acquired by the transmitted signal, $\Delta\varphi = \varphi_\text{t} - \varphi_\text{ref}$. The phase relation of signals generated by independent sources is *a-priori* unknown. By our method we are able to determine the phase relation before the sample (by reference measurement) and after (by signal measurement). Moreover they are down–converted by the same microwave generator ensuring no phase difference induced by the down–conversion between the two signals. The subtraction of the transmitted phase by phase reference allows to only keep the phase difference due to the different path of the two

signals. Finally, we extract all the information of the signal transmitted by the sample with two parameters A_t and $\Delta\varphi$.

A measurement is generally repeated in order to increase the signal-to-noise ratio. We obtain then a mean value and an uncertainty for the two parameters. We denote by $\langle A_t \rangle$, σ_{A_t} and $\langle \Delta\varphi \rangle$, $\sigma_{\Delta\varphi}$ the mean value and the standard deviation of the transmitted amplitude and phase.

2.3.5 Transmission coefficient measurement

Figure 2.14 presents the measurement of a microwave 7 GHz band-rejection filter (see Fig. 2.13) performed with a commercial VNA (R&S ZVL13), blue curve, and with our microwave setup, green curve, described previously. We remark that our microwave setup is perfectly capable to perform S_{21} measurement qualitatively comparable to what a commercial VNA can measure. Furthermore, our microwave setup reaches a better signal-to-noise ratio for some frequency ranges (between 8 GHz and 9 GHz for example). However, we observe spurious oscillations around 4 GHz and 10 GHz for instance. These oscillations are due to standing waves which occur because of slight impedance mismatch between microwave components.

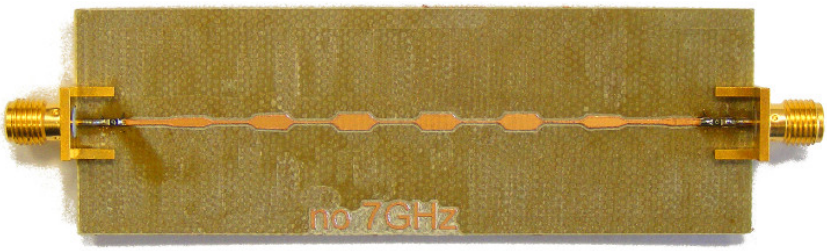

Figure (2.13): Photography of the microwave 7 GHz *band-rejection filter.*

2.3.6 Noise of the measured signal

We perform statistical measurement of the amplitude of the transmitted signal at 9.5 GHz. Figure 2.15 shows probability density function of the measured amplitude. A fit has been realised by assuming a Gaussian distribution of the following form:

$$f(x) = \frac{1}{\sigma\sqrt{2\pi}} \exp\left[-\frac{1}{2}\left(\frac{x-\mu}{\sigma}\right)^2\right] \tag{2.24}$$

where σ and μ are the standard deviation and the expected value of the distribution, respectively. The fit gives $\mu = 1.22\,\text{mV}$ and $\sigma = 13\,\mu\text{V}$. The gain of the amplification chain for this measurement was about 79 dB. We then estimate the standard deviation at the input of the amplification chain dividing by the gain of the chain, we get 13 nV.

We can compare this experimental value to an expected one obtained from different calibrated parameters. Assuming that the main noise source is the cold amplifier, see Section 2.2.2,

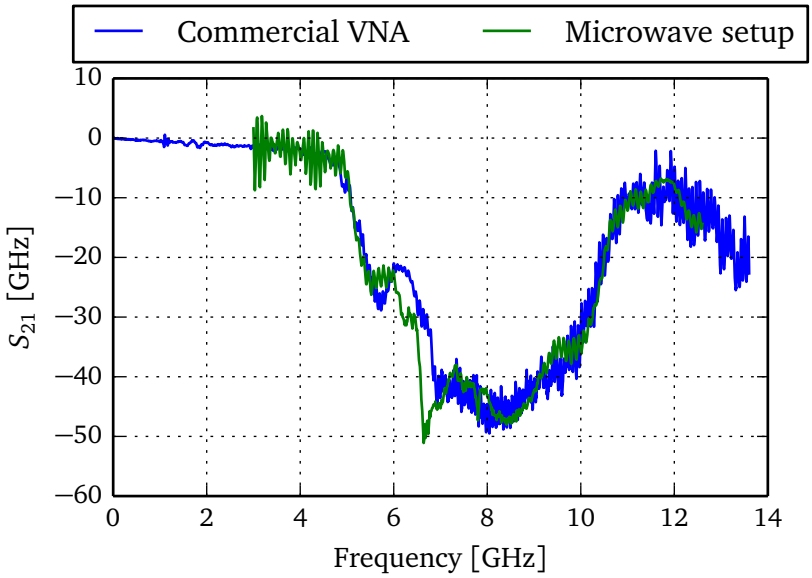

Figure (2.14): Measurement of microwave 7 GHz *band-rejection filter shown in Fig. 2.13. The blue curve shown S_{21} parameter measured with a commercial VNA (R&S ZVL13) and the green curve with our microwave setup. Both measurements have been performed with a bandwith of* 1 kHz.

we can write the root-mean-square of the voltage as[69]:

$$V_{\mathrm{RMS}} = \sqrt{4k_{\mathrm{B}}TR\Delta\nu} \tag{2.25}$$

where k_{B} is Boltzmann's constant, R the resistance of the noise emitter, T the temperature of the noise emitter, and $\Delta\nu$ the bandwidth of the measurement chain. The noise temperature has been calibrated to be about 4.5 K and the bandwidth is given by the integration time of the board $1/\Delta t \approx 3.33\,\mathrm{MHz}$. The histogram shown in Fig. 2.15 has been measured with 10^4 repetitions. In order to take into account this averaging, we divide[23] the Eq. (2.25) by $\sqrt{N}$. We obtain $V_{\mathrm{RMS}}/\sqrt{N} = 2.7\,\mathrm{nV}$.

[23]This operation is correct under following conditions: signal and noise are uncorrelated, signal strength is constant in the replicate measurements and noise is random, with a mean of zero and constant variance in the replicate measurements.

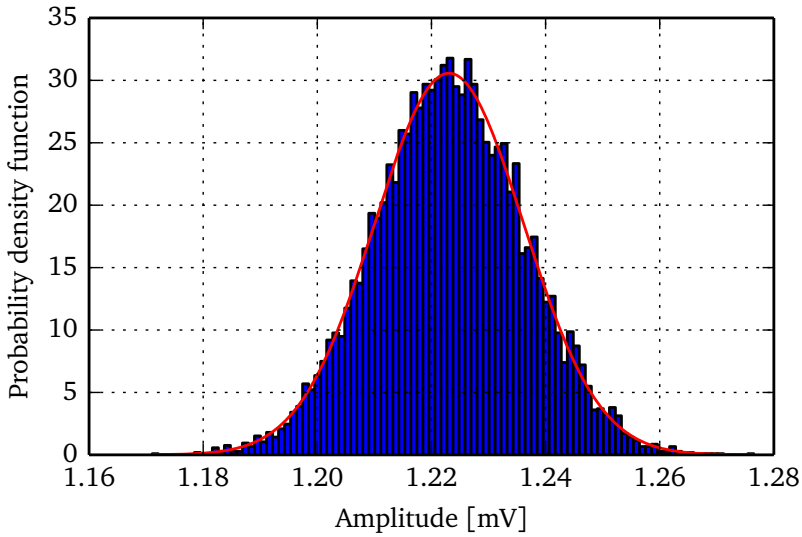

Figure (2.15): Probability density function of the amplitude measured by heterodyne technique.

2.4 Software environment

2.4.1 Python

The experimental environment has been developed at the beginning of my thesis. It was the occasion to start a new software environment from scratch. The decision to use Python has been taken by considering all the advantages offered by this choice. The previous measurement platform used Labview to perform experiment, Matlab to perform numerical calculation and Maple for symbolic computation.

Python allows to use the same programming language on all the steps of the data treatment (acquisition, analysis, plot) thanks to the large number of available libraries. The base of scientific library is composed of Numpy[84] and SciPy[85] which allow, among other things, fast linear algebra operation Fourier transform, and powerful optimisation algorithms. The graphics are handled by Matplotlib[86]. Symbolic computations are done with Sympy[87] and IPython Notebook[88] with direct LaTeX output.

Python is platform independent and can work on GNU/Linux, Mac, or Windows. This aspect is important in our group where the three operating systems are used. The different scripts can be exchanged, used and updated by anybody in the group without worry about compatibility.

Python is free and open-source. We never have to pay to get Python and do not have to be worried about the software licence agreement. Since everything is open-source you can always have a look on the source code. There is no “black box”.

Python can be used with the object-oriented paradigm. The object-oriented paradigm is powerful in the case of data acquisition. In our setup a real object like a micro-wave source is then represented like a python object in the measurement script.

Numpy, through its implementation of universal function (built-in functions implemented in compiled C code), allows fast treatment of large arrays of numbers. The condition is to define a data type for the array. The experiments are performed with the numpy.float32 data type which gives enough precision considering our acquisition setup.

2.4.2 Qtlab

QTLab is an IPython-based measurement environment. It has been written by Reinier Heeres, Pieter de Groot, and Martijn Schaafsma. We use it as a general framework for our software environment.

The QTLab framework is based on several classes interacting together. Figure 2.16 shows an example of such interaction. The different classes of QTLab are described in the following.

Instrument

Instrument is used as a model to control and manage the different instruments handled by the computer. The class introduces an abstraction layer by defining the notion of “virtual instrument” in contrast to “physical instrument”. For example, a microwave source and a pulse generator correspond to the physical instruments “mwsrc” and “dc_pulser”, respectively.

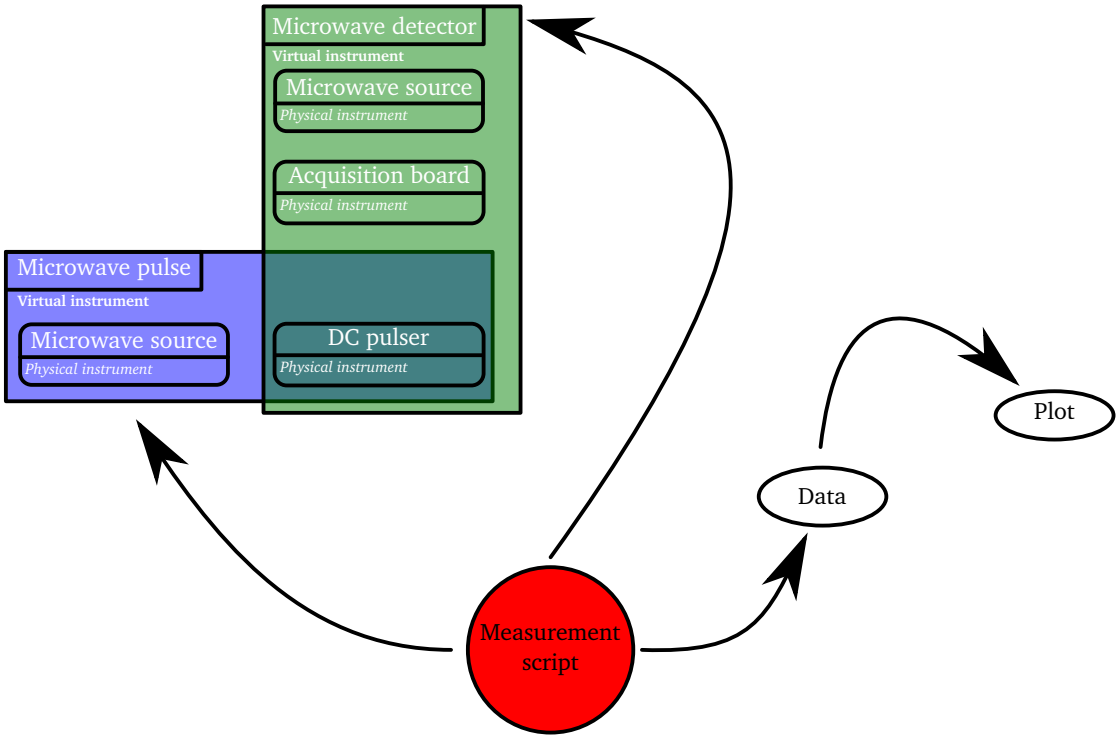

Figure (2.16): Sketch of the interaction between the different classes in QTLab. All devices are represented in python by an object under the generated name physical instrument. Virtual instruments are composed of various physical instruments. A physical instrument can be used by several virtual instruments.

Together they form the virtual instrument "mw_pulse" which generates microwave pulses. When all the instruments of the experiment are correctly integrated in QTLab, the user mainly drives virtual instruments.

In our experiment, a virtual instrument called "Microwave_pulse" is composed of two physical instruments, the "Highland pulse generator" and a "R&S SMA 100A" microwave source. The virtual instrument has four methods (set_frequency, set_power, set_width, and set_status) which allow to modify the properties of the microwave pulse. We note that, for a user of the virtual instrument, it is equivalent to tune the frequency or the width of the pulse. However these two modifications involve two different devices, the microwave source to change the frequency and the pulse generator to change the width. By the mean of the virtual instrument abstraction, the complexity of using several real instruments for one purpose is hidden making the experiment easier to perform.

Data

The class Data is used to organise and save data during measurement, and to retrieve data from files afterwards. It also handles the directory tree in which data are stored. By default the

name of one measurement is preceded by the timestamp corresponding to the launch of the measurement. The stored data classified as one of two types called “coordinate” and “value”. The coordinates correspond to the physical parameters which are set during a measurement while the values correspond to the physical parameters which are measured. Units in which coordinates and values are stored are also saved.

For example, the stored data of a typical S_{21} transmission measurement save, as “coordinate”, the frequency and, as “value”, the amplitude and phase difference (see Section 2.3.4).

Independently of coordinates and values, all parameters of the instruments managed by Qtlab are stored in a “snapshot” at the beginning of the measurement.

Plot

In QTLab the graphics are handled by Gnuplot[89] through the class Plot. An object of the class is instanced by indicating the Data object in which the data to plot are stored. The plot is then automatically updated while the measurement is progressing. 2D and 3D plots are available as well as various options to customize plots.

Gnuplot is the only element of the environment which is not in python. To keep the environment homogeneous, we think to adopt PyQtGraph[90] as graphics library for live plotting. Indeed Matplotlib is powerful to produce publication quality figure but has the drawback to be slow.

2.5 Superconducting coil

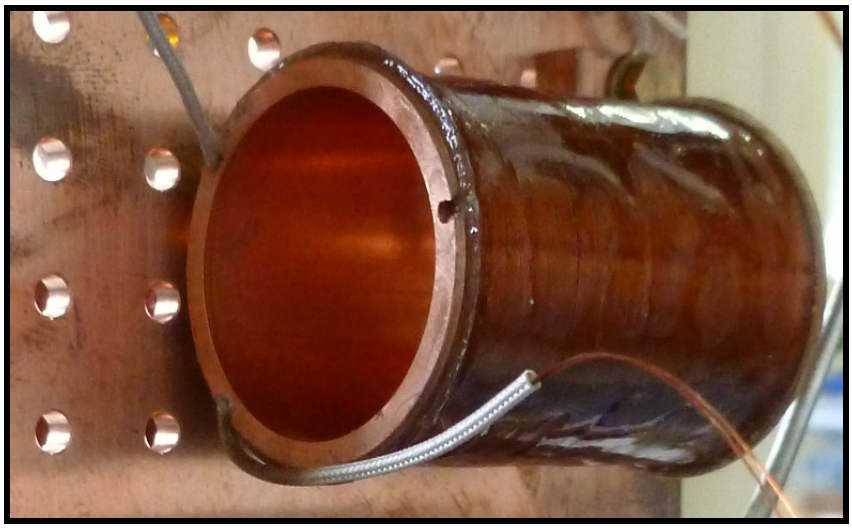

Figure (2.17): Superconducting coil screwed on the mixing chamber cold plate.

In our experiments, a magnetic field is used to tune the $(E_J/E_C)^*$ ratio of the qubit but also to tune the resonant frequency of the microwave resonator. We take advantage of the

Characteristics	coil 1	coil 2
Height [mm]	38	38
Layers	12	4
Turns	2325	775
Calculated inductance [mH]	100	25
Calculated current to field ratio [mT·A^{-1}]	77	19

Table (2.1): Characteristics of superconducting coils used during experiments.

superconducting coils which have been installed in the past by Thomas Weißl and Iulian Matei. Figure 2.17 shows a photograph of one coil mounted in the cryostat. Characteristic parameters of the coils are summarised in Table 2.1. The coils have been fabricated at the Neel institute by the "Pôle cryogénie".

The coil is realised with niobium-titanium wires in copper matrix to improve the thermalisation of the coil. From the mixing chamber to the 4 K stage, the wires are superconducting niobium-titan in copper-nickel matrix. A low contact resistance between the coil wire in niobium-titan and the superconducting wire in niobium-titan embedded copper-nickel matrix is achieved by soldering the two wires along 25 cm with tin. Between 4 K and room temperature, the coil is contacted by constantan wires.

2.6 Sample holder

2.6.1 Presentation

Figure 2.18 shows a photograph of the sample holder. The top left picture shows the inside of the sample holder. At the centre of the sample holder, a chip is visible. The bottom left image is a zoom in the chip. Coplanar waveguides on the chip are connected to coplanar waveguides on the PCB (printed circuit board) via aluminium wire bonds.

The PCB circuit was designed in collaboration with Christophe Hoarau from "Pôle service electronique". The substrate is in FR-4[24] with a thickness of 360 µm. The metal at the surface is a pure copper layer of 18 µm. The PCB has been fabricated by EURO CIRCUITS[25].

For coplanar waveguides on the chip and on the PCB, it is really important to have a well-defined ground. By well-defined ground we mean a ground at the same potential all along the lines. The connection of the ground of the PCB backside to the sample holder is

[24] Flame Resistant 4
[25] http://www.eurocircuits.com/

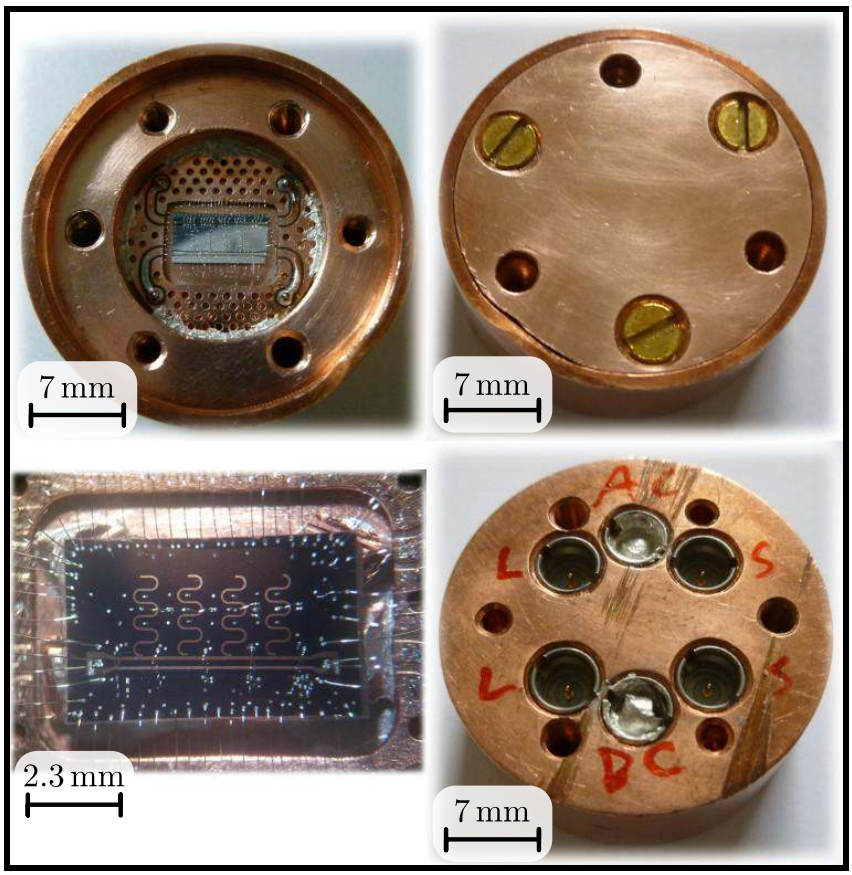

Figure (2.18): Photography of the sample holder used for experiments. The top left shows the inside of the sample holder, the bottom left is a zoom in the chip. The top right picture is the top of the sample holder when it is closed and the bottom right is the bottom of the sample holder.

realised with silver epoxy[26]. Moreover we also covered borders of the PCB with the same epoxy (this is visible on the photo). The epoxy assure then a good electrical conductivity between the PCB and the sample holder. Vias are also visible on all area of the PCB. The aim of these vias is to short-circuit the frontside and the backside of the PCB. By this way the two sides have the same potential which is the potential of the sample holder. The ground of the chip is connected to the sample holder and to the PCB by wire bonds. To ensure a good electrical conductivity, many bondings are used as we can see on the photo.

The thermal conductivity is also primordial for our experiment. The sample holder is thermalised to the mixing chamber stage via a metal-metal contact realised with three screws. The silver epoxy ensures a good thermal conduction between the PCB and the sample holder. The chip is glued to the sample holder with GE varnish[27] pressed between the backside

[26]FERRO laque L-200
[27]cryospare C5-101

of the chip and the sample holder. The thermal conductivity of the GE varnish is about $3.2 \times 10^{-6}\,\mathrm{W{\cdot}m^{-1}{\cdot}K^{-1}}$ at 4 K.

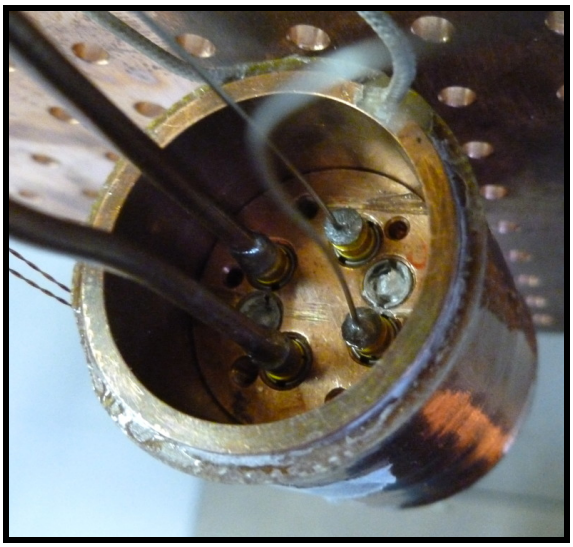

Figure (2.19): Photograph of the sample holder inside the magnetic coil. Two BeCu/BeCu coax cable are connected to the sample holder via SMP connectors. Two microcoax SS-SS cables are also connected to the sample holder via SMP connectors.

In Fig. 2.19 the backside of the sample holder is presented. Four SMP connectors[28] connect the chip to the electrical setup. We can see, on the left side, two coax cables used for the transmission of the microwave signal through the sample, and on the right side, two microcoax cables used to current-bias the sample.

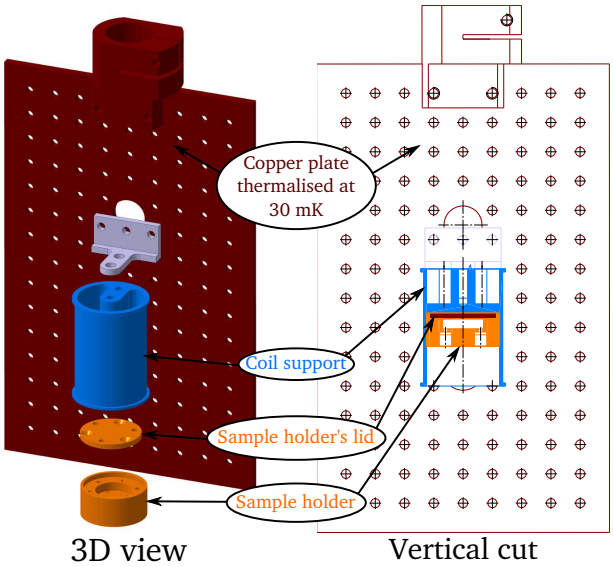

Figure (2.20): Schematic view of the sample holder with the coil support.

Figure 2.20 schematises the sample holder and the magnetic coil support. Once the sample holder is screwed inside the magnetic coil, the chip is positioned at the centre of the coil where the magnetic field is most homogeneous.

2.6.2 Microwave properties

Figure 2.21 presents the measurement of the S-parameters of the sample holder realised with a commercial VNA[29]. We see a linear decrease of the transmission as function of the frequency. This feature is a typical signature of losses in the dielectric. Moreover, a dip of about 5 dB occurs in transmission at 15.2 GHz. Hereafter we propose a simple explanation of the origin of this dip.

The sample holder has a cylindrical internal cavity which contains a PCB and a chip. However, this cavity can act as a microwave resonator. The derivation of the internal electromagnetic mode frequencies which exist in such a cylindrical cavity is a textbook problem and we will here give the result found in the Pozar[61]:

[28] Radiall R222.051.000
[29] Agilent E8362C

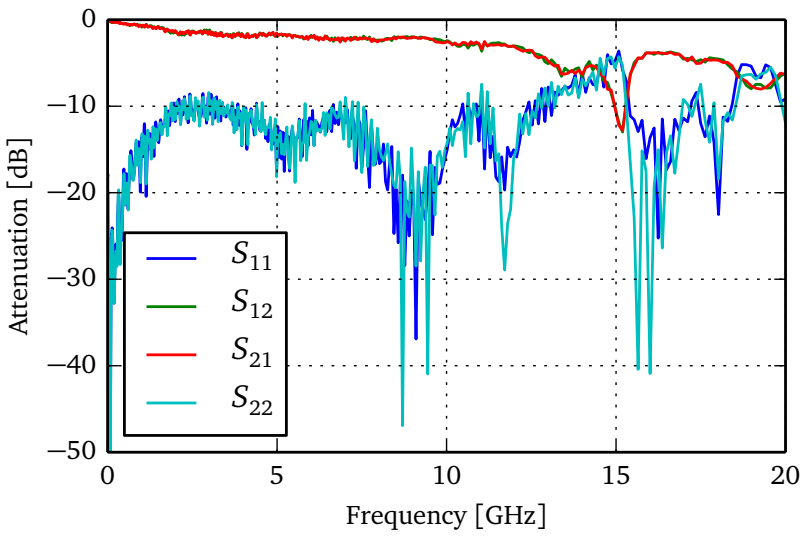

Figure (2.21): S parameters of the sample holder measured with a through connected to the PCB. Measurements have been realised with a commercial calibrated VNA: the Agilent E8362C, at room temperature.

$$f(n,m,l) = \frac{c}{2\pi\sqrt{\mu_r \epsilon_r}} \sqrt{\left(\frac{p'_{n,m}}{r}\right)^2 + \left(\frac{l\pi}{h}\right)^2} \qquad \text{TE}_{n,m,l} \text{ mode frequency}$$

$$f(n,m,l) = \frac{c}{2\pi\sqrt{\mu_r \epsilon_r}} \sqrt{\left(\frac{p_{n,m}}{r}\right)^2 + \left(\frac{l\pi}{h}\right)^2} \qquad \text{TM}_{n,m,l} \text{ mode frequency} \tag{2.26}$$

where h and r denote the height and the radius of the cylinder. $p_{n,m}$ denotes the m-th zero of the n-th Bessel function of the first type, and $p'_{n,m}$ denotes the m-th zero of the derivative of the n-th Bessel function of the first type. The mode number is denoted l.

Our cavity is 4 mm high with a radius of 7 mm. The mode with the lowest resonant frequency is the TM_{010} which occurs at 16.39 GHz when we consider the permittivity of the vacuum. However, the presence of the PCB changes the effective permittivity, reducing the resonance frequency of the mode. A simple estimation of the total permittivity gives[30] $\epsilon_{\text{tot}} = \frac{h_{\text{cavity}} \epsilon_r^{\text{vacuum}} \epsilon_r^{\text{FR-4}}}{(h_{\text{cavity}} - h_{\text{PCB}}) \epsilon_r^{\text{FR-4}} + h_{\text{PCB}} \epsilon_r^{\text{vacuum}}} = 1.08$, reducing the resonance frequency of the TM_{010} mode to 15.77 GHz. We then conclude that the dip in transmission visible in Fig. 2.21 is due to the TM_{010} mode of the sample holder cavity.

[30] Manufacturer gives $\epsilon_r^{\text{FR-4}} = 4.8$

2.7 Shielding

Both the microwave resonator and SQUID are highly sensitive to thermal radiation[91] and spurious magnetic field[92–94]. In this section we present the different shields implemented to screen as much as possible the electromagnetic field.

2.7.1 Electromagnetic shielding

Electromagnetic field fluctuations are screened inside the cryostat which acts as a Faraday cage. The sample is placed inside a cylindrical cavity whose first electromagnetic resonance is about 15.8 GHz, far away from the characteristic frequency of our sample.

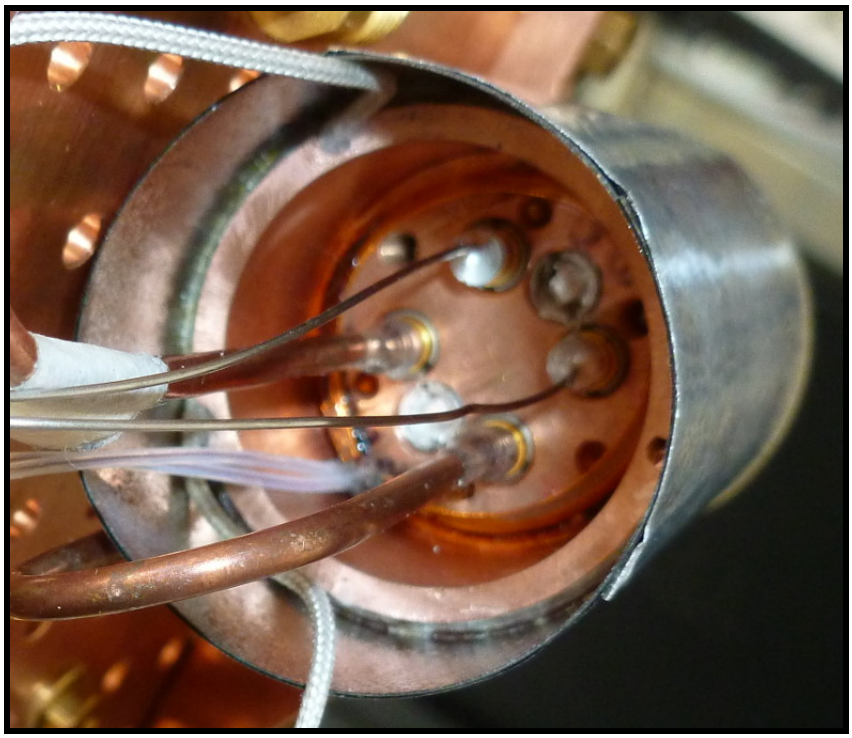

Figure (2.22): Photography of the magnetic shield made from Metglas ribbon.

The magnetic shielding is ensured by three different protections. Outside the cryostat a cylinder shield from MμMetal with a thickness of 2 mm surrounds the cryostat to protect the inner vacuum chamber against external magnetic field fluctuations. A second magnetic shield has been realised by wrapping the still temperature shield with one layer of Metglas[31] ribbon. Figure 2.22 shows the third magnetic shield which consists of the sample holder wrapped with several layers of Metglas.

The Metglas has a magnetic permeability which decreases at low temperature but which does not drop to zero. At room temperature, with annealed material, the relative permeability

[31] Metglas 2714A Magnetic Alloy

can reach 1×10^6. Hung P. Quach and Talso C. P. Chui have shown[95] that at 4 K the permeability of the Metglas goes down to reach a plateau at $\mu_r = 1 \times 10^4$.

We have to notice that the SMP connectors, male and female, used to connect coax cables to the sample holder, visible on Fig. 2.22, contain beryllium, gold and nickel metal. Nickel is ferromagnetic and so will create a magnetic field inside our magnetic shield. This is a defect which has been solved in a new sample holder by moving the connectors further away from the sample.

Chapter 3

Sample fabrication

Contents

3.1 Introduction **123**
3.2 Aluminium quantum circuits **124**
3.2.1 Design considerations 124
3.2.2 Fabrication of the different patterns 132
3.2.3 A fight against the screening effect 140
3.2.4 Test junctions 140
3.3 Rhenium microwave resonators **143**
3.3.1 Epitaxy of rhenium 144
3.3.2 Design of coplanar waveguide resonator 147
3.3.3 Microwave resonator fabrication 149

3.1 Introduction

The work realised during my Ph.D can be decomposed in two parts. The main project is the experimental fabrication of a V-shape level scheme in superconducting quantum circuit. It required the fabrication of a quite complex, quantum circuit with several Josephson junctions, a microwave resonator, and various control lines. We first present various considerations that we have taken into account to design the chip. We next present the fabrication which has mainly been carried out by Alexey Feofanov and Bruno Küng at the "PTA" and "Nanofab" facilities. We explain the different steps of the sample fabrication recipe. Finally we discuss the screening of magnetic field effects which occurs in the case of a quarterwave microwave resonator and the solution adopted to avoid it.

The second project of my Ph.D was to fabricate microwave resonators from epitaxial layers of rhenium. The rhenium has been grown by Benjamin Delsol[46] during his Ph.D. In the first

section, we summarise the key fabrication steps. After growth, the sample was fabricated by laser lithography. The second section is dedicated to the design of coplanar waveguide resonators. We summarise equations necessary to design microwave resonators with a precise resonance frequency. The third section presents the fabrication of the microwave resonators. We present the process developed in collaboration with "Nanofab" to realise such samples.

3.2 Aluminium quantum circuits

3.2.1 Design considerations

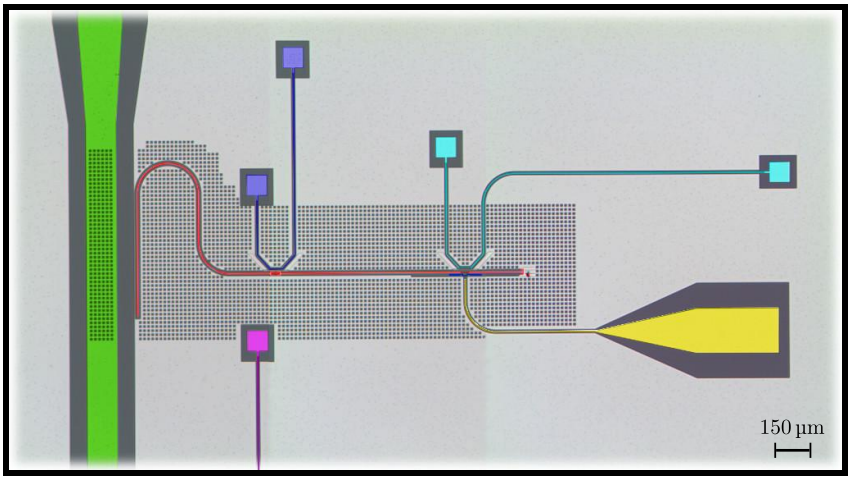

Figure (3.1): SEM image of a chip zoom in one microwave resonator. The feedline is coloured in green at the left of the picture. The $\lambda/4$ resonator is in red at the centre of the image. Three DC flux bias lines are visible in purple, blue and cyan. The cyan line is used to flux bias the qubit and the blue line to flux bias the SQUID. The purple line is only used to connect DC lines of the two microwave resonators (the second one being not visible in the picture). The yellow line is a microwave capacitive excitation line capacitively coupled to the qubit.

In Chapter 1, we presented an original circuit which exhibits a V-shape energy diagram. To obtain a V-shape, the quantum device should have two important properties. First, it should have two internal modes of oscillations that we have called *in-phase* and *out-of-phase* oscillations. This can be achieved by implementing a loop inductance which is of the order of the Josephson inductance of the junctions $L_{\text{loop}} \approx L_{\text{JJ}}$. Next the symmetry in the energy diagram between the two oscillation modes should be broken. The key parameter for this effect is the coupling g_{zz}. We design our device in order to get a g_{zz} larger than 100 MHz. Figure 3.1 shows an SEM picture of our quantum device having a V-shape energy diagram. The quantum device, too small to be visible on the picture, is positioned close to the shorted end of a quaterwave resonator colored in red. At this position the qubit and the ancilla mode will be coupled to the fundamental mode of the resonator, see Section 1.3.2. The microwave resonator is capacitively connected to a feedline, in green, through which transmission

measurement will be performed. We also see flux bias lines which allow local flux tunability, in cyan and blue. A microwave line in yellow is capacitively coupled to the qubit mode to excite directly the qubit without exciting photons in the resonator. Hereafter we discussed in details the design of each component.

Logical and ancilla qubits

The logical qubit mode is similar to the Transmon mode since it corresponds to the *in-phase* current oscillations through the junctions. Then to avoid decoherence due to spurious charge fluctuation, the ratio $(E_J/E_C)^*$ has to be about 50[18]. Furthermore to avoid thermal population of the logical qubit levels (the ancilla qubit has always larger eigenfrequencies), its resonant frequency has to be large compared to the base temperature of the cryostat ($\hbar\omega \gg k_B T$). We can estimate the effect of the thermal environment on the qubit by deriving the average energy of a harmonic oscillator coupled to a bath at a temperature T. This textbook calculation is written in the "Quantum mechanics" from Cohen-Tannoudji *et al.*[58] and the result is:

$$\langle \mathscr{H} \rangle = \frac{\hbar\omega}{2} + \frac{\hbar\omega}{\exp\left(\frac{\hbar\omega}{k_B T}\right) - 1} \tag{3.1}$$

with ω the eigenfrequency of the oscillator. For a base temperature of 30 mK and a qubit frequency of 3.6 GHz we obtain $\langle \mathscr{H} \rangle / (\hbar\omega/2) = 1.006$, which means that the population of higher state than the fundamental is negligible for our experimental parameters.

It is preferable to have small junctions to not be coupled to spurious two-level systems[96]. In order to fulfil the conditions of a small junction area and a large $(E_J/E_C)^*$ ratio, we add in parallel of the junction an inter-digital capacitance. Moreover, by this way we can almost independently choose, by design, the value of the critical current and of the capacitance of the junction.

We have seen in Section 1.3.2 that, due to the physical nature of the qubit and ancilla modes, the qubit can only be excited via electric field and the ancilla only via magnetic field. We also showed that this feature leads to different coupling strength, denoted g_{qb}, g_a, between the qubit, ancilla and the fundamental mode of the resonator. However, this picture is correct if the spatial extension of the SQUID is small compared to the wavelength of the resonance frequency. Indeed we supposed so far that the electromagnetic field is homogeneous all along the SQUID. But we know that, due to boundary conditions of the quarterwave resonator, the current and voltage distribution vary with a cosine dependence, (see Eq. (1.83)). We can then imagine a situation where the two Josephson junctions of the SQUID are coupled to a different electromagnetic field. In this case an electric field can excite the ancilla and a magnetic field can excite the qubit. To avoid such situation, the spatial extension of the SQUID should be small compared to the wavelength of the resonance frequency, $l_{SQUID} \ll \lambda_{resonator} = 4 l_{resonator}$. For this reason we designed inter-digital capacitances with narrow and deep fingers which allows to reach large capacitance with short arms length[1].

[1] This solution leads to an intense electric field between fingers. If spurious elements are in between the arms of the capacitor, a coupling can occur between them. To minimise this coupling we can dilute the electric field. One example can be found in [97] where there are almost no fingers in the inter-digital capacitors.

The loop inductance of the SQUID has to be very large (tens of nano-Henry). We tried two different implementations to reach such large inductance. The first one was realise by a very thin and long wire between the two junctions. Indeed when the width of the wire is thin enough, the kinetic inductance due to Cooper-pairs becomes important[98,99]. Nevertheless the length requires to reach few tens of nano-henry makes necessary to have very long distance between the two junctions (typically for a wire width of 0.1 µm and a length of 400 µm we obtain a kinetic inductance[2] of about 15 nH). As we explained before, it is preferable in our circuit to have a compact SQUID. We so prefer the second design where a Josephson junction chain produces a super-inductor. We can obtain about 10 nH in only 15 µm. The plasma frequency of the junctions chain has to be much higher than the plasma frequency of the logical and ancilla qubit junctions in order to avoid resonant coupling.

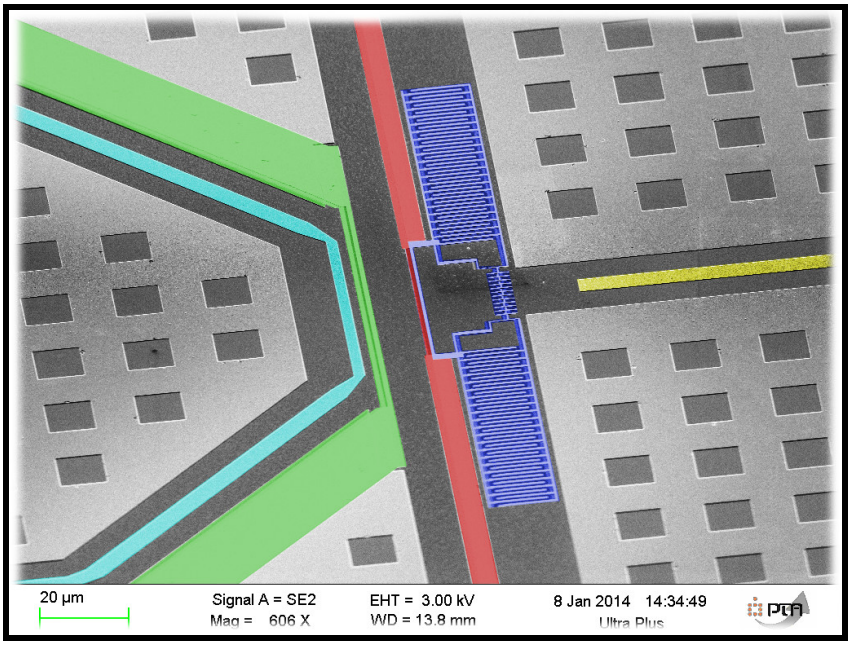

Figure (3.2): SEM image of the SQUID used to implement the logical and ancilla qubits. A part of the central line of the resonator is visible and coloured in red. The flux DC line is depicted in cyan and the microwave excitation line is in yellow. The SQUID is coloured in blue. The inter-digital capacitances are fabricated parallel to the junctions. The SQUID is galvanically coupled to the microwave resonator. A chain of junctions is used as a super-inductor. A big capacitor is coloured in green. This capacitor has been designed to avoid a screening effect between the flux bias line and the SQUID. The screening effect is discussed in more details in Section 3.2.3.

[2]This value has been obtained by measuring the DC resistance of the wire with a probe station. Florent Lecocq derived in his thesis[53] that $L_K = \mu_0 \lambda_L^2 \xi_0 R_N / k$ with λ_L the London penetration depth, ξ_0 the coherence length on the clean limit, R_N the resistance in the normal state and, $k = \rho l^*$ a constant of material which is the product of ρ the conductance and l^* the mean free path. Experimentally, we use the rule $L_K/R_N = 1.1\,\mathrm{nH{\cdot}k\Omega^{-1}}$ which has been derived by Florent Lecocq for aluminium.

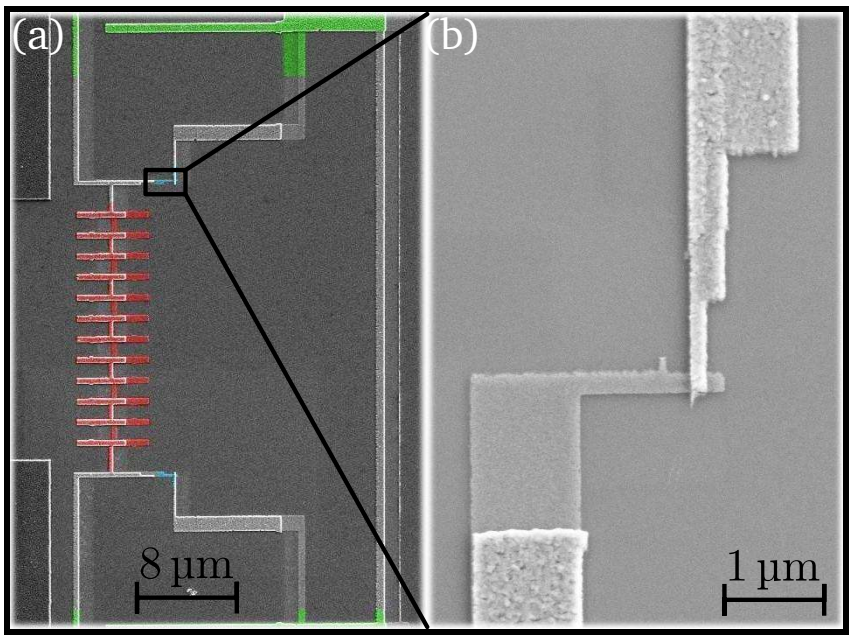

Figure (3.3): (a) SEM image of a the SQUID used to implement the logical and ancilla qubits. This picture is a zoom in the central part of the SQUID shown in Fig. 3.2. The superinductor is coloured in red, the two Josephson junctions in cyan, and the inter-digital capacitance in green. (b) SEM image of one Josephson junction of the SQUID. The junction corresponds to the square shape overlap between the two metallic layers at the center of the picture.

Figure 3.2 presents the SQUID fabricated to implement the logical and the ancilla qubit. The total length of the device is of 215 µm with $2 \times 87.5\,\mu$m for the inter-digital capacitors. The loop area is about $468\,\mu\text{m}^2$.

The fingers of the inter-digital capacitors have a length and width of $12.2 \times 0.6\mu\text{m}^2$ and are separated by a constant gap of 0.8 µm. It is possible to estimate the capacitance of such structure with a textbook formula[50]:

$$C = (\epsilon_r + 1)\,\ell\,[(N-3)A_1 + A_2] \;\; (\text{pF}) \tag{3.2}$$

with:

$$A_1 = 4.409 \tanh\left[0.55\left(\frac{h}{W}\right)^{0.45}\right] \times 10^{-6} \;\; \left(\text{pF}\cdot\mu\text{m}^{-1}\right), \tag{3.3}$$

$$A_2 = 9.92 \;\; \tanh\left[0.52\left(\frac{h}{W}\right)^{0.5}\right] \times 10^{-6} \;\; \left(\text{pF}\cdot\mu\text{m}^{-1}\right), \tag{3.4}$$

where ϵ_r is the relative permittivity, ℓ the width of the inter-digital capacitor, N the number of fingers, h the height of the substrate, and W the width of the metal strip. Equation (3.2) gives a capacitance of 53 fF. Capacitance extracted from data presented in Chapter 5 is around 40 fF, which is consistent with the design value.

The Josephson junctions are shown in Fig. 3.3, their size is $125 \times 125\,\mathrm{nm}^2$. Their self capacitance is estimated through a simple model of a parallel plate capacitance $C = \epsilon A/d$ with $\epsilon = \epsilon_0 \epsilon_\mathrm{r}$ the permittivity ($\epsilon_\mathrm{r}^{\mathrm{Al_2O_3}} \approx 10.5$), A the area of the junction, and d the thickness of the insulating layer (between 1 and 3 nm). We obtain a self capacitance between 0.5 fF to 1.5 fF[3]. The critical current depends exponentially of the thickness of the insulated layer and its value is adjusted empirically by successive fabrications. The fitted critical current from experimental data discussed in Chapter 5 is $I_\mathrm{c} = 8.1\,\mathrm{nA}$.

The superinductor is shown in Fig. 3.3. It is composed of twelve identical Josephson junctions of area $0.3 \times 1.2\,\mu\mathrm{m}^2$. The estimated capacitance is between 10 and 35 fF. Since they are fabricated in the same step as the Josephson junction, they have the same insulate layer thickness. Thus if we note $\alpha = A_\mathrm{JJ}^\mathrm{chain}/A_\mathrm{JJ}^\mathrm{qubits} = 22.4$, the area ratio between the Josephson junction of the chain and of the SQUID, we have $I_\mathrm{c}^\mathrm{chain} = \alpha I_\mathrm{c}^\mathrm{qubits} = 180\,\mathrm{nA}$. Test junctions gives, at room temperature, a tunnel resistance ratio of 25, close to the area ratio. The inductance of the chain is then given by $L_\mathrm{chain}^\mathrm{tot} = N L_\mathrm{JJ}^\mathrm{chain} = N\phi_0/(2\pi I_\mathrm{c}^\mathrm{chain})$ with $N = 12$ in our samples. We obtain therefore $L_\mathrm{chain}^\mathrm{tot} = 22\,\mathrm{nH}$. In Chapter 5, we extract from data a loop inductance of 7.5 nH. The resonance frequency of the Josephson junctions of the chain is estimated to be higher than 25 GHz so, much higher than the typical microwave signal frequencies in our experiments.

The tunable resonator

The fast qubit readout protocol presented in the first section requires to have the ancilla qubit in resonance with the microwave resonator. Nevertheless the optimal point for the logical and the ancilla qubit is at $\phi_\mathrm{b} = 0$. It is then highly preferable to set the magnetic flux in the SQUID and keep the logical and ancilla qubit at zero flux.

To reach resonant conditions between the resonator and the ancilla qubit we add a SQUID within the central conductor of the microwave resonator to make the resonance frequency tunable. Indeed in the simple case of a SQUID composed of identical Josephson junction without loop inductance, the SQUID acts like a single Josephson junction with a flux tunable critical current:

$$I_{\mathrm{c_{SQUID}}} = 2I_{\mathrm{c_{JJ}}} \left| \cos\left(\pi \frac{\phi_\mathrm{b}}{\phi_0}\right) \right| \tag{3.5}$$

where $I_{\mathrm{c_{JJ}}}$ is the critical current of a single Josephson junction. When the resonance frequency of the SQUID, ω_SQUID, is much higher than the resonance frequency of the microwave resonator, ω_r, we can consider the SQUID as an inductor[4]:

$$L_\mathrm{SQUID} = \frac{\phi_0}{2\pi} \frac{1}{2I_{\mathrm{c_{JJ}}}} \frac{1}{\left| \cos\left(\pi \frac{\phi_\mathrm{b}}{\phi_0}\right) \right|}. \tag{3.6}$$

[3] An empirical rule frequently used consists in assuming a capacitance per area unit of $50\,\mathrm{fF{\cdot}\mu m^{-2}}$. By using this rule we get a capacitance of 0.8 fF which is in consistent with value calculated from parallel plate capacitor model.

[4] Another way to understand this assumption it to consider the Josephson junction as a capacitor in parallel with an inductor. The resonance occurs when $Z_\mathrm{capacitor} = Z_\mathrm{inductor}$. Far below the resonance frequency $Z_\mathrm{capacitor} \gg Z_\mathrm{inductor}$ so, only the inductor has to be take into account.

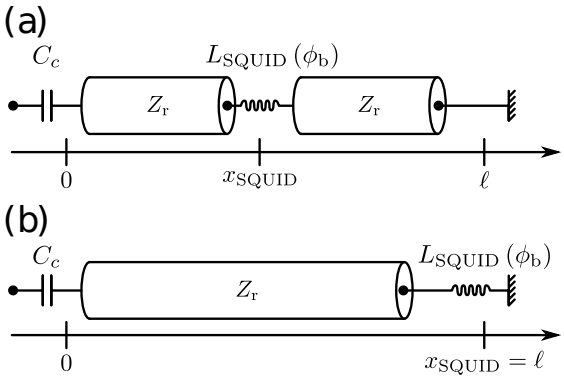

Figure (3.4): Sketch of a tunable inductor embedded in a distributed microwave resonator in two different cases. (a) The SQUID can be positioned all along the resonator ($x_{SQUID} \in [0;\ell]$). At these positions current and voltage distributions are modified by the presence of the SQUID. (b) The SQUID is positioned at the grounded end of the resonator ($x_{SQUID} = \ell$). At this specific position, the current is maximum.

Figure 3.4 shows an equivalent electrical circuit of a tunable inductance embedded in a distributed microwave resonator. In the general case sketched in sub-figure (a), calculating the frequency shift caused by the SQUID requires the solution of a transcendental equation, which can be done numerically. Indeed the current and voltage distributions along the resonator are strongly non-uniform. When a perturbation, like our tunable inductance, occurs somewhere along the resonator, it is the whole field distribution which is modified. In contrast when the SQUID is positioned at the end of the resonator, sub-figure (b), the perturbation modified one boundary condition. This configuration simplifies the analytical derivation. Hereafter we present the derivation of this simple case which, even if it does not correspond to the reality of our sample, gives a physical understanding of the resonator tunability. The input impedance of the circuit shown in Fig. 3.4 (b) is:

$$Z_{\mathrm{tot}} = \mathrm{i}\left(\frac{\omega L_{\mathrm{SQUID}} + Z_{\mathrm{r}}\tan(\beta\ell)}{-\omega L_{\mathrm{SQUID}}\tan(\beta\ell) + Z_{\mathrm{r}}} Z_{\mathrm{r}} - \frac{1}{C_{\mathrm{c}}\omega}\right). \tag{3.7}$$

Considering that the perturbation caused by the SQUID to the resonator is small, we can approximate that, close to the resonance frequency of the resonator, $\tan(\beta\ell) \approx (2\omega_{\mathrm{r}})/(\pi\Delta\omega_{\mathrm{r}})$. The total impedance is then:

$$Z_{\mathrm{tot}} = i\left(Z_{\mathrm{r}}\frac{\omega L_{\mathrm{SQUID}} - \frac{2}{\pi}\frac{\omega_{\mathrm{r}}}{\Delta\omega_{\mathrm{r}}}Z_{\mathrm{r}}}{Z_{\mathrm{r}} + \frac{2}{\pi}\frac{\omega_{\mathrm{r}}}{\Delta\omega_{\mathrm{r}}}L_{\mathrm{SQUID}}\omega} - \frac{1}{C_{\mathrm{c}}\omega}\right). \tag{3.8}$$

The resonance occurs when $\Im\mathrm{m}(Z_{\mathrm{tot}}) = 0$. Assuming that $L_{\mathrm{SQUID}}C_{\mathrm{c}}\omega_0^2 \ll 1$, we get:

$$\omega_0 = \frac{\omega_{\mathrm{r}}}{1 + \frac{C_{\mathrm{c}}}{\ell C_\ell} + \frac{L_{\mathrm{SQUID}}}{\ell L_\ell}} \tag{3.9}$$

where C_ℓ and L_ℓ are the capacitance and inductance per unit length of the microwave resonator.

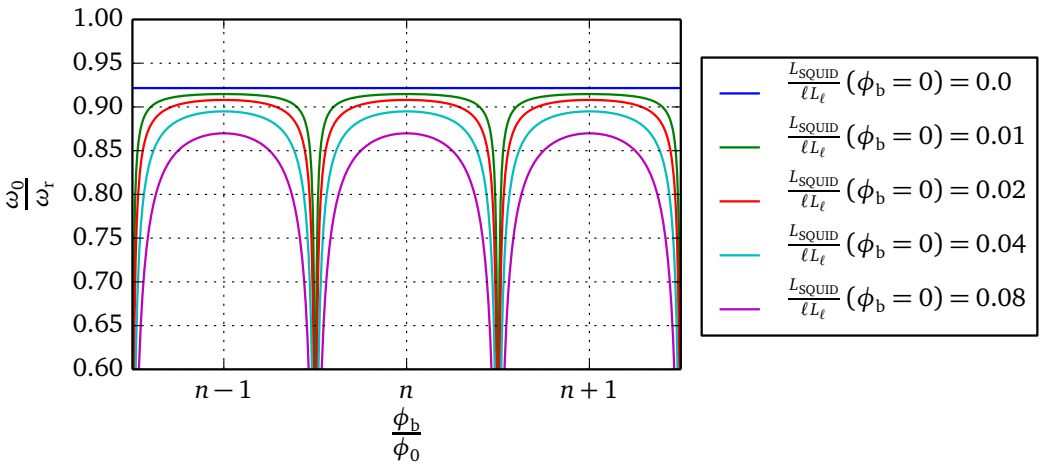

Figure (3.5): Shift in frequency of a quarter-wave tunable resonator due to a SQUID located at the short circuit (see Fig. 3.4 (b)). The different curves correspond to different $L_{SQUID}/(\ell L_\ell)$ ratios.

Figure 3.5 shows the dependence of the microwave resonator frequency as a function of the magnetic flux. The different curves correspond to different $L_{\text{SQUID}}/(\ell L_\ell)$ ratios. For $L_{\text{SQUID}}/(\ell L_\ell) = 0$ we obtain a flat curve which shows the frequency shift only due to the coupling capacitance C_c. Since the capacitance is flux–independent, we obtain a flat curve. For other $L_{\text{SQUID}}/(\ell L_\ell)$ ratio, we see a dependence of the resonance frequency with respect to the flux. For small $L_{\text{SQUID}}/(\ell L_\ell)$ ratio, the curves show a strong dependence on the magnetic flux whereas for higher ratio the curves become smoother. At half a quantum of flux, the inductance tends to be infinite so the resonance frequency drops to zero. Around these points, the flux dependence of the resonance frequency is too large and experimentally the resonance will be dominated by flux noise. Thus it is preferable to have smooth dependence since that allows a larger tunability without being affected by flux noise. For this, the SQUID inductance should be at least 10 % of the resonator inductance.

Beyond the physical understanding given by the analytical formula in Eq. (3.9), numerical calculation describes the effect of the SQUID position along the microwave resonator. Figure 3.6 shows the resonance frequency of the resonator as function of magnetic field for different SQUID positions. The case where the SQUID is positioned at the short circuit ($x_{\text{SQUID}} = \ell$) corresponds to the case analytically solved previously. The other curve show how the flux dependence is modified as function of the SQUID position. When the SQUID position tends to 0 (which corresponds to the open circuit position), the flux dependence becomes smaller. This effect can be understood by considering the current distribution along the resonator. The current is maximum as $x_{\text{SQUID}} = \ell$ and minimum at $x_{\text{SQUID}} = 0$ with a cosine dependence between these two extrema (see Eq. (1.83)). Thus the current amplitude through the inductance depends on the SQUID position. When there is no current, the SQUID has no effect. In contrast when the current through the inductor is maximum, the resonance

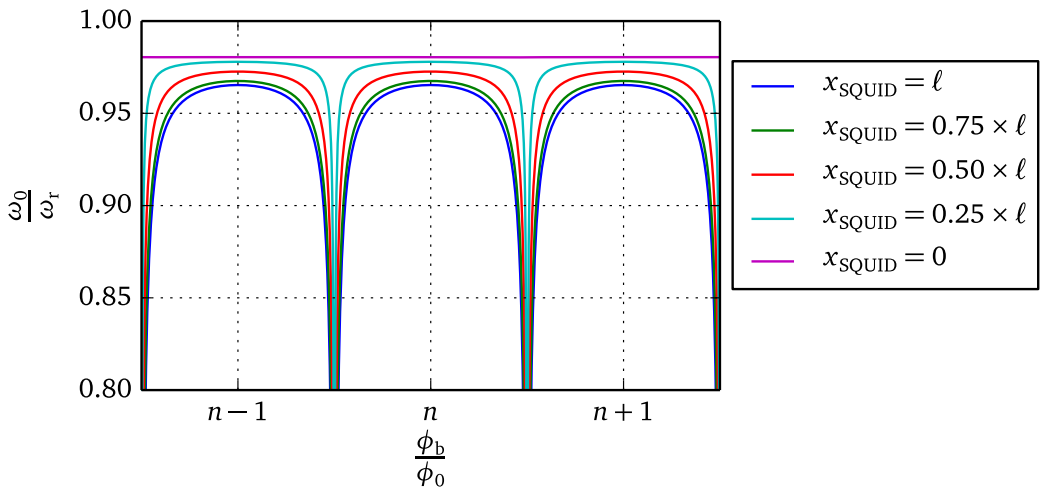

Figure (3.6): Shift in frequency of a quarter-wave tunable resonator as a function of magnetic flux. We took $L_{SQUID}/(\ell L_\ell) = 0.08$ for calculation. The different curves correspond to different position of the SQUID in respect to the resonator ($x_{SQUID} = 0$ means a SQUID at the position of the open circuit whereas $x_{SQUID} = \ell$ means a SQUID at the short circuit).

shift due to the inductor will also be maximum. The effect of the tunable inductance depends on the SQUID position.

Figure 3.7 shows the fabrication of a SQUID within the central line of the resonator. The two Josephson junctions are identical with an area of $2 \times 3.4\,\mu\text{m}^2$. Their self-capacitance is about 340 fF and from measurement of identical test junctions we estimate a critical current of about 550 nA. Thus the resonance of such a SQUID should occur at a frequency higher than 11.0 GHz. The loop area of the SQUID is about $515\,\mu\text{m}^2$ which is slightly larger than the loop of the logical and ancilla qubit device.

Coupling between the resonator and the feedline

The resonator is capacitively coupled to the feedline. Figure 3.8 shows that the implementation of the coupling has been realised by using the so-called "elbow" geometry. The feedline width is 150 µm with a gap of 83 µm and a thickness of 100 nm which ensure a characteristic impedance of 50 Ω. The ground plane in between the feedline and the resonator is 5 µm wide. In the "elbow" geometry only the length of the resonator which is parallel to the feedline produces a coupling. This feature gives a powerful and easy way to calibrate the coupling with the design. The design has been realised in order to be in the limit where the length of the resonator which is effectively coupled to the feedline is small compared to the wavelength of a resonant signal. In this limit, we can model the coupling as a discrete element, here a capacitance. In our sample the length which produces a coupling is about 600 µm which is far below the total length of the resonator, about 3 mm and so is far below the wavelength of the resonant signal which is about 4×3 mm. The complete model of the resonator coupled

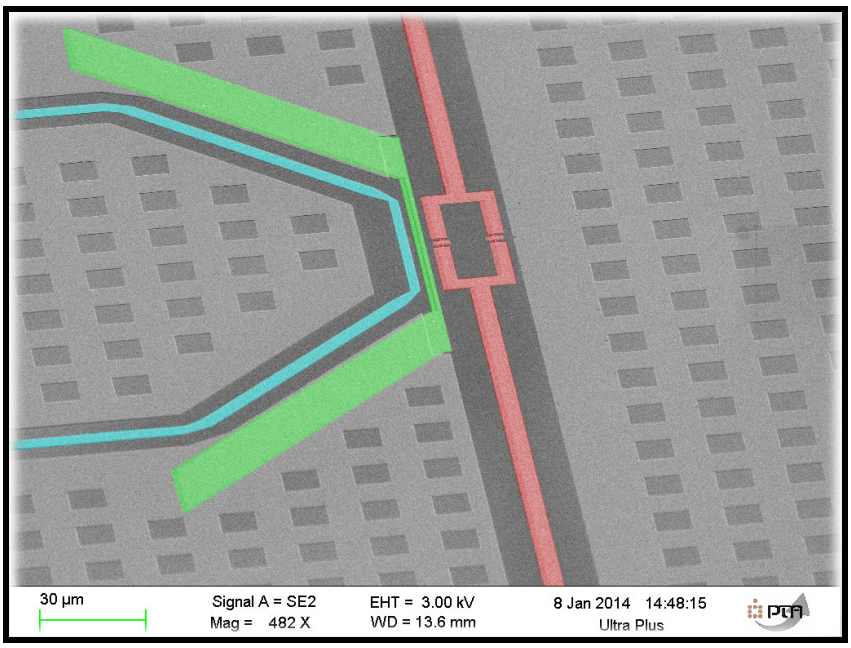

Figure (3.7): SEM image of a the SQUID used to make the resonator tunable. A part of the central line of the resonator is visible and coloured in red. A flux DC line is depicted in cyan. A big capacitance is coloured in green. This capacitance has been designed to avoid a screening effect between the flux bias line and the SQUID. The screening effect is discussed in more details in Section 3.2.3.

to the feedline is described in Appendix B. By using this model we are able to extract the equivalent capacitance which is about 7 fF.

3.2.2 Fabrication of the different patterns

The Qubit samples have been fabricated by Bruno Küng in the PTA and Nanofab facilities. The fabrication consists of three steps. The first one is the fabrication of alignment crosses on the wafer. The second one is the realisation of coarse patterns like the feedline and the DC flux bias lines. The last one is the fabrication of the Josephson junctions, of the central line of the microwave resonator, and of the flux bias line capacitances.

Alignment crosses

Table 3.1 presents the recipe to realise the alignment crosses. The exposure, the development, the gold evaporation and the lift-off have to be done without waiting time. Indeed the resist "UV5" is not stable after exposure. Manufactor datasheet gives no guarantee after 2 hours. To keep a good contrast in the mask, it is preferable to be far below this duration.

[5]We have used Nanofab or PTA facilities without distinction

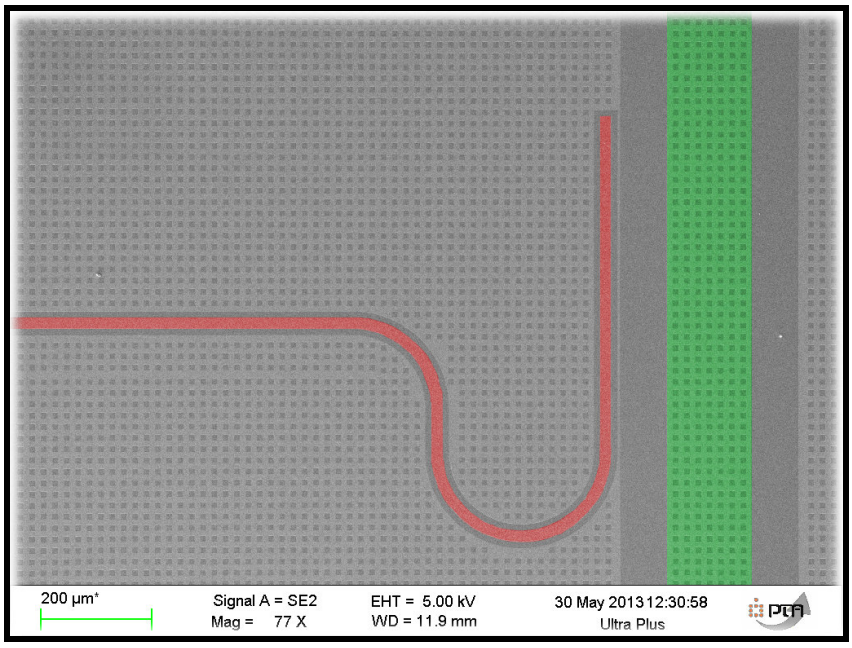

Figure (3.8): SEM image of resonator capacitively coupled to a feedline.

Step	Description	Equipment used	Precision
1	UV5 resist deposition	Spinner	1 min at 4000 rpm
2	Baking	Hotplate	1.5 min at 130 °C
3	E-beam lithography	JEOL JBX-6300 FS	Acceleration voltage: 100 kV Aperture: 5 (60 µm) Beam current: 5 nA Dose: 70 µC·cm^{-2}
4	Postbake	Hotplate	1 min at 130 °C
5	Development	AZ326MIF	Duration 50 s Rinse in DIW N_2 blow dry
6	Au evaporation	Plassys MEB 550S[5]	5 nm Ti and 80 nm Au
7	Lift-off	Acetone	Duration 60 min Rinse in IPA N_2 blow dry

Table (3.1): Recipe for the alignment crosses in gold.

Coarse patterns

Step	Description	Equipment used	Precision
1	Native oxide removal	1 % HF	Duration 2 min Rinse in DIW N_2 blow dry
2	Al deposition	Plassys MEB 550S	100 nm at 1 nm·s^{-1}
3	UV5 resist coating	Spinner	1 min at 4000 rpm
4	Baking	Hotplate	1.5 min at 130 °C
5	E-beam lithography	JEOL JBK-6300 FS	Acceleration voltage: 100 kV Aperture: 5 (60 µm) Beam current: 5 nA Dose: 40 µC·cm^{-2}
6	Postbake	Hotplate	1 min at 130 °C
7	Development and etching	AZ326MIF	Duration 50 s Rinse in DIW N_2 blow dry
8	Lift-off	Acetone	Duration 60 min Rinse in IPA N_2 blow dry

Table (3.2): Recipe for the feedline, flux traps, microwave resonator cavities and DC flux bias lines.

Table 3.2 presents the recipe to realise the coarse patterns of the Qubit sample. We use silicon wafers[6] of 2 inches diameter. The wafers are undoped and show a resistivity higher than 10 000 Ω·cm. They are 280 µm thick and since they have been in contact with air, a thin layer of silicon oxide is formed at the surface.

The first step is to remove the native oxide of the wafer with hydrofluoric acid. G. Mende *et al.* have shown[100] that silicon oxide grows at a rate of 0.02 nm·min^{-1} on ⟨100⟩ oriented silicon wafer in air at room temperature. They also confirmed the observation of S. I. Raider *et al.* who showed[101] that the equilibrium oxide thickness is between 1.1 nm to 1.4 nm. Thus to avoid formation of silicon oxide the wafer is placed in a evaporator for aluminium deposition as fast as possible (typically less than 5 min). The total aluminium deposited thickness is 100 nm. The development of the resist and the etching of the aluminium are done in one step because of the UV5 resist . The duration given in the recipe is 50 s but in order to decide when to stop the etching a visual control is preferable than a strict respect of the instructions.

Figure 3.9 presents two SEM pictures of the sample after the fabrication of the large patterns. In Fig. 3.9 (a), the feedline is visible at the extreme left. The cavity which will contain the central conductor of the resonator is the central structure with a crook shape.

[6] BT electronics: WAFERS SILICIUM FZ DIAMETRE 2".

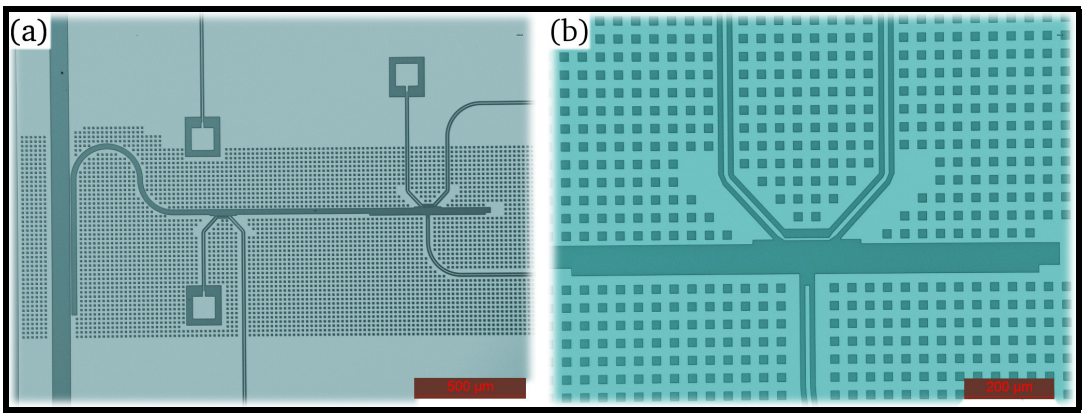

Figure (3.9): (a) Global optical image of one sample after the fabrication of the coarse patterns. The feedline is the vertical line at the left of the picture. Three DC flux bias lines are visible on the picture as well as the microwave excitation line for the logical qubit. A cavity which will contain the microwave resonator is at the center of the picture. (b) Zoom in the place where the qubit will be fabricated. The line coming from the top will be used as a bias flux line. Coming from the bottom, the line will be used as an excitation line for the logical qubit.

The DC flux bias lines and the excitation lines are also fabricated here. A lot of holes inserted inside the ground plane surround the resonator cavity. These holes are made to trap spurious magnetic flux and therefore to avoid flux jumps. Indeed the resonance frequency of the resonator depends on the magnetic flux applied to the SQUID. It is crucial for our experiment to have stable magnetic environment. Figure 3.9 (b) presents a zoom in the future position of the Josephson quantum circuit which will realise the logical and ancilla qubits. We note that the top ground of the future quarterwave resonator is interrupted at the position where the flux bias line is close to the resonator cavity. This has been made in order to avoid circulating current around the resonator cavity. A more detailed explanation is writtend in the next section where the fabrication of the junction is done.

Josephson junctions and small patterns

The process to fabricate Josephson Junctions and small patterns is displayed in Table 3.3. The characteristic of a Josephson Junction are given by two parameters, the intrinsic capacitance of the junction and its critical current. The capacitance scales as the ratio A/d where A is the area of the capacitor plate and d the thickness of the barrier. The critical current is related to the tunnel effect and depends exponentially on the barrier thickness d. The key parameter during the Josephson junction fabrication is then the control of the insulate layer. The barrier is typically made by oxidising the aluminium. Moreover the quality of the junction strongly depends on the quality of the oxide as well as the quality of the metal–oxide interface.

Step	Description	Equipment used	Precision
1	Resist coating	92 % ARP 617-08 P(MMA-MAA) 2:1 8 % in ethyl lactate	45 s at 2000 rpm
2	Baking	Hotplate	10 min at 200 °C
3	Resist coating	96 % ARP 679-04 (PMMA 950 k) 4 % in ethyl lactate	50 s at 6000 rpm
4	Baking	Hotplate	4 min at 180 °C
5	E-beam lithography	JEOL JBK-6300 FS	Acceleration voltage: 100 kV Aperture: 4 (25 μm) Beam current: 1 nA Undercut dose: 400 μC·cm^{-2} Opening dose: 1050 μC·cm^{-2}
6	Development	1:3 MIBK:IPA	Duration 30 s Rinse in IPA 35 s N_2 blow dry
7	Cleaning	ICP Oxford plasmalab 100	Process: BKNettoyageO2 Pressure 40 mtorr Duration 20 s Power 30 W
8	Al deposition	Plassys MEB 550S	19 nm at 0.1 nm·s^{-1} and −45° Oxidation 5 min at 3.3 torr 50 nm at 0.1 nm·s^{-1} and 45°
9	Lift-off	Shipley Remover 1165	Temperature 80 °C Ultrasonic bath (pulses mode) Rinse in DIW N_2 blow dry

Table (3.3): Recipe for the SQUIDs and the microwave resonators.

Our fabrication technique involves a vacuum chamber in which metal is deposited by evaporation. We pump during a whole night the vacuum chamber in order to remove as much as possible residual gas. At the beginning of the process, a crucible containing solid pieces of aluminium is placed vertically below the wafer (at 30 cm of distance). The wafer is tilted in respect to this vertical line to realise an evaporation at oblique angle. At this point of the process, the wafer is isolated from the crucible with a metal plate to avoid aluminium deposition during the calibration of the deposition rate. The aluminium is heated by using an electron beam. The electrons are produced by thermionic emission from a tungsten filament. They are accelerated by a cathode and deflected with a magnetic field. A permanent magnet give the main path for the electrons and two small coils allow precise displacement of the electron beam to only heat aluminium inside the crucible. Due to the electron beam aluminium evaporates from the crucible in a cone of evaporation. Due to very low pressure the evaporated atoms of aluminium propagate in straight lines[7]. A quartz crystal microbalance gives the rate of the deposition of the evaporated aluminium. Once the deposition rate reaches the target value, the metal plate isolating the wafer from the evaporation cone is removed. In order to obtain high film quality, it is better to have high rate of deposition since this minimises the relative rate of spurious impurity inclusion. However the deposition rate has to be keeped under a certain threshold to avoid unstable deposition rate. A feedback allows to keep the same rate of evaporation during all the deposition process. When the desired thickness is reached, the metal plate is put back and the electron beam is stopped. The vacuum pumping is stopped by closing a valve between the pump and the chamber. The oxidation of the aluminium is realised by opening a micro-valve between the deposition chamber and an oxygen bottle. Once the pressure inside the chamber reaches the target value, the micro-valve is closed and the oxidation continues during 5 minutes. When the oxidation time is finished, the valve between the vacuum chamber is reopened to relaunch the pumping. The pressure decreases rapidly to less than 1×10^{-6} mbar. A second layer of aluminium is deposited with the same process but with a different angle between the wafer and the vertical line and a different thickness.

The Josephson Junctions are fabricated by using two different techniques, the "Dolan bridge technique"[106] for small junctions (125×125 nm^2 for the logical and ancilla qubits) and the "Control undercut technique"[107] for larger one (from 0.3×1.2 μm^2 for the Josephson junction chain to 2×3.4 μm^2 for the SQUID making the microwave resonator tunable).

The Dolan bridge technique is used in a perpendicular configuration to obtain small area junctions, 100×100 nm^2. Indeed 100×100 nm^2 is the limit of feasibility of the Controlled

[7] An estimation of the mean free path can be obtained by using the formula[102,103]:

$$l = \frac{k_B T}{\sqrt{2}\pi d^2 P} \tag{3.10}$$

where k_B is the Boltzmann constant, T is the temperature, P is pressure, and d is the diameter of the gas particles. The boiling point of aluminium is about 2750 K at standard pressure and drop to[104] 1100 K at the vacuum chamber pressure $P = 2 \times 10^{-7}$ mbar. Atoms diameter are about[105] 125 pF. The estimated mean free path is about $l = 11\,000$ m, much longer than the distance between the crucible and the wafer which is about 30 cm. More realistic calculations take into account the fact that the evaporated particle diameters are not well defined. Nevertheless the results obtained from these models give a mean free path of several hundred of meters.

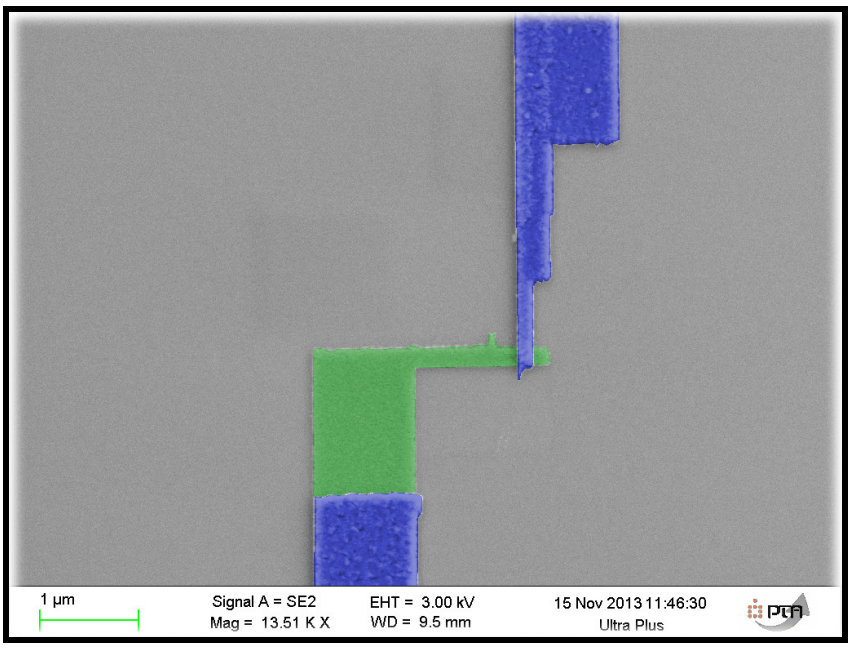

Figure (3.10): SEM image of a Josephson junction fabricated with the Dolan bridge technique. The Junction, in parallel with another one, is used to implement the qubit and ancilla two levels system. The first and second angle evaporation are coloured in green and blue, respectively.

Undercut Technique. Moreover in the perpendicular configuration, the area of the Jospehson junction is very well controlled. Figure 3.10 shows such junction. The first and second angle evaporation are coloured in green and blue, respectively. The junction is then delimited by the square defined by the overlapping of the two junctions.

The Controlled Undercut Technique has been developed by Florent Lecocq during his Ph.D thesis at the Neel institute. The technique has the big advantage to give a more robust resist mask. Moreover we have a direct access to the wafer underneath the junction. It is then easier to clean the wafer with an oxygen plasma before the metal deposition. The cleaning step is crucial to obtain good quality Josephson junction. Figure 3.11 shows junctions fabricated with such technique. Finally, it is simple to combine the “Controlled undercut technique” with other angle evaporation technique on the same design.

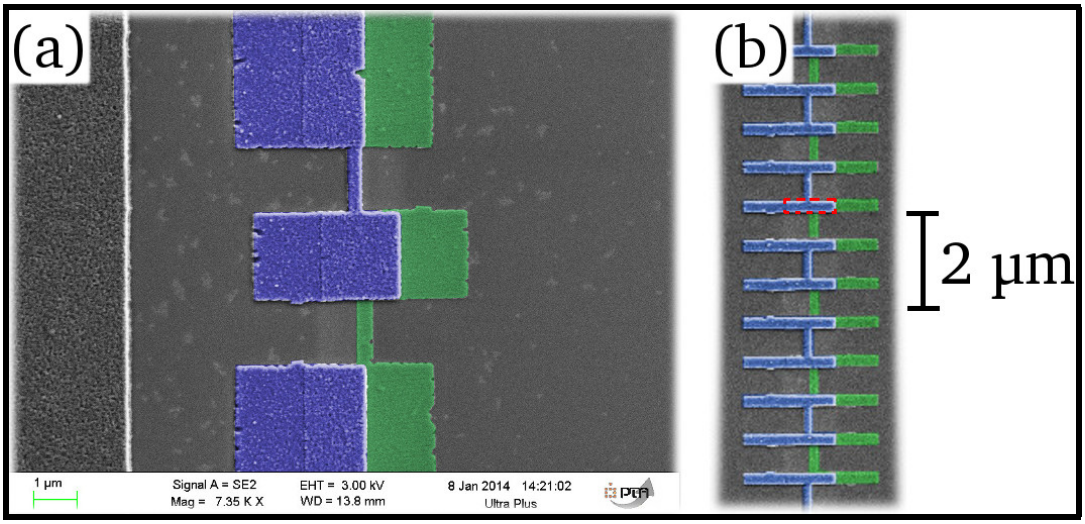

Figure (3.11): SEM picture of the Josephson junction fabricated with the controlled undercut technique. The first and second angle evaporation are coloured in green and blue, respectively. (a) The junction shown, which is in parallel with another one (not shown), form a SQUID making the resonator tunable with magnetic field. The Josephson junction occurs at the overlap between the two evaporations at the center of the picture ($2 \times 3.4\ \mu m^2$). (b) The chain consist of Josephson junctions of are: $0.3 \times 1.2\ \mu m^2$. The junctions are formed by the overlap of the two evaporations. It is difficult to see, we so have enhance the position of one of the junction by a dashed red line.

3.2.3 A fight against the screening effect

The sample has two differents SQUID. One of them is used to make the resonator tunable while the other is the qubit circuit. Both have their own flux bias line in order to be tuned independently. Figures 3.2 and 3.7 show the two SQUIDs and their flux bias line. On the two pictures we also see a big capacitance coloured in light green. The capacitances have been implemented to avoid superconductor screening between the flux bias line and the SQUID's.

Indeed in the initial chip design the ground plane around the resonator and the two SQUIDs was closed. A hole surrounded by a superconductor was then formed. When a magnetic field is applied to a superconductor, direct screening current appears at the border of the superconductor due to the Meissner effect. The flux is quantised through each closed path in the superconductor and therefore through the hole. In this first experiment we were only able to cover 7 % to 8 % of one flux period of the SQUID. The surface area of the SQUID loop is about 515 μm^2 which gives a field amplitude of 0.3 µT inside the SQUID loop so, a mutual inductance of $M_{\text{DC line}\rightarrow\text{SQUID}} = 26.5\,\phi_0\cdot\text{mA}^{-1}$. This mutual inductance is far too low since the upper limit of current amplitude in our DC line is about 1 mA.

To reduce the screening effect, we changed our design from Fig. 3.12 (a) to Fig. 3.12 (b). The first aluminium layer is open between the cavity of the microwave resonator and the flux bias line (see Fig. 3.9 (b)). Next during the junction fabrication, a capacitor closes the cavity of the resonator. The thickness of native aluminium oxide is about[108] 4 nm which leads, with an area of 2000 μm^2 and a relative permittivity of 10.44, to a capacitance of 46 pF. The largest estimated kinetic inductance of the narrow wire separating the two plate capacitor is about 22.5 pH. If we simulate the circuit as two capacitors in series with an inductor, we obtain that at 10 GHz its impedance is about 1.4 Ω, much smaller than the characteristic impedance of the resonator which is about 72 Ω. Thus this big capacitance will act as short circuit for our microwave signal and as an open circuit for direct screening currents. We are able to cover one flux period with a current biased from −300 µA to 300 µA so, a mutual inductance of $M_{\text{DC line}\rightarrow\text{SQUID}} = 1.6\,\phi_0\cdot\text{mA}^{-1}$.

3.2.4 Test junctions

In order to estimate the junctions parameters, a batch of so-called "test junctions" are fabricated together with the sample. The test junctions have the same design as the junction in the experimental sample and are fabricated at the same time. Consequently the test junctions should have approximately the same circuit parameters, critical current and self-capacitance, as the junctions of our sample.

Figure 3.13 shows the design to fabricate the test sample. With a probe station, we measure the DC resistance of different circuits between the pad A and the other pads. ch-1 and ch-2 corresponds to the Josephson junction of the superinductor, qb-1 and qb-2 of the logical and ancilla qubits and sq-1 of the SQUID making the resonator tunable. We extract the junction resistance by subtracting the resistance of lines. All lines are equivalent and their resistance is measured with circuit "line". We note that to increase the signal-to-noise ratio of the SQUID Josephson resistance we put three junctions in series. We use the well-known

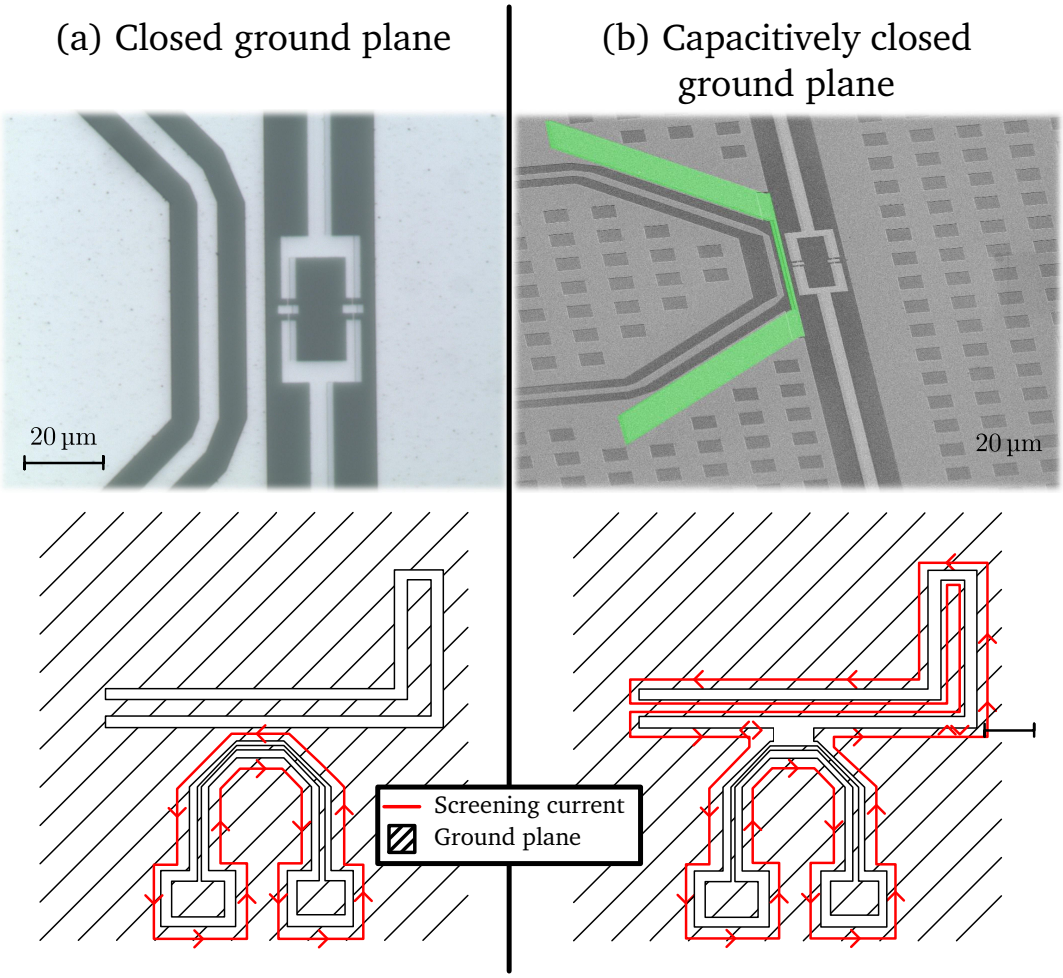

Figure (3.12): Circulation of the screening current with a closed ground plane (a) and with the capacitance (b). The top pictures have been obtained from optical microscope and SEM. They show the SQUID with its flux bias line. The two bottom sketches give an idea of the modification brought by the opening of the microwave cavity on the direct screening current.

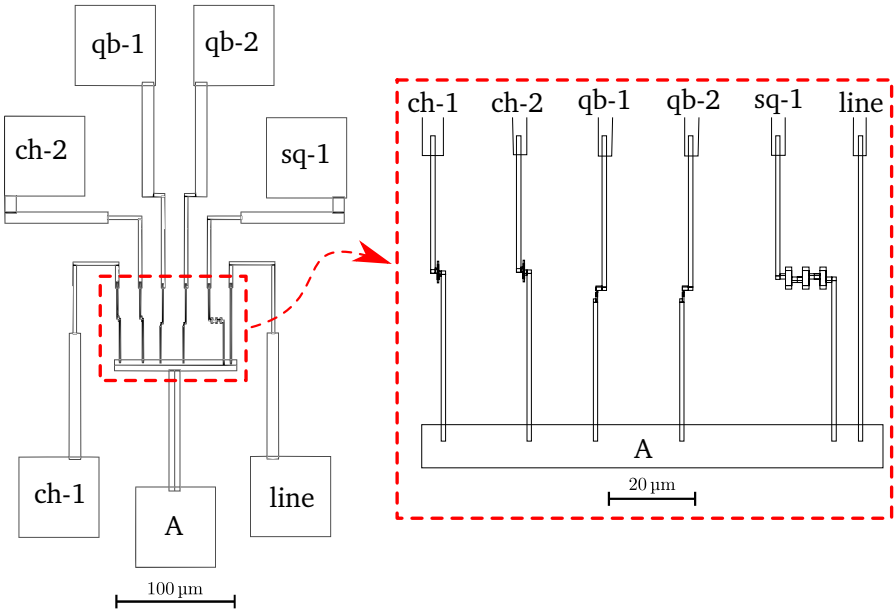

Figure (3.13): Design of the test junction chip. On the left, we show a sketch of the whole design of the test sample and on the right we make a zoom in the Josephson junctions area. Different paths allow to measure different Josephson junction resistances. From pads "ch-1,2" to pad "A", we measure the resistance of junctions of the superinductor. From pads "qb-1,2" to pad "A", we measure the resistance of junctions used to make the logical and ancilla qubits. From pad "sq-1" to pad "A", we measure the resistance of three junctions identical of SQUID junctions used to make the resonator tunable. Finally, from pad "line" to pad "A", we measure the resistance of the line. By design all measurement lines have the same length which allows to extract the resistance of Josephson junctions by simple subtraction.

Ambegaokar-Baratoff formula to calculate the critical current from the resistance[49]:

$$I_c R_n^{4K} = \frac{\pi\Delta}{2e} \tanh\left(\frac{\Delta}{2k_B T}\right) \overset{k_B T \ll \Delta}{\approx} \frac{\pi\Delta}{2e}, \tag{3.11}$$

where Δ is the superconducting gap and R_n^{4K} the normal state resistance of the tunnel junction at low temperature. The tunnel resistance measured at room temperature is smaller by 30 % to 50 % compared to the resistance at 4 K. We apply then a correction factor $R_n^{4K} = 1.4 R_n^{300K}$. The value of the critical currents measured with test junctions compared to critical currents extracted from data presented in Chapters 4 and 5 are between 2 and 5 times smaller.

3.3 Rhenium microwave resonators

One aspect on my thesis project was to realise superconducting microwave resonators in rhenium. Indeed the rhenium material can be deposited on a sapphire wafer by molecular beam epitaxy. The quality of the rhenium layer obtained as well as the interface between the sapphire and the rhenium is very high, (see Fig. 3.14 as an example of epitaxial layer of rhenium). Moreover the rhenium does not oxidise, leading to cleaner interfaces. A microwave resonator fabricated in such high quality metal layer should exhibit high internal quality factor. Hereafter we present the process implemented for the realisation of a quarter wave microwave resonators in epitaxial rhenium layer. We also give the design equation to fabricate microwave resonators with target physical parameters.

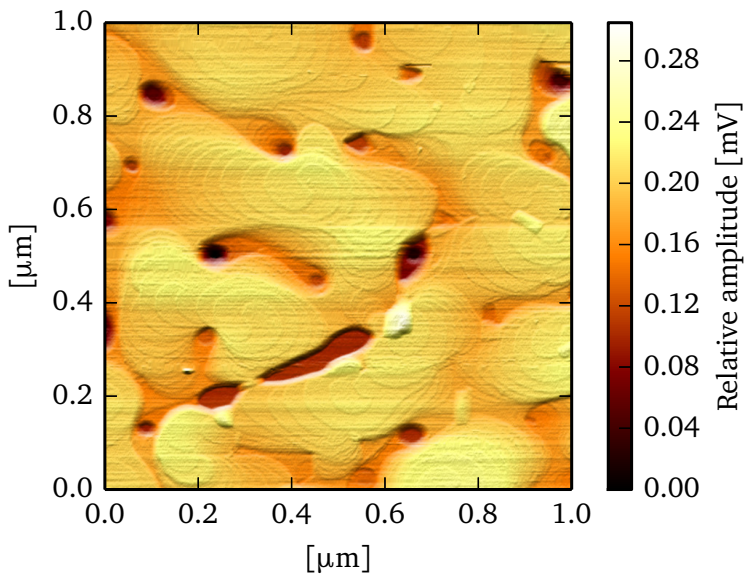

Figure (3.14): AFM picture in amplitude of a epitaxial layer of rhenium. We note the presence of large epitaxial areas visible through clear atomic steps. Some holes are visible but they represent a tiny percent of the total layer surface.

3.3.1 Epitaxy of rhenium

The epitaxy of the rhenium has been realised by Benjamin Delsol in the team of Bruno Gilles at the SIMaP "Laboratoire de Science et Ingénierie des Matériaux et Procédés". I was not personally involved in the fabrication of the epitaxial layer of rhenium. I propose a summary of the crucial steps to obtain a high quality sample.

Cleaning of the sapphire substrate

In order to achieve epitaxial deposition of rhenium, it is crucial to have the surface of the substrate as clean as possible. Indeed it is easy to understand that any defects at the surface will produce defects in the rhenium layer.

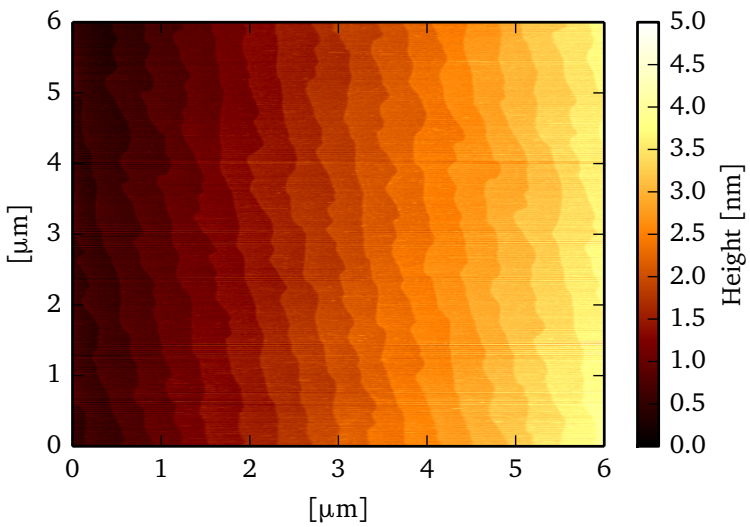

Figure (3.15): AFM picture in height of a sapphire substrate after cleaning and baking. The atomic steps are clearly visible.

The substrates for the epitaxy were covered by small beads of ≈ 50 nm of diameter. These objects are surely a residue of the wafer polishing process in which small beads of aluminium oxide are used as an abrasive. These residues can be removed with peroxysulfuric acid, or Caro's acid. In more detail the recipe is to plunge the wafer in the Caro's acid during 5 min. Next the wafer is rinsed in DIW, after in ethanol and finally dried with N_2. The substrate is baked at 1400 K during 1 h under controlled atmosphere composed of argon (80 %) and oxygen (20 %) in order to relax tensions. The result of the process is shown in Fig. 3.15. The atomic steps are clearly visible and no contaminations are visible.

Tungsten on the backside

In order to realise epitaxial growth of rhenium, it is crucial to ensure a good mobility of adatoms which are deposited on the substrate. The adatoms need to diffuse to reach their

position of least energy. The easiest way to reach such a condition is to bring energy to the adatoms by heating the substrate to about 1000 K. This is usually done by using a current–biased tungsten wire. By Joule effect, the wire emits thermal radiation. The substrate is placed close to the tungsten wire in order to be heated by the radiation. However, the sapphire is mostly transparent to the infrared and so, it is difficult to correctly heat the substrate by this way at the beginning of the growth (indeed once some rhenium layers are deposited on the substrate, they absorb thermal radiation and ensure a good mobility for adatoms).

To solve this problem, a layer of tungsten of 300 nm has been deposited by sputtering at the backside of the wafer. The deposition has been realised by Philippe David at the Neel institute. By thermal conduction the sapphire is then correctly and homogeneously heated. The tungsten has been chosen because of its high melting temperature 3422 °C.

Rhenium epitaxy

Different sample of epitaxial rhenium have been fabricated by B. Delsol. The conditions of the growth have been modified from sample to sample in order to find optimal parameters. Hereafter we restrict ourself to a simple description of the process[8].

The rhenium is grown under ultra high vacuum ($\approx 1 \times 10^{-10}$ mbar) to avoid pollution of the rhenium layers (see the deposition chamber in Fig. 3.16). At the typical deposition speed of 0.1 Å·s^{-1} , the growth of a sample takes several hours.

Once the growth is finished, the wafer is cut in several chips of roughly 7 × 5 mm. The fabrication of the microwave resonator is realised on such chips.

[8]The interested reader can find all the detail in the Thesis of B. Delsol[46]

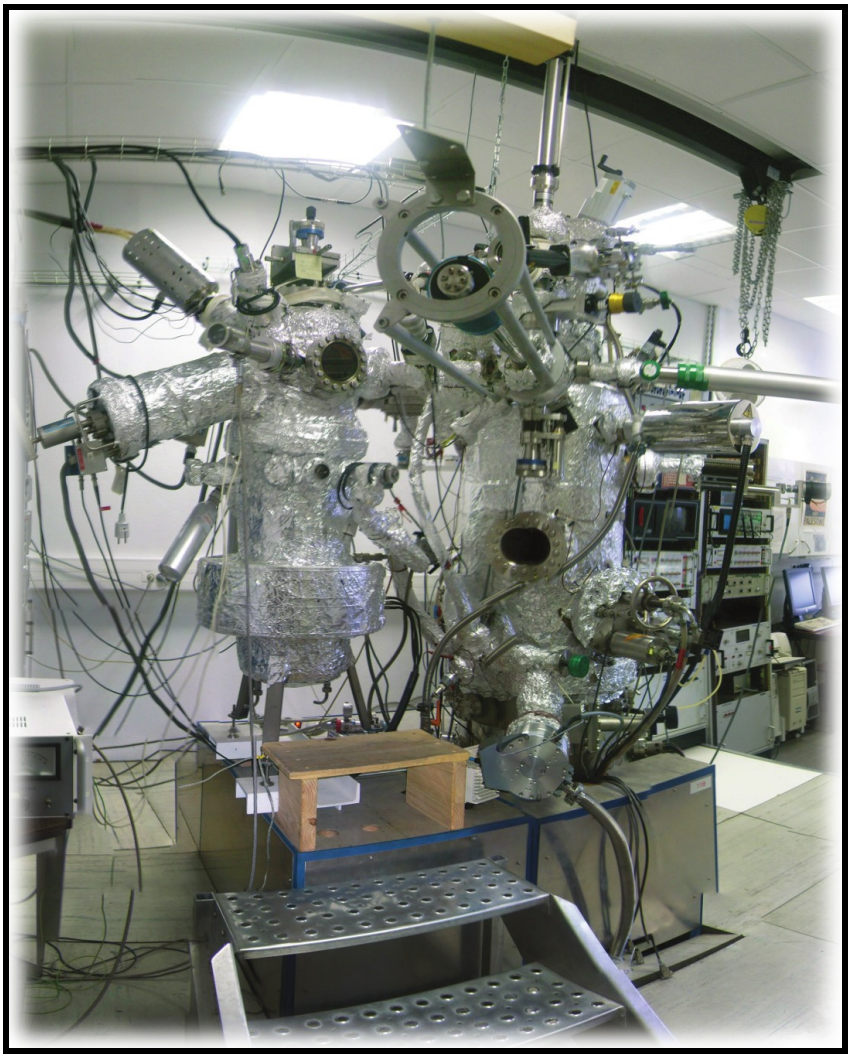

Figure (3.16): Ultra high vacuum chamber used for the rhenium epitaxy. The deposition chamber is on the right and the characterisation chamber is on the left.

3.3.2 Design of coplanar waveguide resonator

The microwave resonators are fabricated in the coplanar waveguide geometry. The typical mapping as well as the electromagnetic field distribution of such a microwave line is shown in Fig. 3.17 (a) and (b).

Design equations[109] for CPW geometry can be found in various books as, for instance, "Microstrip lines and slotlines"[110] from K. C. Gupta. A general approach is to solve the problem in the *quasi-static* approximation by using conformal transformation[111]. This approach consists of transforming the CPW geometry in a simple parallel–plate capacitor, see Fig. 3.17 (c). In the simplest analysis, the metal thickness is considered negligible and the substrate height is considered infinite. The capacitance per unit length is the sum of the air and substrate capacitance. The total capacitance is then:

$$C_\ell = 4\epsilon_0\epsilon_{\text{eff}}\frac{K(k_1)}{K(k_1')} \tag{3.12}$$

with $\epsilon_{\text{eff}} = (\epsilon_{\text{r}} + 1)/2$ is the effective permittivity, $K(k_1)$ is the complete elliptic integral of the first kind[9], $k_1 = w/(w+2s)$ and $k_1^2 + k_1'^2 = 1$.

In practice, the substrate height is finite. A preliminary conformal mapping transforms then the finite thickness of the substrate into an infinite thickness one. Only the effective permittivity is altered, it becomes:

$$\epsilon_{\text{eff}} = 1 + \frac{\epsilon_{\text{r}} - 1}{2}\frac{K(k_2)}{K(k_2')}\frac{K(k_1')}{K(k_1)} \tag{3.13}$$

with:

$$k_2 = \frac{\sinh\left(\frac{\pi w}{4h}\right)}{\sinh\left(\frac{\pi(w+2s)}{4h}\right)}, \tag{3.14}$$

$$k_2' = \sqrt{1-k_2^2}. \tag{3.15}$$

The characteristic impedance is given by:

$$Z = \frac{30\pi}{\sqrt{\epsilon_{\text{eff}}}}\frac{K(k_1')}{K(k_1)}. \tag{3.16}$$

[9]The module "special" of the SciPy library contains the function "ellipk" to easily calculate the complete elliptic integral of the first kind. One note that the argument of the function is $m = k^2$. Also when $m \approx 1$, the function "ellipkm1" should be used instead.

(a) Coplanar waveguide (CPW) geometry

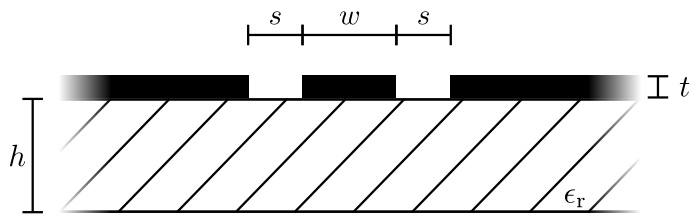

(b) Electromagnetic field distributions in CPW

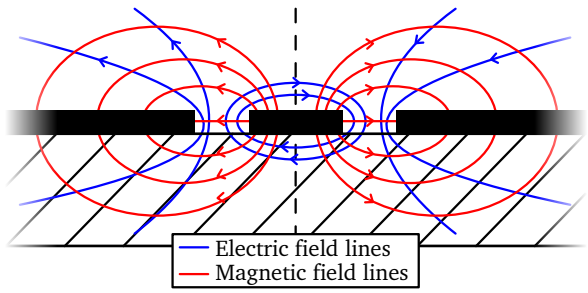

(c) Conformal transformation of CPW half plane

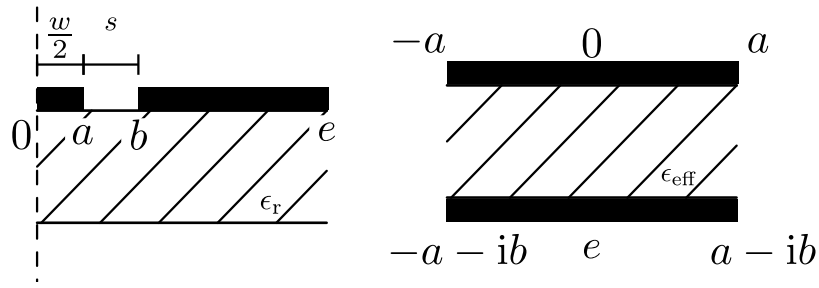

Figure (3.17): Sketch of coplanar waveguide. (a) Coplanar waveguide (CPW) geometry with ϵ_r. the relative permittivity, h the substrate height, t the metal layer thickness, s the gap width and, w the central line width. (b) Electromagnetic field distributions in CPW. (c) Conformal transformation of CPW half plane. The point e is suppose to be infinitely far from the origin.

The magnetic inductance per unit length follows from the equation for the propagation speed $v = c/\sqrt{\epsilon_{\text{eff}}} = 1/\sqrt{L_\ell C_\ell}$ giving:

$$L_\ell = \frac{\mu_0}{4}\frac{K\left(k_1'\right)}{K\left(k_1\right)} \tag{3.17}$$

where μ_0 are the vacuum susceptibility. Due to the small width and small thickness of the central line of our resonators, the kinetic inductance has to be taken into account to correctly model the inductance per unit length. The kinetic inductance can be written as[112]:

$$L_{\text{k}} = \mu_0 \lambda_{\text{eff}} g \coth\left(\frac{t}{\lambda_{\text{eff}}}\right) \tag{3.18}$$

where t is the thickness of the metal layer and λ_{eff} the effective penetration depth. The parameter g allows the calculation of the kinetic inductance for a coplanar waveguide geometry. It is defined as follow[113,114]:

$$g = \frac{1}{32K^2\left(k_1\right)}\frac{\left(w+2s\right)^2}{s\left(w+s\right)}\left[\frac{2}{w}\ln\left(\frac{w}{\delta}\frac{s}{w+s}\right) + \frac{2}{w+2s}\ln\left(\frac{w+2s}{\delta}\frac{s}{w+s}\right)\right], \tag{3.19}$$

with the width $\delta = t/(4\pi e^{\pi})$. A useful expression for calculating the effective penetration depth from material parameters is:

$$\lambda_{\text{eff}} = \sqrt{\frac{\hbar \rho_N}{\mu_0 \pi \Delta}} \tag{3.20}$$

where ρ_N is the resistivity of the metal just above the superconducting–normal transition and Δ is the superconducting gap. In the case of a $\lambda/4$ resonator, a simple derivation gives the following resonance frequency formula:

$$\nu_r = \frac{1}{4\ell_{\frac{\lambda}{4}}}\sqrt{\frac{1}{\left(L_\ell + L_{\text{k}}\right)C_\ell}} \tag{3.21}$$

where $\ell_{\frac{\lambda}{4}}$ is the total length of the quaterwave resonator.

3.3.3 Microwave resonator fabrication

Removal of the tungsten backside layer

The first step of the microwave resonator fabrication is to remove the backside layer of tungsten. The tungsten has been evaporated only to allow a good heating of the sapphire for the rhenium epitaxy, without consideration about its electrical properties. To avoid losses due to the tungsten layer, we completely remove it.

Table 3.4 presents the recipe to etch the 300 nm of the tungsten layer. The first step consists to deposit resist on the rhenium layer to protect it during the etching of the tungsten. Figure 3.18 shows a sketch of the method. A drop of resist S1818 is deposited on a support

Step	Description	Equipment used	Precision
1	Resist coating	S1818	Deposit a drop of resist on a surface and drop the chip on it (rhenium layer in contact with the resist)
2	Cleaning	Plassys nanofab, Process RES	Duration: 30 s Plasma: O_2 Flow: 20 sccm Pressure: 2×10^{-1} mbar Power: 50 W
3	RIE	Plassys nanofab, Process NbT	Duration: 20 min Plasma: SF_6 Flow: 20 sccm Pressure: 2×10^{-2} mbar Power: 20 W
4	Resists removal	ethanol	Duration 10 min Rinse in isopropanol N_2 blow dry

Table (3.4): Recipe to remove the tungsten backside layer.

Si wafer. Next the chip of rhenium is turned over and dropped on the resist. With a clamp we push the chip in the resist to cover the sides of the chip. The idea is to protect the sides of the rhenium layer to avoid unwanted chemical etching.

In the RIE, the first step is to apply an oxygen plasma of about 30 s to remove residue of resist on the tungsten.

The tungsten layer thickness is 300 nm. The layer is removed with a plasma of SF_6. After some test, a duration of 20 min seems enough to remove entire the tungsten layer. Typically we over-etch the tungsten. Indeed the tungsten has been deposited on an unpolished surface of Sapphire. Due to the high roughness, an over-etching is required to completely etch the tungsten.

The final step consists of removing the resist. The sample is immersed in ethanol during 10 min. Next it is rinsed with isopropanol and dried with clean nitrogen gas.

Etching of the microwave resonators

Table 3.5 presents the recipe developed for the fabrication of microwave resonators on rhenium chip. The first step is the deposition of S1805 resist on rhenium layer. Next a baking of one minute at 115 °C allows the fast evaporation of solvent present in the resist.

The laser lithography is realised on a "Heidelberg DWL66FS" machine by Bruno Fernandez. Due to the small size of the chip (5 × 8 mm), we have to find the centre of the chip manually.

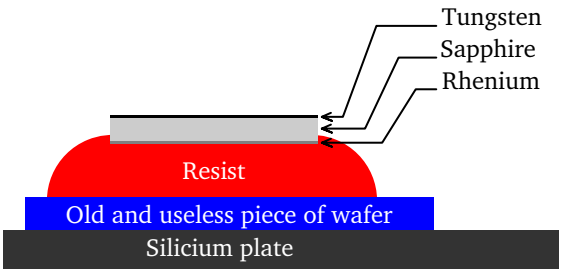

Figure (3.18): Sketch showing the protection of the rhenium layer by the use of resist. We note that the resist covers the rhenium layer, even at the sides, but not the tungsten.

The focus is adjusted manually. The small size of the chip also induced an excess of resist at the borders. The design is then adapted to have an exposure only on the flat part of the resist which corresponds to a surface of 3.5 × 6.5 mm.

The development uses a mixture of deionised water and microdev in 1:1 proportion. A visual control during the development is useful to check the success of the operation. Once the development is finished, the chip has to be immersed in deionised water to stop the chemical etching reaction.

The process RES is used to remove residues of resist and the process NbT to etch the rhenium. An etching speed for rhenium has been calibrated at 11 nm·min^{-1}.

The resist is removed by immersing the chip in acetone during 10 min. Next, we pass the chip by an isopropanol bath before cleaning it with deionised water. Finally the chip is dried with clean nitrogen.

Figure 3.19 shows two pictures of the "Re-EJM-186" sample. The left picture presents four microwave resonators coupled to the same feedline. Resonators are designed in order that their resonances occur between 7 GHz and 10 GHz which corresponds to the bandwidth of our microwave measurement line (see Fig. 2.14). Each resonator is detuned to its nearest neighbour by 130 MHz. Indeed each resonator have a length difference of 80 µm. The readout of each resonator is then performed by using the "Frequency-division multiplexing" technique. The right picture presents a zoom in one of the microwave resonators. The central conductor of the resonator measures 5 µm and the gap measures 20 µm. To obtain a $\lambda/4$ resonator the resonator is shorted on one side and open on the other. A capacitive coupling is obtained by positioning the open side close to the feedline.

[10] Zeiss Ultra plus

Step	Description	Equipment used	Precision
1	Resist coating	S1805	30 s at 4000 rpm Ac: 6000 rpm·min^{-1}
2	Baking	Hotplate	1 min at 115 °C
5	Laser lithography	Heidelberg DWL66FS	Sample position: 8 Alignment angle <15 mrad Energy: 65 Find manually chip centre Make the focus manually
6	Development	Microposit Developpeur:DIW 1:1	Duration 60 s Rinse in DIW (keep under) N_2 blow dry
7	RIE	Plassys nanofab, process RES Plassys nanofab, process Nbt	Duration 5 s Etch speed: 11 nm·min^{-1}
9	Lift-off	Acetone	Duration 10 min Rinse in isopropanol Rinse in DIW N_2 blow dry

Table (3.5): Recipe for the microwave resonators.

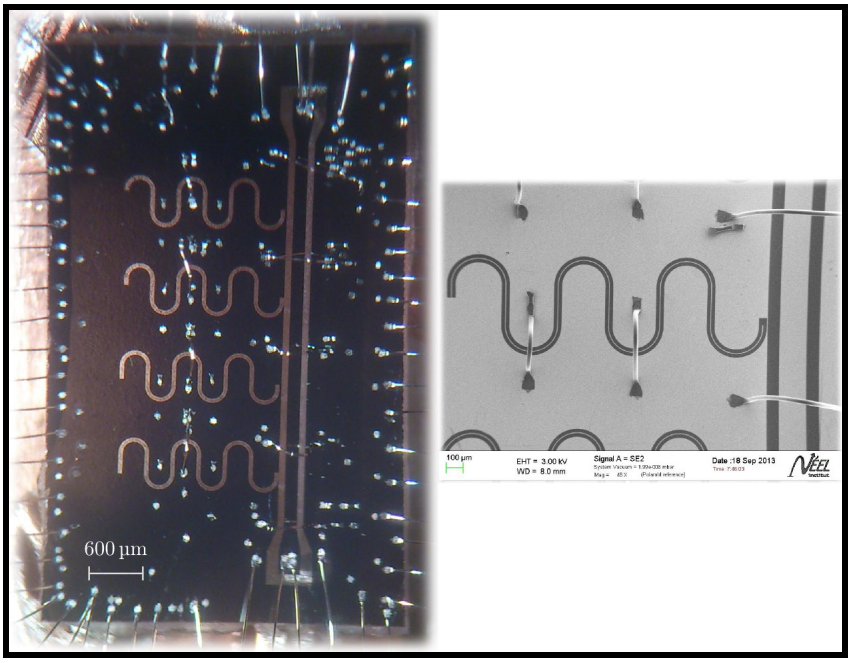

Figure (3.19): At the left, photography of a rhenium chip with four $\lambda/4$ resonators and a feedline. Bondings used for ground and feedline connection are visible. At the right, a SEM[10] picture of one resonator. Both pictures show the "Re-EJM-186" sample.

Chapter 4

Superconducting quarterwave microwave resonators

Contents

4.1 Introduction **153**
4.2 Model of the quarterwave resonator **154**
4.3 Lumped–element model **154**
4.4 Transmission of a feedline capacitevely coupled to a quarterwave resonator **156**
4.4.1 Why certain resonances are asymmetric ? 157
4.5 Rhenium microwave resonator **159**
4.5.1 Extraction of resonator parameters 159
4.5.2 Measurement of the resonance frequency as function of temperature 162
4.5.3 Low internal quality factor 167
4.6 Aluminium resonators **168**
4.6.1 Characterisation of the resonance 168
4.6.2 A tunable resonance frequency 171

4.1 Introduction

The characterisation of the microwave resonator is important in order to determine the regime, under- or over-coupled, of the system. Moreover, as we will see in Chapter 5, the characterisation of artifical atom parameters requires a good knowledge of the resonator parameters.

From Section 4.2 to Section 4.4 of the chapter we introduce models and concepts used to analyse microwave resonance curve measurements. In particular in Section 4.4 we discuss the asymmetric, or Fano, resonance shape. We will show that this effect can be understood as

an interference between two signals. Moreover, we explain the asymmetry by the inductance of the bonding wires connecting the sample chip to the rest of the microwave lines. A model taking into account these bondings is presented and discussed.

In Section 4.5 we present measurements on microwave resonators made from rhenium. Temperature dependence is shown. In particular we discuss qualitatively the temperature dependence of the quality factors using a two–fluid model. An extraction of the London penetration length via cavity resonance frequency measurement is also presented. The section ends by a discussion about low internal quality factor measured in our experiments.

The Section 4.6 is dedicated to the measurement on a frequency–tunable microwave resonator made from aluminium. We show a way to calibrate the transmission measurement by taking advantage of the tunability of the resonator frequency. We present measurements of resonator parameters as function of applied magnetic flux. We will show how the inductance of the SQUID leads to a hysteretic behaviour of the cavity resonance frequency as function of magnetic flux.

4.2 Model of the quarterwave resonator

A simple schematic view of the system is shown in Fig. 4.1. Our resonators used the "elbow" geometry[99] to be coupled to the feedline. This design allows to couple a small part of the resonator to the feedline. Moreover the length of the elbow part is small compared to the length of the resonator and the microwave wavelength at the resonance frequency. Only the part where the electric field is predominant is coupled to the feedline (see Section 3.2.1). We can then neglect the inductive coupling. The capacitive coupling is modelled by a discrete element, a single capacitor C_c (Fig. 4.1). The resonator is modelled as a transmission line with characteristic impedance Z_r which is shorted to ground at one side and opened at the other side.

4.3 Lumped–element model

Despite the fact that our microwave resonators are implemented by using transmission lines, it is interesting to describe these distributed resonators as lumped-element resonators. The transformation is illustrated in Fig. 4.2.

This transformation requires that:

$$\alpha \ell \ll 1 \tag{4.1}$$

$$\frac{\Delta\omega_r}{\omega_r} \ll 1 \tag{4.2}$$

with α the attenuation of the transmission line and ω_r the resonance frequency of the resonator. We also introduced $\Delta\omega_r = \omega - \omega_r$ the relative angular frequency where ω is the applied angular frequency. Equation (4.1) implies low loss in the resonator and Eq. (4.2) restrains the frequency validity range close to the resonance frequency. When both conditions

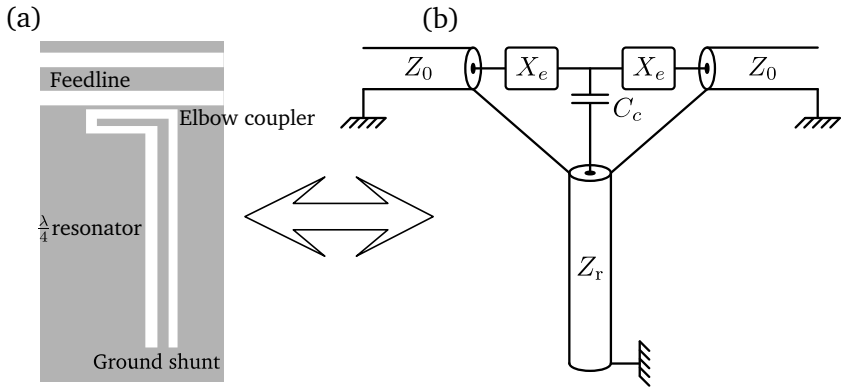

Figure (4.1): (a) Sketch of a $\lambda/4$ microwave resonator coupled to a feedline. The coupling is realised with an elbow coupling geometry. The superconductor is shown in grey and the substrate in white. (b) Equivalent electrical circuit. The coupling is modelled as a single capacitor C_c and the feedline as a transmission line of characteristic impedance Z_0. The resonator is modelled as a transmission line of characteristic impedance Z_r which is shorted to ground at one side and opened at the other. Impedances X_e model impedance mismatch due to aluminium bondings between the sample chip and the printed circuit board, see Section 4.4.1.

are fulfilled, the impedance of Eq. (1.60) becomes:

$$Z_{\text{in}} = \frac{Z_{\text{r}}}{\alpha\ell + i\frac{\pi}{2}\frac{\Delta\omega_{\text{r}}}{\omega_{\text{r}}}}. \tag{4.3}$$

By comparing Eq. (4.3) and the impedance of a parallel RLC resonator we identify the equivalent lumped element of a quarterwave resonator, see Table 4.1.

Denomination	Equivalence
Capacitance	$C_{\lambda/4} = \frac{\ell}{2}C_\ell$
Inductance	$L_{\lambda/4} = \frac{8\ell L_\ell}{\pi^2}$
Losses	$R_{\lambda/4} = \frac{Z_{\text{r}}}{\alpha\ell}$
Internal quality factor[61]	$Q_{\text{i}} = R_{\lambda/4}\sqrt{\frac{C_{\lambda/4}}{L_{\lambda/4}}} = \frac{\pi}{4}\frac{1}{\alpha\ell}$

Table (4.1): Correspondence between electrical components of a lumped-element and a distributed $\lambda_L/4$ resonator.

We note that the equivalent RLC circuit only has one mode of resonance, in contrast with the distributed resonator in which harmonic resonances exist. This limitation implies that the transformation described above is only correct at the vicinity of one resonance frequency.

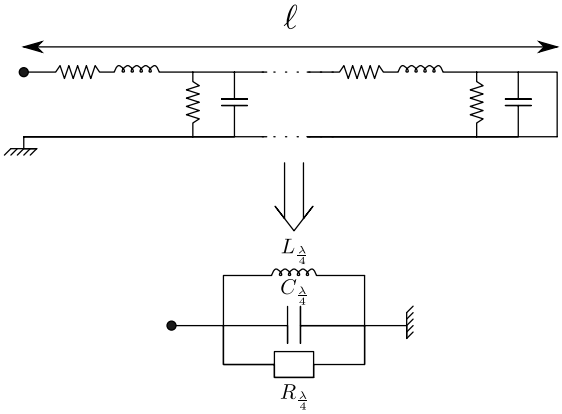

Figure (4.2): Illustration of the transformation between a distributed $\lambda_L/4$ resonator to a lumped RLC element resonator. In both cases, the resonator is opened at one end and shorted to ground at the other end.

4.4 Transmission of a feedline capacitevely coupled to a quarter-wave resonator

The derivation of the transmission of the system is detailed in Appendix B. The final result is:

$$S_{21} = \frac{1 + 2iQ_i \frac{\Delta\omega_0}{\omega_0}}{1 + \frac{Q_i}{Q_c} + 2iQ_i \frac{\Delta\omega_0}{\omega_0}} \tag{4.4}$$

Q_i is the internal quality factor already defined in Table 4.1 and Q_c is the external quality factor (see Eq. (B.15)). The resonance frequency of the resonator coupled to the feedline is denoted ω_0 and the drive frequency relative to the cavity resonance frequency is $\Delta\omega_0 = \omega - \omega_0$. To understand the physical meaning of these terms, we derive the internal loss rate $\kappa_i = \omega_r/Q_i$ and the external coupling rate as $\kappa_c = \omega_0/Q_c$. κ_i gives the rate at which energy stored in the resonator cavity is lost to the environment, while κ_c informs us about the rate at which energy stored in the cavity goes into the feedline. The decay times are:

$$T_{\text{cav}}^{\text{ext}} = \frac{2Q_c}{\omega_0} = \frac{2}{\kappa_c}, \qquad T_{\text{cav}}^{\text{int}} = \frac{2Q_i}{\omega_r} = \frac{2}{\kappa_i}. \tag{4.5}$$

The transmission of the signal amplitude is given by $|S_{21}|$ while $|S_{21}|^2$ corresponds to power transmission of the signal. $|S_{21}|^2$ as function of the frequency follows a Cauchy–Lorentz distribution shape:

$$|S_{21}|^2 = 1 - \frac{1 - \left(\frac{Q_0}{Q_i}\right)^2}{1 + \left(2Q_0 \frac{\Delta\omega_0}{\omega_0}\right)^2} = 1 - \frac{I}{1 + \left(2\frac{\Delta\omega_0}{\delta_{\text{FWHM}}}\right)^2} \tag{4.6}$$

where $Q_0^{-1} = Q_i^{-1} + Q_c^{-1}$ is the total quality factor. The depth of the resonance dip and the full width at half maximum are given by $I = 1 - (Q_0/Q_i)^2$ and $\delta_{FWHM} = \omega_0/Q_0$, respectively.

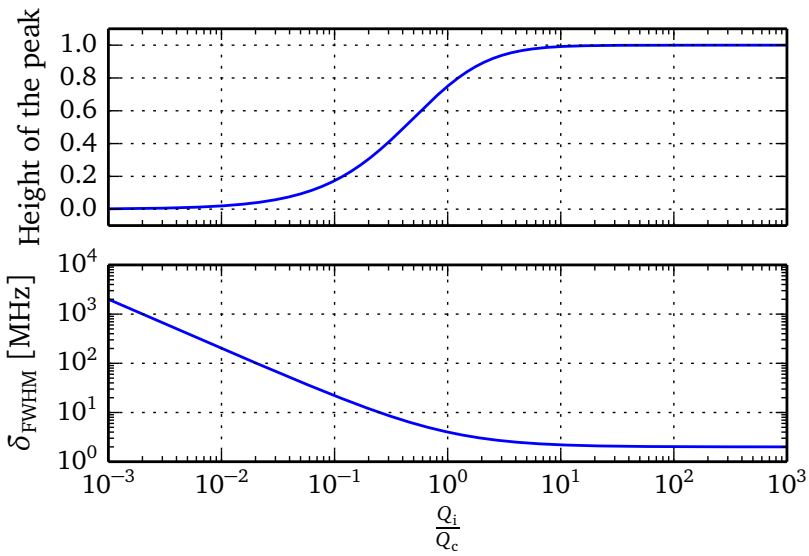

Figure (4.3): Depth of the dip and full width at half maximum as a function of the Q_i/Q_c ratio.

Figure 4.3 shows the depth of the dip and the FWHM as function of the Q_i/Q_c ratio. For $Q_i/Q_c \gtrsim 10$ the depth of the dip as well as the FWHM are constant. We call this regime the undecoupled regime. In this limit the internal losses become negligible and we can consider that energy entering inside the resonator will not be lost before being sent back to the feedline. The linewidth of the resonator depends only on its external coupling $\kappa_c = \omega_0/Q_c$. For $Q_i/Q_c < 10$, the overcoupled regime, the dynamics of the resonator depend on the external coupling but also on the internal losses.

4.4.1 Why certain resonances are asymmetric ?

Measured resonance dips may have an asymmetric shape and not a simple Lorentzian shape. Such asymmetric shapes can be attributed to an impedance mismatch in the feedline[115,116] on either side of the resonator as indicated in Fig. 4.1 by the two X_e impedances. Our interpretation attributes these impedances to wire–bondings between the chip and the printed circuit board.

To evaluate this effect, a complete derivation of that problem is described in Appendix B. The transmission formula becomes:

$$S_{21} = \frac{Z_0}{Z_0 + iX_e} \frac{1 + 2iQ_i \frac{\Delta\omega_0}{\omega_0}}{1 + \frac{Q_i}{Q_c Z_0}(Z_0 + iX_e) + 2iQ_i \frac{\Delta\omega_0}{\omega_0}} \tag{4.7}$$

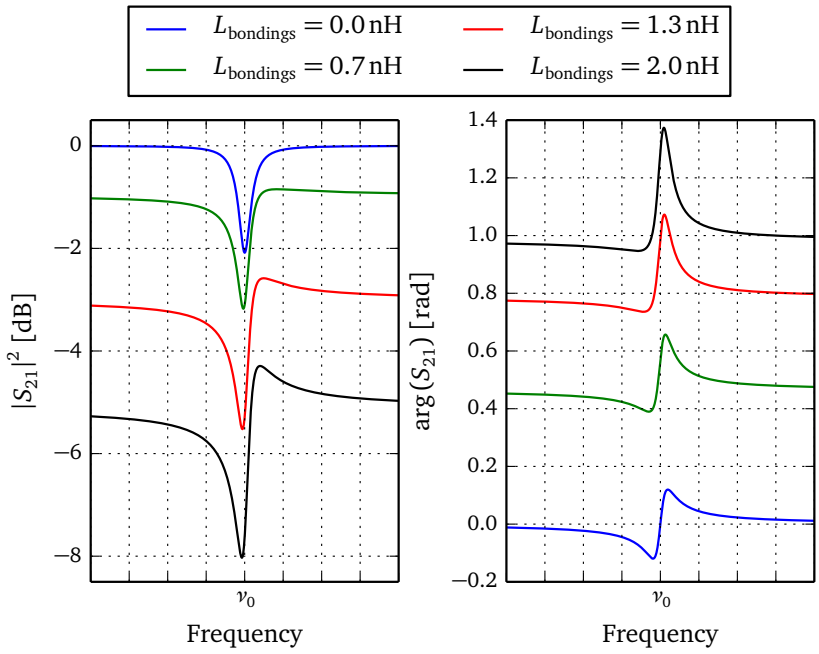

Figure (4.4): $|S_{21}(\nu)|^2$ for different asymmetry value. The left panel presents transmission is in decibel and the right one in radian.

Figure 4.4 shows the effect of the inductance of the bondings on the resonance shape. Without inductance of the bondings, the impedance matching is perfect and the resonance is symmetric. Indeed, Eq. (4.7) simplifies to Eq. (4.4) when the inductance of the bondings can be neglected. The transmission is described by a Cauchy–Lorentz distribution. As the inductance of the bondings increases from 0 nH to 2 nH, the transmission power decreases from 0 dB to −5 dB. An offset also occurs on the phase of the transmitted signal. These effects come from reflections which arise because of the impedance mismatch. Futhermore, the resonance becomes more and more asymmetric as the inductance of the bondings increases. The shape becomes asymmetrical because of constructive and destructive interferences which occurs on both sides of the resonance. Indeed due to the impedance mismatch caused by inductance of the bondings, the transmitted signal has a phase delay compared to the same signal without this additional inductance. Moreover the resonance causes a phase shift, first negative and next positive, along the frequency sweep. When both effects arise together, the resulting signal is lowered when the interference is destructive and amplified when the interference is constructive. This is what we observe at the left and right of the resonance, respectively. The resonance frequency is also slightly shifted when the asymmetry increases. This effect is also due to the inductance of the bondings which changes the frequency at which the imaginary part of the transmitted signal will be zero. Nevertheless this frequency shift is really small, less than 0.1 MHz (0.001 % of the resonance frequency) for a 2 nH inductance of the bondings.

4.5 Rhenium microwave resonator

Several samples of rhenium microwave resonators have been fabricated and characterised during my thesis. Hereafter we present a series of measurements performed on the same rhenium sample chip. The rhenium layer, of thickness 25 nm, has been deposited at 970 K. It exhibits a resistivity at room temperature of 21.2 μΩ·cm and a residual resistance ratio of 4.45. The intrinsic coherence length and the mean free path have been extracted by transport measurements. We obtain $\xi_0 = 120\,\text{nm}$ and $\ell_{\text{mfp}} = 45\,\text{nm}$, respectively. Figure 4.5 shows the sample chip connected to the sample holder with four quarterwave resonators made from rhenium. Figure 4.6 shows the microwave transmission of that sample. We observe three dips, each of them corresponding to one microwave resonator. An SEM observation showed us that the longest resonator was shorted to ground, explaining why only three resonances were visible.

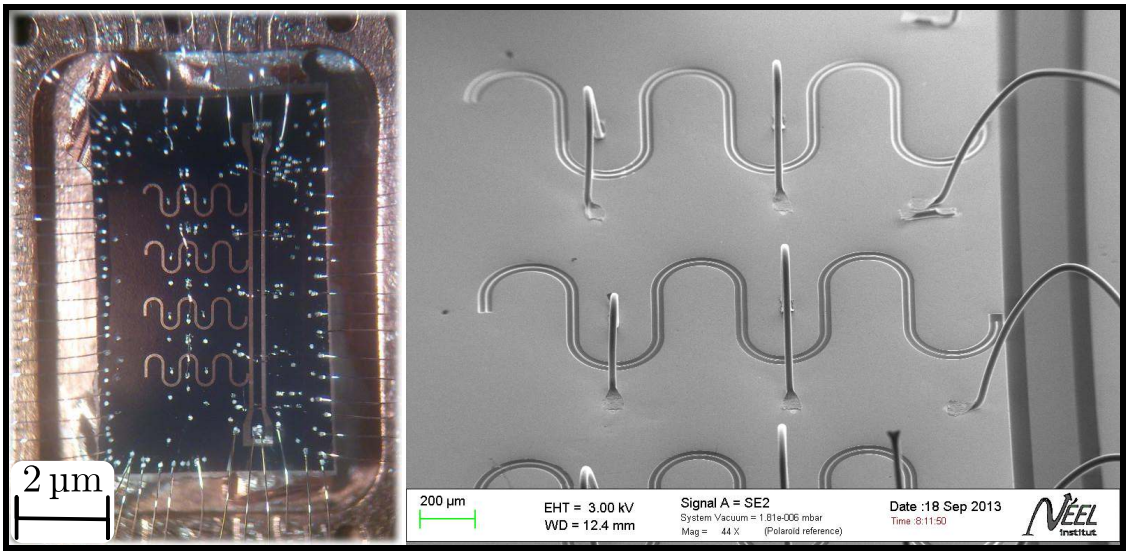

Figure (4.5): Left side, a photography of microwave resonators etched in a rhenium layer. The chip is connected to the sample holder via tens of microbondings. Right side, a SEM picture of the microwave resonators.

4.5.1 Extraction of resonator parameters

Figure 4.7 shows a zoom of the lowest frequency resonance at 6.038 GHz. The data are displayed in blue points and the model of Eq. (4.7) is plotted in dashed red. The model to fit resonance dips contains four independent parameters, namely the internal quality factor Q_i, the external quality factor Q_c, the resonance frequency ν_0, and the bonding wire impedance X_e. These extracted parameters are listed in the caption of Fig. 4.7.

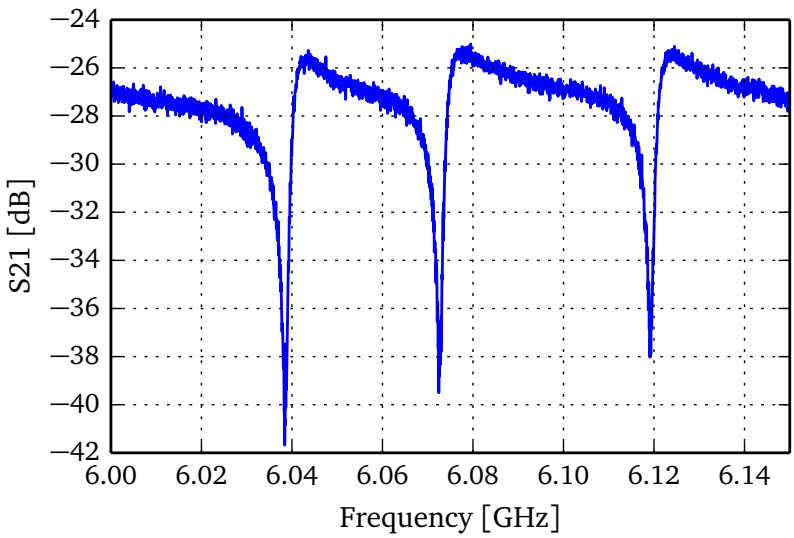

Figure (4.6): Three resonances measured on the same chip with the frequency division multiplexing method. Measurement was performed with a commercial VNA "R&S ZVL13" with a bandwidth of 1 kHz*, a power at the output of the VNA of* −30 dBm *and was averaged 10 times. The base temperature was* $T = 60\,\mathrm{mK}$.

Inductance of the bondings between feedline and the PCB

As we explained in Section 4.4.1, the asymmetric shape is due to an impedance mismatch causes by inductance of the bondings. We estimate the value of the inductance of the bondings at the resonance frequency by calculating $L_{\mathrm{bonding}} = |X_{\mathrm{e}}|/\omega_0$. In Fig. 4.7, the asymmetry is quite pronounced and the estimation gives a inductance of the bondings of 1.9 nH. To confirm the extracted inductance of the bondings we measure their length, approximately 4 mm. From that, we roughly estimate the inductance of the bondings[1] to be about 2 nH. Discrepancy between our estimation and our fit is about 5 %, only.

Coupling between resonator and feedline

The extraction of the coupling capacitance from the external quality factor requires to estimate the impedance of the resonator from its geometry. This estimation is performed from design via equations discussed in Section 3.3.2. The external quality factor is related to the coupling capacitance between the microwave resonator and the feedline, see Eq. (B.15). In Fig. 4.7 the coupling capacitance is $C_{\mathrm{c}} = 4.6\,\mathrm{fF}$.

[1]The inductance per unit length for bonding wires is $L_{\ell}^{\mathrm{bondings}} \approx 1\,\mathrm{nH{\cdot}mm^{-1}}$.

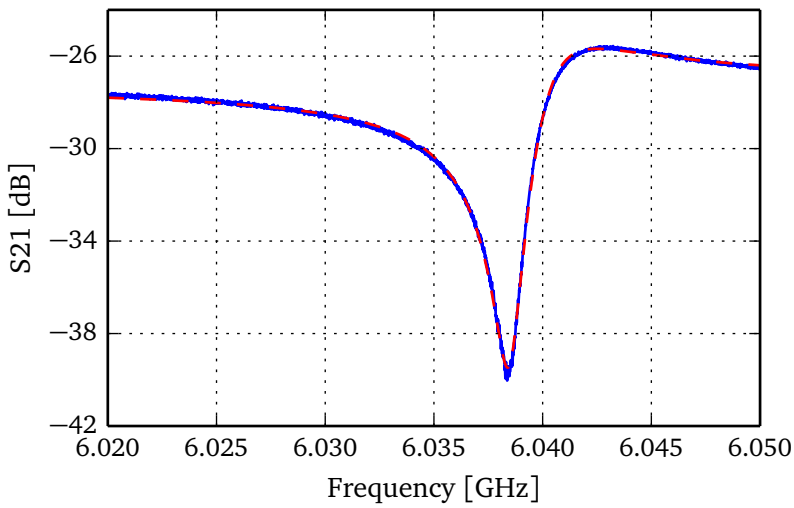

Figure (4.7): Zoom in the first resonance shown in Fig. 4.6. The result of the fit using Eq. (4.7) is plotted in dashed red. Fit parameters are $Q_i = 5500$, $Q_c = 2200$, $\nu_0 = 6.038\,\mathrm{GHz}$, and $L_{bondings} = 1.9\,\mathrm{nH}$. Measurement was performed with a commercial VNA "R&S ZVL13" with a bandwitdh of 1 kHz, a power at the output of the VNA of −30 dBm and was averaged 25 times. The base temperature was $T = 60\,\mathrm{mK}$.

Resonator parameters

We show in Section 4.3 that a quarterwave resonator can be described as a simple RLC parallel oscillator. If we assume the system as a RLC resonator coupled through a capacitance to a feedline, we can demonstrate:

$$\omega_0 = \sqrt{\frac{1}{L_{\lambda/4}\left(C_{\lambda/4} + C_c\right)}}. \tag{4.8}$$

This equation is true only when[2] $C_c^2\omega_0^2 Z_0^2/4 \ll 1$. From Eq. (4.8) and the definition of the characteristic impedance $Z_r = \sqrt{L_\ell/C_\ell}$, we obtain[3]:

$$C_{\lambda/4} = \frac{\pi}{4Z_r\omega_0} - \frac{C_c}{2} \tag{4.9}$$

By using Eq. (4.9) and Eq. (4.8), we extract $C_{\lambda/4}$ and $L_{\lambda/4}$ from the fit parameters. From Fig. 4.7 we obtain $C_{\lambda/4} = 222\,\mathrm{fF}$ and $L_{\lambda/4} = 3.1\,\mathrm{nH}$. The equivalent capacitance and

[2]This condition corresponds to the limit of validity for the transformation of a RC series circuit to a parallel one[117]. It corresponds to the square ratio of the feedline impedance seen by the resonator (so $Z_0/2$) over the coupling capacitor impedance which should be negligible. Physically it means that the capacitance should be small enough in order that the open circuit assumption of the quarterwave resonator stays correct.

[3]The equation is only true for $C_c \ll (2Q_i)/(R_{\lambda/4}\omega_0)$. This condition means that the coupling capacitance should be small compared to the capacitance of the equivalent RLC resonator. Experimentally this condition is always fulfilled since C_c is two orders of magnitude smaller than $C_{\lambda/4}$.

inductance are important since they inform us about the participation ratio of the electric and magnetic field in the resonator.

4.5.2 Measurement of the resonance frequency as function of temperature

In order to observe the effect of the temperature on the resonance line shape, we perform a series of resonance line shape measurements for the three resonances shown in Fig. 4.6 for various temperature (from 60 mK to 560 mK with steps of 50 mK). The temperature was controlled by a "proportional-integral-derivative controller"[4].

Figure 4.8 presents the results of the experiment. The three resonance line shapes exhibit the same behaviour with a shift to smaller frequency and a reduction of the dip depth when the temperature increases.

From Eq. (4.7), we extract resonator parameters as function of temperature. The quality factors and the relative frequencies are shown in Fig. 4.9.

Internal and external quality factor

The external quality factor obtained by this analysis is independent of temperature (Fig. 4.9 (a)). The rate at which energy leaves the resonator to go into the feedline is due to the electrical coupling between the open extremity of the resonator and the feedline. At this position, the electrical field can be considered as temperature-independent.

The internal quality factors decrease for the three resonators when the temperature increases. Moreover the resonators exhibit different internal quality factors at $T \approx 0\,\mathrm{K}$ but they have the same internal quality factor for high temperature. These two features can be both explained by the two-fluid model proposed by Gorter and Casimir[118]. They assume that the quasiparticle density n_n follows the empirical temperature dependence for $T < T_\mathrm{c}$:

$$\frac{n_\mathrm{n}}{n_\mathrm{e}} = \left(\frac{T}{T_\mathrm{c}}\right)^4 \tag{4.10}$$

with n_e the total electron density. At very low temperature the density of quasiparticles is negligible. The internal quality factor is then limited by other factors (see Section 4.5.3 for a discussion about the internal quality factor values). When the temperature is high enough, the density of quasiparticles cause losses which decrease the value of the internal quality factor. At high temperature, the quasiparticle density becomes the main source of losses and the three internal quality factor tend to the same value.

[4] iMACRT from "service électronique du département MCBT". http://neel.cnrs.fr/spip.php?article2402&lang=fr

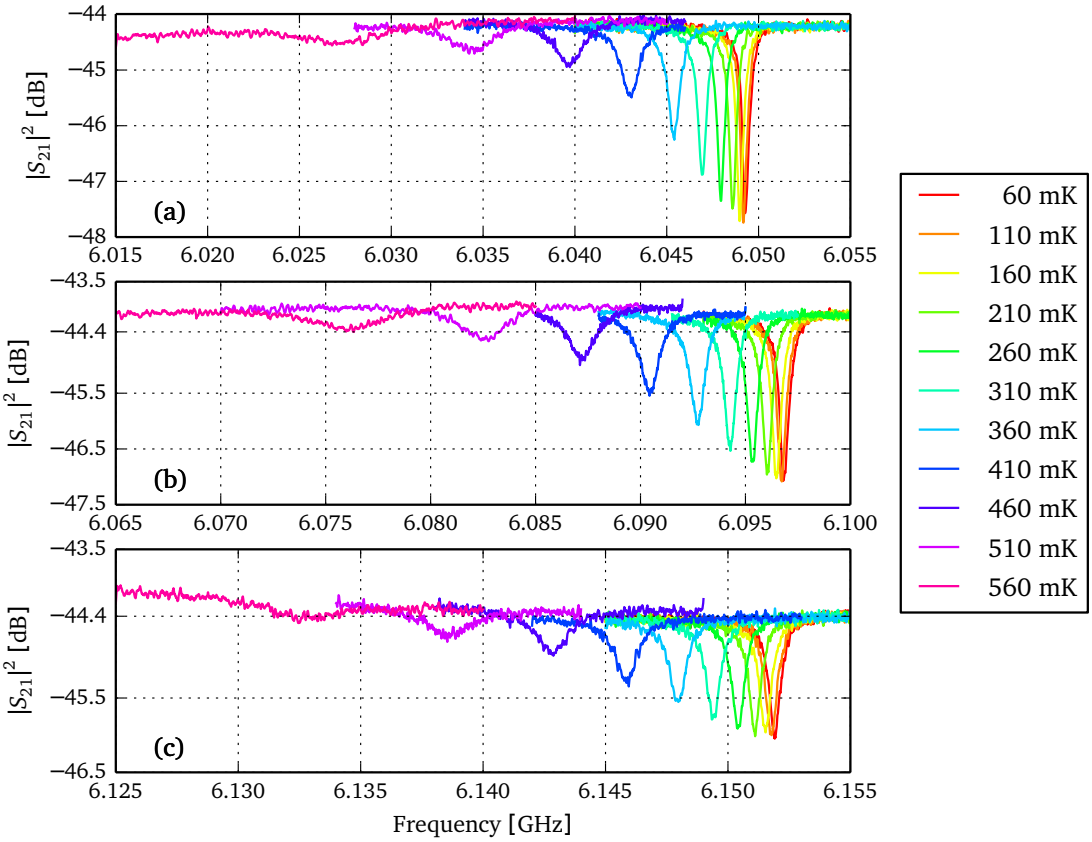

Figure (4.8): Measurement of the resonance line shape of (a) the first, (b) the second and (c) the third resonance presented in Fig. 4.6 for various mixing chamber temperature. The three resonance line shapes exhibit the same behaviour with a shift to smaller frequency and a reduction of the dip depth when the temperature increases. Measurements have been performed with a commercial VNA "R&S ZVL13" with a bandwitdh of 0.1 kHz*, a power at the output of the VNA of* −52 dBm*. Data have been averaged 10 times. Curves presented in this figure have been smoothed with a Savitzky–Golay filter*[82,83].

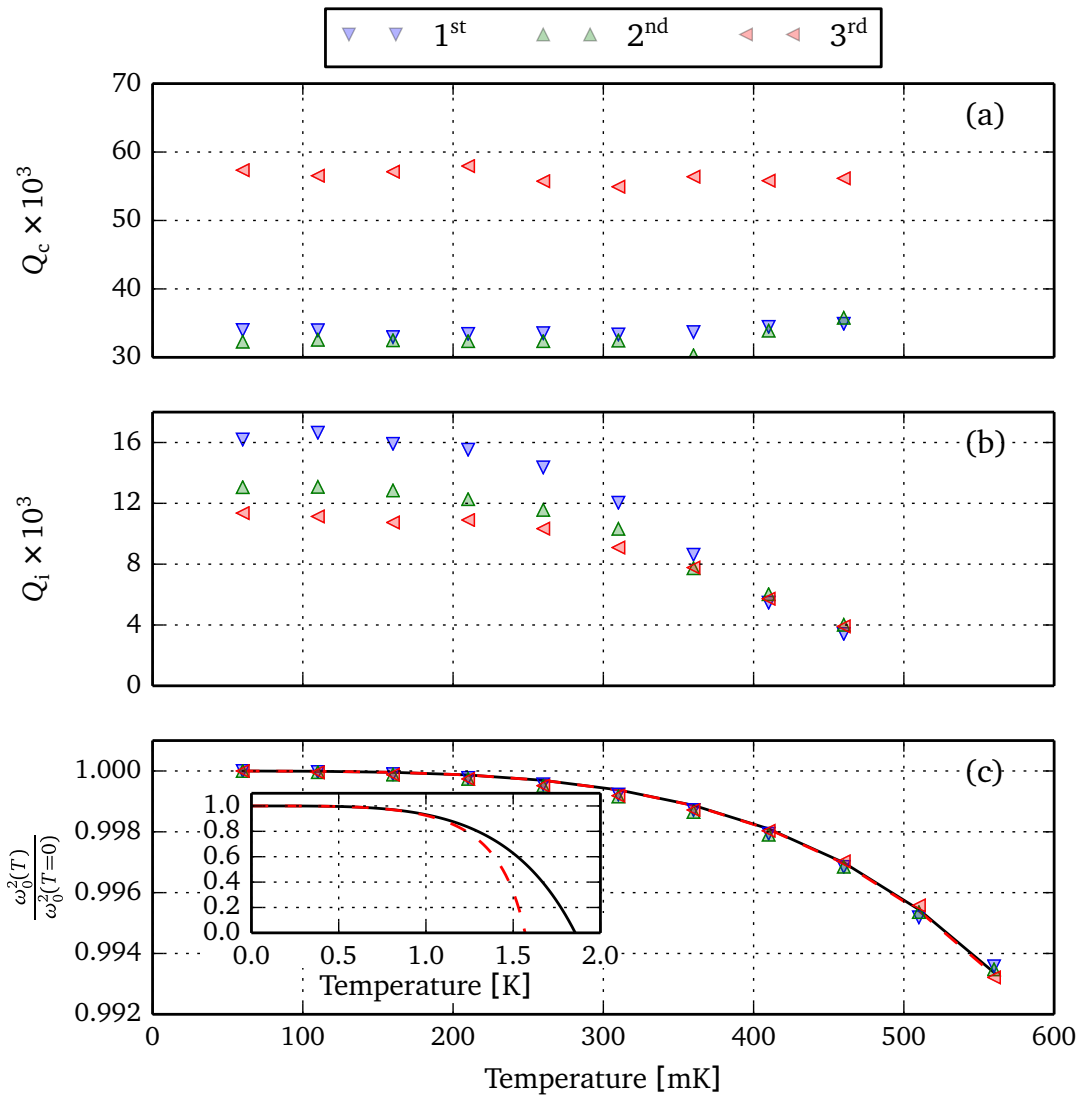

Figure (4.9): Temperature dependence of resonance parameters for three resonators fabricated on the same chip. Panel (a) presents the temperature dependence of the external quality factor, panel (b) of the internal quality factor, and panel (c) shows the evolution of the relative resonance frequency squared $\omega_0^2(T)/\omega_0^2(0)$ in temperature. The dashed black and red curves are calculated from Eq. (4.14) with $\alpha_k = 0.8$, $T_c = 1.9\,\mathrm{K}$ and $\alpha_k = 0.4$, $T_c = 1.6\,\mathrm{K}$, respectively. We remark that in the range of temperature covers by data points, the two theoritical curves seems equivalent. The inset shows a zoom out of the temperature dependence for theoretical curves. We observe that the discrepancy between the too curves occurs only for T close to T_c.

Extraction of the effective penetration depth

The relative resonance frequency for the three resonators presents the same behaviour with less than 0.04 % of discrepancy between values up to 560 mK. From Eq. (3.21) we calculate the relative resonance frequency as:

$$\frac{\omega_0^2(T)}{\omega_0^2(0)} = \frac{L_\ell + L_k(0)}{L_\ell + L_k(T)}. \tag{4.11}$$

where L_ℓ and L_k are the magnetic and kinetic inductance per unit length. The kinetic inductance given in Eq. (3.18) can be linearised when $t/\lambda_{eff} \ll 1$ as:

$$L_k = \mu_0 g \frac{\lambda_{eff}^2}{t}. \tag{4.12}$$

From the Gorter Casimir law, the temperature dependence of the penetration depth is given by:

$$\lambda_{eff}^2(T) = \frac{\lambda_{eff}^2(0)}{1-\left(\frac{T}{T_c}\right)^4}. \tag{4.13}$$

Leading to the relative resonance frequency temperature dependence:

$$\frac{\omega_0^2(T)}{\omega_0^2(0)} = \frac{1-\left(\frac{T}{T_c}\right)^4}{1-\left(\frac{T}{T_c}\right)^4(1-\alpha_k)} \tag{4.14}$$

with $\alpha_k = L_k/(L_\ell + L_k)$, the fraction of kinetic inductance. Data shown in Fig. 4.9 (c) are very well fitted by Eq. (4.14) with T_c and α_k as free parameters (see the dashed black and red curves for the theoretical laws). The extracted parameters are $\alpha_k = 0.6 \pm 0.2$ and $T_c = 1.7 \pm 0.2$ K. However, due to the small dependence of the resonance frequency in this experiment, the errors on the fit parameters are important.

As an example, we plot in Fig. 4.9 (c) the theoretical predictions with $\alpha_k = 0.8$ and $T_c = 1.9$ K for the black curve, and $\alpha_k = 0.4$ and $T_c = 1.6$ K for the dashed red curve. In the temperature range of the experiment, *i.e.* at $T \ll T_c$, the two curves do not exhibit a visible difference. The inset in Fig. 4.9 shows that the two curves deviates only at $T \to T_c$. We conclude that our measurement does not allow a precise determination of the fit parameters.

By using the extraction of resonator parameters described in Section 4.5.1 we obtain a total inductance per unit length of 1070 nH·m^{-1} leading to a magnetic inductance per unit length of $L_\ell = 400 \pm 200$ nH·m^{-1} and a kinetic inductance per unit length of $L_k = 650 \pm 200$ nH·m^{-1}. From Eq. (4.12) the effective penetration depth is deduced, $\lambda_{eff} = 225 \pm 40$ nm.

Extraction of the London penetration depth

Since the rhenium film is in the so-called *dirty* limit, the London penetration depth is related to the effective penetration depth as[119]:

$$\lambda_L = \lambda_{eff}\sqrt{\frac{\xi_{eff}}{\xi_0}} \tag{4.15}$$

with $\xi_{\text{eff}}^{-1} = \xi_0^{-1} + \ell_{\text{mfp}}^{-1}$ the effective coherence length where, ξ_0 and ℓ_{mfp} are the intrinsic coherence length and the mean free path, respectively. We calculate the London penetration depth $\lambda_{\text{L}} = 130 \pm 20\,\text{nm}$ for rhenium.

Comparison with other measurements and estimations

The critical temperature can be compared to the critical temperature deduced from resistance versus temperature measurements, see Fig. 4.10. The transition between superconductor and normal metal is unusual with a kind of two sub-transitions, the first one at about 1.85 K and the second one at 2.125 K. The critical temperature extracted through the temperature dependence of the resonance frequency is lower than the critical temperature suggested by the two sub-transitions.

The magnetic inductance per unit length can be compared to the estimation from the geometry of the resonator. Equation (3.17) gives $L_\ell = 716\,\text{nH}\cdot\text{m}^{-1}$ which is twice larger than the extracted magnetic inductance from temperature measurement.

These discrepancies between extracted values suggest that further measurements are necessary to conclude about the value of the different parameters. The error on the extracted parameters can be lifted by measuring the cavity resonances at higher temperature or by fabricating microwave resonators with higher kinetic inductance ratio. The first solution is difficult to realise since due to the low quality factor of the resonator at high temperature, the resonance dip becomes really shallow. The second solution would be easier since by designing a microwave resonator with a narrower central line, the inductance ratio will increase. Currently the width w of the central line is 5 µm, this can be reduced to 1 µm leading to an inductance ratio twice larger according to Eq. (3.18).

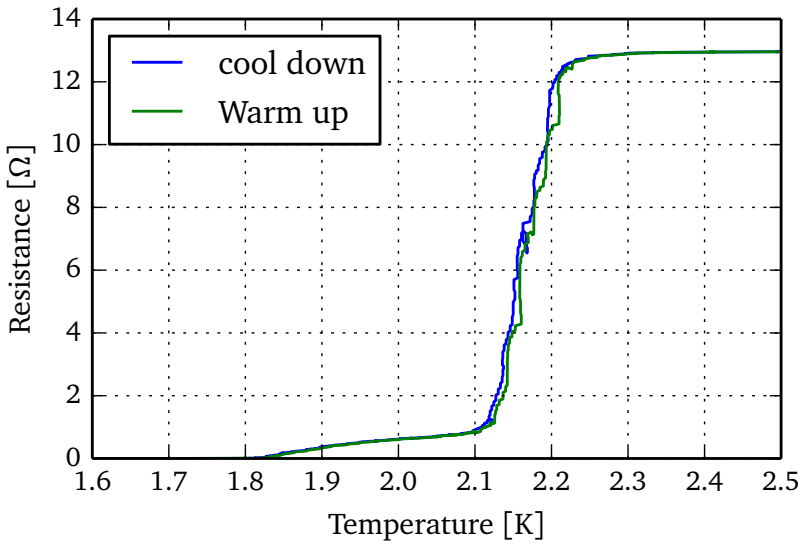

Figure (4.10): Measurement of the resistance of the same epitaxial layer of rhenium as the one we used to fabricate our microwave resonator.

4.5.3 Low internal quality factor

In the previous section, we have extracted an internal quality factor of about 15×10^3. These measurements have been performed on a rhenium layer of thickness 25 nm and deposited at 970 K. The crystallographic quality of this rhenium layer was not epitaxial and presented a granular texture. We then performed measurements on another rhenium layer deposited at 1040 K for a thickness of 100 nm. This rhenium film is a complete epitaxial layer (see Benjamin Delsol's thesis in [46]). Figure 4.11 presents resonances for these two different layers. The internal quality factor of resonators are very close with $Q_i = 13 \times 10^3$ and $Q_i = 15 \times 10^3$ for low and high crystallographic quality, respectively. The fact that the two different quality films present similar internal quality factor suggests that the limiting factor is not the quality of the rhenium film. Hereafter we propose a list of explanations about the cause of low internal quality factor and possible solutions.

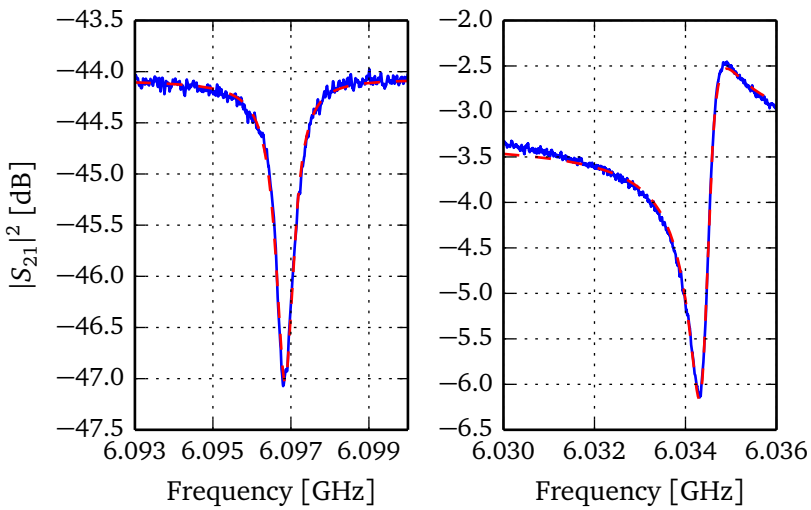

Figure (4.11): Two resonances measured on two different rhenium films. The left panel present the low crystallographic quality layer whereas the right panel the high quality one. Both of them exhibit approximately the same quality factor with $Q_i = 13 \times 10^3$ for the left panel and $Q_i = 14 \times 10^3$ for the right panel. However, due to the quality difference between the two films, an higher internal quality factor was expected for the right resonance.

Losses in our superconducting resonator may come from high frequencies radiation which enter by our coax cables and causes quasiparticles excitation. We can then add microwave filter at the input and output line in order to prevent high frequency radiation to reach the sample. Such filters are usually made with Eccosorb[120,121] which offers a good trade-off between low attenuation at some giga-hertz and strong attenuation for high microwave frequency.

Barends *et al.* showed the importance of having a multistage shielding to avoid losses due to infrared light[91]. They add a light-tight box surrounding the sample holder. The box is designed in order to avoid as much as possible photon leakage from outside to inside.

Moreover, the inside walls are painted with a black coating[122] to absorb residual photons. They show that the internal quality factors of a superconducting resonator can be increased by one order of magnitude by this strategy of a "box-in-a-box" compared to standard approaches.

Residual magnetic field may also cause losses in the superconducting resonator. The perpendicular magnetic field creates vortices in the superconducting layer. The motion of these vortices due to the application of a microwave signal to the resonator leads to energy dissipation. One strategy to prevent such losses is to etch holes in the superconductor layer[93,94]. These holes will act as pinning centers for Abrikosov vortices. Since the vortices are then blocked, the energy dissipation due to their motion disappears. In a coplanar waveguide geometry, holes have to be etched in the central line of the microwave resonator but also on the edges of the ground plane in order to prevent Abrikosov vortices motion due to counter-currents. Finally, authors of Ref. [93] showed that holes in the feedline improve the quality factor of resonator coupled to that feedline. Another approach is to make a resonator with a small central line (few micro-meters). The magnetic field needed to create a vortex is approximately equal to[123] ϕ_0/w^2 with ϕ_0 the flux quantum and w the width of the central line. For our design ($w \approx 5\,\mu$m), the residual magnetic field must be below $13\,\mu$T, which is acheivable using magnetic shielding.

4.6 Aluminium resonators

The characterisation of the aluminium microwave resonators presented in Section 3.2 is complicated due to the various elements coupled to the resonator. Indeed in order to make the resonator tunable, a SQUID is implemented within the central line of the resonator. It is placed approximately in the middle of the quarterwave resonator, see Fig. 3.7. There is also a shared inductor to magnetically couple the ancilla qubit which is close to the grounded end of the microwave resonator. Each element requires several parameters to be correctly modelled. This approach will lead to a complex description of the circuit with many adjustable parameters. In a first subsection we will prefer a description of the resonator as an equivalent RLC resonator. That way we will extract an equivalent inductance and capacitance of the circuit which will be useful in the following to determine the inductance of the SQUID. In a second subsection we will discuss the tunability and the extracted circuit parameters. In the last subsection, we will study the magnetic-flux dependence of the internal quality factor.

4.6.1 Characterisation of the resonance

By taking advantage of the tunability of the resonance frequency, we can calibrate the transmission measurement in order to only obtain the response of the microwave resonator. Indeed to realise the calibration we measure the transmission at a magnetic field close to $\phi_b/\phi_0 \approx 0.5$. This curve, in blue in Fig. 4.12, will be the reference curve. To obtain the calibrated transmission, we divide the measured transmission (in green in Fig. 4.12) by the reference transmission. This method allows to calibrates S_{21} measurement for any magnetic field far away from $\phi_b/\phi_0 \approx 0.5$, the magnetic field at which the reference S_{21} has been measured.

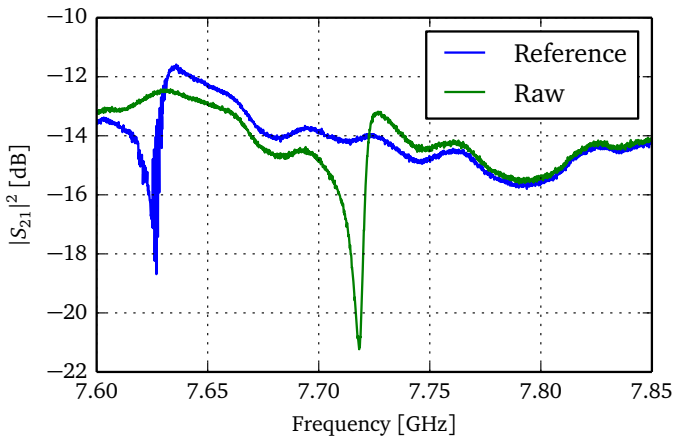

Figure (4.12): Measurement of $|S_{21}|^2$ for two different magnetic fields. One measurement, the blue curve, has been measured with at a magnetic field corresponding to the lowest resonance frequency of the resonator. This curve will be used as a reference for the calibration. The second curve, the green one, corresponds to the highest resonance frequency of the resonator. It is possible to calibrate the second measurement by using the reference curve, see Fig. 4.13

Figure 4.13 shows the result of the calibration for amplitude, top panel, and phase, bottom panel. We note that by this way we have corrected the data for the effect of spurious reflections along the transmission line. Then we fit the result of the calibration with Eq. (4.7). We extract the following parameters for the resonance: $Q_i = 2000$, $Q_c = 2000$, $L_{\text{bondings}} = 0.95\,\text{nH}$. With the method described above, we get the equivalent inductance and capacitance $L_{\lambda/4} = 1.9\,\text{nH}$ and $C_{\lambda/4} = 220\,\text{fF}$. The coupling capacitance is 9.5 fF.

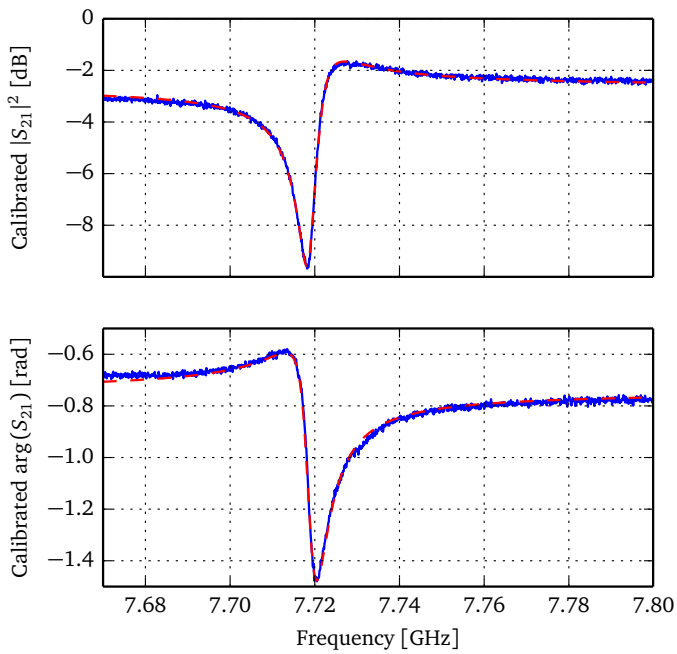

Figure (4.13): Relative resonance of a microwave resonator made from aluminium. The top panel presents the attenuation in decibel and the bottom panel, the phase response of the resonator. The dashed red line is the fit calculated from the model in Eq. (4.7). The fit gives the following parameters for the resonance: $Q_i = 2000$, $Q_c = 2000$, $L_{bondings} = 0.95\,\mathrm{nH}$.

4.6.2 A tunable resonance frequency

As we discussed in Section 3.2.1 the resonance frequency of the resonators is made tunable by the magnetic flux applied to a SQUID positioned along the central line of the resonator. Figure 4.14 presents transmission measurement as function of frequency and magnetic field. For these measurements, we use the magnetic coil presented in Section 2.5. The top/bottom panel were obtained by increasing/decreasing magnetic field. A hysteretic behaviour of the resonance as function of magnetic field is clearly visible.

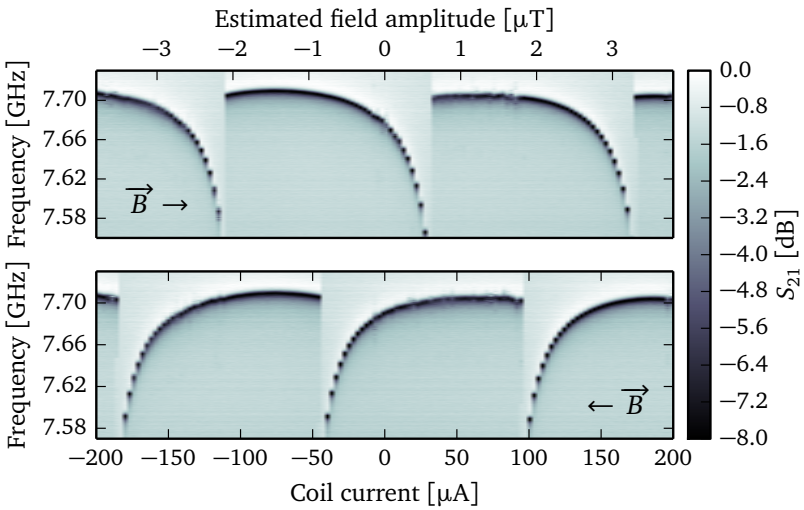

Figure (4.14): Transmission measurement as function of frequency and magnetic field. The magnetic field is shown via the current sent to the coil, in bottom, or via the estimated magnetic field, at the top (see Table 2.1). The estimation of the magnetic field does not take into account the effect of field concentration due to the superconductor ground plane which surround the SQUID. The top panel shows a sweep in magnetic field from negative to positive values and the bottom panel shows a sweep from positive to negative values. A hysteretic behaviour of the resonance dip as function of magnetic field is clearly visible.

Hysteretic behaviour of the resonance under a magnetic field.

We extract the resonance parameter with Eq. (4.7). Figure 4.15 presents the resonance frequency of the microwave resonator as function of the magnetic field. The sweep from negative to positive and from positive to negative magnetic field have been superimposed to enhance the hysteresis.

The model based on a SQUID embedded in a resonator (presented in Section 3.2.1) is unable to explain the hysteresis of our measurements. In this model we neglect the inductance of the SQUID which is not correct in this experiment. Taking into account the inductance

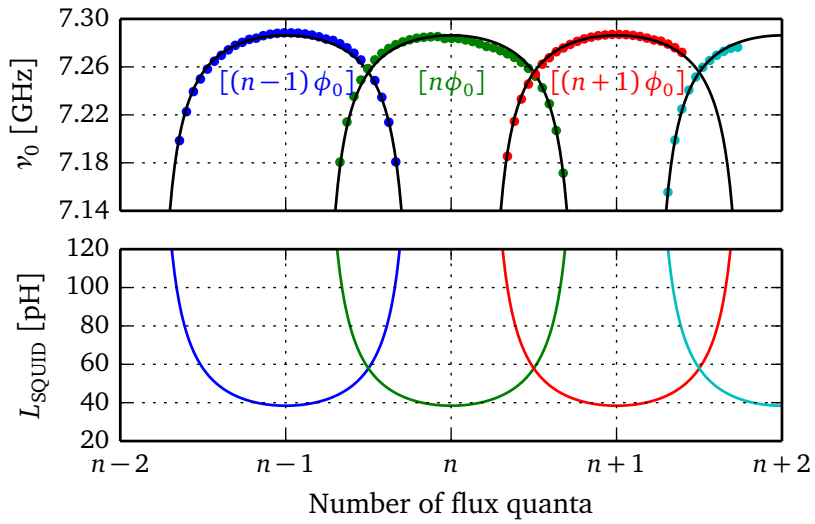

Figure (4.15): The top panel presents the resonance frequency of the microwave resonator as function of the number of flux quanta. The different arches are depicted in different colour, each arches corresponding to a defined flux state. The black solid line is the resonance dependence given by the model. The bottom panel presents the estimated SQUID inductance as function of the flux quanta.

related to the *in-phase* oscillations, we derive the SQUID inductance as:

$$L_{\mathrm{SQUID}}(\phi_{\mathrm{b}}) = \frac{\phi_0}{2\pi}\frac{1}{2I_c}\frac{1}{\cos[y(\phi_{\mathrm{b}})]} \tag{4.16}$$

where $y(\phi_{\mathrm{b}})$ is defined in Eq. (1.35). When the loop inductance becomes negligible $y \to \pi\phi_{\mathrm{b}}/\phi_0$, we recover the usual inductance of a SQUID derived in Eq. (3.6). When the loop inductance becomes comparable to the Josephson inductance, the internal flux is not equal anymore to the applied flux due to the apparition of screening current: $\phi_{\mathrm{int}} = \phi_{\mathrm{b}} + L_{\mathrm{loop}} I_{\mathrm{screening}}$. This effect creates the overlap between arches visible in Fig. 4.15 and the hysteretic behaviour. The SQUID inductance depends then on the Josephson inductance but also on the loop inductance.

By using the inductance in Eq. (4.16) to calculate the resonance frequency, we are able to correctly reproduce its dependence in magnetic flux. We extract from the fit the SQUID loop inductance, the critical current of SQUID junctions, and the resonator equivalent inductance. Moreover the fit leads to the calibration of the mutual inductance between the coil and the SQUID loop ($M_{\mathrm{coil}\to\mathrm{SQUID}} = 8.44\,\phi_0{\cdot}\mathrm{mA}^{-1}$).

The fit requires the value of the shared inductor between the resonator and the artificial atom. This value has been estimated through the geometry to be about 180 pH. The position of the SQUID and the total length of the resonator are also needed. We took the value defined by the circuit design.

The extracted SQUID inductance is of $L_{\mathrm{SQUID\ loop}} = 351\,\mathrm{pH}$ and the critical current of

$I_c = 1.8\,\mu$A. These extracted parameters are consistent with independent estimations. Indeed an estimation of the loop inductance with the design of the SQUID gives a value of $L_{\text{SQUID loop}}$ about 300 pH (a discrepancy of 15 %). The test junctions have a tunnel resistance at room temperature of 565 Ω which gives an expected critical current of about 0.78 μA (about twice smaller than the extracted value).

Dependence of the internal quality factor on magnetic flux

Figure 4.16 (b) and (c) show the internal and external quality factor as function of magnetic flux. The two curves show a flat behaviour when the flux is close to an integer number of flux quanta. Around half of flux quanta, the internal quality factor seems rather to become larger and the external quality factor smaller.

These results suggest that the internal quality factor of our resonator is not limited by the flux noise. Indeed a flux noise would induce[124] a growth of the resonance width proportionally to $\partial\,\nu_0/\partial\,\phi_{\text{b}}$. The internal quality factor should then exhibit its highest value around an integer value of flux quanta and shows a minimum value around half of flux quanta. This is in contradiction with the experimental results, indicating that the flux noise is not the limiting factor for the internal quality factor in our experiments.

Moreover, the internal quality factor is not limited by quasiparticles[125]. Indeed the SQUID can be seen as an inductor in parallel with a resistor. At $\phi_{\text{int}} = 0$, the SQUID inductance is very low so current can freely flow through it. When ϕ_{int} tends to half of flux quanta, the inductance increases by a factor two. As the inductance is increased, more of the current will flow in the resistor leading to an increase of the dissipation. The internal quality factor should exhibit its highest value at zero flux and should show a decrease as the magnetic field becomes closer to half of flux quanta. Our measurements presenting a flat dependence of the internal quality factor as function of the magnetic field, the presence of quasiparticles does not appear to be the limiting factor.

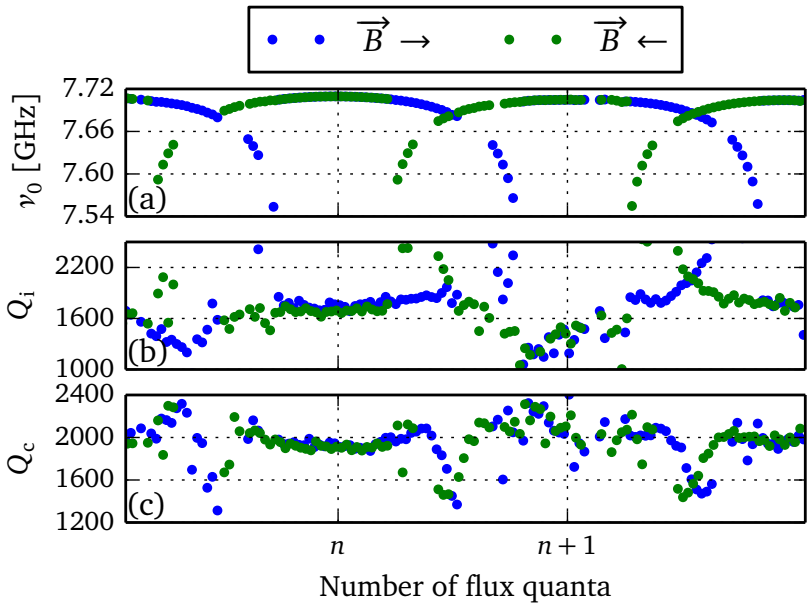

Figure (4.16): Resonance parameters extracted from data shown in Fig. 4.14. Blue points correspond to resonance parameters extracted from a magnetic field sweep from negative to positive values and green points correspond to a sweep from negative to positive values. Panel (a) shows the resonance frequency and the panel (b), and panel (c) presents the internal and external quality factor, respectively.

Chapter 5

The V-shape superconducting artificial atom

Contents

5.1 Introduction **176**
5.2 The V-shape coupled to a resonator **176**
5.2.1 Two-tone spectroscopy 176
5.2.2 Spectroscopy as function of the magnetic field 178
5.2.3 Extraction of the V-shape parameters 181
5.2.4 Estimation of the coupling strength 185
5.3 Logical qubit **185**
5.3.1 Coherent oscillations 185
5.3.2 Coherent oscillations as function of detuning and power 188
5.3.3 Relaxation time 191
5.3.4 AC-Stark shift and measurement-induced dephasing 192
5.3.5 Dependence of the qubit coherence versus probe power 196
5.4 Logical qubit anharmonicity measurements **200**
5.4.1 Two-photon process 200
5.4.2 Direct spectroscopy of the second level of the *in-phase* mode 201
5.4.3 A transition forbidden at $\phi_b = 0$ 203
5.5 Ancilla qubit **204**
5.5.1 Coherent oscillations of the ancilla qubit 204
5.5.2 Relaxation time of the ancilla qubit 206
5.6 Cross-anharmonicity **208**
5.6.1 Measurement via pulse sequence 208
5.6.2 Measurement via continuous drive 210
5.7 Experimental realisation of a V-shape energy diagram ? **212**

5.1 Introduction

This chapter is dedicated to the experimental study of the V-shape devices fabricated during my thesis. We present measurements performed on two nominally identical samples, called "V-shape-1" and "V-shape-2". The two quantum devices are coupled to two spatially separated microwave resonators. The two resonators are connected to the same feedline and exhibit a resonance frequency of 7.281 GHz and 7.719 GHz, respectively. This allows multiplexing measurement of the two V-shape samples during the same cool-down. The extracted parameters of the two samples are summarised in Appendix C.

In the first section, we will show a spectroscopy of the V-shape devices as function of the magnetic flux. Through the magnetic flux dependence of the different resonances, we will identify the logical and ancilla qubit energy level. An extraction of the V-shape circuit parameters will be realised with the analytical model presented in Chapter 1 and with a numerical solution of the Hamiltonian by using Kwant[126].

In the second and third section, we will investigate the dynamics of the logical qubit. We will present coherent oscillations between the two levels of the qubit, the so-called Rabi oscillations. Relaxation time of half a microsecond is measured and compared to other transmon qubit relaxation times presented in literature. The coherence of the logical qubit as function of the microwave field intensity is also presented and discussed.

In a fourth section, we will present coherent oscillations and relaxation time measurement performed on the ancilla qubit. We will show that the ancilla qubit has a relaxation time comparable to the logical qubit but a much shorter coherence time. Explanations of this shorter time will be discussed.

In the fifth section, we will present measurements demonstrating a large cross-anharmonicity between the logical and ancilla qubit. This feature is crucial to yield a V-shape energy diagram. The extracted cross-anharmonicity of the two samples will be compared to the theoretical prediction from the analytical model of the Chapter 1. A good agreement will be found, validating the circuit model of our experimental quantum device.

In the last section we will discuss the validity of our claim: The experimental realisation of a V-shape energy diagram. We will summarise the different properties that a quantum device should have to be a V-shape. We will show that our experimental realisation fulfills every point of the list allowing us to consider our quantum device as a V-shape quantum device.

5.2 The V-shape coupled to a resonator

5.2.1 Two-tone spectroscopy

The two-tone measurement allows to perform the spectroscopy of the V-shape via the microwave resonator. As its name suggests, the two-tone measurement involves two different microwave signals sent simultaneously. The first tone, called the *readout* tone, measures the transmission of the sample at a fixed frequency $\nu_{readout}$ which is slightly detuned from the resonance frequency of the resonator ν_0. The readout frequency is adjusted by measuring

the transmission of the resonator around its resonance frequency. The second tone, called the *probe* tone, performs the excitation of the V-shape energy levels. Its frequency ν_{probe} is swept to probe the resonance frequency of the V-shape levels while we keep measuring the transmission at $\nu_{readout}$.

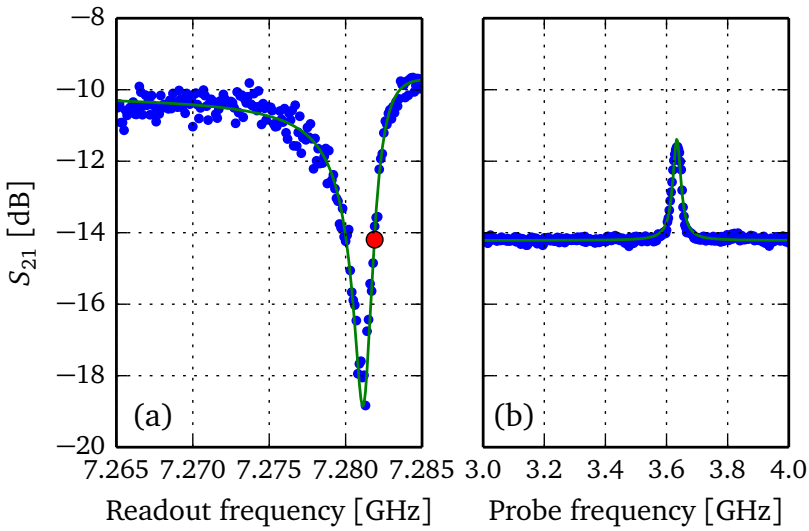

Figure (5.1): (a) Spectroscopy of the microwave resonator. The fit has been realised with the model in Eq. (4.7). (b) spectroscopy of the qubit resonance frequency. Data are fitted with a Cauchy–Lorentz distribution. Both measurements were performed at a temperature $T = 78\,\text{mK}$ *with an internal flux* $\phi_{in} \approx 0$ *and tone powers* $P_{readout} = -30\,\text{dBm}$ *and* $P_{probe} = -3\,\text{dBm}$ *at the output of the microwave sources.*

In Fig. 5.1 (a), we show the transmission measurement required to adjust the *readout frequency*. In the following, we have fixed the *readout frequency* to 7.282 GHz at 0.7 MHz above the cavity resonance frequency, as indicated by a red dot on the curve. For this *readout frequency*, the transmission is about −14 dB. In Fig. 5.1 (b), we present the transmission of the system while the probe frequency is swept around the logical qubit resonance frequency ν_{qb}. When ν_{probe} is far detuned from ν_{qb}, the transmission shows a flat dependence indicating no excitation of the qubit. As ν_{probe} is tuned in resonance with ν_{qb}, it may excite the logical qubit, leading to shift of ν_0 and consequently to a change in the transmission at ν_{readout}.

The shift of the resonator frequency as function of the qubit state observed in our two-tone spectroscopy is due to the so-called "dispersive shift"[18,27]. In the dispersive limit, when the detuning $\Delta = \omega_{\text{r}} - \omega_{\text{qb}}$ is large compared to the coupling strength g between the qubit and

the resonator, the Hamiltonian can be written as:

$$\begin{aligned}\mathscr{H} &= \overbrace{\hbar\omega_{\mathrm{r}}\widehat{n}}^{\text{resonator}} + \overbrace{\hbar\chi\widehat{\sigma}_{\mathrm{z}}\widehat{n}}^{\text{dispersive coupling}} + \overbrace{\frac{\hbar}{2}\omega_{\mathrm{qb}}\widehat{\sigma}_{\mathrm{z}}}^{\text{qubit}} \\ &= \hbar(\omega_{\mathrm{r}} + \chi\widehat{\sigma}_{\mathrm{z}})\widehat{n} + \frac{\hbar}{2}\omega_{\mathrm{qb}}\widehat{\sigma}_{\mathrm{z}} \end{aligned} \tag{5.1}$$

with $\chi = g^2/\Delta$ the dispersive coupling strength. Equation (5.1) indicates that the resonance frequency of the resonator depends on the qubit state through the dispersive coupling strength χ. Thus depending on the qubit state, the cavity resonance frequency can change by an amount of 2χ. It is this frequency shift that is measured via the two-tone spectroscopy in Fig. 5.1 (b).

5.2.2 Spectroscopy as function of the magnetic field

Magnetic flux dependence of the V-shape is measured via two-tone spectroscopy performed at different magnetic field. The magnetic field is applied via a magnetic coil surrounding the sample (coil 2 in Table 2.1). Due to the SQUID embedded in the central line of the resonator, the readout frequency has to be adjusted at each change of magnetic field. Thus the complete protocol explained in the previous section is entirely repeated for each magnetic flux. We note that the readout frequency changes with magnetic flux as well as the transmission background. In Fig. 5.2, we present the adjusted readout frequency as function of magnetic field. We observe more than three periods as function of the magnetic flux.

In Fig. 5.3 (a), (b) and (c), we present the magnetic flux dependence of the three resonances observed in the two-tone spectroscopy. For sake of clarity, we present here results where the background of each two-tone measurement has been subtracted. We observe two periods for the V-shape resonances. The two lowest resonances, panels (a) and (b), exhibit strong flux dependence and seem to drop to zero between two maxima. The third resonance, panel (c), presents a limiting variation of the resonance frequency.

We will show in the next section that the two lowest resonances correspond to the first and second transition of the logical qubit and the highest resonance to the first transition of the ancilla qubit.

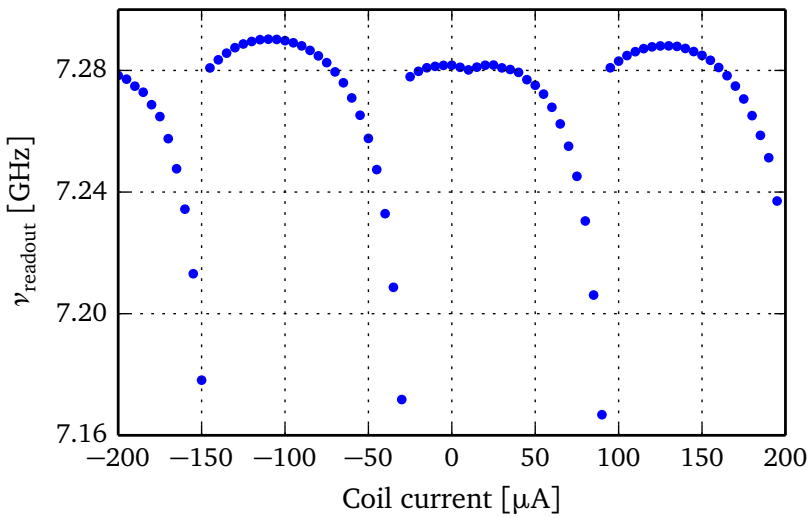

Figure (5.2): Readout frequency chosen to perform the two-tone spectroscopy as function of magnetic field. The measurement has been performed on the sample "V-shape-1" with a base temperature $T = 65\,\text{mK}$ *and a tone powers* $P_{readout} = -40\,\text{dBm}$ *and* $P_{probe} = -15\,\text{dBm}$. *Data were acquired during* $T_{readout} = 99\,\mu\text{s}$ *and averaged* 100 *times.*

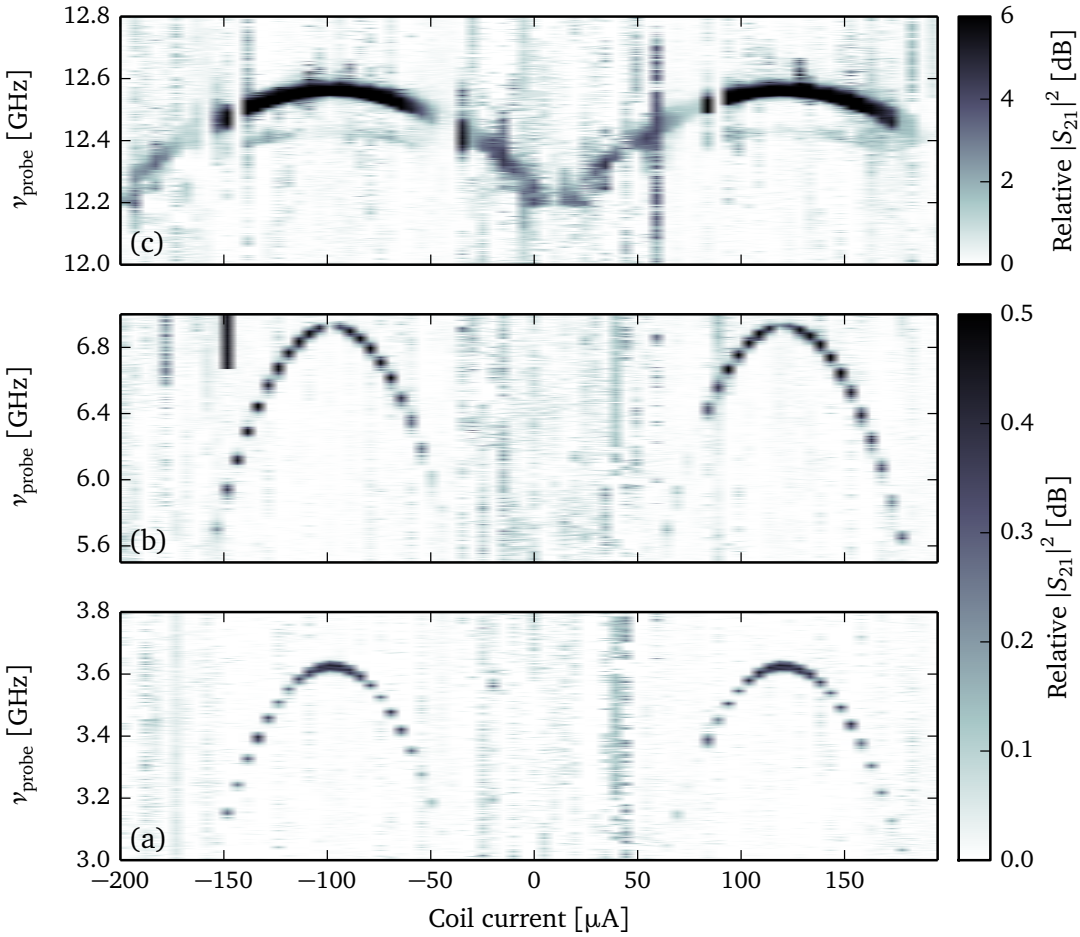

Figure (5.3): (a), (b) and (c) first, second, and third resonances of the V-shape energy diagram. We note that the background of each two-tone measurement has been subtracted for the sake of clarity. The panel (a) and (c) corresponds to the transition of the logical and ancilla qubit resonance, respectively. The panel (b) shows the second transition of the logical qubit. The measurement has been performed on the sample "V-shape-1" with a base temperature $T = 65\,\text{mK}$ *and tone powers* $P_{readout} = -40\,\text{dBm}$ *and* $P_{probe} = -15\,\text{dBm}$. *Data were acquired during* $T_{readout} = 99\,\mu\text{s}$ *and averaged* 100 *times.*

5.2.3 Extraction of the V-shape parameters

From Fig. 5.3, we extract the resonance frequencies of the V-shape energy levels. Resonance frequencies versus flux are plotted in Fig. 5.4. The magnetic-flux dependence of the artificial atom resonances can be fitted with the analytical model presented in Section 1.1.3. We remind that, in this model, only three parameters are necessary to fit data namely, the critical current and the capacitance of junctions, and the loop inductance. With Eq. (1.46) we fit the magnetic flux dependence of the resonance frequencies (see solid black line in Fig. 5.4), the extracted parameters are $I_c = 6.4\,\text{nA}$, $C = 30.5\,\text{fF}$, and $L_{\text{loop}} = 11.4\,\text{nH}$.

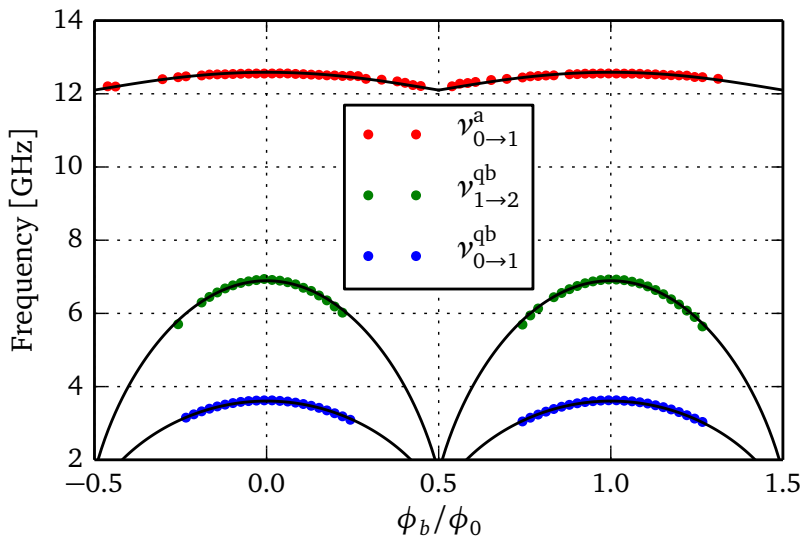

Figure (5.4): Data points extracted from resonances shown in Fig. 5.3 (sample "V-shape-1"). From Eq. (1.46) we obtain the theoretical curves, depicted in solid black line, with the following parameters $I_c = 6.4\,\text{nA}$, $C = 30.5\,\text{fF}$, and $L_{loop} = 11.4\,\text{nH}$.

However such extracted parameters do not validate the assumptions of the analytical model used for the calculation. Indeed one of the main assumptions made during the derivation in Chapter 1 was to perform a Taylor expansion of the two-dimensional potential close to the bottom of one potential well (see Section 1.1.2). This supposes a strong localisation of the states in one potential. This assumption is correct when the energy barrier between the potential well and its first neighbouring well is largecompared to the energy of the levels. From the extracted parameters, we can calculate the barrier height. At $\phi_b = 0$, $\Delta U = 4E_J = 12.7\,\text{GHz}$ which is only two times larger than the second transition frequency of the logical qubit. When ϕ_b increases and comes closer to 0.5, the ratio $\Delta U/\nu^{qb}_{0\to2}$ decreases down to 0. The analytical calculation is no more valid and is unable to give correct values of the circuit parameters of our measured V-shape samples. Therefore we decided to fit data by numerically solving the Hamiltonian derived in Eq. (1.30).

For this purpose we used the Python library Kwant[126] written by Christoph W. Groth *et*

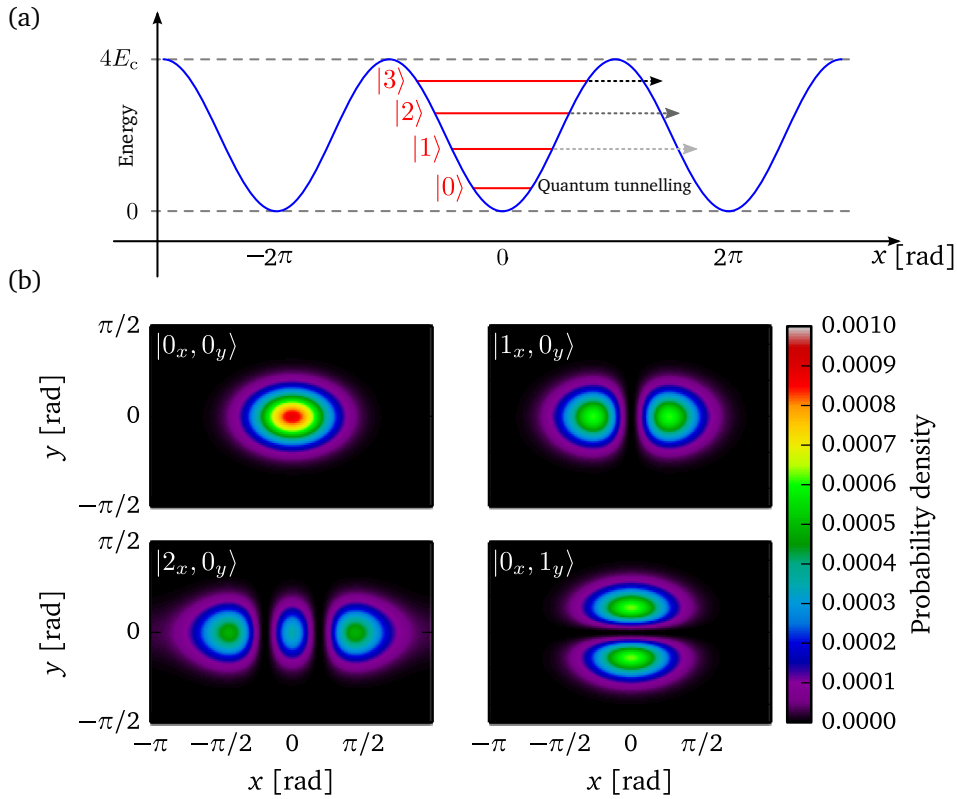

Figure (5.5): (a) cut of the potential along the x direction at $\phi_b = 0$. The three first energy levels of the logical qubit mode are depicted by solid red lines in the potential well center at $x = 0$. The quantum tunnelling rate is illustrated by dashed grey lines which become darker when the rate increases. (b) Probability density calculated numerically[126] *for the state (from left to right and top to bottom) $|0_x, 0_y\rangle$, $|1_x, 0_y\rangle$, $|2_x, 0_y\rangle$, and $|0_x, 1_y\rangle$ at $\phi_b = 0$. We note that the second excited state of the logical qubit has a nonzero probability density at the boundary between potential wells at $x = \pm\pi$.*

al.. The numerical calculation consists of a solution of the discretized Schrödinger equation on a square lattice in the (x, y) plane[1]. To get an idea about the delocalisation of the eigenstates, we performed the calculation of the eigenstates of the system, see Fig. 5.5 (b), for the states $|0_x, 0_y\rangle$, $|1_x, 0_y\rangle$, $|2_x, 0_y\rangle$, and $|0_x, 1_y\rangle$. We observe a very good localisation of the states $|0_x, 0_y\rangle$, $|1_x, 0_y\rangle$, and $|0_x, 1_y\rangle$ which correspond to the ground, the logical qubit, and the ancilla qubit state, respectively. In contrast, we note a delocalisation of the $|2_x, 0_y\rangle$ state (which corresponds to the second transition of the logical qubit) to its neighbouring wells visible with a purple cloud on the left and right of the plot. This is a proof that our measured

[1]Along the x direction Kwant used periodic boundary conditions to, virtually, take into account all potential wells. Along the y direction, the parabola due to the inductor energy creates a well in which the energy is confined. Numerically the boundary along y limits the system to energy below 100 GHz, well above energy considered in our problem.

V-shape resonance frequencies have to be fitted by taking into account the full phase space of the potential.

With Kwant, we perform numerical calculation of the energy levels spectrum as function of magnetic flux. By fitting the experimental spectrum with these numerical results in Fig. 5.6 we extract a second set of circuit parameters: $I_c = 8\,\mathrm{nA}$, $C = 40\,\mathrm{fF}$, and $L_{\mathrm{loop}} = 7.5\,\mathrm{nH}$.

We observe on Fig. 5.6 that the magnetic flux dependence of V-shape resonances is well predicted by the numerical calculation. In particular, at $\phi_b = 0$, the value of the V-shape resonances are very well predicted by the numerical calculation.

We remark in Fig. 5.6 a small discrepancy between the measured magnetic flux dependence of the ancilla resonance and the dependence predicted by the numerical integration. The maximum of difference is reached at $\phi_b = 0.5$, with a discrepancy of 1.5 %. This discrepancy is still not fully understood but our main explanation is based on an incorrect modelling of the super inductor. Indeed the Josephson junctions chain was modeled as an single linear inductor. We then neglect the capacitance of the Josephson junctions. These capacitances could modify the magnetic flux dependence of the ancilla resonance frequency.

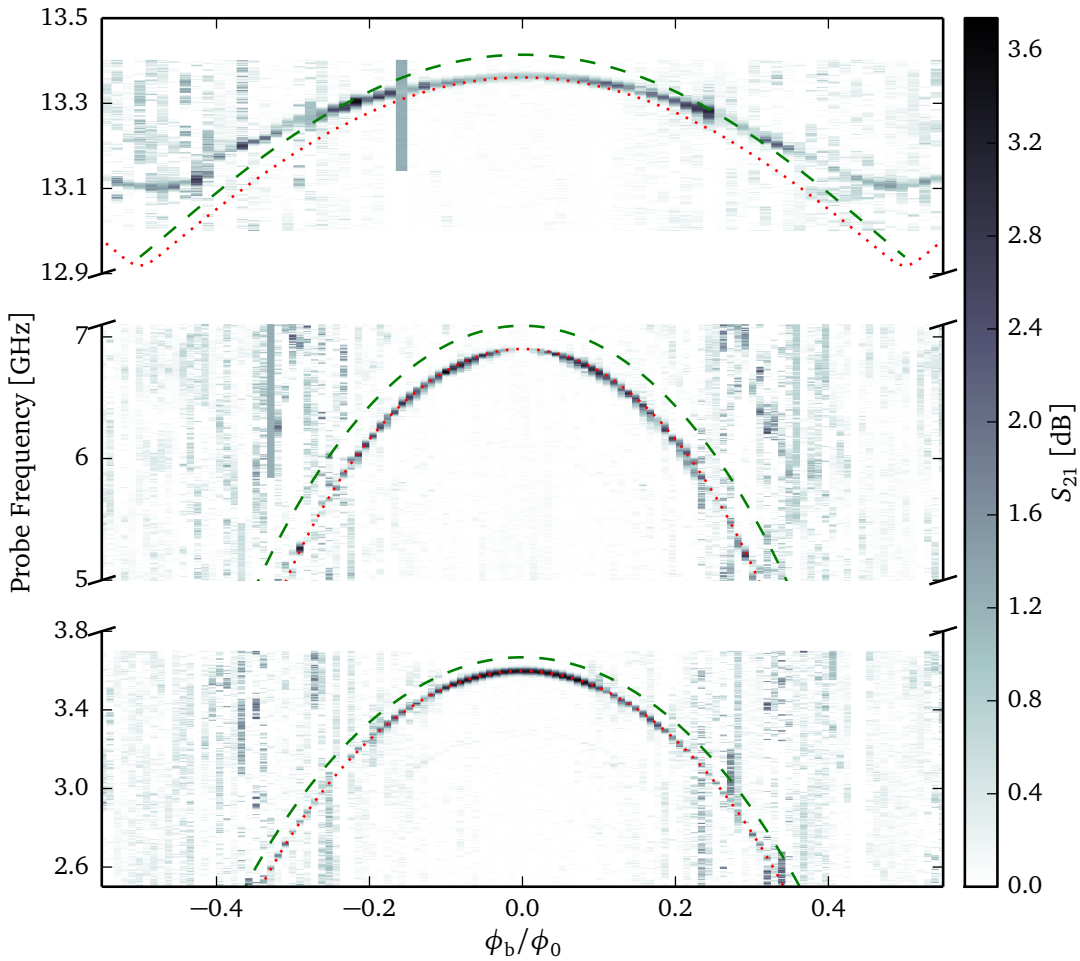

Figure (5.6): Two-tone spectroscopy as function of the magnetic field for sample "V-shape-2". From the following parameters $I_c = 8\,\mathrm{nA}$, $C = 40\,\mathrm{fF}$, and $L_{loop} = 7.5\,\mathrm{nH}$, we plot the eigenenergies calculated from Kwant, in dotted red, and the analytical formula, in dashed green. The measurement has been performed on the sample "V-shape-1" with a base temperature $T = 35\,\mathrm{mK}$ and tone powers $P_{readout} = -33\,\mathrm{dBm}$ and $P_{probe} = -10\,\mathrm{dBm}$. Data were acquired during $T_{readout} = 2\,\mu\mathrm{s}$ and averaged 10^4 times.

5.2.4 Estimation of the coupling strength

The dispersive coupling between the resonator and the qubits produces a shift of the resonance frequency of the microwave resonator of 2χ depending on the qubit state. We present here a measurement of the χ value for the logical and ancilla qubit. We present the protocol to realise this experiment for the logical qubit. The same protocol has been used for the ancilla qubit.

The experiment consists of two microwave pulses sent sequentially, see Fig. 5.7 (a). The logical qubit is prepared from in the $|e\rangle$ state by a calibrated microwave pulse called a π pulse. The π pulse for the logical qubit has been calibrated through Rabi oscillations. We obtained a duration of $T^{\mathrm{qb}}_{\pi\mathrm{pulse}} = 116\,\mathrm{ns}$ with a power $P^{\mathrm{qb}}_{\mathrm{probe}} = -6\,\mathrm{dBm}$. After this first pulse, we suppose the qubit to be in its excited state. A second microwave pulse is then sent to perform the readout of the cavity. Since the qubit is excited, the cavity exhibits a new resonance frequency $\widetilde{\omega}_{\mathrm{r}} = \omega_{\mathrm{r}} - 2\chi_{\mathrm{qb}}$.

Figure 5.7 (b) presents such measurements for the logical and ancilla qubit. From these curves, we extract $\chi_{\mathrm{qb}}/(2\pi) = 1.25\,\mathrm{MHz}$ and $\chi_{\mathrm{a}}/(2\pi) = 0.45\,\mathrm{MHz}$.

However, the relaxation time of the logical and ancilla qubit are about half a microsecond approximately, see Section 5.3.3 and Section 5.5.2, which corresponds to the same duration as the readout pulse. We then estimate the error made on the dispersive coupling shift extraction to be about 50 %. In the case of the logical qubit, the measured dispersive shift is lowered of 0.625 MHz and for the ancilla of 0.225 MHz. By taking into account the relaxation, we obtain the corrected dispersive shift $\chi_{\mathrm{qb}}/(2\pi) = 1.9\,\mathrm{MHz}$ and $\chi_{\mathrm{a}}/(2\pi) = 0.75\,\mathrm{MHz}$. From the detuning between the resonator and the qubits $\Delta_{\mathrm{qb,\,r}}/(2\pi) = 3.644\,\mathrm{GHz}$ and $\Delta_{\mathrm{a,\,r}}/(2\pi) = 5.341\,\mathrm{GHz}$, we extract the coupling strengths $g_{\mathrm{qb}}/(2\pi) = 83\,\mathrm{MHz}$ and $g_{\mathrm{a}}/(2\pi) = 63\,\mathrm{MHz}$.

From sample design, we estimate the value of coupling strength $g_{\mathrm{qb}}/(2\pi) = 95\,\mathrm{MHz}$ and $g_{\mathrm{a}}/(2\pi) = 196\,\mathrm{MHz}$ (see Eq. (1.90) and Eq. (1.91)). We remark a large discrepancy between the extracted coupling strength and their estimation from design parameters. This can be explained by the complexity of Eq. (1.90) and Eq. (1.91). Indeed the estimation of the coupling strengths requires the knowledge of nine design parameters. Furthermore, Eq. (1.90) and Eq. (1.91) do not take into account the SQUID of the resonator. Since the SQUID modifies the electromagnetic field distribution along the microwave resonator, it influences the strength of the coupling at the position of the V-shape device.

5.3 Logical qubit

5.3.1 Coherent oscillations

The observation of coherent oscillations, also called Rabi oscillations is performed via a two-tone measurement. It consists of a sequence of two pulses as shown in Fig. 5.8 (a). The first pulse, called excitation pulse, is sent at the resonance frequency of the qubit ν_{qb} during a variable duration Δt. During this duration it will drive the qubit and eventually inverse its population. The second pulse, called readout pulse, is sent just after the first one to perform the readout of the cavity. Indeed due to the dispersive coupling, the population of the qubit

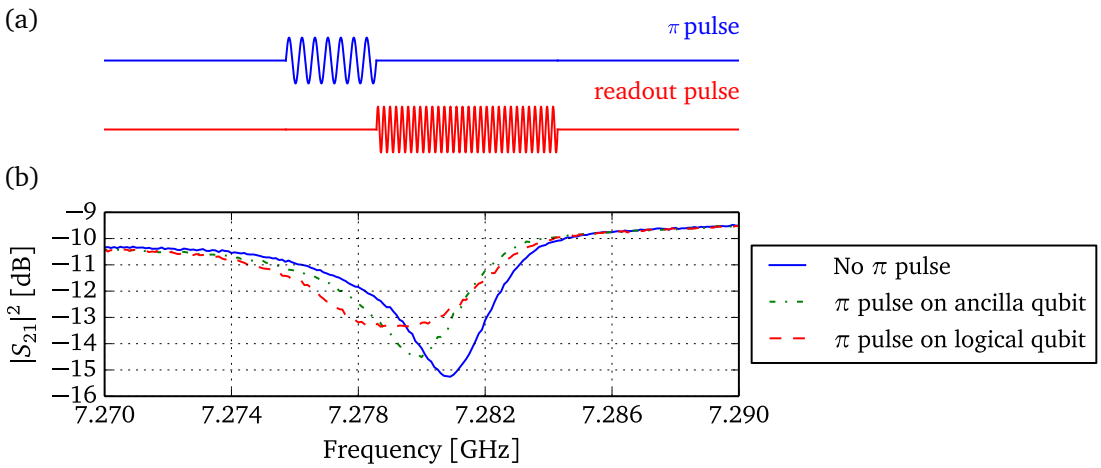

Figure (5.7): (a) Scheme of the pulse sequence. (b) Spectroscopy of the microwave resonator resonance dip. In solid blue we show a spectroscopy of the resonator with no excitation pulses sent to the qubits. The readout pulse duration was $T_{readout} = 416\,\text{ns}$ *for a readout power of* $P_{readout} = -25\,\text{dBm}$*. The dashed red line shows the same spectroscopy but with a* π *pulse,* $T^{qb}_{\pi pulse} = 116\,\text{ns}$ *and* $P^{qb}_{probe} = -6\,\text{dBm}$*, sent to the logical qubit before the measurement of the cavity. The green dashed-dot curve presents the same measurement with a* π *pulse,* $T^{a}_{\pi pulse} = 32\,\text{ns}$ *and* $P^{a}_{probe} = -9\,\text{dBm}$*, on the ancilla qubit. The measurement have been performed at a base temperature* $T = 65\,\text{mK}$ *and close to* $\phi_b = 0$ *on the sample "V-shape-1". Data were averaged* 75×10^3 *times.*

excited level will affect the cavity resonance frequency. This modification is measured via a change in the transmission at the readout frequency ν_{readout}. In order to reach a high enough signal-to-noise ratio, the measurement is repeated 10^5 times.

Figure 5.8 shows typical oscillations for the logical qubit. We observe oscillations related to the population of the qubit levels. The frequency of these oscillation is denoted Ω_{Rabi} and depends on the amplitude of the excitation pulse (see Fig. 5.10). At $\Delta t = 0$, no excitation pulse is sent and the qubit is in its ground state. At $\Delta t \approx 30\,\text{ns}$, the population of the qubit is inverted with a major part of the population sitting at the excited level. A pulse of this duration, which inverses the qubit population, is usually called a π pulse.

Figure 5.8 also presents exponential damping of the oscillations. The characteristic Rabi decay time of the damping is denoted T_2^{Rabi} and it is related to qubit decoherence under a microwave field. Due to the damping, a π pulse will never fully invert the qubit population. We will see later that it is possible to estimate the population of the excited state after a π pulse by taking into account the Rabi decay time.

Julien Claudon discussed the dynamics of an anharmonic oscillator driven by an oscillating electromagnetic field in his thesis [56]. In the simple case where the anharmonic oscillator can be considered as a two level system, the population of the excited state and the Rabi

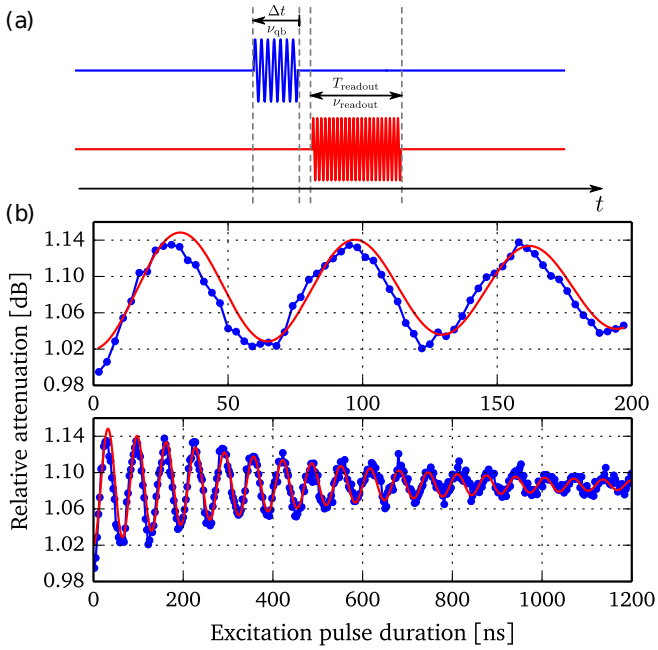

Figure (5.8): (a) Scheme of pulses sequence. The excitation pulse at the top (blue) has a variable duration Δt. Its frequency corresponds to the resonance frequency of the logical qubit. The readout pulse at the bottom (red) is sent just after the excitation pulse. It has a fixed duration, $T_{readout}$. (b) Shift of the cavity resonance peak as function of excitation pulse duration. We observe damped oscillations related to population of the excited level of the qubit. The damping is a signature of the decoherence of the system under a microwave field. From Eq. (5.2), we extract a Rabi frequency of $\Omega_{Rabi}/(2\pi) = 15.41 \pm 0.01$ MHz and $T_2^{Rabi} = 480 \pm 22$ ns. The measurement has been performed at a base temperature $T = 65$ mK with a excitation power $P_{excitation} = 5$ dBm, a readout power $P_{readout} = -25$ dBm and a magnetic flux $\phi_b = 0$ on the sample "V-shape-1". Data were acquired during $T_{readout} = 192$ ns and averaged 10^5 times.

frequency are given by[58]:

$$P_e(t) = \frac{1}{2}\left[1 - \cos(\Omega_{\text{Rabi}} t)\exp\left(-\frac{t}{T_2^{\text{Rabi}}}\right)\right], \tag{5.2}$$

$$\Omega_{\text{Rabi}} = \sqrt{\Omega_{\text{field}}^2 + \left(\omega_{\text{excitation}} - \omega_{\text{qb}}\right)^2}, \tag{5.3}$$

where Ω_{field} corresponds to the amplitude of the excited field. Figure 5.8 shows the fit performed using Eq. (5.2). We extract $\Omega_{\text{Rabi}}/(2\pi) = 15.41$ MHz and $T_2^{\text{Rabi}} = 480 \pm 22$ ns. We also get the duration of a π pulse, $T_{\pi\text{ pulse}} = 32$ ns.

From the Rabi decay time and Rabi frequency, we estimate to 96.7 ± 0.3 % the population of the qubit excited state after a π pulse.

5.3.2 Coherent oscillations as function of detuning and power

We performed measurements of Rabi oscillation as function of the excitation frequency. We follow the same protocol described in the previous section but the frequency of the excitation tone is now swept around the qubit resonance frequency.

We obtain a 2D plot with the transmission $|S_{21}|^2$ versus excitation frequency and pulse duration in Fig. 5.9 (a). Each vertical line exhibits Rabi oscillations with different Rabi frequency. The overall picture exhibits a "chevron" pattern with a Rabi frequency minimum at the qubit resonance frequency.

We fit Rabi oscillations for all excitation frequencies with Eq. (5.2). We show the extracted Rabi frequency as function of the excitation frequency in Fig. 5.9 (b). From Eq. (5.3) we can precisely describe the Rabi frequency versus the detuning (see Fig. 5.9 (c)). We extract $\nu_{\mathrm{qb}} = 3.630\,\mathrm{GHz}$ and $\Omega_{\mathrm{field}}/(2\pi) = 6.28\,\mathrm{MHz}$, the qubit resonance frequency and the amplitude of the microwave field, respectively.

The extracted microwave field amplitude is consistent with our experimental setup. Indeed these measurements were realised with an output power of the microwave source of $-5\,\mathrm{dBm}$. We estimate the attenuation of the line to be about $-99\,\mathrm{dB}$. We deduce a microwave power propagating along the feedline at about $P_{\mathrm{feedline}} = 40\,\mathrm{fW}$. Using Eq. (2.10) to calculate the intra-cavity energy due to the excitation drive at the qubit frequency, we obtain $\Omega_{\mathrm{field}}^{\mathrm{estimation}} = |S(\omega)|^2 P_{\mathrm{feedline}}/h = 6.7\,\mathrm{MHz}$. The discrepancy between the estimated value and the measurement is below 10 % which is reasonable.

In Fig. 5.10 (a), we present coherent oscillations as function of the excitation tone power. We observe an increase of the Rabi frequency as the excitation power increases. Using Eq. (5.2), we extract Rabi frequency oscillations versus the excitation tone power (see Fig. 5.10 (b)).

From Eq. (5.3) we can extract the microwave amplitude of the field Ω_{field} as function of the Rabi frequency Ω_{Rabi}. This calibration leads to the curve shown in Fig. 5.10 (c) where the Rabi frequency is plotted as function of the excitation field amplitude. We remark that the theoretical curve does not drop to zero at zero field amplitude. This is due to a small detuning between the frequency of the excitation tone and the qubit frequency, here about 1 MHz, which leads to a qubit frequency of $\nu_{\mathrm{qb}} = 3.637\,\mathrm{GHz}$. The qubit resonance frequency extracted from the Rabi excitation power dependence is in agreement with the qubit frequency extracted via the Rabi excitation frequency dependence. We remark a linear dependence of the Rabi frequency on the amplitude of the driving field. This linear dependence is an indication of the two-level dynamics of the system. Indeed if higher energy levels were involved in the dynamics of the Rabi oscillations, the curve would show a deviation from the linear dependence at high drive power[56], which is not the case here. In Section 5.4 we will show that the logical qubit anharmonicity is about 300 MHz, well above the Rabi frequencies observed here. This validates the approximation of a two-level system in these range of microwave amplitude.

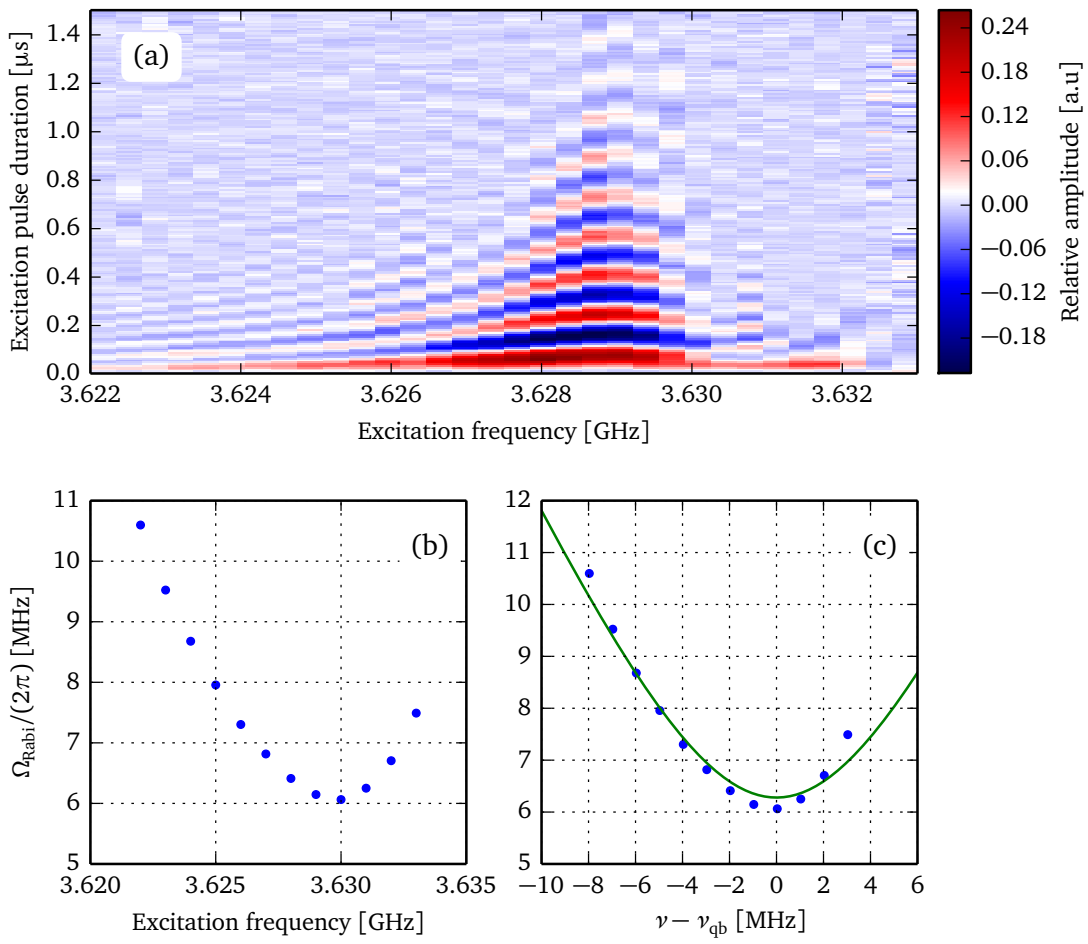

Figure (5.9): (a) Rabi oscillations as function of the excitation frequency. A Savitzky–Golay low-pass filter[82,83] *whose equivalent cutoff frequency is about* 0.2 MHz *has been used to filter low frequency noise. (b) and (c) Rabi frequency extracted from (a) as function of the excitation frequency and detuning, respectively. The green solid line shows fit result from Eq.* (5.3)*. We extract* $\nu_{qb} = 3.6303\,\text{GHz}$ *and* $\Omega_{field}/(2\pi) = 6.11 \pm 0.08\,\text{MHz}$*, the qubit resonance frequency and the amplitude of the microwave field, respectively. The experiment has been performed at a base temperature* $T = 65\,\text{mK}$ *with an excitation power* $P_{excitation} = -5\,\text{dBm}$*, a readout power* $P_{readout} = -25\,\text{dBm}$ *and a magnetic flux* $\phi_b = 0$ *on the sample "V-shape-1". Data were acquired during* $T_{readout} = 192\,\text{ns}$ *and averaged* 2×10^5 *times.*

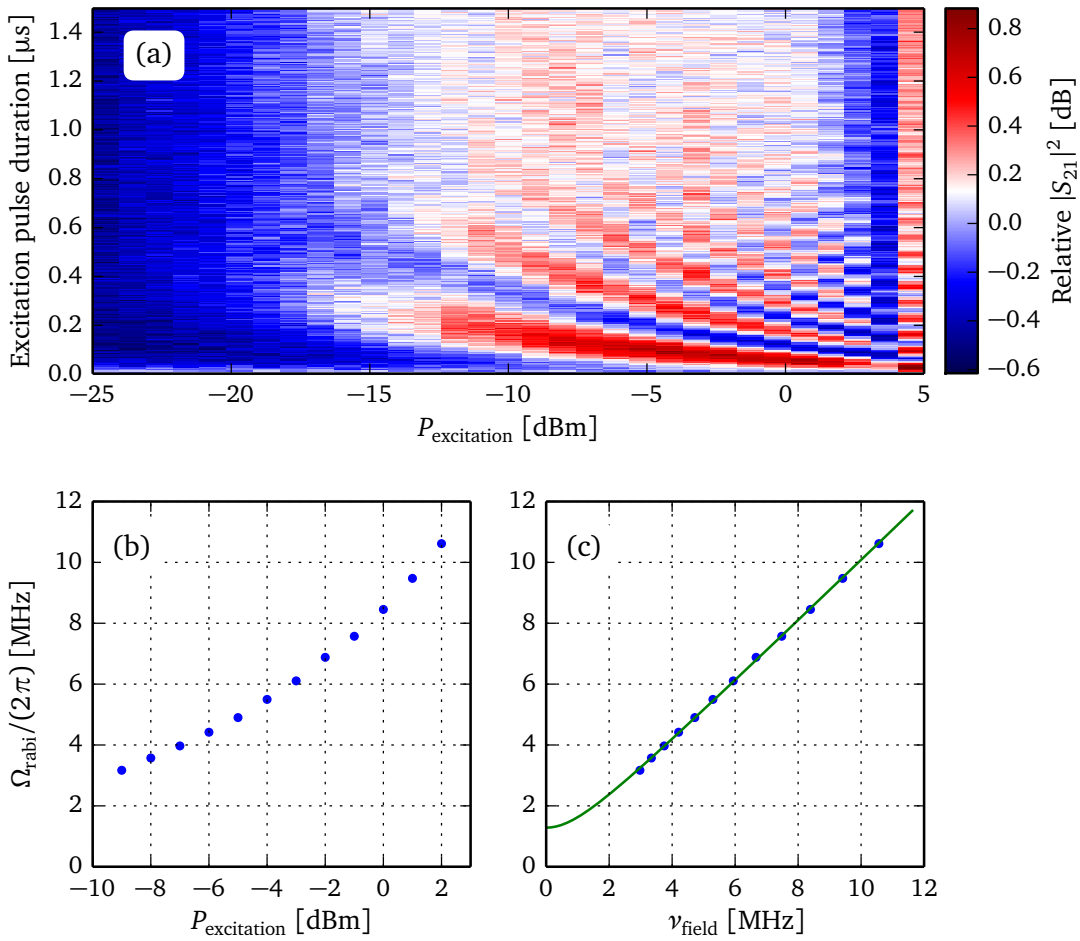

Figure (5.10): (a) Rabi oscillations as function of the excitation power. (b) Rabi frequency extracted from (a) as function of the excitation power at the output of the microwave source. (c) Rabi frequency as function of the amplitude of the electromagnetic field. The green solid line shows the fit result from Eq. (5.3). We extract the detuning between the excitation frequency and the qubit frequency $\nu_{probe} - \nu_{qb} = 1.28\,\text{MHz}$ *leading to a qubit frequency of* $\nu_{qb} = 3.6367\,\text{GHz}$. *The experiment has been performed at a base temperature* $T = 65\,\text{mK}$ *with a probe frequency* $\nu_{probe} = 3.638\,\text{GHz}$ *, a readout power* $P_{readout} = -25\,\text{dBm}$ *and a magnetic flux* $\phi_b = 0$ *on the sample "V-shape-1". Data were acquired during* $T_{readout} = 384\,\text{ns}$ *and averaged* 4×10^5 *times.*

5.3.3 Relaxation time

The measurement of the relaxation time T_1 is performed via a two-tone measurement. It consists of a sequence of two pulses as shown in Fig. 5.11 (a). The first pulse, called excitation pulse, has been calibrated to inverse the population of the qubit from $|g\rangle \rightarrow |e\rangle$. After this first pulse, we send a second pulse, the readout pulse, which perform the readout of the cavity. We vary the delay between the first and second pulse to observe the energy relaxation of the qubit. The measurement is averaged 10^5 times.

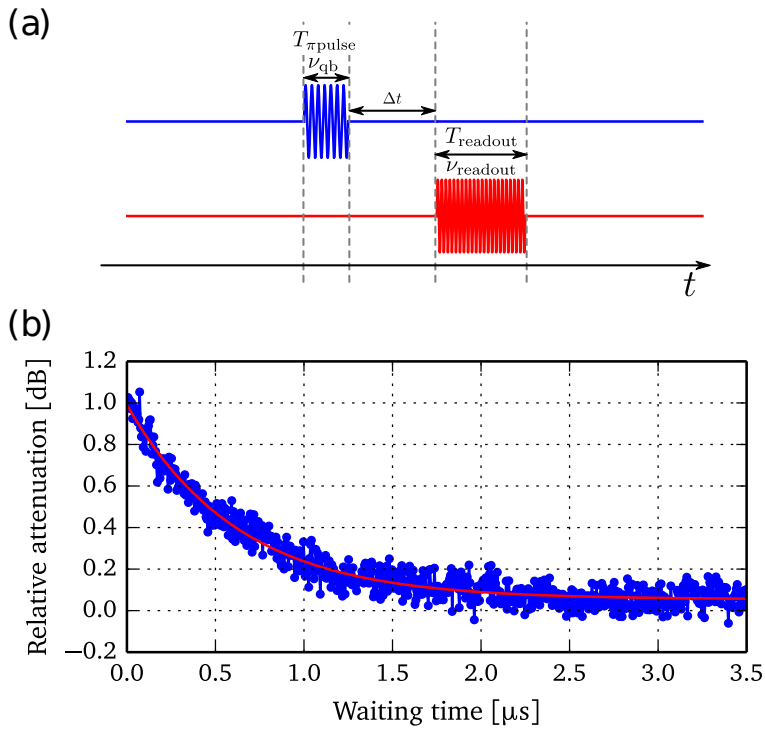

Figure (5.11): (a) Scheme of pulses sequence. The excitation pulse, in top blue, is calibrated to inverse the population of the qubit from $|g\rangle \rightarrow |e\rangle$. After this first pulse, we wait during a variable delay before to send a second pulse, the readout pulse in bottom red, which perform the readout of the cavity. (b) Shift in the transmission at the readout frequency as function of the waiting time. We observe exponential decay related to the population of the excited state. By fitting the data with an exponential decay law, we extract the relaxation time $T_1 = 600 \pm 10$ ns. The measurement has been performed at a base temperature $T = 65$ mK with a excitation power $P_{excitation} = 5$ dBm, a readout power $P_{readout} = -25$ dBm and a magnetic flux $\phi_b = 0$ on the sample "V-shape-1". Data were acquired during about $T_{readout} = 192$ ns and averaged 10^5 times.

Figure 5.11 (b) presents typical relaxation decay for the logical qubit. At $\Delta t = 0$ the population of the excited state is maximum. When the delay time increases, the population of

the excited state decreases down to zero. By fitting the experimental data with an exponential decay law, we extract the relaxation time $T_1 = 600 \pm 10\,\text{ns}$.

The relaxation time of our logical qubit is comparable with the first generation of transmon qubit[54]. Thus D. I. Schuster *et al.*[127] measured a transmon with a relaxation time of 500 ns ($(E_J/E_C)^* \approx 20$) and J. Majer *et al.*[128] a relaxation time of 200 ns ($(E_J/E_C)^* \approx 37$) in 2007. However, A. A. Houck *et al.*[129] have demonstrated that the measured T_1 was due to an enhancement of the Purcell effect via the microwave resonator. The Purcell decay rate calculated for our circuit gives $\Gamma^{-1}_{\text{purcell}} = (\Delta/g)^2\kappa^{-1} = 230\,\mu\text{s}$. Our measured relaxation time is three orders of magnitude shorter (half a micro second), indicating the presence of other relaxation processes.

Dielectric losses can be significant for superconducting qubits[130]. In dielectric material, the losses are usually modelled through a parameter, $\tan(\delta)$, corresponding to the ratio (or angle in a complex plane) of the lossy permittivity to the lossless one[131]. The loss tangent of silicon and oxidised silicon have been measured at low temperature ($T < 100\,\text{mK}$) by Aaron D. O'Connell *et al.*[132] to be about $\tan(\delta) = 10^{-6}$ and 10^{-4}, respectively. These loss tangent lead to longer relaxation times than the ones measured, suggesting another loss process.

Dielectric losses can also arise from the electric fields coupling spurious two-level systems to the V-shape device. These two-level system reside predominantly in surface oxides and interfaces[133]. These losses depend strongly on the electric field intensity[133]. Increasing the interdigital fingers width should reduce the electrical field intensity and consequently, decreases the coupling between the V-shape device and the spurious two-level systems. In the next generation of sample, the design of the interdigital capacitors will be modified in order to reduce the influence of surface defects.

On the other side, the short relaxation time of the qubit and decay time of the microwave resonator suggests a common limiting factor. To improve the common environment of our sample we fabricate a new generation of sample holder with a better radiative and magnetic shielding based on the work of R. Barends *et al.*[91].

5.3.4 AC-Stark shift and measurement-induced dephasing

Due to the coupling between the artificial atom and the microwave cavity, any measurement on one system will have an effect on the other. For instance, the two-tone spectroscopy presented in a previous section is based on a frequency shift of the microwave resonator as function of the qubit state. The reverse effect also exists with a modification of the qubit resonance depending on the photon number in the cavity. We show here a measurement of the qubit resonance line shape as function of the photon number. The experiment consists of two-tone spectroscopies of the qubit resonance (as explained in Section 5.2.1) versus readout power. Typical measurements are presented in Fig. 5.12. When the readout power increases, we observe a broadening and a shift to smaller frequency of the resonance peak. Each curve is fitted with a Cauchy–Lorentz formula from which we extract the resonance position of the peak ν_0^{qb} and its width δ_{FWHM}. These two parameters are plotted as function of the readout power in Fig. 5.13 (a) and (b). Error bars reflect estimated uncertainties in the extracted parameters from the fit. The lowering of the resonance frequency and the broadening of the

peak exhibit a linear dependence as function of the readout power.

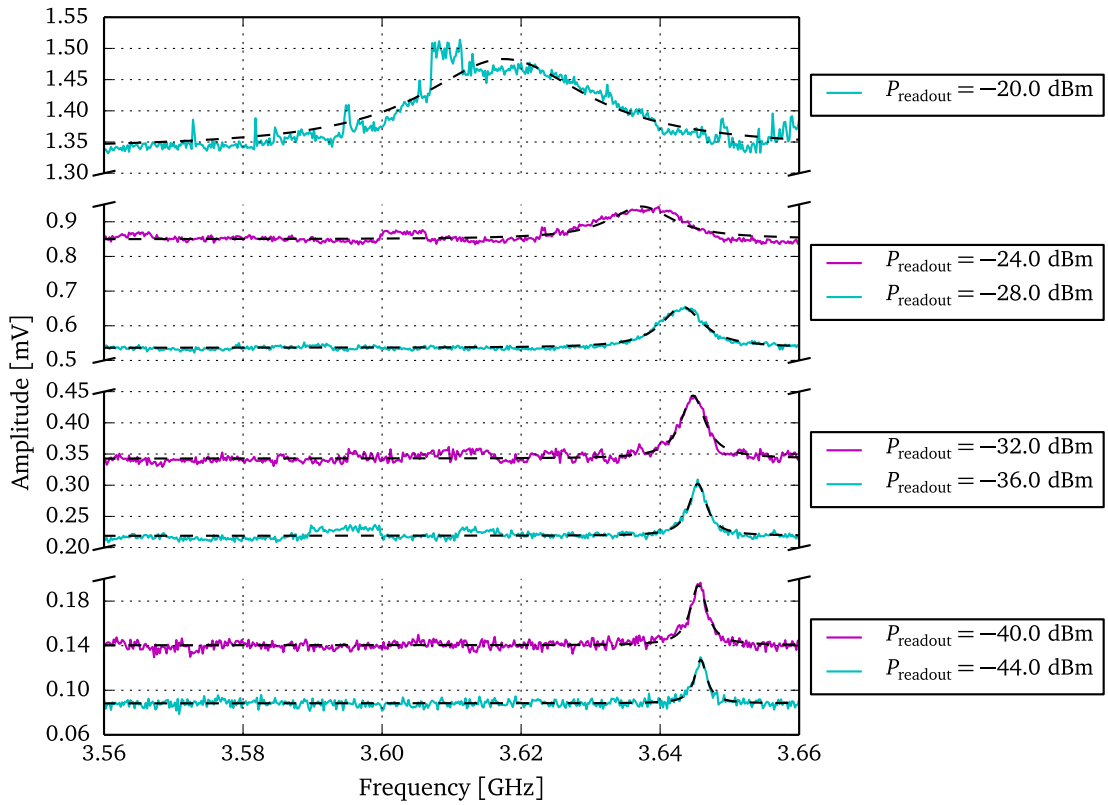

Figure (5.12): Spectroscopy of the qubit resonance for different readout tone powers. We observe a broadening and a shift to smaller frequency of the resonance peak when the readout power increases. In dashed black lines, we show fits applied to each data curve with Cauchy–Lorentz formula. We extract from the fit the resonance position of the peak ν_0^{qb} and its width δ_{FWHM}. These two parameters are shown in Fig. 5.13 (a) and (b). Measurements have been performed on sample "V-shape-2" with a probe power of $P_{probe} = -20\,\text{dBm}$ and a magnetic flux $\phi_b = 0$. Data were acquired during $T_{readout} = 2\,\mu\text{s}$ and averaged 10^5 times.

We attribute the shift of the resonance frequency to the so-called "AC-Stark shift" and the broadening of the peak to the so-called "measurement-induced dephasing"[27,79,134]. The AC-Stark shift is proportional to the number of photons at the cavity frequency as:

$$\omega_{\text{ac}} = 2n\frac{g^2}{\Delta} = 2n\chi_{\text{qb}} \tag{5.4}$$

with χ_{qb} and n the dispersive coupling strength and the mean photon number at the cavity frequency, respectively. Furthermore, the cavity is driven with a coherent field whose photon distribution is described by a Poissonian distribution. The intrinsic width of the photon distribution adds an additional dephasing to the qubit. D. I. Schuster, *et al.*[79] and J.

Gambetta, *et al.*[134] demonstrate that the qubit line shape taking into account these both effects are:

$$S(\omega) = \sum_{j=0}^{\infty} \frac{(-1)^j}{\pi} \frac{\left(\frac{4\chi_{\mathrm{qb}}\sqrt{n}}{\kappa}\right)^{2j}}{j!} \frac{\frac{1}{T_\phi} + \frac{\kappa}{2}\left[\left(\frac{4\chi_{\mathrm{qb}}\sqrt{n}}{\kappa}\right)^2 + j\right]}{\left[\omega - \left(\omega_{\mathrm{qb}} + (2n+1)\chi_{\mathrm{qb}}\right)\right]^2 + \left(\frac{1}{T_\phi} + \frac{\kappa}{2}\left[\left(\frac{4\chi_{\mathrm{qb}}\sqrt{n}}{\kappa}\right)^2 + j\right]\right)^2} \tag{5.5}$$

where κ is the cavity decay rate, and T_ϕ the pure dephasing time of the qubit. Equation (5.5) can be understood as a sum of Lorentzian curves. Indeed the readout field has a Poissonian distribution with a mean photon number and a certain width. The resonance of the qubit can then be viewed as a sum of resonance peaks, each peak for a precise number of photon in the cavity.

We use Eq. (5.5) and Eq. (5.4) to fit data shown in Fig. 5.13 (a) and (b), respectively. The photon decay rate $\kappa/(2\pi) = 3.80 \pm 0.01\,\mathrm{MHz}$ has been estimated from an independent measurement, the spectroscopy of the resonator dip in Section 4.6. The dispersive coupling $\chi_{\mathrm{qb}}/(2\pi) = 2.5\,\mathrm{MHz}$ has also be estimated independently from the dispersive measurement. There is then only two fit parameters, the pure dephasing time T_ϕ and the proportionality between the readout power and the number of photons in the cavity. The AC-Stack shift and the measurement-induced dephasing are fitted together allowing a better estimation of the fit parameters. From the fit procedure, we extract the pure dephasing rate $T_\phi = 150 \pm 100\,\mathrm{ns}$ and a calibration of the mean photon number versus readout power. The result is shown in Fig. 5.13 (c) and (d). The sub-figure (c) presents $T_2' = 1/(\pi\delta_{\mathrm{FWHM}})$ as function of photon number.

We can compare the calibration of mean photon number to an estimation obtained via the input–output theory:

$$n = A\frac{P_{\mathrm{rf}}}{\hbar\omega_{\mathrm{rf}}}\frac{2}{\kappa} \tag{5.6}$$

with A the attenuation along the microwave line[2], P_{rf} and ω_{rf} the power and the angular frequency of the microwave source. A discrepancy of only 20 % is found between a rough estimation of the mean photon number via Eq. (5.6) and the calibration via the AC-Stark shift effect (Eq. (5.4)).

[2]For this measurement the attenuation of the line has been estimated to be −99 dB

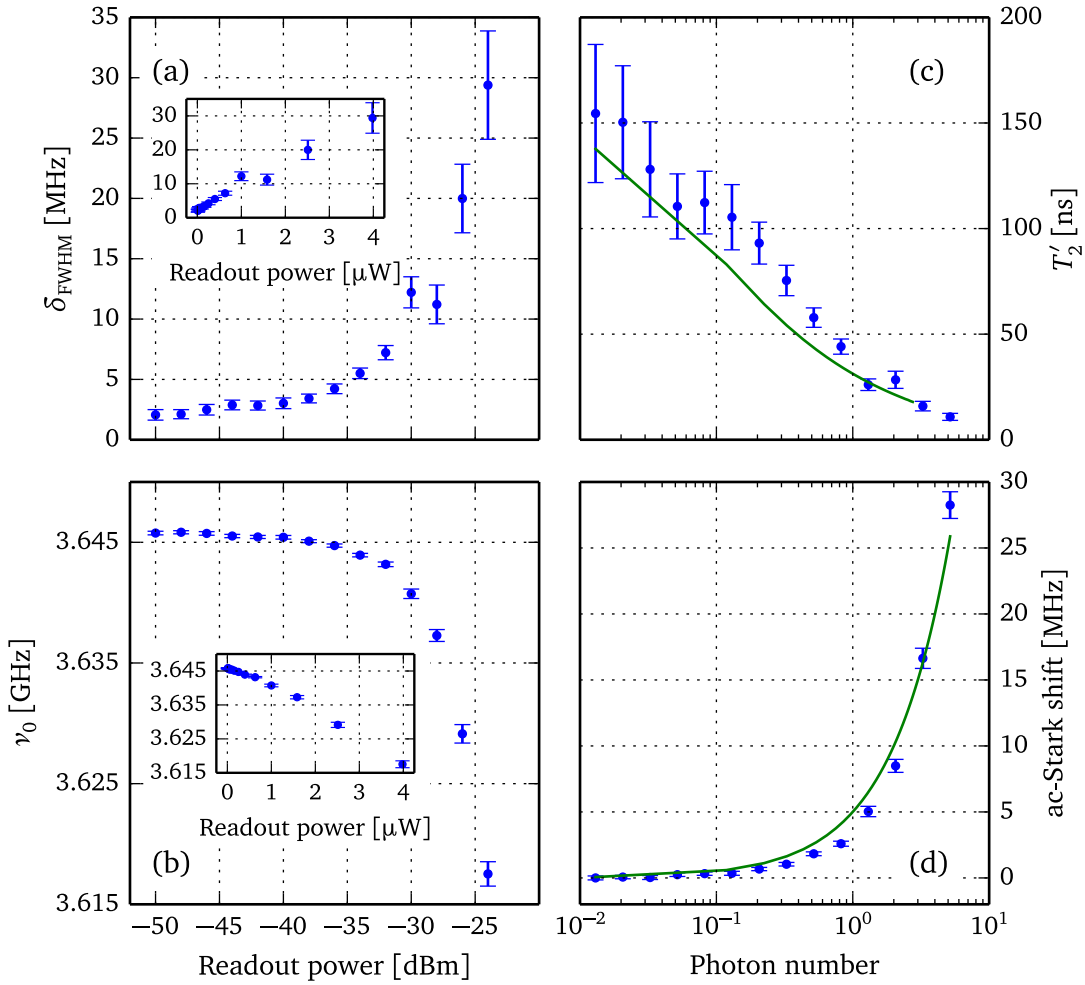

Figure (5.13): (a) and (b) Full width at half maximum and resonance frequencies extracted from curves in Fig. 5.12 as a function of the readout power. (c) and (d) T_2' and AC-Stark shift as function of mean photon number at the cavity frequency. We calculate $T_2' = 1/(\pi\delta_{FWHM})$ where the FWHM comes from the line shape given at Eq. (5.5). The theoretical AC-Stark shift is calculated with Eq. (5.4). Measurements have been performed on sample "V-shape-2".

5.3.5 Dependence of the qubit coherence versus probe power

In the previous section, we have considered the effect on the qubit line shape of a microwave field in resonance with the cavity. Hereafter, we will consider the influence of the probe tone power on the qubit resonance line shape. The experiment consists of two–tone spectroscopies of the qubit resonance as explained in Section 5.2.1 performed for different probe power. Moreover, in order to be in a steady-state regime, the duration of the microwaves pulses will be long compared to the different characteristic times of the system.

In Fig. 5.14, we present the measured amplitude of qubit resonance line shape as function of the probe power. We observe a broadening of the peak width and a growth of the peak height when the probe power increases. Each curve is fitted with a Cauchy–Lorentz formula from which we extract the peak height P_{height} and the resonance linewidth δ_{FWHM}. These two parameters are shown in Fig. 5.15 (a) and (b). Error bars reflect estimated uncertainties in the extracted parameters from the fit.

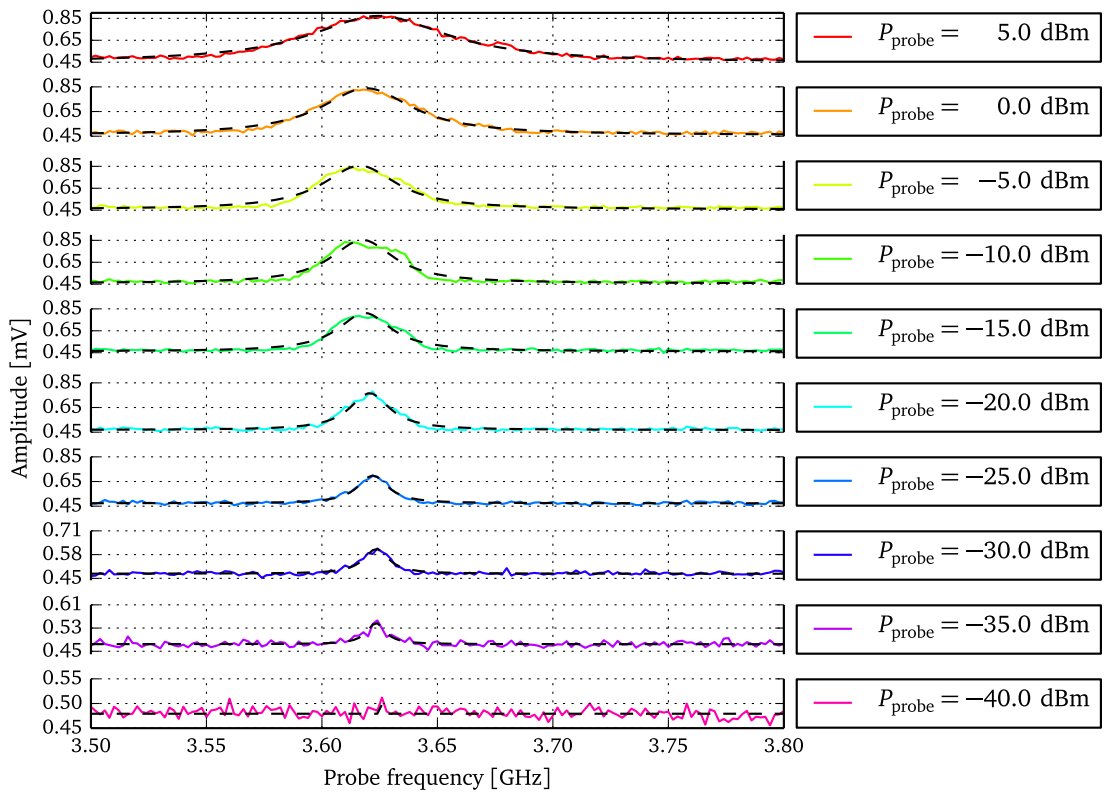

Figure (5.14): Spectroscopies of the logical qubit resonance peak for different probe power. We observe a broadening of the peak width and a growth of the peak height when the probe power increases. Fitted Lorentzian laws are depicted as dashed black lines. Measurements have been performed on sample "V-shape-1" with a readout power of $P_{readout} = -35$ dBm and a magnetic flux $\phi_b = 0$. Data were acquired during $T_{readout} = 39\,\mu$s and averaged 200 times.

From steady-state solution of Bloch equation[135], D. I. Schuster[79] showed that the qubit line-shape depends on the probe power, the qubit coherence, and the coupling strength g_{qb} between the logical qubit and the microwave resonator as:

$$P_{\uparrow} = \frac{1}{2}\frac{n_{\mathrm{s}}\left(2g_{\mathrm{qb}}\right)^2 T_1 T_2}{1+\left[T_2\left(\omega-\omega_{\mathrm{qb}}-(2n+1)\chi\right)\right]^2+n_{\mathrm{s}}\left(2g_{\mathrm{qb}}\right)^2 T_1 T_2} \tag{5.7}$$

where n_{s} is the mean number of probe tone photons in the resonator, T_1 the relaxation time and T_2 the coherence time of the qubit. Equation (5.7) has a Lorentzian shape from which we derive the full width at half maximum and the height of the peak as:

$$\delta_{\mathrm{FWHM}} = \frac{1}{\pi}\sqrt{\frac{1}{T_2^2}+n_{\mathrm{s}}\left(2g_{\mathrm{qb}}\right)^2\frac{T_1}{T_2}} = \frac{1}{\pi T_2'}, \tag{5.8}$$

$$P_{\mathrm{height}} = \frac{1}{2}\frac{n_{\mathrm{s}}\left(2g_{\mathrm{qb}}\right)^2 T_1 T_2}{1+n_{\mathrm{s}}\left(2g_{\mathrm{qb}}\right)^2 T_1 T_2}. \tag{5.9}$$

Equation (5.8) shows that the width of the peak depends on the lifetime and of the coherence time of the qubit. It also precises the influence of the power on the peak width. Equation (5.9) shows the dependence of the peak as function of the power. We note that the population of the excited state cannot be larger than one half. Indeed at high power the absorption and the relaxation compensate each other.

We use Eq. (5.8) and Eq. (5.9) to fit data shown in **??** (a) and (b), respectively. The coupling strength between the qubit and the microwave resonator $g_{\mathrm{qb}}/(2\pi) = 83\,\mathrm{MHz}$ has been estimated from an independent measurement, the dispersive shift, see Section 5.2.4. The value the relaxation time $T_1 = 600 \pm 10\,\mathrm{ns}$ was determined from time-resolved measurements, see Section 5.3.3. There are then two fit parameters, the pure dephasing time T_ϕ and the proportionality between the probe power and the number of photons in the cavity at the qubit frequency. The growth of the peak height as well as the broadening of the peak are fitted together allowing a better estimation of the fit parameters. From the fit procedure, we extract the pure dephasing rate $T_\phi = 30 \pm 4\,\mathrm{ns}$ and a calibration of the mean photon number versus probe power. The results are shown in Fig. 5.15 (c) and (d). The sub-figure (c) presents $T_2' = 1/(\pi\delta_{\mathrm{FWHM}})$ as function of photon number.

The pure dephasing time extracted by the mean of the qubit peak broadening and extracted via the measurement-induced dephasing, see Section 5.3.4, are quite small compared to the measured dephasing time of the first transmon generation. Indeed D. I. Schuster *et al.*[127] measured a transmon with a pure dephasing time of 500 ns ($(E_{\mathrm{J}}/E_{\mathrm{C}})^* \approx 20$) and J. Majer *et al.*[128] a pure dephasing time of 500 ns ($(E_{\mathrm{J}}/E_{\mathrm{C}})^* \approx 37$) in 2007. In our circuit, the $(E_{\mathrm{J}}/E_{\mathrm{C}})^*$ ratio is about 30 so comparable with the Schuster's transmon. We think that the relatively low coherence time of our V-shape device may come from the thermal noise of the cold amplifier. Indeed we see in Fig. 2.2 that there is only one cold isolator at 30 mK. The circulator has, from datasheet, an isolation of $-17\,\mathrm{dB}$. By using Eq. (2.4) we estimate the equivalent noise temperature to be about 113 mK at the sample stage. From Eq. (2.14) we estimate that the

number of photons at the cavity frequency due to thermal radiation to be about 0.1 photon so, hundred times more than if the amplification line was ideally thermalised. This noise induced dephasing to the qubit[127] and set an upper limit to its coherence time. We estimate the coherence time limited to 250 ns because of the thermal noise coming from the cold amplifier. For the future, we will place the two isolators at 30 mK in order to reach a thermalisation equivalent to that of the input line.

Transmons with longer coherence time need a $(E_J/E_C)^*$ ratio about 50[22]. This is in agreement with the theoretical prediction of J. Koch *et al.* for the transmon $1/f$ charge noise dependence[18]. These results may indicate that the $(E_J/E_C)^*$ ratio is too small in our device and must be increased for next sample generation.

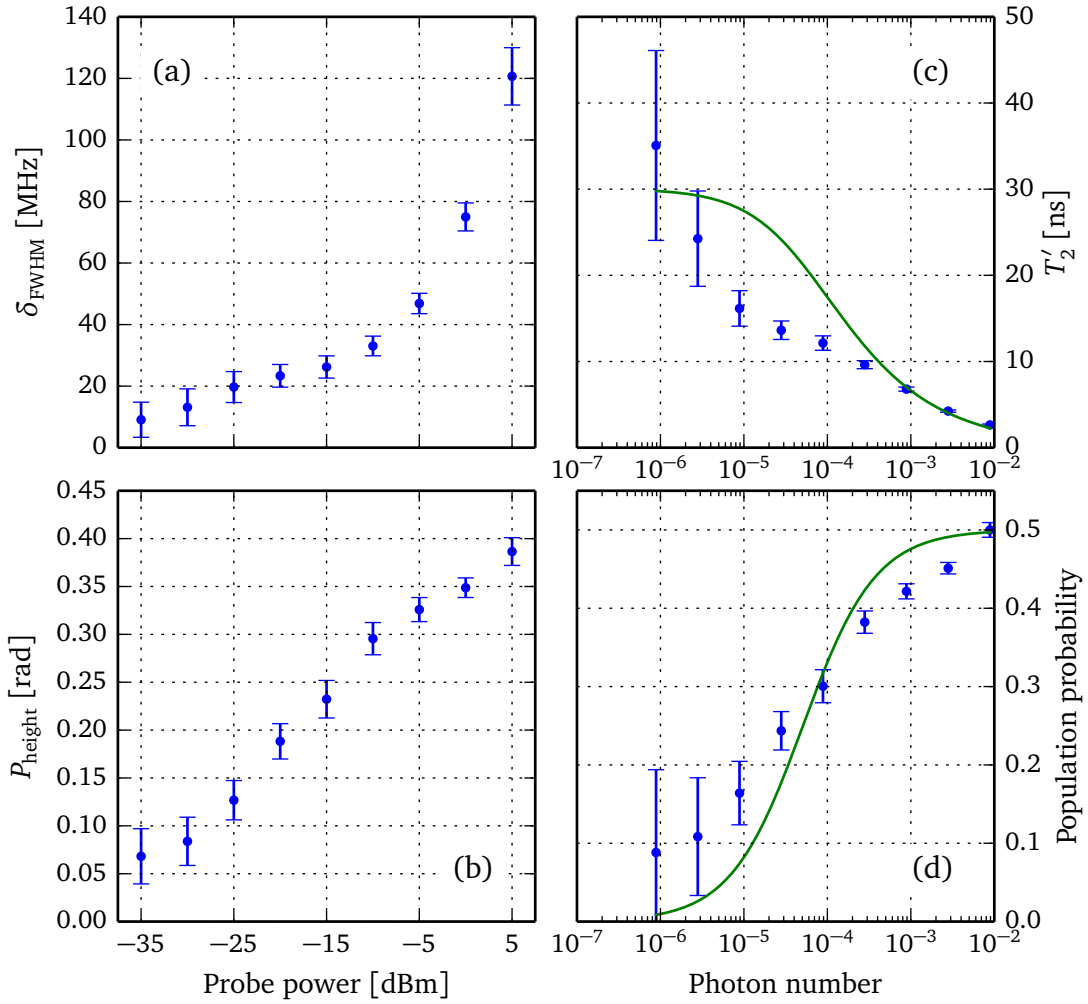

Figure (5.15): (a) and (b) Full width at half maximum and height of the qubit peak extracted with a Lorentzian fit from Fig. 5.14. (c) Rabi decay time calculated from the full width at half maximum as $T_2^{Rabi} = 1/(\pi\delta_{FWHM})$. Data are fitted with Eq. (5.8). (d) Population probability of the first excited level of the in-phase mode. Data are fitted with Eq. (5.9). Measurements have been performed on sample "V-shape-1".

5.4 Logical qubit anharmonicity measurements

The logical qubit is formed by the two first energy levels of the *in-phase* mode, see Section 1.1.4. Indeed when the anharmonicity is large compared to the energy excitation, only the two first level are involved in the dynamics of the system. Hereafter, we will measure the anharmonicity of the qubit defined as $\Delta_x/h = \nu_2^{\mathrm{qb}} - 2\nu_1^{\mathrm{qb}}$ (see Section 1.1.3). By comparing the measured anharmonicity to the amplitude of the microwave field calibrated through Rabi oscillation we will discuss the validity of the two-level system assumption.

5.4.1 Two-photon process

The anharmonicity can be extracted from two–tone spectroscopy performed at high power in order to realise a two photons transition between the ground and the second excited state of the *in-phase* mode. To enhance the emergence of the peak due to the two–photon process, we measured several two–tone spectroscopies at different probe powers.

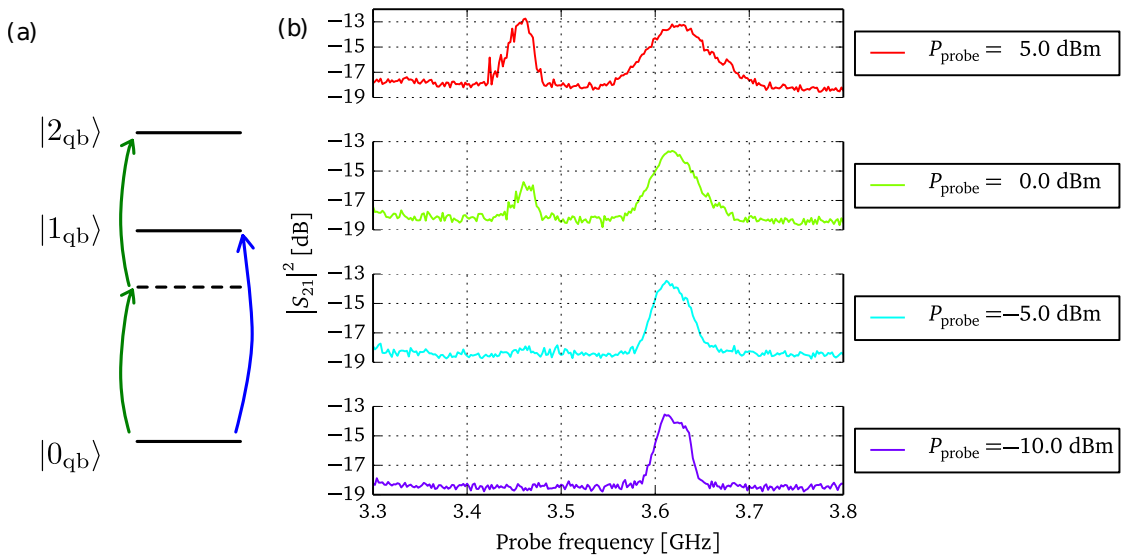

Figure (5.16): (a) Scheme of the two-photon transition between the ground and the second excited state of the qubit compared to the direct transition between the ground and the first excited state of the qubit. (b) Spectroscopy of the logical qubit resonance peak for different probe powers. We observe the appearance of a second peak at smaller frequency. The effect of the increase of the probe power on the resoance peak of the qubit is discussed in Section 5.3.5. The measurements have been performed on the sample "V-shape-1" with a base temperature $T = 65\,\mathrm{mK}$ *with a readout power of* $P_{readout} = -35\,\mathrm{dBm}$. *Data were acquired during about* $T_{readout} = 39\,\mu\mathrm{s}$ *and averaged* 200 *times.*

Figure 5.16 shows the power transmission of the qubit line shape at different probe power. We observe the qubit resonance peak at about 3.63 GHz for all the measurement curves. In the high power limit, we note the appearance of a second peak at lower frequency 3.46 GHz.

The peak which emerges at high power corresponds to a transition from the ground state to the second excited state via a two–photon process. Thus the resonance frequency of this peak is equal to half of the resonance frequency of the second excited level. From data presented in Fig. 5.16, we extract an anharmonicity $\Delta_x/h = 340\,\text{MHz}$.

5.4.2 Direct spectroscopy of the second level of the *in-phase* mode

We present in Fig. 5.17 a zoom in the spectroscopy of the two first excited levels on the *in-phase* mode for the samples "V-shape-1", left panels, and "V-shape-2", right panels, already presented in Fig. 5.3 and Fig. 5.6, respectively. We observe the magnetic flux dependence on the two first excited levels. They have a maximum at $\phi_\text{b} = 0$ and drop towards zero at $|\phi_\text{b}| \approx 0.5$.

From Fig. 5.17, we extract the resonance frequency of the first and the second excited energy levels ν_1^qb and ν_2^qb, respectively. The anharmonicity is calculated as $\Delta_x/h = \nu_2^\text{qb} - 2\nu_1^\text{qb}$. We obtain 340 MHz for the sample "V-shape-1" and 320 MHz for the sample "V-shape-2". This measure is in agreement with the measurement of the second level resonance frequency shown in the previous section.

So far we have considered the anharmonic oscillator of the *in-phase* mode as a two-level system, the logical qubit. In the last two sections, we measured an anharmonicity of 340 MHz, about 9 % of the qubit resonance frequency. The anharmonicity can be compared[12] to the microwave field amplitude calibrated in Section 5.3.2. Indeed we saw that for typical excitation tone amplitude, the amplitude of the microwave field was below 10 MHz. We have then a ratio of ≈ 30 between the microwave field amplitude and the anharmonicity, ensuring a dynamics restrained to the two levels of the qubit (see Julien Claudon's thesis[56]).

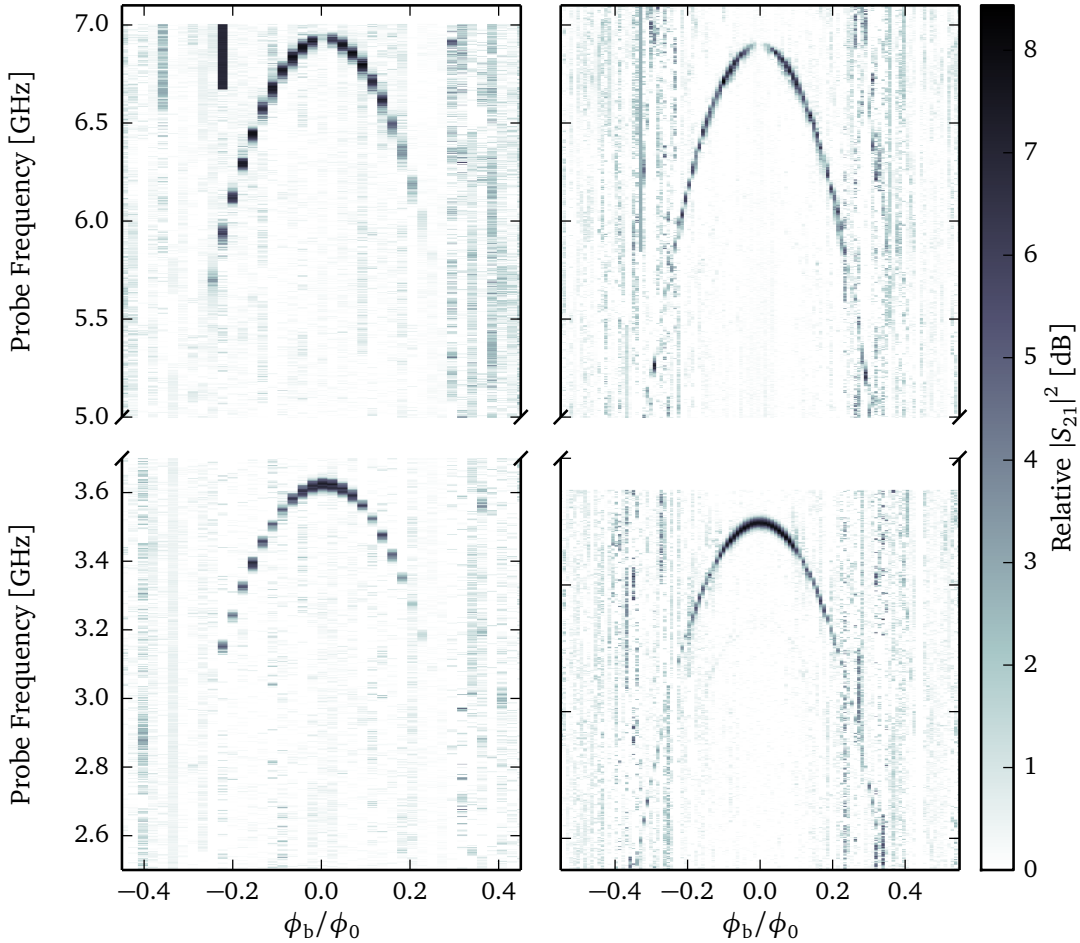

Figure (5.17): Spectroscopy of the two first level of the in-phase oscillating mode as function of the magnetic field. The top panels present the second level and the bottom ones, the first level. Measurements have been performed on sample "V-shape-1" for the left panels and "V-shape-2" for the right ones.

5.4.3 A transition forbidden at $\phi_b = 0$

As we already mentioned, the *in-phase* mode is equivalent to the oscillating mode which exists in the transmon. Thus it is quite surprising to be able to measure a resonance peak corresponding to the second transition of the *in-phase* directly, see Fig. 5.17. Indeed in the transmon this transition is forbidden. Moreover, close to zero magnetic field, we observe in our experiment a disappearance of the peak, see Fig. 5.18. We have then to answer two questions: why are we able to directly measure the peak of the second level of the *in-phase* mode and why the peak vanishes at zero magnetic field.

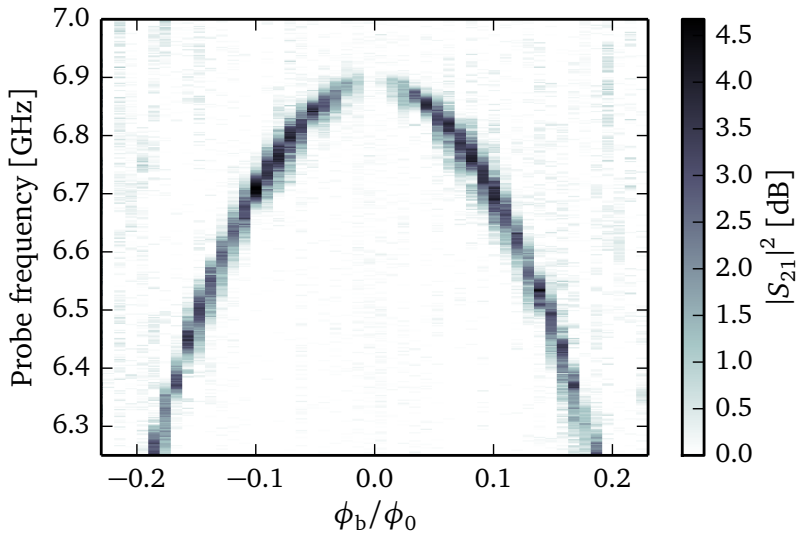

Figure (5.18): Spectroscopy of the gap in the second transition of the in-phase mode. A clear disappearance of the resonance dip is visible at a magnetic field corresponding at a zero internal flux of the SQUID loop. The measurement has been performed on the sample "V-shape-2" at a base temperature of $T = 65\,\mathrm{mK}$ with a probe power $P_{probe} = -10\,\mathrm{dBm}$ and a readout power of $P_{readout} = -33\,\mathrm{dBm}$ at $\phi_b = 0$. Data were acquired during about $T_{readout} = 2\,\mu\mathrm{s}$ and averaged 10^4 times.

The probability of transition between the ground state and the second excited state $\mathscr{P}_{0\to 2}$ is proportional to $|\langle\psi_2|\widehat{\mathscr{W}}_x^{\delta I(t)} + \widehat{\mathscr{W}}_y^{\delta\phi(t)}|\psi_0\rangle|^2$ with $\widehat{\mathscr{W}}_x^{\delta I(t)}$, $\widehat{\mathscr{W}}_y^{\delta\phi(t)}$ the coupling between the *in-phase*, *out-of-phase* mode and the electrical, magnetic field, respectively (see Section 1.3.1). When $|\langle\psi_2|\widehat{\mathscr{W}}_x^{\delta I(t)} + \widehat{\mathscr{W}}_y^{\delta\phi(t)}|\psi_0\rangle|^2$ is zero the transition is so-called "forbidden". A simple way to know if a transition is forbidden is to look at the parity of the initial and final state as well as of the coupling operator. Indeed if the overall function is odd, the transition is forbidden for symmetry reason. When we consider low energy and resonant excitation[3], the coupling is modelled via the Jaynes–Cummings model. Such an operator has

[3]Here, low energy excitation means that the Rabi frequency of the probe excitation should be much less than the transition frequency. In our system the Rabi frequency is tens of megahertz at most and the qubit frequency is

an odd parity since it transfers one excitation from one system to another. Thus $\widehat{\mathscr{W}}_x^{\delta I(t)}$ is odd in x and $\widehat{\mathscr{W}}_y^{\delta\phi(t)}$ is odd in y.

In a first time, we consider our system at $\phi_b = 0$. At this particular flux, the two modes become only coupled via a cross-Kerr term. The coupling term $\widehat{\mathscr{W}}_y^{\delta\phi(t)}$ is then unable to induce transitions between states of the *in-phase* mode. The ground state and the second excited state exhibit, both, an even parity. The coupling term $\widehat{\mathscr{W}}_x$ being odd, the overall function is odd making the transition between these two states forbidden. At zero flux, we then recover the dynamics of the transmon with a forbidden transition between the ground and the second excited state. This explain the absence of resonance in the direct spectroscopy in Fig. 5.18 at $\phi_b = 0$.

When the applied magnetic flux is non zero, $\phi_b \neq 0$, other coupling terms take part to the dynamics of the system. The *in-phase* mode is no more equivalent to the transmon mode. In first approximation a nonlinear coupling strength[13] ω_{21} couples the *in-phase* and *out-of-phase* mode (see Section 1.1.3). The presence of this coupling breaks the even parity of the ground and second excited states. The calculation of the eigenstate of the V-shape is a hard problem and in our work we only consider the corrected eigenstate at the first-order by quantum perturbation theory. The general formula given the corrected eigenstate is given in Appendix D. We observe that the corrected eigenstates become contaminated by states of higher and lower energy, and more importantly, they mix states of the *in-phase* and *out-of-phase* mode due to non-linear couplings. By using the corrected eigenstate we derive the matrix element[4]:

$$\left|\langle\psi_2|\,\widehat{\mathscr{W}}_y\,|\psi_0\rangle\right|^2 \approx \left|\frac{\hbar}{2} g_a \frac{\omega_{21}}{2\omega_x - \omega_y}\right|^2 \tag{5.10}$$

where g_a is the coupling strength between the *out-of-phase* mode and the resonator, ω_{21} is a non-linear coupling strength and $\omega_{x,y}$ is the plasma frequency of the *in-phase* and *out-of-phase* mode, respectively (we remind that all these terms are defined in Table 1.4 and in Section 1.3.2). Equation (5.10) is non zero at non zero magnetic field. Due to the nonlinear coupling between the two oscillating modes ω_{21}, the transition from the ground state to the second excited state is available.

Moreover, through Eq. (5.10), we remark that the transition is induced by the $\widehat{\mathscr{W}}_y$ coupling operator. Indeed we have to keep in mind that at $\phi_b \neq 0$, the different eigenstates of the system are a linear combination of *in-phase* and *out-of-phase* states.

5.5 Ancilla qubit

5.5.1 Coherent oscillations of the ancilla qubit

The experiment to realise coherent oscillations on the ancilla qubit was the same as for logical qubit, see Section 5.3.1. The pulse sequence is illustrated in Fig. 5.19 (a) and the

at some gigahertz.

[4]The result only presents first-order term, the higher-order terms are neglected. However all terms, even those which are neglected here, present the same behaviour at zero flux, they drop to zero.

result of the measurement is shown in Fig. 5.19 (b). By fitting data with Eq. (5.2), we extract the oscillation frequency $\Omega/(2\pi) = 86.3 \pm 0.7\,\text{MHz}$ and the characteristic decay time $\tau = 90 \pm 60\,\text{ns}$.

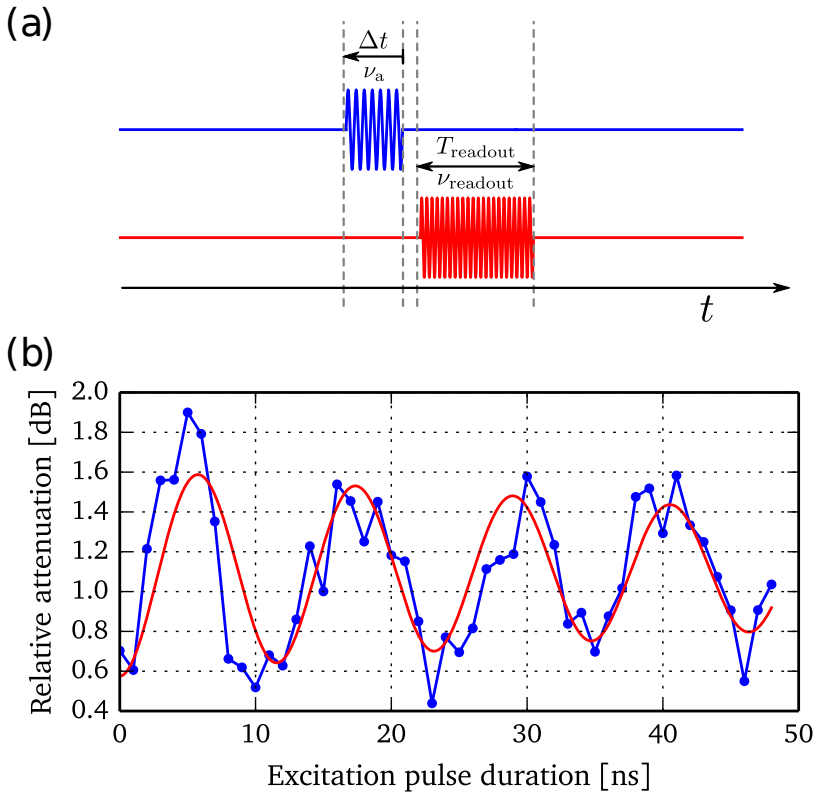

Figure (5.19): (a) Scheme of pulse sequence. The excitation pulse at the top (blue) has a variable duration Δt. Its frequency corresponds to the resonance frequency of the ancilla qubit. The readout pulse at the bottom (red) is sent just after the excitation pulse. It has a fixed duration, $T_{readout}$. (b) Transmission variation as function of excitation pulse duration. We observe damped oscillations related to population of the excited level of the ancilla. From Eq. (5.2), we extract a Rabi frequency of $\Omega/(2\pi) = 86.3 \pm 0.7\,\text{MHz}$ and $\tau = 90 \pm 60\,\text{ns}$. The measurement has been performed at a base temperature $T = 65\,\text{mK}$ with a probe power $P_{probe} = 10\,\text{dBm}$, a readout power $P_{readout} = -25\,\text{dBm}$ and a magnetic flux $\phi_b = 0$ on the sample "V-shape-1". Data were acquired during about $T_{readout} = 192\,\text{ns}$ and averaged 10^4 times.

We remark that the characteristic decay time is short, less than hundred nanoseconds. Due to the fast decay time of the oscillations, we need a quite high excitation power to observe a few oscillations. With an oscillations frequency of $\Omega/(2\pi) = 86.3\,\text{MHz}$, the amplitude of the microwave field is well above the anharmonicity of the ancilla qubit theoretically predicted about $\Delta_y/h = 20\,\text{MHz}$ (see Eq. (1.48)). In this microwave amplitude domain, the measured

oscillations involves more than the two first level of the ancilla qubit[12]. For this reason, the extracted oscillation frequency is not equivalent to the Rabi frequency.

The characteristic decay time is one order of magnitude shorter than the logical qubit decay time. We explain this fact by the large number of Josephson junctions involved in the ancilla mode. Indeed the ancilla qubit consists of the two first levels of the *out-of-phase* oscillating mode. This mode presents an oscillating current inside the two Josephson junctions of the V-shape device but also inside the junction chain (see Section 1.1.2). The twelve junctions of the chain have, together, a large area leading to a higher probability to be coupled to spurious two-level systems. Indeed such two-level spurious resonance were observed sometimes in the ancilla spectroscopy but never in the logical qubit spectroscopy.

5.5.2 Relaxation time of the ancilla qubit

We use the same experimental protocol to measure the relaxation of the ancilla qubit as for the logical qubit. The pulse sequence is summarised Fig. 5.20 (a) and the relaxation decay curve is plotted in Fig. 5.20 (b). By fitting data with an exponential decay law, we extract the relaxation time $T_1^{\text{ancilla}} = 630 \pm 30\,\text{ns}$. The relaxation time of the ancilla is comparable to the relaxation time of the logical qubit. This fact may suggest a common limiting factor for the relaxation time of the two qubits in our sample.

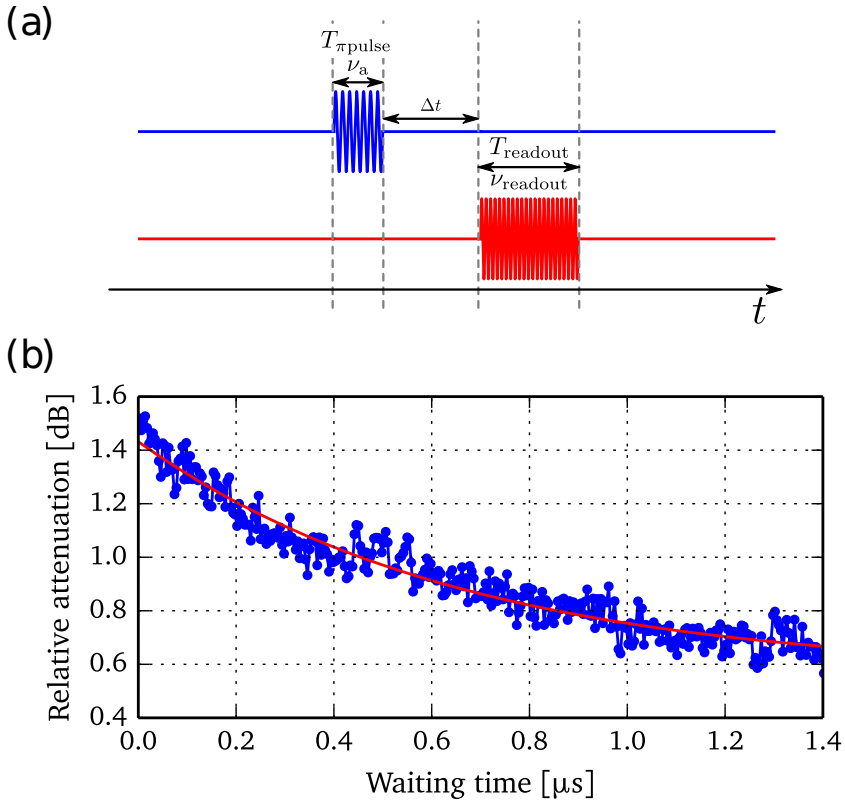

Figure (5.20): (a) Scheme of pulse sequence. The excitation pulse at the top (blue) is calibrated to inverse the population of the ancilla qubit from $|g\rangle \rightarrow |e\rangle$. After this first pulse, we wait during a variable delay before sending a second pulse, the readout pulse at the bottom (red), which performs the readout of the cavity. (b) Shift in the transmission at the readout frequency as function of the waiting time. We observe exponential decay related to the population of the excited state. By fitting the data with an exponential decay law, we extract the relaxation time $T_1^{ancilla} = 630 \pm 30\,\text{ns}$. The measurement has been performed at a base temperature $T = 65\,\text{mK}$ with a probe power $P_{probe} = -3\,\text{dBm}$, a readout power $P_{readout} = -25\,\text{dBm}$ and a magnetic flux $\phi_b = 0$ on the sample "V-shape-1". Data were acquired during about $T_{readout} = 192\,\text{ns}$ and averaged 2×10^5 times.

5.6 Cross-anharmonicity

A remarkable property of our system is to present a $\widehat{\sigma}_z^{qb}\widehat{\sigma}_z^{a}$ coupling high enough to realise a V-shape spectrum in a superconducting circuit. As we show in Section 1.1.4, the Hamiltonian of the system at $\phi_b = 0$ can be written as:

$$\widehat{\mathscr{H}} = \frac{\hbar}{2}\omega_{qb}\widehat{\sigma}_z^{qb} + \frac{\hbar}{2}\omega_a\widehat{\sigma}_z^{a} + \frac{\hbar}{2}g_{zz}\widehat{\sigma}_z^{qb}\widehat{\sigma}_z^{a}. \tag{5.11}$$

The coupling g_{zz} modifies the transition energy of one qubit depending on the other qubit state. Hereafter, we present a demonstration of this coupling and a measurement of its strength. To realise these experiments, we need therefore a three-tone spectroscopy. The first tone to excite one qubit, the second tone to excite the other qubit and the third tone to realise the readout of the cavity.

5.6.1 Measurement via pulse sequence

In order to measure the cross-anharmonicity, we performed sequential pulse three-tone spectroscopy. The first pulse, at the resonance frequency of the ancilla $\omega_a/(2\pi)$, realised the transition $|g\rangle \rightarrow |a\rangle$ from the ground state to the excited state of the ancilla. The second pulse probe the qubit resonance frequency. The third pulse performs the readout of the cavity at the frequency $\omega_{readout}/(2\pi)$. In the measurement shown in Fig. 5.21 (a), the power of the first tone is gradually increased from top to bottom.

In weak excitation power curve in Fig. 5.21, we observe a single dip corresponding to the qubit transition $|g\rangle \rightarrow |e\rangle$ as shown in the level scheme in Fig. 5.21 (b). Increasing the microwave excitation of the ancilla qubit, a second dip emerges below the first one. As indicated in the level scheme in Fig. 5.21 (c), the second dip appears due to the non zero population of the excited ancilla state $|a\rangle$ induced by the first pulse. The transition $|a\rangle \rightarrow |p\rangle$ thus becomes available. This transition is not exactly at the same frequency as the $|g\rangle \rightarrow |e\rangle$ transition. The relative shift of the two peaks is due to the cross-anharmonicity (see Eq. (5.11)). The frequency difference between the two peaks allows the extraction of the coupling strength $(2g_{zz})/(2\pi) = 119\,\text{MHz}$. We note that, at large excitation pulse power Fig. 5.21 (a), a third peaks begins to emerge with a frequency shift of about 258 MHz. This shift is roughly twice larger than the frequency shift between the $|g\rangle \rightarrow |e\rangle$ and $|a\rangle \rightarrow |p\rangle$ resonance peaks. We interpret this as an indicator of the population of the second excited state of the ancilla as indicated in Fig. 5.21 (e).

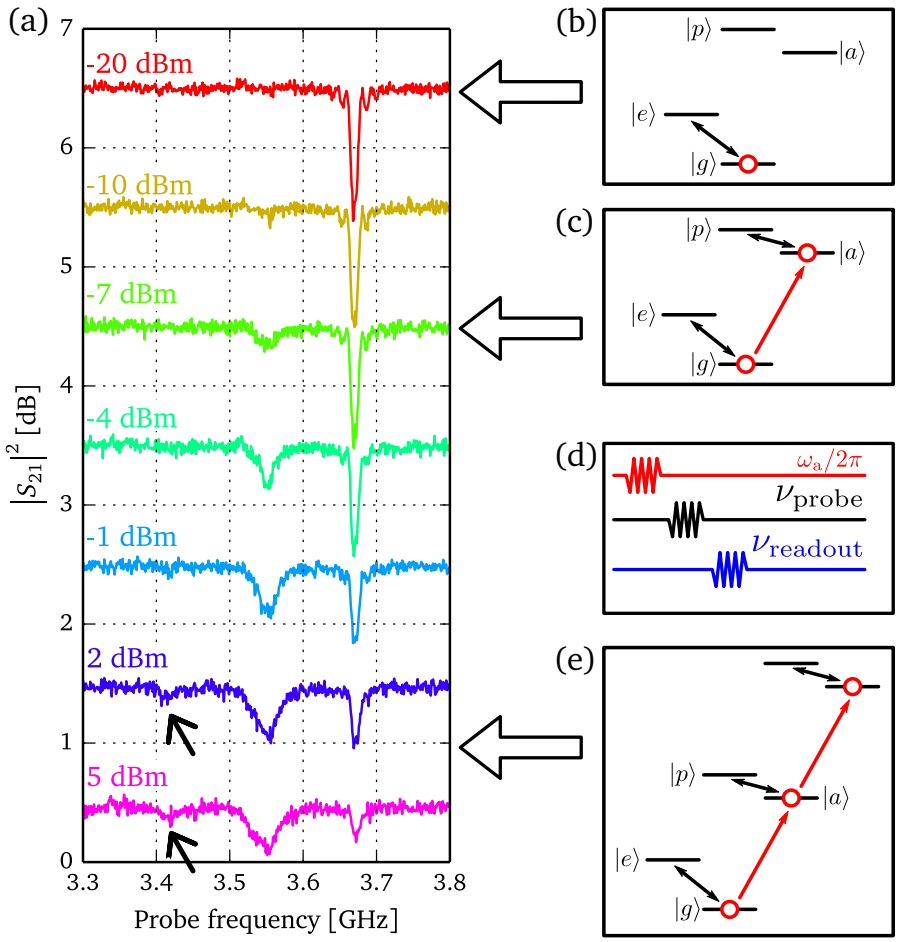

Figure (5.21): (a) Three-tone measurement of the mode coupling strength g_{zz} based on a sequence involving a pulse at $\omega_a/(2\pi)$ to populate the ancilla, a pulse at $\omega_{probe}/(2\pi)$ to scan over the qubit transition, and a readout pulse at $\omega_{readout}$ close to the cavity resonance frequency, see a pulse sequence scheme in (d). From the topmost to the lowest curve, we increase the power of the first pulse in steps, causing a peak to emerge below the resonance peak of the qubit. Their separation is a measure of the cross-anharmonicity extracted here at $(2g_{zz})/(2\pi) = 119\,\text{MHz}$. The situation without and with the first pulse are represented in the diagrams in (b) and (c). The measurement has been performed at a base temperature $T = 35\,\text{mK}$ with a probe power $P_{probe} = 5\,\text{dBm}$, a readout power $P_{readout} = -25\,\text{dBm}$ and a magnetic flux $\phi_b = 0$ on the sample "V-shape-1". Data were acquired during about $T_{readout} = 192\,\text{ns}$ and averaged 3×10^5 times.

5.6.2 Measurement via continuous drive

Another way to measure the cross-anharmonicity is to send continuous microwave instead of working with pulses sequence. A third tone called the excitation tone is continuously driven at the ancilla transition at $\omega_a/(2\pi)$. Next the probe tone is swept around the qubit resonance frequency and the readout is performed via the readout tone. The measured curve is presented in Fig. 5.22 (a) with the blue solid curve. We observe two peaks, one at the qubit resonance frequency 3.634 GHz and another, shifted by 110 MHz. We also remark that the two peaks have the same height.

As reference, we measure the same curve but with the excitation tone switched off. The result is shwon in Fig. 5.22 (a) with the green dashed curve. We observe the qubit resonance peak centered at 3.634 GHz.

The qubit resonance peak corresponds to the transition between $|g\rangle \rightarrow |e\rangle$. We identify the second peak as the transition $|a\rangle \rightarrow |p\rangle$. This second peak is made possible because of the third tone excitation which populates the higher energy level of the ancilla. The frequency shift between the two peaks corresponds then to the cross-anharmonicity $(2g_{zz})/(2\pi) = 110\,\text{MHz}$.

From the circuit parameters extracted with Kwant[126], $I_c = 8\,\text{nA}$, $C = 40\,\text{fF}$ and $L_{loop} = 7.5\,\text{nH}$, the theoretical predicted value of the cross-anharmonicity is, at $\phi_b = 0$, (see Chapter 1 for detail):

$$(2g_{zz})/(2\pi) = \frac{1}{2\pi}\frac{E_C}{8\hbar}\sqrt{\frac{1}{1+2b}} = 140\,\text{MHz} \tag{5.12}$$

The discrepancy between the two values is about 27 %.

We performed further measurement to test the reproducibility and consistency of this result. We interchanged the role of the qubit and the ancilla. In Fig. 5.22 (b) we plot in dashed green and solid blue, a measurement showing a spectroscopy around the ancilla frequency while the excitation tone on the qubit turned off and turned on, respectively. The result is exactly consistent with that in Fig. 5.22 (a), with a peak separation of about 110 MHz.

We remark that, when the excitation on the qubit is turned on, the ancilla resonance peak has a negative Lorentzian shape. This feature is not yet fully understood. We think that this behaviour is related to the effect of the dispersive shifts of the logical and ancilla qubit which act simultaneously on the resonance peak of the resonator. It is possible that the two frequency shift due to the excitation of the ancilla and logical excited state ends up with a positive frequency shift of the microwave resonator frequency and consequently to a negative resonance peak in the three–tone measurement.

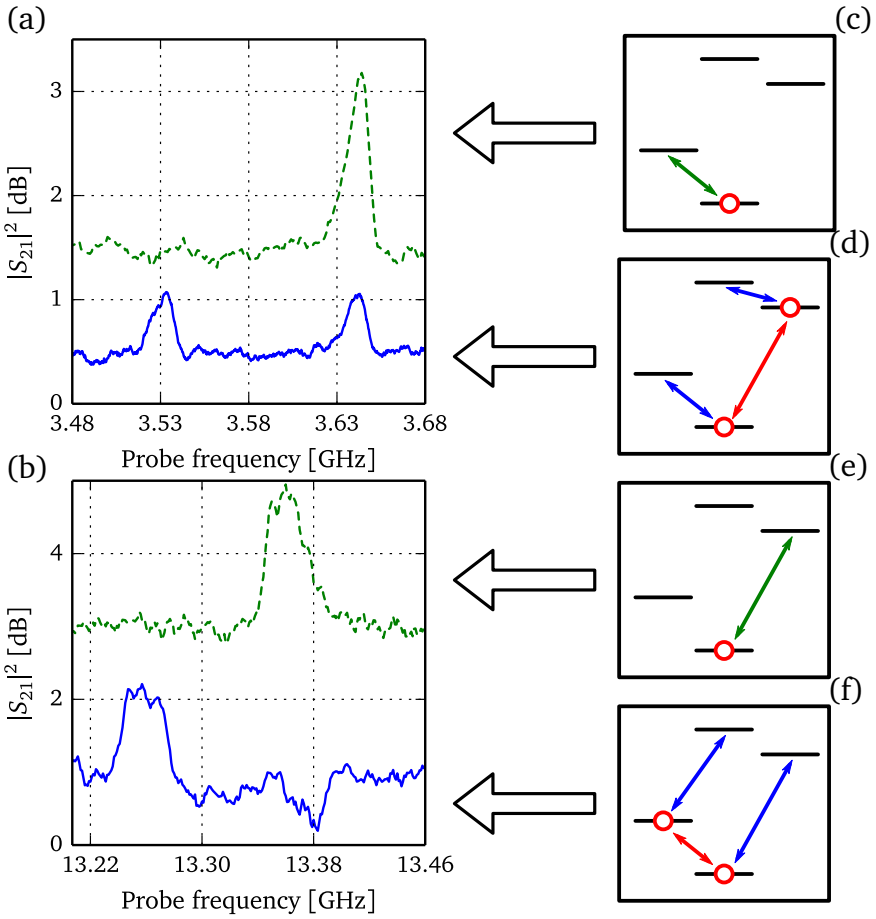

Figure (5.22): (a) Top green dashed curve, two–tone measurement of the qubit resonance, see energy diagram (c). Bottom blue solid curve, three–tone measurement. An excitation tone continuously drives the ancilla transition, while the probe tone scans the qubit transition, see (d). We observe the emergence of a second peak separated from the qubit resonance peak by the cross anharmonicity $(2g_{zz})/(2\pi)$. *(b) Control measurement of the cross-anharmonicity with inverted roles of logical and ancilla qubit, i.e., the probe tone is swept around the ancilla resonance frequency, whereas the excitation drive is resonant with the ancilla at* $\omega_a/(2\pi)$ *as shown in (e) and (f). The two measurements are consistent together with a cross-anharmonicity of* $(2g_{zz})/(2\pi) = 110\,\mathrm{MHz}$. *The measurement has been performed at a base temperature* $T = 35\,\mathrm{mK}$ *and a magnetic flux* $\phi_b = 0$ *on the sample "V-shape-2". For the panel (a), the probe power was* $P^{qb}_{probe} = -17.5\,\mathrm{dBm}$ *and* $P^{a}_{probe} = -10\,\mathrm{dBm}$ *with a readout power* $P_{readout} = -30\,\mathrm{dBm}$. *Data were acquired during about* $T_{readout} = 2\,\mu\mathrm{s}$ *and averaged* 10^3 *times. For the panel (b), the probe power was* $P^{qb}_{probe} = -1\,\mathrm{dBm}$ *and* $P^{a}_{probe} = 5\,\mathrm{dBm}$ *with a readout power* $P_{readout} = -33\,\mathrm{dBm}$. *Data were acquired during about* $T_{readout} = 192\,\mathrm{ns}$ *and averaged* 10^4 *times.*

5.7 Experimental realisation of a V-shape energy diagram ?

In this section we discuss about the validity of our claim: the experimental realisation of a V-shape energy diagram in a superconducting quantum circuit. To deserve the name of V-shape, an energy diagram must exhibit specific properties. We propose here a list of the minimal necessary properties:

1. The two qubits have to belong to two different modes.
2. One qubit should exhibit a long coherence time in order to be used as logical qubit.
3. Each qubit transition is addressable independently.
4. Any transitions from the logical qubit excited state to higher energy level are far out of resonance of the ancilla transition

In our system, the two qubits are formed from the two first transitions of the *in-phase* and *out-of-phase* oscillating mode of our quantum device. At $\phi_b = 0$, the two oscillating modes reach a symmetry point at which the two modes become only coupled via a cross-Kerr term. The two qubits are then perfectly orthogonal and are only coupled via a $\widehat{\sigma}_z\widehat{\sigma}_z$ term.

The qubit formed by the two first level of the *in-phase* mode is equivalent to the usual transmon qubit. Since the transmon already was proven to be a "good" qubit (long coherence time, easy implementation, possibility to couple several transmons), we use this qubit as a logical qubit. The remaining qubit is then dedicated to the measurement of the logical qubit and it is used an ancilla qubit.

Due to the nature of the modes leading to the two qubits, the logical qubit can only be addressed via electric field and the ancilla qubit by magnetic field. Moreover, the two qubits are detuned by $\approx 10\,\text{GHz}$. These two properties ensure an independent addressing of the two transitions.

Since the system is composed of two coupled qubits, a third excited level arises in the energy diagram. Physically this level corresponds to having the both qubit excited simultaneously. However due to the cross-anharmonicity, this level is detuned from the qubit and ancilla transitions by more than 100 MHz. This remarkable property make this transition out of resonance of the logical and ancilla qubit tone leading to the achievement of a V-shape energy diagram.

To conclude, we have demonstrated through a complete set of quantum experiments that our proposed superconducting quantum circuit exhibits a V-shape diagram. These results open the way to realise very fast QND qubit readout[45] and cross-Kerr interactions at the few-photon level[136,137].

Conclusion and perspectives

Français

Conclusion

Dans ce manuscrit, j'ai discuté la théorie relative à la réalisation d'un atome artificiel supraconducteur avec un diagramme d'énergie en V. Le circuit supraconducteur est basé sur deux transmons couplés inductivement. J'ai décrit le modèle théorique de l'échantillon ainsi que son environnement micro-onde (résonateur quart-d'onde et couplage à la feedline). Ce travail a mené à la prédiction d'un couplage cross-Kerr qui peut atteindre plusieurs centaines de méga-hertz. En utilisant cette caractéristique, nous proposons un protocole pour effectuer une lecture de l'état du qubit tout en le gardant non couplé à la cavité.

Afin de réaliser les expériences sur les atomes artificiels fabriqués, j'ai mis en place une installation micro-onde complète capable d'effectuer des expériences quantiques au niveau de l'état-de-l'art. Ce travail inclus la mise en place de composants micro-ondes dans un frigo à dilution, le calcul de la charge calorifique, le calcul du bruit de photon résiduel, la calibration de la chaîne d'amplification et l'installation d'un bouclier magnétique. Un environnement Python a aussi été mis en place afin d'effectuer toutes les expériences avec des scripts Python. Plusieurs pilotes Python ont été écrit afin de gérer les différents instruments utilisés pour les expériences. Grâce à ce travail, tout l'aspect informatique des mesures en partant des scripts de mesure jusqu'au traitement des données est désormais effectué en Python.

Un important travail a été réalisé sut la caractérisation des résonateurs micro-ondes. Premièrement, la forme asymétrique des formes de résonance a été expliquée par l'inductance des fils de soudure. La réduction de l'inductance de ces fils améliorera l'adaptation d'impédance et donc le rapport signal-sur-bruit des mesures. Afin d'aller dans cette direction, nous avons fabriqué un nouveau porte-échantillon, qui sera bientôt installé, dans lequel la longueur des fils de soudure nécessaire pour connecter la puce au câble coaxial a été drastiquement réduite pour atteindre moins de 1 millimètre. Secondement, le faible facteur de qualité interne mesuré sur les résonateurs en Aluminium et Rhénium suggère un facteur limitant commun. Les explications possibles pourraient être des blindages thermique et magnétique de la puce pas assez efficasse et une mauvaise thermalisation des photons venant de l'amplificateur cryogénique. Ainsi, la prochaine génération de porte-échantillon améliorera le blindage

thermique en adoptant une stratégie de « poupée russe » décrite par R. Barends in [91]. Un meilleur blindage magnétique a aussi été mis en place dans le nouveau porte échantillon. De plus, en déplaçant les connecteurs magnétiques loin de la puce-échantillon, le nouveau porte-échantillon va de nouveau diminuer le champ magnétique au niveau de la puce. Afin d'avoir la même thermalisation des photons dans les lignes d'entrée et de sortie, les deux circulateurs micro-onde de la ligne de sortie vont être thermalisés à 35 mK. Finalement, un filtre micro-onde passe-bas fait à partir d'Eccosorb avec une fréquence de coupure d'environ 30 GHz sera installé afin de filtrer les signaux très hautes fréquences.

Le résonateur micro-onde de l'atome artificiel a été rendu accordable en incorporant un SQUID dans la ligne centrale du résonateur. Une hystérésis a été observée en étudiant la dépendance en flux magnétique de la fréquence de résonance de la cavité. Nous montrons que cette hystérésis vient de l'inductance de la boucle du SQUID qui est comparable à l'inductance Josephson des jonctions. Une description quantitative de la dépendance en champ magnétique de la fréquence de résonance de la cavité a été réalisée menant à une très bonne compréhension du système mesuré.

Des spectroscopies deux-ton ont été utilisés pour mesurer la dépendance en champ magnétique des deux premiers niveaux excités du mode « en-phase » et du premier niveau excité du mode *hors-phase*. Nous avons effectué un calcul numérique avec la bibliothèque Kwant pour ajuster ces niveaux d'énergie avec notre modèle théorique et nous obtenons un très bon accord entre la théorie et les données. Le modèle analytique développé au Chapitre 1 a aussi été utilisé pour ajuster les données mais les paramètres extraits ne valident pas les hypothèses faites pour obtenir ce modèle.

Une propriété intéressante a été mesurée au travers de la dépendance en flux magnétique de la seconde transition du mode « en-phase ». En effet, nous avons mesuré que cette transition devient interdite a $\phi_b = 0$. Nous comprenons cette caractéristique par les différentes symétries de l'atome artificiel. En effet, à $\phi_b = 0$, le mode devient seulement couplé par un terme cross-Kerr. Le mode fondamental et le second niveau excité exhibent alors une symétrie pair rendant impossible une transition directe entre eux. Lorsque $\phi_b \neq 0$, des couplages non-linéaires entre les deux modes apparaissent. La présence de ces couplages casse la parité pair du niveau fondamental et du second niveau excité. La transition devient alors possible. Nous avons effectué un calcul analytique des états-propres du système au premier ordre en utilisant la théorie des perturbations quantique. Nous avons démontré que cette caractéristique peut être expliquée par le couplage non-linéaire ω_{21}.

Pour mériter le nom de diagramme d'énergie en forme de V, un diagramme d'énergie doit avoir des propriétés spécifiques:

1. Les deux qubit doivent appartenir à deux modes différents.

2. Un des qubit doit exhiber des temps de cohérence longs afin de pouvoir être utilisé en tant que qubit logique.

3. Chaque qubit doit être adressable indépendemment.

4. Toutes les transitions partant du niveau excité du qubit logique à des niveaux plus élevés en énergie doivent être non-résonantes avec la transition de l'ancillaire.

Nous avons effectué différentes expériences pour vérifier ces propriétés. À partir de la dépendance en flux magnétique des niveaux d'énergie mesurée par des spectroscopies deux-ton, nous avons confirmé la nature des modes d'oscillation donnant lieu aux qubits logique et ancillaire.

À $\phi_b = 0$, le système peut être vu comme deux qubits couplés uniquement par une anharmonicité croisée. Un de ces qubits est équivalent au qubit transmon et est utilisé comme qubit logique. L'autre qubit est alors dédicacé à la mesure du qubit logique et est utilisé comme qubit ancillaire.

Par des mesures résolues en temps, nous avons mesuré la relaxation et la durée de décroissance Rabi du qubit logique. Nous avons démontré que le qubit logique et ancillaire ont le même temps de relaxation comparable avec la première génération de transmon avec $T_1^{\mathrm{qb,\,a}} \approx 500\,\mathrm{ns}$. De manière surprenante, le qubit ancillaire exhibe le même temps de relaxation que le qubit logique. Cela pourrait suggérer un facteur limitant commun aux deux qubits. Cependant, aucune explication n'a encore été trouvée.

En étudiant la dépendance de la puissance du ton de lecture et du ton de sonde sur le pic de résonance du qubit logique, nous avons estimé le temps de déphasage entre 30 et 100 ns. Le temps de décroissance de Rabi est d'environ 500 ns. Ces temps caractéristiques sont courts comparés à ce qu'un qubit transmon peut atteindre et pourraient être expliqués par le trop faible rapport E_J/E_C de notre atome artificiel ($(E_J/E_C)^* \approx 30$). Nous attendons une amélioration de la cohérence du qubit logique en augmentant ce rapport à 50 et en modifiant la forme de la capacité inter-digitée.

Le temps de cohérence du qubit ancillaire (temps de déphasage et temps de décroissance Rabi) est plus petit que les temps de cohérence du qubit logique. Nous suspectons que la cause de cette perte de cohérence est la super-inductance. En effet en augmentant le nombre de jonctions, nous augmentons la probabilité d'être couplé a un système à deux niveaux parasite. Cette idée est corroborée par les observations de résonance parasite observées dans les spectroscopies du qubit ancillaire lors de certaines périodes de mesure. En comparaison, de telles caractéristiques n'ont jamais été observées dans les spectroscopies du qubit logique et ce pour toutes les périodes de mesure.

Due à la nature des modes donnant lieu aux deux qubits, le qubit logique peut seulement être adressé par un champ électrique et le qubit ancillaire par un champ magnétique. De plus, les deux qubits ont un désaccord de fréquence de résonance de $\approx 10\,\mathrm{GHz}$. Ces deux propriétés assurent un adressage indépendant des deux transitions.

Puisque le système est composé de deux qubits couplés, un troisième niveau excité apparaît spontanément dans le diagramme d'énergie. Physiquement, ce niveau correspond à avoir les deux qubits excités à la fois. Cependant due a l'anharmonicité croisée, la fréquence de cette transition est en désaccord avec la transition des qubits logique et ancillaire. Par des spectroscopies trois-ton nous avons confirmé la nature et la force de l'anharmonicité croisée. Nous avons observé une anharmonicité croisée de 115 MHz, valeur en accord avec les prédictions théoriques.

En conclusion, l'atome artificiel composé de deux qubits transmons inductivement couplés vérifie les principales propriétés d'un atome artificiel possédant un diagramme d'énergie en V.

Perspectives

Lecture QND rapide

La réalisation d'un diagramme d'énergie en V dans un circuit supraconducteur ouvre la voie pour des lectures QND rapides de l'état du qubit logique. Dans ce but, je propose dans le Chapitre 1 de ce manuscrit, la possibilité d'effectuer des mesures quantiques non-destructives extrêmement rapides de l'état du qubit logique en utilisant le diagramme d'énergie en V et un résonateur micro-onde[45].

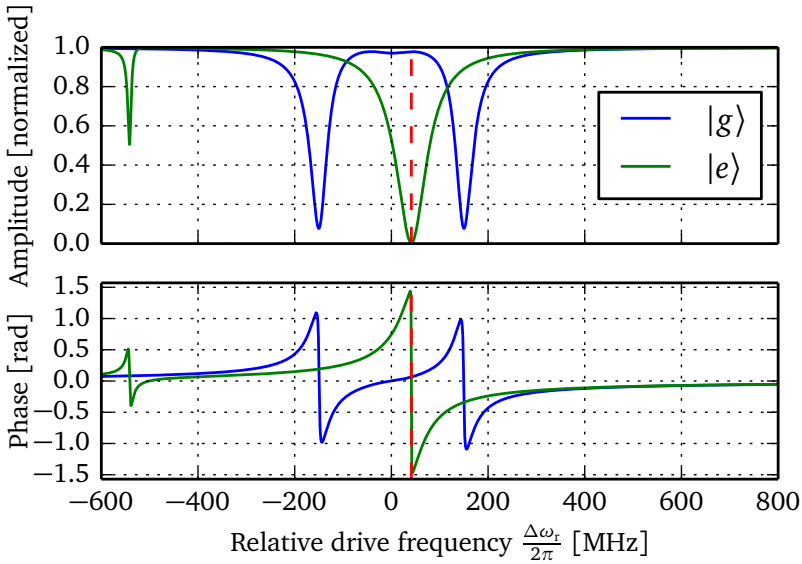

Figure (5.23): Transmission de l'atome artificiel couplé à un résonateur micro-onde en fonction de la fréquence relative du ton d'excitation. La courbe bleue correspond à la transmission du système lorsque le qubit est dans son état fondamental tandis que la courbe verte correspond à la transmission du système lorsque le qubit est dans son état excité.

L'atome artificiel est couplé à un résonateur micro-onde de telle manière que seul le qubit ancillaire est effectivement couplé. Cet état est facilement atteignable en plaçant l'atome artificiel à une position où le champ magnétique est maximal et le champ électrique minimal. Pour un résonateur micro-onde quart-d'onde, cette position correspond simplement au bord court-circuité du résonateur. On doit également avoir la fréquence de résonance du qubit ancillaire égale à la fréquence de résonance du résonateur micro-onde. Dans cette situation, la fréquence de résonance du résonateur va dépendre de l'état du qubit logique, voir Fig. 5.23. Le décalage en fréquence du résonateur peut atteindre plusieurs centaines de méga-hertz soit deux ordres de grandeur plus élevés que ce qu'on obtient avec l'habituel décalage dispersif.

La lecture du qubit logique est effectuée par le couplage cross-Kerr, rendant la mesure non destructive. De plus, dans notre proposition, le qubit logique n'est pas couplé au résonateur micro-onde supprimant l'effect Purcell. En utilisant un amplificateur proche de la limite

quantique ($T_N = 140\,\mathrm{mK}$ et $B = 50\,\mathrm{MHz}$), de tels circuits peuvent atteindre une fidélité de lecture de l'état du qubit logique de 99.7 % avec un temps de mesure de 50 ns.

Nous sommes actuellement en train de tester une deuxième génération d'échantillon dont les paramètres pourraient mener à la réalisation de cette proposition.

Transistor à un photon

En tirant parti de la haute adressabilité des deux qubits, nous pouvons envisager d'utiliser notre atome artificiel comme un transistor à un photon comme récemment proposé par Neumeier *et al.*[137].

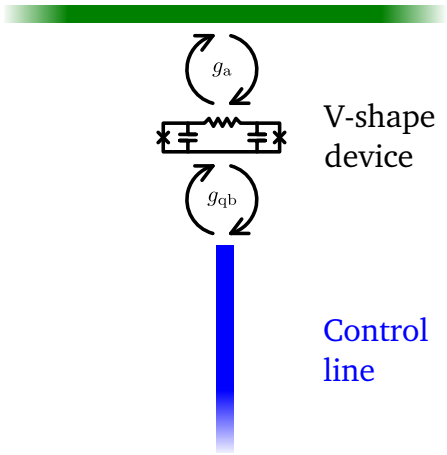

Figure (5.24): Transistor à un photon réalisé avec notre atome artificiel. Le qubit logique est couplé capacitivement à une ligne de contrôle tandis que l'ancillaire est couplé inductivement à une ligne de transmission.

Le circuit est représenté en Fig. 5.24. La ligne de contrôle est seulement couplée au qubit logique tandis que la ligne de transmission est seulement couplée au qubit ancillaire. Lorsque le qubit logique est dans son état fondamental, un photon voyageant dans la ligne en transmission à la fréquence de résonance du qubit ancillaire sera rétrodiffusé. En effet, pour un signal micro-onde arrivant à la fréquence de résonance du qubit ancillaire, l'atome artificiel induira une importante désadaptation d'impédance. Cependant, lorsque le qubit logique est dans son état excité, le signal arrivant sera transmis. En effet, due à l'anharmonicité croisée, la fréquence de résonance du qubit ancillaire sera décalée vers des fréquence plus basse. Il n'y aura donc plus de désadaptation d'impédance induite par l'atome artificiel.

En contrôlant l'état du qubit logique, il a été prédit que nous pouvons créer un transistor à un photon[137,138].

English

Conclusion

In this manuscript I have theoretically discussed the realisation of a superconducting artificial atom with a V-shape energy diagram. The superconducting circuit is based on two inductively coupled transmons. I theoretically described the circuit model of the V-shape sample as well as its microwave environment (quarterwave resonator and coupling to the feedline). This work leads to analytical prediction of a cross-Kerr coupling which can be as high as hundreds of megahertz. By using this feature we propose a protocol to perform the readout of a qubit state by keeping the logical qubit not coupled to the cavity, see the first perspective for details.

In order to realise experiments on the V-shape samples, I installed a complete microwave setup capable to perform state-of-the-art quantum experiments. This work includes installations of microwave components in a dilution fridge, calculation of heat load, calculation of residual photon noise, calibration of amplification chain, and installation of magnetic shieldings. A Python environment has also been installed in order to perform all experiments by Python scripts. Several Python drivers have been written to handle all instruments used for our measurements. Through this work, all the computer coding aspect from measurement script to data treatment is from now on performed in Python language.

A lot of work has been done on the characterisation of the microwave resonators. First, the asymmetric shape of the measured resonance has been explained by wire bonding inductances. The reduction of the inductance of the bondings will improve the impedance matching and so, the signal-to-noise ratio of the measurements. In order to move in this direction, we built a new sample holder, which will be soon installed, in which the length of the wire bondings needed to connect the chip to the coax cables has been drastically reduced from several millimeters to less than one millimeter. Second, the low internal quality factors measured on both aluminium and rhenium microwave resonators suggest a common limiting factor. Possible explanation could be an inefficient thermal and magnetic shielding of the sample chip and a bad thermalisation of photons coming from the cryogenic amplifier. Thus the next generation of sample holder will improve the thermal shielding by adopting the strategy of “box-in-a-box” described by R. Barends in [91]. A better magnetic shielding has also be implemented in the new sample holder. Moreover by moving the magnetic connectors further away from the sample chip the new sample holder will again decrease the magnetic field at the chip position. In order to have the same thermalisation of photons in the input and the amplification lines, the two microwave circulators of the amplification line will be both thermalised at 35 mK. Finally, a microwave low-pass filter made by eccosorb with cut-off frequency about 30 GHz will be installed in order to filter very high frequency signals.

The microwave resonator of the V-shape sample was made tunable by incorporating a SQUID in the central line of the resonator. An hysteresis has been observed by studying the magnetic flux dependence of the cavity frequency. We show that the hysteresis came from the loop inductance of the SQUID which was comparable to the Josephson inductance of the junctions. A quantitative description of the magnetic flux dependence of the cavity resonance has been done leading to a very good understanding of the system.

Two-tone spectroscopy have been used to measure the magnetic flux dependence of the

first two excited levels of the *in-phase* mode and the first excited level of the *out-of-phase* mode. We performed numerical calculations via Kwant library to fit these levels with a good agreement between theory and data. The analytical model developed in Chapter 1 has also been used to fit data but the extracted parameters do not validate the assumptions made to obtain the model.

An interesting property has been measured through the magnetic flux dependence of the second transition of the *in-phase* mode. Indeed we measured that this transition becomes forbidden at $\phi_b = 0$. We understand this feature via the different symmetry of the two modes of the V-shape sample. Indeed at $\phi_b = 0$, the mode becomes only coupled via a cross-Kerr term. The ground and second excited state exhibit then both an even symmetry making impossible direct energy transition between them. When $\phi_b \neq 0$, non linear couplings between the two modes appear. The presence of these couplings breaks the even parity of the ground and second excited states. The transition is then available. We performed a first-order analytical calculation of the eigenestates of the system through the quantum perturbation theory. We demonstrated that this feature can be explained via the non linear coupling term ω_{21}.

To deserve the name of V-shape, an energy diagram must exhibit specific properties:

1. The two qubits have to belong to two different modes.
2. One qubit should exhibit a long coherence time in order to be used as logical qubit.
3. Each qubit transition is addressable independently.
4. Any transitions from the logical qubit excited state to a higher energy level are far out of resonance of the ancilla transition.

We perform different experiments to verify all these properties. From the magnetic field dependence of the energy levels measured via two-tone spectroscopies, we confirm the nature of the oscillating modes giving rise to the logical and ancilla qubit.

At $\phi_b = 0$, the system can be viewed as two qubits only coupled via a cross anharmonicity. One of these qubits is equivalent to the usual transmon qubit and is used as a logical qubit. The other qubit is then dedicated to the measurement of the logical qubit and is the ancilla qubit.

By time-resolved experiments, we measured the relaxation and the Rabi decay time of the logical qubit. We have demonstrated that the logical and ancilla qubit have a relaxation time comparable with the first generation of transmon with $T_1^{\mathrm{qb,\,a}} \approx 500\,\mathrm{ns}$. Surprisingly the ancilla qubit exhibits the same relaxation time as the logical qubit. This may suggest a common limiting factor for the two qubits. However no explanation has been found so far.

By studying readout and probe power dependence of the logical qubit resonance peak, we estimate its pure dephasing time between 30 to 100 ns. The Rabi oscillation decays over a characteristic time of about 500 ns. These times are short compared to what transmon qubits can achieve and could be explained by the too small E_J/E_C ratio in our circuit ($(E_J/E_C)^* \approx 30$). We expect an improvement of the logical qubit coherence by increasing this ratio up to 50 and by modifying the design of the inter-digital capacitance.

The coherence times of the ancilla (Rabi decay time and pure dephasing time) are lower than the coherence times of the logical qubit. We suspect the superinductor to be the cause of this loss of coherence. Indeed by increasing the number of Josephson junctions, we increase the probability to be coupled to spurious two-level systems. This idea is corroborated by the observation of two-level spurious resonances in the ancilla spectroscopy observed in some measurements. In comparison, such spurious features have never been observed in the logical qubit spectroscopy during all our measurements.

Due to the nature of the modes leading to the two qubits, the logical qubit can only be addressed via electric field and the ancilla qubit by magnetic field. Moreover, the two qubits are detuned by $\approx 10\,\mathrm{GHz}$. These two properties ensure an independent addressing of the two transitions.

Since the system is composed of two coupled qubits, a third excited level arises in the energy diagram. Physically this level corresponds to having the two qubits excited simultaneously. However due to the cross-anharmonicity, this level is detuned from the qubit and ancilla transitions. By three-tone spectroscopy we confirm the nature and the strength of the cross-anharmonicity. We observed cross-Kerr anharmonicity of about 115 MHz, value in agreement with the analytical model of the V-shape sample.

In conclusion the two inductively coupled transmon qubits verify the main properties of a V-shape artificial atom.

Perspectives

Fast QND readout

The realisation of a V-shape energy diagram in superconducting circuit opens the way for fast QND readout of the logical qubit state. In this purpose I proposed, in Chapter 1 of this manuscript, the possibility to perform an ultra fast quantum non destructive readout of the logical qubit state by using the V-shape device in circuit quantum electrodynamics architecture with a quarterwave resonator[45].

The V-shape device is coupled to a microwave resonator in such way that only the ancilla qubit is effectively coupled. This is easily achievable by placing the V-shape device at a position where the magnetic field is maximum and the electric field minimum. For a quarterwave microwave resonator this position simply corresponds to the short-circuit side of the resonator. The last requirement is to set the ancilla resonance frequency equal to the microwave resonator frequency. In such a situation, the cavity resonance frequency will depend on the logical qubit state, see Fig. 5.25. The frequency shift of the resonator can be as high as few hundreds of megahertz so two orders of magnitudes higher than what we can obtain by usual dispersive shift.

The readout of the logical qubit is performed via the cross-Kerr coupling, making the measurement non destructive. Moreover, in our proposal, the logical qubit is not coupled to the microwave resonator suppressing relaxation by Purcell effect. By using a near quantum limited amplifier ($T_\mathrm{N} = 140\,\mathrm{mK}$ and $B = 50\,\mathrm{MHz}$), such a circuit should reach a logical qubit readout fidelity of 99.7 % with a measurement duration of 50 ns.

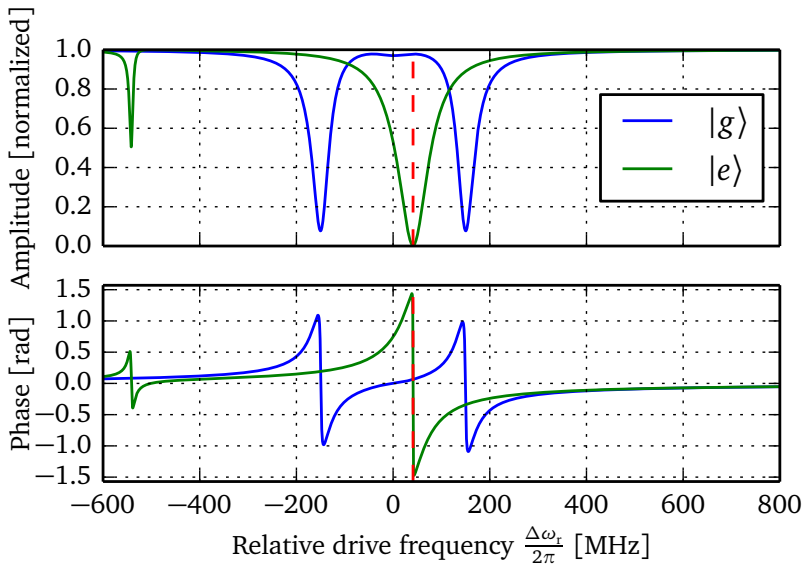

Figure (5.25): Transmission of the V-shape sample embedded in a microwave resonator as a function of the relative drive frequency. The blue line corresponds to the transmission of the system when the qubit is in its ground state while the green line is when it is in its excited state.

We are currently testing a second generation of samples whose parameters may lead to this novel readout proposal.

Single photon transistor

Taking advantage of the high selective addressability of the two qubits, we can envision using our V-shape device as a single photon transitor recently proposed by Neumeier *et al.*[137].

The circuit is sketched in Fig. 5.26. The control line is only coupled to the logical qubit while the transmission line is only coupled to the ancilla qubit. When the logical qubit is in its ground state, a photon travelling in the transmission line at the frequency of the ancilla transition will be backscattered. Indeed, for an incoming microwave signal at the ancilla transition frequency, the V-shape device will induce a strong impedance mismatch. However, when the logical qubit is in its excited state, the incoming signal will be transmitted. Indeed due to the cross-anharmonicity, the ancilla transition will be downshifted to a lower resonance frequency. There will be no impedance mismatch induced by the V-shape device.

By controlling the state of the logical qubit it has been predicted that we can manipulate the flow of photon at the single photon level[137,138].

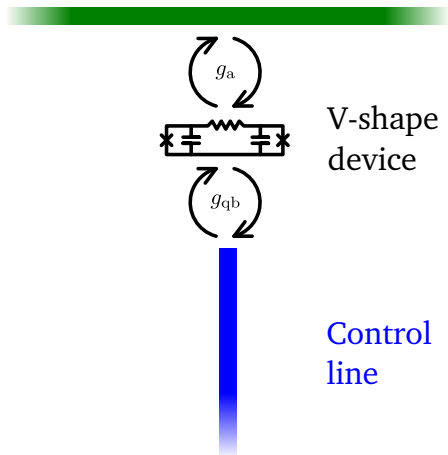

Figure (5.26): Single photon transistor realised with our V-shape device. The logical qubit is coupled capacitively to the control line while the ancilla qubit is coupled inductively to a transmission line.

Appendix A

Software environment

A basic measurement script is displayed below. The script is adapted from an example available in the QTLab documentation. Lot of comments are written directly in the code.

```
#Libraries importation
import numpy as np

# you define two vectors of what you want to sweep.
# In this case a frequency (f_vec)
f_vec = np.arange(0,10,0.01)

# you indicate that a measurement is about to start and
# other processes should stop (like batterycheckers, or
# temperature monitors)
qt.mstart()

# Next a new data object is made.
# The file will be placed in the folder:
# <datadir>/<datestamp>/<timestamp>_testmeasurement/
# and will be called:
# <timestamp>_testmeasurement.dat
# to find out what 'datadir' is set to,
# type: qt.config.get('datadir')
data = qt.Data(name='testmeasurement')

# Now you provide the information of what data will be
# saved in the datafile. A distinction is made between
# 'coordinates', and 'values'.
# Coordinates are the parameters that you sweep, values
# are the parameters that you readout (the result of an
```

```
27 # experiment).
28 # This information is used later for plotting purposes.
29 # Adding coordinate and value info is optional, but
30 # recommended.
31 # If you don't supply it, the data class will guess your
32 # data format.
33 data.add_coordinate('Frequency [GHz]')
34 data.add_value('S21 [dB]')
35
36 # The next command will actually create the dirs and
37 # files, based on the information provided above.
38 # Additionally a settingsfile is created containing the
39 # current settings of all the instruments.
40 data.create_file()
41
42 # Next one plot-objects is created.
43 # First argument is the data object that needs to be
44 # plotted.
45 # To prevent new windows from popping up each measurement
46 # a 'name' can be provided so that window can be reused.
47 # If the 'name' doesn't already exists, a new window with
48 # that name will be created.
49 plot2d = qt.Plot2D(data, name='measure2D',
50                          coorddim=0,
51                          valdim=2,
52                          traceofs=10)
53
54 # Preparation is done, now start the measurement.
55 # It is actually a simple loop.
56 for f in f_vec:
57     # set the frequency
58     fake_mw_src.set_freqency(f)
59
60     # readout
61     result = fake_readout_psw.get_data()
62
63     # save the data point to the file, this will
64     # automatically trigger the plot windows to update
65     data.add_data_point(f, result)
66
67     # the next function is necessary to keep the gui
68     # responsive.
69     # It checks for instance if the 'stop' button is pushed.
```

```
70      # It also checks if the plots need updating.
71      qt.msleep(0.001)
72
73
74  # after the measurement ends, you need to close
75  # the data file.
76  data.close_file()
77  # lastly tell the secondary processes (if any)
78  # that they are allowed to start again.
79  qt.mend()
```

Appendix B

Derivation of the quarter-wave resonator transmission

Contents

B.1 Symmetric model **228**

B.1.1 Calculation of the shift in frequency caused by the coupling capacitor 228

B.1.2 Calculation of the coupling capacitance Q_c 230

B.1.3 Calculation of the transmission coefficient S_{21} 230

B.2 Asymmetric model **231**

B.3 Result **233**

B.3.1 Coupling capacitor 233

B.3.2 Spurious inductance 233

B.3.3 Approximation verification 234

The appendix presents the derivation of the a quarter-wave resonator transmission. The first part describes the transmission of a resonator coupled to a feedline[139]. The result leads to a power transmission having a Cauchy-Lorentz distribution shape, whose the width depends of the internal losses and of the coupling to the environment. In the second part, we develope a model capable to explain asymmetric resonances measured during my thesis. Measured resonance peaks may have an asymmetric shape and not a simple Lorentzian shape. Such asymmetric shapes can be attributed to an impedance mismatch in the feedline[115,116] on either side of the resonator as indicated in Fig. B.2 by the two X_e impedances. Our interpretation attributes these impedances to wire–bondings between the chip and the printed circuit board.

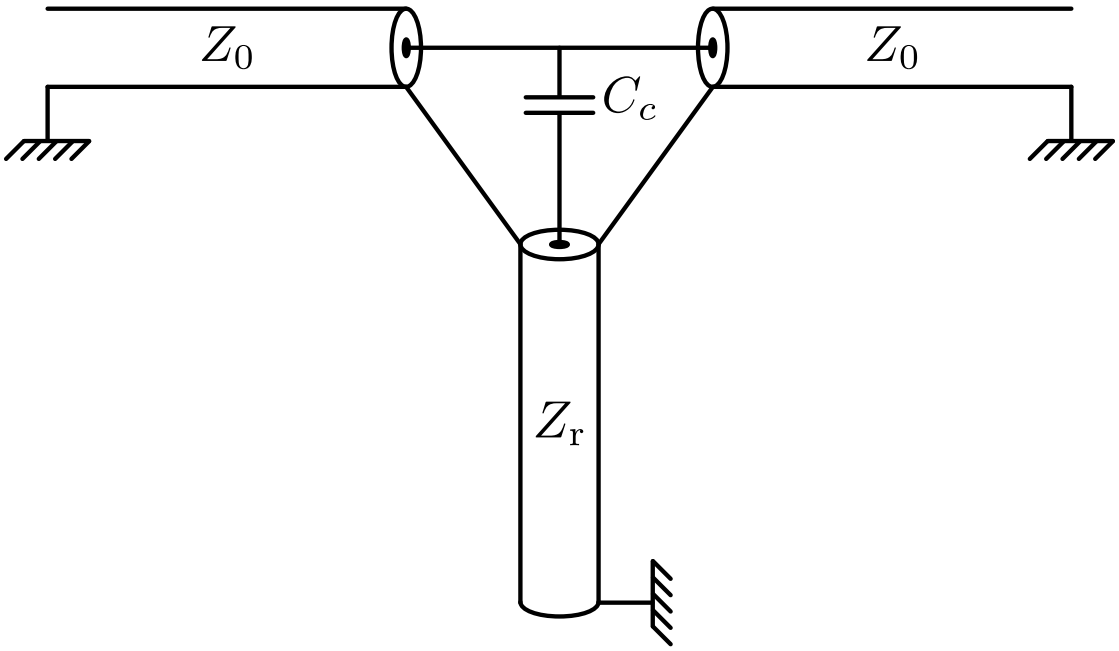

Figure (B.1): Electrical circuit of a $\lambda/4$ resonator.

B.1 Symmetric model

The resonator is depicted by a coaxial cable of characteristic impedance Z_r with an internal quality factor Q_i. Its resonance frequency is denoted by $\omega_r = 2\pi\nu_r$ and the deviation from this particular frequency $\Delta\omega_r = \omega - \omega_r$. Finally the resonator is coupled through a capacitor of impedance $Z_{C_c} = -\frac{i}{\omega C_c}$ to a feedline of characteristic impedance Z_0.

B.1.1 Calculation of the shift in frequency caused by the coupling capacitor

The impedance of the resonator can be written as (see [61] equation 6.29):

$$Z_{\text{resonator}} = \frac{Z_r}{\frac{\pi}{4}\frac{1}{Q_i} + i\frac{\pi}{2}\frac{\Delta\omega_r}{\omega_r}}. \tag{B.1}$$

We can rewrite Eq. (B.1) by expanding the real and imaginary part:

$$Z_{\text{resonator}} = Z_r \frac{4Q_i}{\pi} \frac{1 - i2Q_i\frac{\Delta\omega_r}{\omega_r}}{1 + 4Q_i^2\left(\frac{\Delta\omega_r}{\omega_r}\right)^2}. \tag{B.2}$$

The system is composed of the resonator and a capacitor. The total impedance is simply the sum of the two:

$$Z_{\text{tot}} = Z_{\text{r}} \frac{4Q_{\text{i}}}{\pi} \frac{1 - \text{i}2Q_{\text{i}} \frac{\Delta\omega_{\text{r}}}{\omega_{\text{r}}}}{1 + 4Q_{\text{i}}^2 \left(\frac{\Delta\omega_{\text{r}}}{\omega_{\text{r}}}\right)^2} - \frac{\text{i}}{\omega C_{\text{c}}} \tag{B.3}$$

$$= Z_{\text{r}} \frac{\frac{4Q_{\text{i}}}{\pi} - \text{i}\left(\frac{8Q_{\text{i}}^2}{\pi} \frac{\Delta\omega_{\text{r}}}{\omega_{\text{r}}} + \frac{1}{\omega C_{\text{c}} Z_{\text{r}}} \left[1 + 4Q_{\text{i}}^2 \left(\frac{\Delta\omega_{\text{r}}}{\omega_{\text{r}}}\right)^2\right]\right)}{1 + 4Q_{\text{i}}^2 \left(\frac{\Delta\omega_{\text{r}}}{\omega_{\text{r}}}\right)^2}. \tag{B.4}$$

At the resonance the imaginary part of the total impedance is equal to zero. This leads to:

$$\frac{4Q_{\text{i}}^2}{\omega_0 C_{\text{c}} Z_{\text{r}}} \left(\frac{\Delta\omega_{\text{r}}}{\omega_{\text{r}}}\right)^2 + \frac{8Q_{\text{i}}^2}{\pi} \frac{\Delta\omega_{\text{r}}}{\omega_{\text{r}}} + \frac{1}{\omega_0 C_{\text{c}} Z_{\text{r}}} = 0. \tag{B.5}$$

The two solutions $(\Delta\omega_{\text{r}}/\omega_{\text{r}})_+$ and $(\Delta\omega_{\text{r}}/\omega_{\text{r}})_-$ are:

$$\frac{\Delta\omega_{\text{r}}}{\omega_{\text{r}}}_{\pm} = \frac{\omega_0 C_{\text{c}} Z_{\text{r}}}{2Q_{\text{i}}} \left(-\frac{2Q_{\text{i}}}{\pi} \pm \sqrt{\frac{4Q_{\text{i}}^2}{\pi^2} - \frac{1}{\omega_0^2 C_{\text{c}}^2 Z_{\text{r}}^2}}\right). \tag{B.6}$$

For the following we will assume[1] that $(4Q_{\text{i}}^2)/\pi^2$ is much greater than $1/(\omega_0^2 C_{\text{c}}^2 Z_{\text{r}}^2)$. Equation (B.6) becomes:

$$\frac{\Delta\omega_{\text{r}}}{\omega_{\text{r}}}_{\pm} = \frac{\omega_0 C_{\text{c}} Z_{\text{r}}}{2Q_{\text{i}}} \left(-\frac{2Q_{\text{i}}}{\pi} \pm \frac{2Q_{\text{i}}}{\pi}\right). \tag{B.7}$$

Physically only one solution makes sense, it's the solution which lower the resonance frequency since by adding a capacitor in series with a resonator we make the overall capacitance bigger. In this case the solution is reduce to:

$$\frac{\Delta\omega_{\text{r}}}{\omega_{\text{r}}} = -\frac{2\omega_0 C_{\text{c}} Z_{\text{r}}}{\pi}. \tag{B.8}$$

We can now define ω_0 the resonance frequency of the coupling capacitor and resonator in series and $\Delta\omega_0 = \omega - \omega_0$ the deviation from this particular frequency as:

$$\frac{\Delta\omega_0}{\omega_0} = \frac{\Delta\omega_{\text{r}}}{\omega_{\text{r}}} + \frac{2\omega_0 C_{\text{c}} Z_{\text{r}}}{\pi}. \tag{B.9}$$

[1] By using the definition of the external quality factor Q_{c} given in Eq. (B.15), we can demonstrate that the assumption $(4Q_{\text{i}}^2)/\pi^2 \gg 1/(\omega_0^2 C_{\text{c}}^2 Z_{\text{r}}^2)$ is equivalent to $(Q_{\text{c}}^2 Z_0)/(Q_{\text{i}}^2 Z_{\text{r}}) \ll 1$. Thus, for a matched resonator ($Z_0 = Z_{\text{r}}$), the ratio of the external quality factor to the internal quality factor has to be much smaller than one. Physically, this condition implies to have a resonator in the undercoupled regime. When $Z_{\text{r}} \neq Z_0$, the quality factors ratio is normalized by the ratio of the characteristic impedance of the resonator to the characteristic impedance of the feedline.

B.1.2 Calculation of the coupling capacitance Q_c

At the resonance frequency the total impedance is equal to:

$$Z_{tot} = Z_r \frac{4Q_i}{\pi} \frac{\pi^2}{\pi^2 + 16Q_i^2\omega_0^2C_c^2Z_r^2}. \tag{B.10}$$

We assume[2] that $\pi^2 \ll 16Q_i^2\omega_0^2C_c^2Z_r^2$ which leads to:

$$Z_{tot} = \frac{\pi}{4Q_i\omega_0^2C_c^2Z_r}. \tag{B.11}$$

For our system the transmission coefficient can be calculated as (see [61] table 4.1 and 4.2):

$$S_{21} = \frac{2}{2 + \frac{Z_0}{Z_{tot}}}. \tag{B.12}$$

If we replace Eq. (B.11) in Eq. (B.12), we get:

$$S_{21} = \frac{2\pi}{2\pi + 4Q_i\omega_0^2C_c^2Z_rZ_0}. \tag{B.13}$$

At the resonance frequency a well-known result is that $S_{21} = \frac{Q_c}{Q_i+Q_c}$ (see for example [99] equation 2.42). If we factorize Eq. (B.13) to this form, we have:

$$S_{21} = \frac{\frac{\pi}{2\omega_0^2C_c^2Z_rZ_0}}{\frac{\pi}{2\omega_0^2C_c^2Z_rZ_0} + Q_i}. \tag{B.14}$$

We found a formula which links the coupling capacitance to the coupling quality factor:

$$Q_c = \frac{\pi}{2\omega_0^2C_c^2Z_rZ_0}. \tag{B.15}$$

B.1.3 Calculation of the transmission coefficient S_{21}

We can now calculate the transmission coefficient for all frequency. The first step is to write the coupling capacitance and the shift in frequency as a function of the coupling quality factor. We get:

$$\frac{\Delta\omega_r}{\omega_r} = \frac{\Delta\omega_0}{\omega_0} - \sqrt{\frac{2Z_r}{\pi Z_0 Q_c}} \tag{B.16}$$

$$Z_{C_c} = -i\sqrt{\frac{2Z_0Z_rQ_c}{\pi}}. \tag{B.17}$$

[2]This assumption is, at a factor of 4, the same as done between Eq. (B.6) and Eq. (B.7).

The total impedance becomes:

$$Z_{\text{tot}} = Z_{\text{r}} \frac{\frac{4Q_{\text{i}}}{\pi}}{1 + 2\text{i}Q_{\text{i}}\left(\frac{\Delta\omega_0}{\omega_0} - \sqrt{\frac{2Z_{\text{r}}}{\pi Z_0 Q_{\text{c}}}}\right)} - \text{i}\sqrt{\frac{2Z_0 Z_{\text{r}} Q_{\text{c}}}{\pi}} \tag{B.18}$$

$$= \frac{2Q_{\text{i}}\sqrt{\frac{2Q_{\text{c}}Z_0 Z_{\text{r}}}{\pi}}\frac{\Delta\omega_0}{\omega_0} - \text{i}\sqrt{\frac{2Q_{\text{c}}Z_0 Z_{\text{r}}}{\pi}}}{1 + 2\text{i}Q_{\text{i}}\left(\frac{\Delta\omega_0}{\omega_0} - \sqrt{\frac{2Z_{\text{r}}}{\pi Z_0 Q_{\text{c}}}}\right)}. \tag{B.19}$$

Using Eq. (B.12), we get:

$$S_{21} = \frac{4Q_{\text{i}}\sqrt{\frac{2Q_{\text{c}}Z_0 Z_{\text{r}}}{\pi}}\frac{\Delta\omega_0}{\omega_0} - 2\text{i}\sqrt{\frac{2Q_{\text{c}}Z_0 Z_{\text{r}}}{\pi}}}{4Q_{\text{i}}\sqrt{\frac{2Q_{\text{c}}Z_0 Z_{\text{r}}}{\pi}}\frac{\Delta\omega_0}{\omega_0} - 2\text{i}\sqrt{\frac{2Q_{\text{c}}Z_0 Z_{\text{r}}}{\pi}} + Z_0 + 2\text{i}Q_{\text{i}}Z_0\left(\frac{\Delta\omega_0}{\omega_0} - \sqrt{\frac{2Z_{\text{r}}}{\pi Z_0 Q_{\text{c}}}}\right)} \tag{B.20}$$

$$= \frac{1 + 2\text{i}Q_{\text{i}}\frac{\Delta\omega_0}{\omega_0}}{1 + 2\text{i}Q_{\text{i}}\frac{\Delta\omega_0}{\omega_0} + \text{i}\frac{1}{2}\sqrt{\frac{\pi Z_0}{2Q_{\text{c}}Z_{\text{r}}}} + \frac{Q_{\text{i}}}{Q_{\text{c}}} - Q_{\text{i}}\sqrt{\frac{\pi Z_0}{2Q_{\text{c}}Z_{\text{r}}}}\frac{\Delta\omega_0}{\omega_0}}. \tag{B.21}$$

Here we assume:

$$\frac{1}{2}\sqrt{\frac{\pi Z_0}{2Q_{\text{c}}Z_{\text{r}}}} \ll 2Q_{\text{i}}\frac{\Delta\omega_0}{\omega_0} \tag{B.22}$$

$$Q_{\text{i}}\sqrt{\frac{\pi Z_0}{2Q_{\text{c}}Z_{\text{r}}}}\frac{\Delta\omega_0}{\omega_0} \ll 1 + \frac{Q_{\text{i}}}{Q_{\text{c}}}. \tag{B.23}$$

Which give us the final equation given S_{21} as a function of Q_{i} and Q_{c} :

$$\boxed{S_{21} = \frac{1 + 2\text{i}Q_{\text{i}}\frac{\Delta\omega_0}{\omega_0}}{1 + \frac{Q_{\text{i}}}{Q_{\text{c}}} + 2\text{i}Q_{\text{i}}\frac{\Delta\omega_0}{\omega_0}}} \tag{B.24}$$

B.2 Asymmetric model

To obtain an asymmetry, we have to take into account parasitic modes which can exist in the feedline. Indeed the feedline is generally bonded at its two extremities with small and narrow aluminium wires. When the inductance of these wires are not negligible, they create a halfwave resonator instead of a simple coplanar waveguide. However this complete model leads to a really complicated equation from which it is difficult to obtain an understandable analytical expression. Here we will adopt an intermediate point of view where we will completely neglect the propagation behaviour of the spurious halfwave resonator but we will take into account the impedance mismatch caused by the bondings, see Fig. B.2.

The only new element is the reactance X_{e} between the resonator and the coax line. The external quality factor and the frequency shift stays the same than before (see Eqs. (B.15)

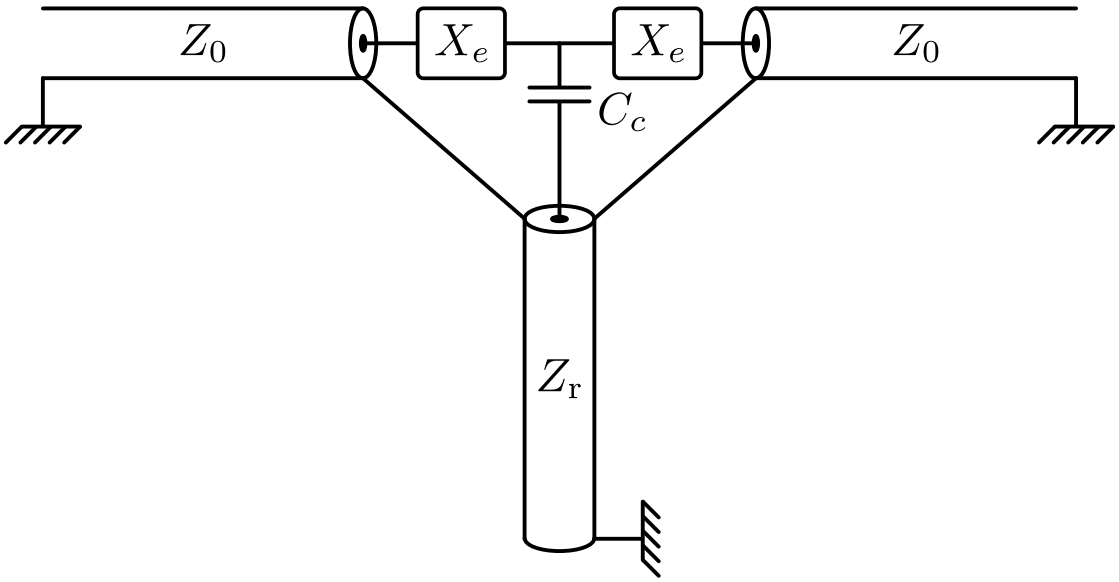

Figure (B.2): Electrical circuit of a $\lambda/4$ resonator with two reactances added on either side of the resonator.

and (B.16)) since the resonator and the coupling capacitor are not modified. However the transmission coefficient is modified to take into account the addition of the two environmental reactances (see [61] table 4.1 and 4.2):

$$S_{21} = \frac{2Z_{\text{tot}}Z_0}{2Z_{\text{tot}}(Z_0 + \mathrm{i}X_{\text{e}}) + (Z_0 + \mathrm{i}X_{\text{e}})^2}. \tag{B.25}$$

We replace Z_{tot} by its expression given in Eq. (B.18), we get:

$$S_{21} = \frac{Z_0}{Z_0 + \mathrm{i}X_{\text{e}}} \frac{4Q_{\text{i}}\sqrt{\frac{2Q_{\text{c}}Z_0Z_{\text{r}}}{\pi}}\frac{\Delta\omega_0}{\omega_0} - 2\mathrm{i}\sqrt{\frac{2Q_{\text{c}}Z_0Z_{\text{r}}}{\pi}}}{4Q_{\text{i}}\sqrt{\frac{2Q_{\text{c}}Z_0Z_{\text{r}}}{\pi}}\frac{\Delta\omega_0}{\omega_0} - 2\mathrm{i}\sqrt{\frac{2Q_{\text{c}}Z_0Z_{\text{r}}}{\pi}} + \left(1 + 2\mathrm{i}Q_{\text{i}}\left(\frac{\Delta\omega_0}{\omega_0} - \sqrt{\frac{2Z_{\text{r}}}{\pi Z_0 Q_{\text{c}}}}\right)\right)(Z_0 + \mathrm{i}X_{\text{e}})} \tag{B.26}$$

$$= \frac{Z_0}{Z_0 + \mathrm{i}X_{\text{e}}} \frac{1 + 2\mathrm{i}Q_{\text{i}}\frac{\Delta\omega_0}{\omega_0}}{\begin{array}{l} 1 + \frac{Q_{\text{i}}}{Q_{\text{c}}} - Q_{\text{i}}\sqrt{\frac{\pi Z_0}{2Q_{\text{c}}Z_{\text{r}}}}\frac{\Delta\omega_0}{\omega_0} - \frac{X_{\text{e}}}{2}\sqrt{\frac{\pi}{2Q_{\text{c}}Z_0Z_{\text{r}}}} \\ + \mathrm{i}\left(\frac{Q_{\text{i}}X_{\text{e}}}{Q_{\text{c}}Z_0} - Q_{\text{i}}X_{\text{e}}\sqrt{\frac{\pi}{2Q_{\text{c}}Z_0Z_{\text{r}}}}\frac{\Delta\omega_0}{\omega_0} + 2Q_{\text{i}}\frac{\Delta\omega_0}{\omega_0} + \frac{Z_0}{2}\sqrt{\frac{\pi}{2Q_{\text{c}}Z_0Z_{\text{r}}}}\right) \end{array}}. \tag{B.27}$$

We assume:

$$\frac{\Delta\omega_0}{\omega_0}\frac{\pi Z_0 Q_\mathrm{i}}{2Q_\mathrm{c}Z_\mathrm{r}} \ll 1 + \frac{Q_\mathrm{i}}{Q_\mathrm{c}} \tag{B.28}$$

$$\frac{X_\mathrm{e}}{2}\sqrt{\frac{\pi Z_0}{2Q_\mathrm{c}Z_\mathrm{r}}} \ll 1 + \frac{Q_\mathrm{i}}{Q_\mathrm{c}}, \tag{B.29}$$

and:

$$\frac{Z_0}{2}\sqrt{\frac{\pi Z_0}{2Q_\mathrm{c}Z_\mathrm{r}}} \ll \frac{Q_\mathrm{i}X_\mathrm{e}}{Q_\mathrm{c}Z_0} + 2Q_\mathrm{i}\frac{\Delta\omega_0}{\omega_0} \tag{B.30}$$

$$Q_\mathrm{i}X_\mathrm{e}\frac{\Delta\omega_0}{\omega_0}\sqrt{\frac{\pi Z_0}{2Q_\mathrm{c}Z_\mathrm{r}}} \ll \frac{Q_\mathrm{i}X_\mathrm{e}}{Q_\mathrm{c}Z_0} + 2Q_\mathrm{i}\frac{\Delta\omega_0}{\omega_0}. \tag{B.31}$$

We get:

$$\boxed{S_{21} = \frac{Z_0}{Z_0 + \mathrm{i}X_\mathrm{e}}\frac{1 + 2\mathrm{i}Q_\mathrm{i}\frac{\Delta\omega_0}{\omega_0}}{1 + \frac{Q_\mathrm{i}}{Q_\mathrm{c}Z_0}(Z_0 + \mathrm{i}X_\mathrm{e}) + 2\mathrm{i}Q_\mathrm{i}\frac{\Delta\omega_0}{\omega_0}}} \tag{B.32}$$

B.3 Result

B.3.1 Coupling capacitor

Thanks to our definition of Q_c in Eq. (B.15), we are able to extract the equivalent coupling capacitance of our electrical circuit. The fit shown in Fig. B.3 gives $Q_\mathrm{c} = 50 \times 10^3$ which leads to $C_\mathrm{c} = 2.13\,\mathrm{fF}$. This value is in good agreement with design since the expected value was around 2 fF.

B.3.2 Spurious inductance

The model explained here is an approximation of a more complicated one where the feedline is described as a halfwave resonator made unintentional with bondings. The reactance X_e is a simplification of the imaginary part of the impedance of this resonator. The sign of X_e is meaningless (physically speaking) since it will be negative when the resonance frequency of the feedline will be greater than the resonance frequency of the resonator and vice-versa. Nevertheless we can approximate X_e as the impedance of the bondings at the resonance frequency ω_0. This approximation leads to an inductance of 1.9 nH which is very close to the inductance found with the complete model which was 1.8 nH. Moreover we estimate the inductance per unit length for bonding wires is about $L_\ell^{\mathrm{bonding}} \approx 1\,\mathrm{nH{\cdot}m^{-1}}$. That leads to a discrepancy between the estimated inductance and the inductance given by the fit about 10 %.

B.3.3 Approximation verification

During our demonstration we have make some approximations and we can now check if they are valid or not. Figure B.3 presents two fits of the same resonance calculated with Eqs. (B.25) and (B.32). We can see that even far away from the resonance dip, the difference between the final analytical formula Eq. (B.32) and the original formula Eq. (B.25) is very small.

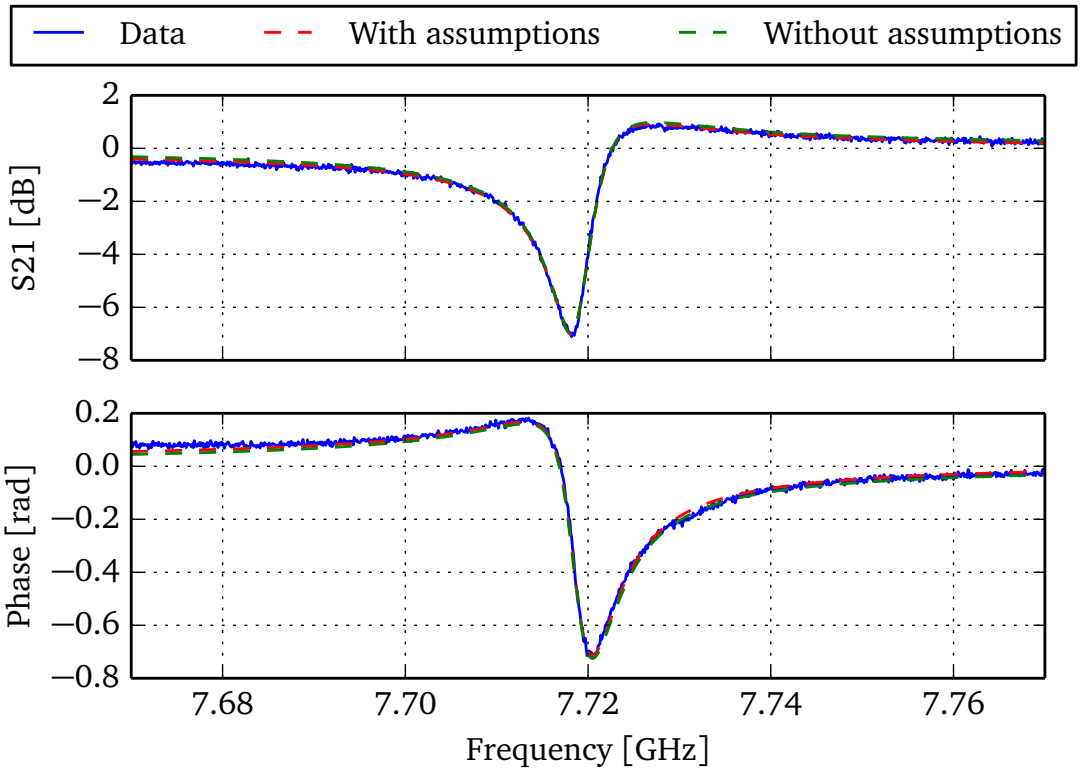

Figure (B.3): Resonance of a quarter-wave resonator fitted with Eq. (B.32) in red and Eq. (B.25) in green.

Appendix C

Samples parameters

Circuit parameters	Symbols	V-shape-1	V-shape-2
Microwave resonator			
Cavity resonance frequency	ν_0	7.281 GHz	7.719 GHz
Cavity decay rate	$\kappa/(2\pi)$	1.94 ± 0.01 MHz	3.80 ± 0.01 MHz
Internal quality factor	Q_i	3020 ± 20	1990 ± 5
External quality factor	Q_c	3750 ± 20	2030 ± 5
Equivalent circuit parameters			
Critical current	I_c		8 nA
Capacitance	C		40 fF
Loop inductance	L_loop		7.5 nH
Characteristic energies			
Josephson energy	E_J		4.07 GHz
Cooper-pair Coulomb energy	E_C		1.95 GHz
Dimensionless quantities			
Inductance ratio	b		5.49
Characteristic energy ratio	$E_\mathrm{J}/E_\mathrm{C}$		2^*
Logical qubit			
Qubit dispersive coupling	$\chi_\mathrm{qb}/(2\pi)$	1.9 MHz	2.5 MHz
Qubit relaxation time	T_1^qb	600 ± 10 ns	
Qubit Rabi decay time	$T_2^\mathrm{Rabi,\ qb}$	480 ± 20 ns	
Qubit pure dephasing time	T_ϕ^qb	30 ± 4 ns	150 ± 100 ns
Qubit anharmonicity	Δ_x/h	340 MHz	320 MHz
Detuning cavity-qubit	Δ_qb	3.644 GHz	4.119 GHz
Ancilla qubit			
Ancilla dispersive coupling	$\chi_\mathrm{a}/(2\pi)$	0.75 MHz	
Ancilla relaxation time	T_1^a	630 ± 30 ns	

Continued on next page

Table C.1 – continued from previous page

Circuit parameters	Symbols	V-shape-1	V-shape-2
Ancilla characteristic decay time	τ	90 ± 60 ns	
Detuning cavity-ancilla	Δ_a	5.269 GHz	6.086 GHz
V-shape			
cross-anharmonicity	$(2g_{zz})/(2\pi)$	119 MHz	110 MHz

Table (C.1): Summary of the different parameters extracted on the sample "V-shape-1" and "V-shape-2". The uncertainty range is given in $\pm\sigma$ with σ the standard deviation.
** Compared to the usual Transmon definition our ratio E_J/E_C should be multiplied by 16. We then obtain a ratio of* 33 *for the "V-shape-2" sample.*

Appendix D

Corrected eigenstates

We present here the result of the eigenstates derivation from Eq. (1.45).

$$
\begin{aligned}
\left|\psi_{\mathrm{n}_x,\mathrm{n}_y}\right\rangle = &\left|\varphi_{\mathrm{n}_x,\mathrm{n}_y}\right\rangle \\
&-\frac{1}{4}\hbar\omega_x\delta_x\left(W_a\left|\varphi_{\mathrm{n}_x+4,\mathrm{n}_y}\right\rangle + W_b\left|\varphi_{\mathrm{n}_x+2,\mathrm{n}_y}\right\rangle + W_c\left|\varphi_{\mathrm{n}_x-2,\mathrm{n}_y}\right\rangle + W_d\left|\varphi_{\mathrm{n}_x-4,\mathrm{n}_y}\right\rangle\right) \\
&-\frac{1}{\sqrt{2^3}}\hbar\omega_y\sigma_y\left(W_e\left|\varphi_{\mathrm{n}_x,\mathrm{n}_y+3}\right\rangle + W_f\left|\varphi_{\mathrm{n}_x,\mathrm{n}_y+1}\right\rangle + W_g\left|\varphi_{\mathrm{n}_x,\mathrm{n}_y-1}\right\rangle + W_h\left|\varphi_{\mathrm{n}_x,\mathrm{n}_y-3}\right\rangle\right) \\
&-\frac{1}{4}\hbar\omega_y\delta_y\left(W_i\left|\varphi_{\mathrm{n}_x,\mathrm{n}_y+4}\right\rangle + W_j\left|\varphi_{\mathrm{n}_x,\mathrm{n}_y+2}\right\rangle + W_k\left|\varphi_{\mathrm{n}_x,\mathrm{n}_y-2}\right\rangle + W_l\left|\varphi_{\mathrm{n}_x,\mathrm{n}_y-4}\right\rangle\right) \\
&-\frac{1}{\sqrt{2^3}}\hbar\omega_{21}\left(W_m\left|\varphi_{\mathrm{n}_x+2,\mathrm{n}_y+1}\right\rangle + W_n\left|\varphi_{\mathrm{n}_x,\mathrm{n}_y+1}\right\rangle + W_o\left|\varphi_{\mathrm{n}_x-2,\mathrm{n}_y+1}\right\rangle\right. \\
&\qquad\left. + W_p\left|\varphi_{\mathrm{n}_x+2,\mathrm{n}_y-1}\right\rangle + W_q\left|\varphi_{\mathrm{n}_x,\mathrm{n}_y-1}\right\rangle + W_r\left|\varphi_{\mathrm{n}_x-2,\mathrm{n}_y-1}\right\rangle\right) \\
&-\frac{1}{4}\hbar\omega_{22}\left(W_s\left|\varphi_{\mathrm{n}_x+2,\mathrm{n}_y+2}\right\rangle + W_t\left|\varphi_{\mathrm{n}_x-2,\mathrm{n}_y+2}\right\rangle + W_u\left|\varphi_{\mathrm{n}_x,\mathrm{n}_y+2}\right\rangle + W_v\left|\varphi_{\mathrm{n}_x+2,\mathrm{n}_y-2}\right\rangle\right. \\
&\qquad\left. + W_w\left|\varphi_{\mathrm{n}_x-2,\mathrm{n}_y-2}\right\rangle + W_x\left|\varphi_{\mathrm{n}_x,\mathrm{n}_y-2}\right\rangle + W_y\left|\varphi_{\mathrm{n}_x+2,\mathrm{n}_y}\right\rangle + W_z\left|\varphi_{\mathrm{n}_x-2,\mathrm{n}_y}\right\rangle\right)
\end{aligned}
\tag{D.1}
$$

with:

$$
\begin{aligned}
W_a &= \frac{\sqrt{\mathrm{n}_x+1}\sqrt{\mathrm{n}_x+2}\sqrt{\mathrm{n}_x+3}\sqrt{\mathrm{n}_x+4}}{E_{\mathrm{n}_x}-E_{\mathrm{n}_x+4}} \\
W_b &= \frac{\sqrt{\mathrm{n}_x+1}\sqrt{\mathrm{n}_x+2}(4\mathrm{n}_x+6)}{E_{\mathrm{n}_x}-E_{\mathrm{n}_x+2}} \\
W_c &= \frac{\sqrt{\mathrm{n}_x}\sqrt{\mathrm{n}_x-1}(4\mathrm{n}_x-1)}{E_{\mathrm{n}_x}-E_{\mathrm{n}_x-2}} \\
W_d &= \frac{\sqrt{\mathrm{n}_x}\sqrt{\mathrm{n}_x-1}\sqrt{\mathrm{n}_x-2}\sqrt{\mathrm{n}_x-3}}{E_{\mathrm{n}_x}-E_{\mathrm{n}_x-4}}
\end{aligned}
\tag{D.2}
$$

$$
\begin{aligned}
W_e &= \frac{\sqrt{\mathrm{n}_y+1}\sqrt{\mathrm{n}_y+2}\sqrt{\mathrm{n}_y+3}}{E_{\mathrm{n}_y}-E_{\mathrm{n}_y+3}} \\
W_f &= \frac{3\sqrt{\left(\mathrm{n}_y+1\right)^3}}{E_{\mathrm{n}_y}-E_{\mathrm{n}_y+1}} \\
W_g &= \frac{3\sqrt{\mathrm{n}_y^3}}{E_{\mathrm{n}_y}-E_{\mathrm{n}_y-1}} \\
W_h &= \frac{\sqrt{\mathrm{n}_y}\sqrt{\mathrm{n}_y-1}\sqrt{\mathrm{n}_y-2}}{E_{\mathrm{n}_y}-E_{\mathrm{n}_y-4}}
\end{aligned}
\tag{D.3}
$$

$$
\begin{aligned}
W_i &= \frac{\sqrt{\mathrm{n}_y+1}\sqrt{\mathrm{n}_y+2}\sqrt{\mathrm{n}_y+3}\sqrt{\mathrm{n}_y+4}}{E_{\mathrm{n}_y}-E_{\mathrm{n}_y+4}} \\
W_j &= \frac{\sqrt{\mathrm{n}_y+1}\sqrt{\mathrm{n}_y+2}\left(4\mathrm{n}_y+6\right)}{E_{\mathrm{n}_y}-E_{\mathrm{n}_y+2}} \\
W_k &= \frac{\sqrt{\mathrm{n}_y}\sqrt{\mathrm{n}_y-1}\left(4\mathrm{n}_y-1\right)}{E_{\mathrm{n}_y}-E_{\mathrm{n}_y-2}} \\
W_l &= \frac{\sqrt{\mathrm{n}_y}\sqrt{\mathrm{n}_y-1}\sqrt{\mathrm{n}_y-2}\sqrt{\mathrm{n}_y-3}}{E_{\mathrm{n}_y}-E_{\mathrm{n}_y-4}}
\end{aligned}
\tag{D.4}
$$

$$
\begin{aligned}
W_m &= \frac{\sqrt{\mathrm{n}_x+1}\sqrt{\mathrm{n}_x+2}\sqrt{\mathrm{n}_y}}{E_{\mathrm{n}_x}+E_{\mathrm{n}_y}-E_{\mathrm{n}_x+2}-E_{\mathrm{n}_y+1}} \\
W_n &= \frac{(2\mathrm{n}_x+1)\sqrt{\mathrm{n}_y+1}}{E_{\mathrm{n}_y}-E_{\mathrm{n}_y-1}} \\
W_o &= \frac{\sqrt{\mathrm{n}_x}\sqrt{\mathrm{n}_x-1}\sqrt{\mathrm{n}_y+1}}{E_{\mathrm{n}_x}+E_{\mathrm{n}_y}-E_{\mathrm{n}_x-2}-E_{\mathrm{n}_y+1}} \\
W_p &= \frac{\sqrt{\mathrm{n}_x+1}\sqrt{\mathrm{n}_x+2}\sqrt{\mathrm{n}_y}}{E_{\mathrm{n}_x}+E_{\mathrm{n}_y}-E_{\mathrm{n}_x+2}-E_{\mathrm{n}_y-1}} \\
W_q &= \frac{(2\mathrm{n}_x+1)\sqrt{\mathrm{n}_y}}{E_{\mathrm{n}_y}-E_{\mathrm{n}_y-1}} \\
W_r &= \frac{\sqrt{\mathrm{n}_x}\sqrt{\mathrm{n}_x-1}\sqrt{\mathrm{n}_y}}{E_{\mathrm{n}_x}+E_{\mathrm{n}_y}-E_{\mathrm{n}_x-2}-E_{\mathrm{n}_y-1}}
\end{aligned}
\tag{D.5}
$$

$$
\begin{aligned}
W_s &= \frac{\sqrt{\mathrm{n}_x+1}\sqrt{\mathrm{n}_x+2}\sqrt{\mathrm{n}_y+1}\sqrt{\mathrm{n}_y+2}}{E_{\mathrm{n}_x}+E_{\mathrm{n}_y}-E_{\mathrm{n}_x+2}-E_{\mathrm{n}_y+2}} \\
W_t &= \frac{\sqrt{\mathrm{n}_x}\sqrt{\mathrm{n}_x-1}\sqrt{\mathrm{n}_y+1}\sqrt{\mathrm{n}_y+2}}{E_{\mathrm{n}_x}+E_{\mathrm{n}_y}-E_{\mathrm{n}_x-2}-E_{\mathrm{n}_y+2}} \\
W_u &= \frac{(2\mathrm{n}_x+1)\sqrt{\mathrm{n}_y+1}\sqrt{\mathrm{n}_y+2}}{E_{\mathrm{n}_y}-E_{\mathrm{n}_y+2}} \\
W_v &= \frac{\sqrt{\mathrm{n}_x+1}\sqrt{\mathrm{n}_x+2}\sqrt{\mathrm{n}_y}\sqrt{\mathrm{n}_y-1}}{E_{\mathrm{n}_x}+E_{\mathrm{n}_y}-E_{\mathrm{n}_x+2}-E_{\mathrm{n}_y-2}} \\
W_w &= \frac{\sqrt{\mathrm{n}_x}\sqrt{\mathrm{n}_x-1}\sqrt{\mathrm{n}_y}\sqrt{\mathrm{n}_y-1}}{E_{\mathrm{n}_x}+E_{\mathrm{n}_y}-E_{\mathrm{n}_x-2}-E_{\mathrm{n}_y-2}} \\
W_x &= \frac{(2\mathrm{n}_x+1)\sqrt{\mathrm{n}_y}\sqrt{\mathrm{n}_y-1}}{E_{\mathrm{n}_y}-E_{\mathrm{n}_y-2}} \\
W_y &= \frac{\sqrt{\mathrm{n}_x+1}\sqrt{\mathrm{n}_x+2}\left(\mathrm{n}_y+1\right)}{E_{\mathrm{n}_x}-E_{\mathrm{n}_x+2}} \\
W_z &= \frac{\sqrt{\mathrm{n}_x}\sqrt{\mathrm{n}_x-1}\left(\mathrm{n}_y+1\right)}{E_{\mathrm{n}_x}-E_{\mathrm{n}_x-2}}
\end{aligned}
\tag{D.6}
$$

Bibliography

[1] Richard P. Feynman. "Simulating physics with computers". In: *International Journal of Theoretical Physics* 21.6-7 (1982), pp. 467–488.
DOI: 10.1007/BF02650179.
Referenced in pages 11, 28

[2] P.W. Shor. "Algorithms for quantum computation: discrete logarithms and factoring". In: *Foundations of Computer Science, 1994 Proceedings., 35th Annual Symposium on*. 1994, pp. 124–134.
DOI: 10.1109/SFCS.1994.365700.
Referenced in pages 11, 28

[3] Lov K. Grover. "A Fast Quantum Mechanical Algorithm for Database Search". In: *Proceedings of the Twenty-eighth Annual ACM Symposium on Theory of Computing*. STOC '96. Philadelphia, Pennsylvania, USA: ACM, 1996, pp. 212–219.
DOI: 10.1145/237814.237866.
Referenced in pages 11, 28

[4] K. Temme et al. "Quantum Metropolis sampling". In: *Nature* 471.7336 (Mar. 2011), pp. 87–90.
DOI: 10.1038/nature09770.
Referenced in pages 11, 28

[5] Adriano Barenco et al. "Elementary gates for quantum computation". In: *Phys. Rev. A* 52 (5 1995), pp. 3457–3467.
DOI: 10.1103/PhysRevA.52.3457.
Referenced in pages 12, 28

[6] David P. DiVincenzo. "The Physical Implementation of Quantum Computation". In: *arXiv preprint quant-ph/0002077* (2000).
EPRINT: http://arxiv.org/abs/quant-ph?0002077.
Referenced in pages 12, 28

[7] A. Lupaşcu et al. "Nondestructive Readout for a Superconducting Flux Qubit". In: *Phys. Rev. Lett.* 93 (17 2004), p. 177006.
DOI: 10.1103/PhysRevLett.93.177006.
Referenced in pages 12, 29

[8] Michel H. Devoret et al. "Resonant Activation from the Zero-Voltage State of a Current-Biased Josephson Junction". In: *Phys. Rev. Lett.* 53 (13 1984), pp. 1260–1263.
DOI: 10.1103/PhysRevLett.53.1260.
Referenced in pages 12, 29

[9] Michel H. Devoret, John M. Martinis, and John Clarke. "Measurements of Macroscopic Quantum Tunneling out of the Zero-Voltage State of a Current-Biased Josephson Junction". In: *Phys. Rev. Lett.* 55 (18 1985), pp. 1908–1911.
DOI: 10.1103/PhysRevLett.55.1908.
Referenced in pages 12, 29

[10] John M. Martinis, Michel H. Devoret, and John Clarke. "Energy-Level Quantization in the Zero-Voltage State of a Current-Biased Josephson Junction". In: *Phys. Rev. Lett.* 55 (15 1985), pp. 1543–1546.
DOI: 10.1103/PhysRevLett.55.1543.
Referenced in pages 12, 29

[11] Y. Nakamura, Yu. A. Pashkin, and J. S. Tsai. "Coherent control of macroscopic quantum states in a single-Cooper-pair box". In: *Nature* 398.6730 (Apr. 1999), pp. 786–788.
DOI: 10.1038/19718.
Referenced in pages 12, 29

[12] J. Claudon et al. "Coherent Oscillations in a Superconducting Multilevel Quantum System". In: *Phys. Rev. Lett.* 93 (18 2004), p. 187003.
DOI: 10.1103/PhysRevLett.93.187003.
Referenced in pages 12, 29, 201, 206

[13] F. Lecocq et al. "Coherent Frequency Conversion in a Superconducting Artificial Atom with Two Internal Degrees of Freedom". In: *Phys. Rev. Lett.* 108 (10 2012), p. 107001.
DOI: 10.1103/PhysRevLett.108.107001.
Referenced in pages 12, 16, 29, 33, 60, 63, 204

[14] JohnM. Martinis. "Superconducting phase qubits". English. In: *Quantum Information Processing* 8.2-3 (2009), pp. 81–103.
DOI: 10.1007/s11128-009-0105-1.
Referenced in pages 12, 29

[15] D Vion et al. "Manipulating the quantum state of an electrical circuit". In: *Science* 296.5569 (2002), pp. 886–889.
DOI: 10.1126/science.1069372.
Referenced in pages 12, 29

[16] O. Buisson and F.W.J. Hekking. "Entangled States in a Josephson Charge Qubit Coupled to a Superconducting Resonator". In: *Macroscopic Quantum Coherence and Quantum Computing*. Ed. by DmitriV. Averin, Berardo Ruggiero, and Paolo Silvestrini. Springer US, 2001, pp. 137–145.
DOI: 10.1007/978-1-4615-1245-5_14.
Referenced in pages 12, 29

[17] Franck Balestro M. G. Vergniory Frank W. J. Hekking Olivier Buisson. "Cooper pair box coupled to a current-biased Josephson junction". In: *Electronic Correlations: From Meso- to Nano-physics*. Ed. by G. Montambaux T. Martin and J. Trân Thanh Vân ed. EDP Sciences, Les Ulis, 2001, p. 515.
EPRINT: http://arxiv.org/abs/cond-mat/0201284.
Referenced in pages 12, 29

[18] Jens Koch et al. "Charge-insensitive qubit design derived from the Cooper pair box". In: *Phys. Rev. A* 76.4 (2007).
DOI: 10.1103/physreva.76.042319.
Referenced in pages 12, 13, 29, 30, 125, 177, 198

[19] Jerry M. Chow et al. "Universal Quantum Gate Set Approaching Fault-Tolerant Thresholds with Superconducting Qubits". In: *Phys. Rev. Lett.* 109 (6 2012), p. 060501.
DOI: 10.1103/PhysRevLett.109.060501.
Referenced in pages 13, 29

[20] Josephine B. Chang et al. "Improved superconducting qubit coherence using titanium nitride". In: *Applied Physics Letters* 103.1, 012602 (2013).
DOI: 10.1063/1.4813269.
Referenced in pages 13, 29

[21] Hanhee Paik et al. "Observation of High Coherence in Josephson Junction Qubits Measured in a Three-Dimensional Circuit QED Architecture". In: *Phys. Rev. Lett.* 107 (24 2011), p. 240501.
DOI: 10.1103/PhysRevLett.107.240501.
Referenced in pages 13, 29

[22] Chad Rigetti et al. "Superconducting qubit in a waveguide cavity with a coherence time approaching 0.1 ms". In: *Phys. Rev. B* 86 (10 2012), p. 100506.
DOI: 10.1103/PhysRevB.86.100506.
Referenced in pages 13, 29, 198

[23] Vladimir E. Manucharyan et al. "Fluxonium: Single Cooper-Pair Circuit Free of Charge Offsets". In: *Science* 326.5949 (2009), pp. 113–116.
DOI: 10.1126/science.1175552.
Referenced in pages 13, 29

[24] Vladimir E. Manucharyan et al. "Evidence for coherent quantum phase slips across a Josephson junction array". In: *Phys. Rev. B* 85 (2 2012), p. 024521.
DOI: 10.1103/PhysRevB.85.024521.
Referenced in pages 13, 29

[25] Nicholas A. Masluk et al. "Microwave Characterization of Josephson Junction Arrays: Implementing a Low Loss Superinductance". In: *Phys. Rev. Lett.* 109 (13 2012), p. 137002.
DOI: 10.1103/PhysRevLett.109.137002.
Referenced in pages 13, 29

[26] Ioan M. Pop et al. "Coherent suppression of electromagnetic dissipation due to superconducting quasiparticles". In: *Nature* 508.7496 (Apr. 2014), pp. 369–372.
DOI: 10.1038/nature13017.
Referenced in pages 13, 29

[27] M. Brune et al. "Manipulation of photons in a cavity by dispersive atom-field coupling: Quantum-nondemolition measurements and generation of "Schrödinger cat" states". In: *Phys. Rev. A* 45 (7 1992), pp. 5193–5214.
DOI: 10.1103/PhysRevA.45.5193.
Referenced in pages 13, 30, 177, 193

[28] M. D. Levenson et al. "Quantum Nondemolition Detection of Optical Quadrature Amplitudes". In: *Phys. Rev. Lett.* 57 (20 1986), pp. 2473–2476.
DOI: 10.1103/PhysRevLett.57.2473.
Referenced in pages 13, 30

[29] N. Imoto, S. Watkins, and Y. Sasaki. "A nonlinear optical-fiber interferometer for nondemolitional measurement of photon number". In: *Optics Communications* 61.2 (1987), pp. 159 –163.
DOI: 10.1016/0030-4018(87)90240-9.
Referenced in pages 13, 30

[30] A. La Porta, R. E. Slusher, and B. Yurke. "Back-Action Evading Measurements of an Optical Field Using Parametric Down Conversion". In: *Phys. Rev. Lett.* 62 (1 1989), pp. 28–31.
DOI: 10.1103/PhysRevLett.62.28.
Referenced in pages 13, 30

[31] Philippe Grangier, Jean-Fran çois Roch, and Gérard Roger. "Observation of backaction-evading measurement of an optical intensity in a three-level atomic nonlinear system". In: *Phys. Rev. Lett.* 66 (11 1991), pp. 1418–1421.
DOI: 10.1103/PhysRevLett.66.1418.
Referenced in pages 13, 30

[32] E.M.Purcell. "Proceedings of the American Physical Society". In: *Phys. Rev.* 69 (11-12 1946), p. 681.
DOI: 10.1103/PhysRev.69.674.2.
Referenced in pages 13, 30

[33] A. Wallraff et al. "Approaching Unit Visibility for Control of a Superconducting Qubit with Dispersive Readout". In: *Phys. Rev. Lett.* 95 (6 2005), p. 060501.
DOI: 10.1103/PhysRevLett.95.060501.
Referenced in pages 13, 30

[34] Maxime Boissonneault, J. M. Gambetta, and Alexandre Blais. "Dispersive regime of circuit QED: Photon-dependent qubit dephasing and relaxation rates". In: *Phys. Rev. A* 79 (1 2009), p. 013819.
DOI: 10.1103/PhysRevA.79.013819.
Referenced in pages 13, 30

[35] Carlton M. Caves. "Quantum limits on noise in linear amplifiers". In: *Phys. Rev. D* 26 (8 1982), pp. 1817–1839.
DOI: 10.1103/PhysRevD.26.1817.
Referenced in pages 13, 30

[36] M. Hatridge et al. "Quantum Back-Action of an Individual Variable-Strength Measurement". In: *Science* 339.6116 (2013), pp. 178–181.
DOI: 10.1126/science.1226897.
Referenced in pages 13, 30, 89

[37] Christopher E Langer. "High fidelity quantum information processing with trapped ions". University of Colorado, 2006.
Referenced in pages 14, 30

[38] Hans G. Dehmelt. "Proposed 10^{14} D $\nu < \nu$ Laser Florescence Spectroscopy on Ti^{+} Mono-Ion". In: vol. 20. 1975, p. 1521.
Referenced in pages 14, 30

[39] D. J. Wineland et al. "Double-resonance and optical-pumping experiments on electromagnetically confined, laser-cooled ions". In: *Opt. Lett.* 5.6 (1980), pp. 245–247.
DOI: 10.1364/OL.5.000245.
Referenced in pages 14, 30

[40] Warren Nagourney, Jon Sandberg, and Hans Dehmelt. "Shelved optical electron amplifier: Observation of quantum jumps". In: *Phys. Rev. Lett.* 56 (26 1986), pp. 2797–2799.
DOI: 10.1103/PhysRevLett.56.2797.
Referenced in pages 14, 30

[41] Th. Sauter et al. "Observation of Quantum Jumps". In: *Phys. Rev. Lett.* 57 (14 1986), pp. 1696–1698.
DOI: 10.1103/PhysRevLett.57.1696.
Referenced in pages 14, 15, 30, 32

[42] J. C. Bergquist et al. "Observation of Quantum Jumps in a Single Atom". In: *Phys. Rev. Lett.* 57 (14 1986), pp. 1699–1702.
DOI: 10.1103/PhysRevLett.57.1699.
Referenced in pages 14, 30

[43] D. Leibfried et al. "Quantum dynamics of single trapped ions". In: *Rev. Mod. Phys.* 75 (1 2003), pp. 281–324.
DOI: 10.1103/RevModPhys.75.281.
Referenced in pages 14, 15, 31, 32

[44] Alexandre Blais et al. "Cavity quantum electrodynamics for superconducting electrical circuits: An architecture for quantum computation". In: *Phys. Rev. A* 69 (6 2004), p. 062320.
DOI: 10.1103/PhysRevA.69.062320.
Referenced in pages 16, 33, 72

[45] I. Diniz et al. "Ultrafast quantum nondemolition measurements based on a diamond-shaped artificial atom". In: *Phys. Rev. A* 87 (3 2013), p. 033837.
DOI: 10.1103/PhysRevA.87.033837.
Referenced in pages 18, 35, 85, 212, 216, 220

[46] Delsol Benjamin. "Élaboration et Caractérisation de couches minces supraconductrices epitaxiées de rhenium sur saphir". Université de Grenoble, 2015.
Referenced in pages 21, 39, 123, 145, 167

[47] B.D. Josephson. "Possible new effects in superconductive tunnelling". In: *Physics Letters* 1.7 (1962), pp. 251 –253.
DOI: 10.1016/0031-9163(62)91369-0.
Referenced in page 45

[48] B. D. Josephson. "Coupled Superconductors". In: *Rev. Mod. Phys.* 36 (1 1964), pp. 216–220.
DOI: 10.1103/RevModPhys.36.216.
Referenced in page 46

[49] Michael Tinkham. *Introduction to superconductivity*. Courier Dover Publications, 2012.
Referenced in pages 46, 50, 143

[50] Inder J Bahl. *Lumped elements for RF and microwave circuits*. Artech house, 2003.
Referenced in pages 47, 127

[51] Michel H. Devoret. "Course 10 Quantum fluctuations in electrical circuits". In: *Quantum Fluctuations École d' été de Physique des Houches Session LXIII*. Ed. by E. Giacobino S. Reynaud and eds J. Zinn-Justin. Vol. 63. Les Houches. Elsevier, 1997, pp. 355 –386.
Referenced in pages 47, 72

[52] R. C. Jaklevic et al. "Quantum Interference Effects in Josephson Tunneling". In: *Phys. Rev. Lett.* 12 (7 1964), pp. 159–160.
DOI: 10.1103/PhysRevLett.12.159.
Referenced in page 48

[53] Florent Lecocq. "Quantum dynamics in a dcSQUID : from the phase qubit to the 2D quantum oscillator". Université de Grenoble, May 2011.
Referenced in pages 48, 52, 63, 65, 126

[54] A.A. Houck et al. "Life after charge noise: recent results with transmon qubits". In: *Quantum Information Processing* 8.2-3 (2009), pp. 105–115.
DOI: 10.1007/s11128-009-0100-6.
Referenced in pages 52, 192

[55] Valérie Lefevre-Seguin et al. "Thermal activation of a hysteretic dc superconducting quantum interference device from its different zero-voltage states". In: *Phys. Rev. B* 46 (9 1992), pp. 5507–5522.
DOI: 10.1103/PhysRevB.46.5507.
Referenced in page 53

[56] Julien Claudon. "Coherent oscillations in a superconducting quantum circuit: the dc SQUID". Université Joseph-Fourier - Grenoble I, Sept. 2005.
Referenced in pages 57, 75, 186, 188, 201

[57] James Stewart. *Multivariable calculus: concepts and contexts*. Cengage Learning, 2009.
Referenced in page 57

[58] Claude Cohen-Tannoudji, Bernard Diu, Franck Laloë, et al. *Mécanique quantique*. 1986.

Referenced in pages 61, 125, 187

[59] P. Weinberger. "John Kerr and his effects found in 1877 and 1878". In: *Philosophical Magazine Letters* 88.12 (2008), pp. 897–907.
DOI: 10.1080/09500830802526604.

Referenced in page 64

[60] J.R. Johansson, P.D. Nation, and Franco Nori. "QuTiP 2: A Python framework for the dynamics of open quantum systems". In: *Computer Physics Communications* 184.4 (2013), 1234–1240.
DOI: 10.1016/j.cpc.2012.11.019.

Referenced in page 67

[61] David M Pozar. *Microwave engineering*. John Wiley & Sons, 2009.

Referenced in pages 71, 119, 155, 228, 230, 232

[62] Bernard Yurke and John S. Denker. "Quantum network theory". In: *Phys. Rev. A* 29 (3 1984), pp. 1419–1437.
DOI: 10.1103/PhysRevA.29.1419.

Referenced in page 72

[63] C. W. Gardiner and M. J. Collett. "Input and output in damped quantum systems: Quantum stochastic differential equations and the master equation". In: *Phys. Rev. A* 31 (6 1985), pp. 3761–3774.
DOI: 10.1103/PhysRevA.31.3761.

Referenced in page 78

[64] B Peropadre et al. "Scattering of coherent states on a single artificial atom". In: *New Journal of Physics* 15.3 (2013), p. 035009.
DOI: doi:10.1088/1367-2630/15/3/035009.

Referenced in page 78

[65] B. R. Johnson et al. "Quantum non-demolition detection of single microwave photons in a circuit". In: *Nat Phys* 6.9 (Sept. 2010), pp. 663–667.
DOI: 10.1038/nphys1710.

Referenced in page 81

[66] J. M. Chow et al. "Detecting highly entangled states with a joint qubit readout". In: *Phys. Rev. A* 81 (6 2010), p. 062325.
DOI: 10.1103/PhysRevA.81.062325.

Referenced in page 81

[67] J.M. Raimond. *What is a QND measurements*. http://www.cqed.org/english/rydberg/resonant/qnd/qnd.html. 1999.

Referenced in page 82

[68] Serge Haroche and Jean-Michel Raimond. *Exploring the quantum: atoms, cavities, and photons*. Oxford University Press, USA, 2013.

Referenced in page 82

[69] H. Nyquist. "Thermal Agitation of Electric Charge in Conductors". In: *Phys. Rev.* 32 (1 1928), pp. 110–113.
DOI: 10.1103/PhysRev.32.110.
Referenced in pages 84, 111

[70] Roy J. Glauber. "Coherent and Incoherent States of the Radiation Field". In: *Phys. Rev.* 131 (6 1963), pp. 2766–2788.
DOI: 10.1103/PhysRev.131.2766.
Referenced in page 85

[71] Leonard Mandel and Emil Wolf. *Optical coherence and quantum optics*. Cambridge university press, 1995.
Referenced in page 85

[72] Igor Diniz. "Electrodynamique quantique des les atomes artificiels supraconducteurs". Université de Grenoble, 2012.
Referenced in page 87

[73] J. E. Johnson et al. "Heralded State Preparation in a Superconducting Qubit". In: *Phys. Rev. Lett.* 109 (5 2012), p. 050506.
DOI: 10.1103/PhysRevLett.109.050506.
Referenced in page 88

[74] Evan Jeffrey et al. "Fast Accurate State Measurement with Superconducting Qubits". In: *Phys. Rev. Lett.* 112 (19 2014), p. 190504.
DOI: 10.1103/PhysRevLett.112.190504.
Referenced in page 89

[75] Frank Pobell. *Matter and methods at low temperatures*. Vol. 2. Springer, 2007.
Referenced in page 94

[76] Daniel F Walls and Gerard J Milburn. *Quantum optics*. Springer, 2007.
Referenced in page 95

[77] J. B. Johnson. "Thermal Agitation of Electricity in Conductors". In: *Phys. Rev.* 32 (1 1928), pp. 97–109.
DOI: 10.1103/PhysRev.32.97.
Referenced in page 96

[78] A. Van Der Ziel. *Noise in Solid State Devices and Circuits*. Wiley, 1986.
Referenced in page 97

[79] D. I. Schuster et al. "ac Stark Shift and Dephasing of a Superconducting Qubit Strongly Coupled to a Cavity Field". In: *Phys. Rev. Lett.* 94 (12 2005), p. 123602.
DOI: 10.1103/PhysRevLett.94.123602.
Referenced in pages 98, 193, 197

[80] H.T. Friis. "Noise Figures of Radio Receivers". In: *Proceedings of the IRE* 32.7 (1944), pp. 419–422.
DOI: 10.1109/JRPROC.1944.232049.
Referenced in page 98

[81] T. Mimura. "The early history of the high electron mobility transistor (HEMT)". In: *Microwave Theory and Techniques, IEEE Transactions on* 50.3 (2002), pp. 780–782.
DOI: 10.1109/22.989961.
Referenced in page 98

[82] William H Press. *Numerical recipes 3rd edition: The art of scientific computing*. Cambridge university press, 2007.
Referenced in pages 102, 163, 189

[83] Abraham. Savitzky and M. J. E. Golay. "Smoothing and Differentiation of Data by Simplified Least Squares Procedures." In: *Analytical Chemistry* 36.8 (1964), pp. 1627–1639.
DOI: 10.1021/ac60214a047.
Referenced in pages 102, 163, 189

[84] Stéfan van der Walt, S. Chris Colbert, and Gaël Varoquaux. "The NumPy Array: A Structure for Efficient Numerical Computation". In: *Computing in Science & Engineering* 13.2 (2011), pp. 22–30.
DOI: 10.1109/MCSE.2011.37.
Referenced in page 113

[85] Eric Jones, Travis Oliphant, Pearu Peterson, et al. *SciPy: Open source scientific tools for Python*. http://www.scipy.org. 2001.
Referenced in page 113

[86] John D. Hunter. "Matplotlib: A 2D Graphics Environment". In: *Computing in Science & Engineering* 9.3 (2007), pp. 90–95.
DOI: 10.1109/MCSE.2007.55.
Referenced in page 113

[87] SymPy Development Team. *SymPy: Python library for symbolic mathematics*. http://www.sympy.org. 2014.
Referenced in page 113

[88] Fernando Pérez and Brian E. Granger. "IPython: A System for Interactive Scientific Computing". In: *Computing in Science & Engineering* 9.3 (2007), pp. 21–29.
DOI: 10.1109/MCSE.2007.53.
Referenced in page 113

[89] Thomas Williams, Colin Kelley, and many others. *Gnuplot 4.4: an interactive plotting program*. http://gnuplot.sourceforge.net. 2010.
Referenced in page 115

[90] Luke Campagnola. *PyQtGraph - Scientific Graphics and GUI Library for Python*. www.pyqtgraph.org. 2014.
Referenced in page 115

[91] R. Barends et al. "Minimizing quasiparticle generation from stray infrared light in superconducting quantum circuits". In: *Applied Physics Letters* 99.11, 113507 (2011).
DOI: 10.1063/1.3638063.
Referenced in pages 121, 167, 192, 214, 218

[92] C. Song et al. "Reducing microwave loss in superconducting resonators due to trapped vortices". In: *Applied Physics Letters* 95.23, 232501 (2009).
DOI: 10.1063/1.3271523.
Referenced in page 121

[93] D. Bothner et al. "Improving the performance of superconducting microwave resonators in magnetic fields". In: *Applied Physics Letters* 98.10, 102504 (2011).
DOI: 10.1063/1.3560480.
Referenced in pages 121, 168

[94] D. Bothner et al. "Reducing vortex losses in superconducting microwave resonators with microsphere patterned antidot arrays". In: *Applied Physics Letters* 100.1, 012601 (2012).
DOI: 10.1063/1.3673869.
Referenced in pages 121, 168

[95] Hung P Quach and Talso C.P Chui. "Low temperature magnetic properties of Metglas 2714A and its potential use as core material for {EMI} filters". In: *Cryogenics* 44.6–8 (2004). 2003 Space Cryogenics Workshop, pp. 445 –449.
DOI: 10.1016/j.cryogenics.2004.01.006.
Referenced in page 122

[96] C. M. Quintana et al. "Characterization and reduction of microfabrication-induced decoherence in superconducting quantum circuits". In: *Applied Physics Letters* 105.6, 062601 (2014).
DOI: 10.1063/1.4893297.
Referenced in page 125

[97] Io-Chun Hoi et al. "Giant Cross-Kerr Effect for Propagating Microwaves Induced by an Artificial Atom". In: *Phys. Rev. Lett.* 111 (5 2013), p. 053601.
DOI: 10.1103/PhysRevLett.111.053601.
Referenced in page 125

[98] Koki Watanabe et al. "Kinetic Inductance of Superconducting Coplanar Waveguides". In: *Japanese Journal of Applied Physics* 33.10R (1994), p. 5708.
DOI: 10.1143/JJAP.33.5708.
Referenced in page 126

[99] Benjamin A Mazin. "Microwave kinetic inductance detectors". California Institute of Technology, 2004.
Referenced in pages 126, 154, 230

[100] G. Mende et al. "Oxidation of etched silicon in air at room temperature; Measurements with ultrasoft X-ray photoelectron spectroscopy (ESCA) and neutron activation analysis". In: *Surface Science* 128.1 (1983), pp. 169 –175.
DOI: 10.1016/0039-6028(83)90388-6.
Referenced in page 134

[101] S. I. Raider, R. Flitsch, and M. J. Palmer. "Oxide Growth on Etched Silicon in Air at Room Temperature". In: *Journal of The Electrochemical Society* 122.3 (1975), pp. 413–418.
DOI: 10.1149/1.2134225.
Referenced in page 134

[102] Sydney Chapman and Thomas George Cowling. *The mathematical theory of non-uniform gases: an account of the kinetic theory of viscosity, thermal conduction and diffusion in gases*. Cambridge university press, 1970.
Referenced in page 137

[103] Carl Rod Nave. *Mean Free Path, Molecular Collisions*. http://hyperphysics.phy-astr.gsu.edu/hbase/kinetic/menfre.html. 1998.
Referenced in page 137

[104] Richard E Honig and Harvey O Hook. "Vapor pressure data for some common gases". In: *RCA review* 21.3 (1960), pp. 360–368.
Referenced in page 137

[105] J. C. Slater. "Atomic Radii in Crystals". In: *The Journal of Chemical Physics* 41.10 (1964), pp. 3199–3204.
DOI: 10.1063/1.1725697.
Referenced in page 137

[106] G. J. Dolan. "Offset masks for lift-off photoprocessing". In: *Applied Physics Letters* 31.5 (1977), pp. 337–339.
DOI: 10.1063/1.89690.
Referenced in page 137

[107] Florent Lecocq et al. "Junction fabrication by shadow evaporation without a suspended bridge". In: *Nanotechnology* 22.31 (2011), p. 315302.
DOI: 10.1088/0957-4484/22/31/315302.
Referenced in page 137

[108] Timothy Campbell et al. "Dynamics of Oxidation of Aluminum Nanoclusters using Variable Charge Molecular-Dynamics Simulations on Parallel Computers". In: *Phys. Rev. Lett.* 82 (24 1999), pp. 4866–4869.
DOI: 10.1103/PhysRevLett.82.4866.
Referenced in page 140

[109] Stefan Jahn. *Coplanar waveguides (CPW)*. http://qucs.sourceforge.net/tech/node86.html. 2007.
Referenced in page 147

[110] Kuldip C Gupta, Ramesh Garg, and Inder J Bahl. *Microstrip lines and slotlines*. Artech house, 1979.
Referenced in page 147

[111] Robert E Collin. *Foundations for microwave engineering*. John Wiley & Sons, 2007.
Referenced in page 147

[112] Rami Barends. "Photon-detecting superconducting resonators". Delft University of Technology, 2009.

Referenced in page 149

[113] C.L. Holloway and Edward F. Kuester. "A quasi-closed form expression for the conductor loss of CPW lines, with an investigation of edge shape effects". In: *Microwave Theory and Techniques, IEEE Transactions on* 43.12 (1995), pp. 2695–2701. DOI: 10.1109/22.477846.

Referenced in page 149

[114] E. F. C. Driessen et al. "Strongly Disordered TiN and NbTiN *s*-Wave Superconductors Probed by Microwave Electrodynamics". In: *Phys. Rev. Lett.* 109 (10 2012), p. 107003. DOI: 10.1103/PhysRevLett.109.107003.

Referenced in page 149

[115] A. Megrant et al. "Planar superconducting resonators with internal quality factors above one million". In: *Applied Physics Letters* 100.11, 113510 (2012). DOI: 10.1063/1.3693409.

Referenced in pages 157, 227

[116] M. S. Khalil et al. "An analysis method for asymmetric resonator transmission applied to superconducting devices". In: *Journal of Applied Physics* 111.5, 054510 (2012). DOI: http://dx.doi.org/10.1063/1.3692073.

Referenced in pages 157, 227

[117] M. Baur R. Bianchetti S. Filipp J. M. Fink P. J. Leek G. Puebla L. Steffen M. Göppl A. Fragner and A. Wallraff. "Coplanar waveguide resonators for circuit quantum electrodynamics". In: *J. Appl. Phys* 104 (2008), p. 113904. DOI: 10.1063/1.3010859.

Referenced in page 161

[118] C. J. Gorter and H. Casimir. "The thermodynamics of the superconducting state". In: *Z. tech. Phys* 15 (1934), pp. 539–42.

Referenced in page 162

[119] Theodore Van Duzer and Charles William Turner. *Principles of superconductive devices and circuits*. Vol. 31.

Referenced in page 165

[120] D F Santavicca and D E Prober. "Impedance-matched low-pass stripline filters". In: *Measurement Science and Technology* 19.8 (2008), p. 087001. DOI: 10.1088/0957-0233/19/8/087001.

Referenced in page 167

[121] D. H. Slichter. "Quantum Jumps and Measurement Backaction in a Superconducting Qubit". University of California, Berkeley, 2011.

Referenced in page 167

[122] T.O. Klaassen et al. "Absorbing coatings and diffuse reflectors for the Herschel platform sub-millimeter spectrometers HIFI and PACS". In: *Terahertz Electronics Proceedings, 2002. IEEE Tenth International Conference on*. 2002, pp. 32–35.
DOI: 10.1109/THZ.2002.1037582.
Referenced in page 168

[123] H. Wang et al. "Improving the coherence time of superconducting coplanar resonators". In: *Applied Physics Letters* 95.23, 233508 (2009).
DOI: 10.1063/1.3273372.
Referenced in page 168

[124] E. Hoskinson et al. "Quantum Dynamics in a Camelback Potential of a dc SQUID". In: *Phys. Rev. Lett.* 102 (9 2009), p. 097004.
DOI: 10.1103/PhysRevLett.102.097004.
Referenced in page 173

[125] Martin Sandberg. *Fast-tunable resonators and quantum electrical circuits.* Chalmers University of Technology, 2009.
Referenced in page 173

[126] Christoph W Groth et al. "Kwant: a software package for quantum transport". In: *New Journal of Physics* 16.6 (2014), p. 063065.
DOI: 10.1088/1367-2630/16/6/063065.
Referenced in pages 176, 181, 182, 210

[127] D. I. Schuster et al. "Resolving photon number states in a superconducting circuit". In: *Nature* 445.7127 (Feb. 2007), pp. 515–518.
DOI: 10.1038/nature05461.
Referenced in pages 192, 197, 198

[128] J. Majer et al. "Coupling superconducting qubits via a cavity bus". In: *Nature* 449.7161 (Sept. 2007), pp. 443–447.
DOI: 10.1038/nature06184.
Referenced in pages 192, 197

[129] A. A. Houck et al. "Controlling the Spontaneous Emission of a Superconducting Transmon Qubit". In: *Phys. Rev. Lett.* 101 (8 2008), p. 080502.
DOI: 10.1103/PhysRevLett.101.080502.
Referenced in page 192

[130] John M. Martinis et al. "Decoherence in Josephson Qubits from Dielectric Loss". In: *Phys. Rev. Lett.* 95 (21 2005), p. 210503.
DOI: 10.1103/PhysRevLett.95.210503.
Referenced in page 192

[131] Lin Feng Chen et al. *Microwave electronics: measurement and materials characterization*. John Wiley & Sons, 2004.
Referenced in page 192

[132] Aaron D. O'Connell et al. "Microwave dielectric loss at single photon energies and millikelvin temperatures". In: *Applied Physics Letters* 92.11, 112903 (2008). DOI: 10.1063/1.2898887.

Referenced in page 192

[133] J. Wenner et al. "Surface loss simulations of superconducting coplanar waveguide resonators". In: *Applied Physics Letters* 99.11, 113513 (2011). DOI: 10.1063/1.3637047.

Referenced in page 192

[134] Jay Gambetta et al. "Qubit-photon interactions in a cavity: Measurement-induced dephasing and number splitting". In: *Phys. Rev. A* 74 (4 2006), p. 042318. DOI: 10.1103/PhysRevA.74.042318.

Referenced in pages 193, 194

[135] Bernard Cagnac and Jean-Pierre Faroux. *Lasers: interaction lumière-atomes*. EDP sciences, 2012.

Referenced in page 197

[136] Yong Hu et al. "Cross-Kerr-effect induced by coupled Josephson qubits in circuit quantum electrodynamics". In: *Phys. Rev. A* 84 (1 2011), p. 012329. DOI: 10.1103/PhysRevA.84.012329.

Referenced in page 212

[137] Lukas Neumeier, Martin Leib, and Michael J. Hartmann. "Single-Photon Transistor in Circuit Quantum Electrodynamics". In: *Phys. Rev. Lett.* 111 (6 2013), p. 063601. DOI: 10.1103/PhysRevLett.111.063601.

Referenced in pages 212, 217, 221

[138] Alexia Auffèves-Garnier et al. "Giant optical nonlinearity induced by a single two-level system interacting with a cavity in the Purcell regime". In: *Phys. Rev. A* 75 (5 2007), p. 053823. DOI: 10.1103/PhysRevA.75.053823.

Referenced in pages 217, 221

[139] P. J. de Visser et al. "Evidence of a Nonequilibrium Distribution of Quasiparticles in the Microwave Response of a Superconducting Aluminum Resonator". In: *Phys. Rev. Lett.* 112 (4 2014), p. 047004. DOI: 10.1103/PhysRevLett.112.047004.

Referenced in page 227

Abstract

This thesis focuses on the experimental realisation of an artificial atom with a V-shape energy level diagram. Inspired by trapped-ion experiments, we theoretically predict an ultra fast and high fidelity quantum non destructive readout of qubit state by using the V-shape artificial atom in a circuit quantum electrodynamics architecture.

To realise this experiment, we have developed an experimental setup to perform transmission measurements of our superconducting quantum circuits by heterodyne technique at very low temperatures (30 mK) and very low signal amplitude (fW). We also implemented a hardware and software environment enabling multi-tone spectroscopies and time-resolved measurements in order to control the quantum state of the artificial atom and the coherent field in the resonator. In addition, in order to optimise the experiment circuits we have characterised quarterwave microwave resonators made from aluminium and epitaxial rhenium thin films.

The original quantum device is fabricated by two inductively coupled transmons. When the coupling inductance is of the order of the Josephson inductance, we observe "in-phase" and "out-of-phase" oscillating modes of the superconducting phase across the junctions. The energy spectrum of the system, measured by two-tone spectroscopy, is magnetic flux dependent. It is precisely described by our theoretical model leading to an accurate determination of the circuit parameters. Because of their anharmonicity, in the low-energy limit, the two modes can be considered as two-level systems called qubits. At zero magnetic field, it has been observed that the two qubits become coupled only by a cross-anharmonicity. This has been revealed, through three-tone spectroscopy, by a conditional frequency shift as large as 115 MHz of one qubit transition depending on the other qubit state. All these experimental results demonstrate a V-shape energy diagram for our artificial atom which paves the way to an original and high performance read-out.

Keywords:

Quantum nano-electronic, Superconductor quantum bit, Dc-SQUID, quantum electrodynamics

Résumé

Cette thèse porte sur la réalisation expérimentale d'un atome artificiel possédant un diagramme énergétique en forme de "V". Inspirés par les expériences des ions piégés, nous avons théoriquement prédit une lecture ultra rapide et de haute fidélité de l'état d'un qubit en utilisant un atome artificiel en forme de V dans une stratégie d'électrodynamique quantique utilisant les circuits supraconducteurs.

Pour réaliser cette expérience, nous avons développé un dispositif expérimental permettant des mesures de transmissions de nos circuits quantiques supra-conducteurs par une méthode hétérodyne aux très basses températures (30 mK) et très faible amplitude (fW). Afin de contrôler l'état quantique de l'atome artificiel et le champ cohérent dans le résonateur, ce dispositif expérimental permet des spectroscopies multi-tons et des mesures résolues en temps. De plus, afin d'optimiser les circuits supraconducteurs, nous avons caractérisé des résonateurs micro-ondes quart d'ondes fabriqués à partir d'aluminium et de rhénium épitaxiés.

Le dispositif quantique original est fabriqué en couplant inductivement deux transmons. Lorsque le couplage inductif est de l'ordre de grandeur de l'inductance Josephson, nous observons des modes d'oscillations "en-phase" et "hors-phase" de la phase supraconductrice à travers les jonctions. Le spectre d'énergie du système, mesuré par des spectroscopies deux-tons, est précisément décrit par notre modèle analytique. Dû à leur anharmonicité, les deux modes peuvent être considérés comme des systèmes à deux niveaux appelés qubits dans la limite des excitations de petite énergies. À zéro champ magnétique, il a été observé que les deux qubits deviennent couplés uniquement par une anharmonicité croisée. Cela a été révélé à travers des spectroscopies trois-tons par un décalage conditionnel de la fréquence de transition de 115 MHz d'un qubit dépendant de l'état de l'autre qubit. L'ensemble de ces résultats expérimentaux démontrent que le circuit développé présente un diagramme énergétique en V. Cette nouvelle propriété ouvre la voie pour une expérience originale et de haute performance pour la lecture de l'état d'un qubit.

Mots-clefs :

Nano-électronique quantique, Bit quantique supraconducteur, SQUID-dc, électrodynamique quantique